PROPERTIES OF $[SF_3][MF_6]$ (M = Sb, As), WOF_4 DERIVATIVES, 1-ETHYL-3-METHYLIMIDAZOLIUM BIFLUORIDE, PERFLUOROCARBOXYLIC ACIDS AND PERFLUOROCARBOXYLATES

PRAVEEN CHAUDHARY
Master of Science, University of Lethbridge, 2011

A Thesis
Submitted to the School of Graduate Studies
of the University of Lethbridge
in Partial Fulfillment of the
Requirements for the Degree

DOCTOR OF PHILOSOPHY

Department of Chemistry and Biochemistry
University of Lethbridge
LETHBRIDGE, ALBERTA, CANADA

PROPERTIES OF $[SF_3][MF_6]$ (M = Sb, As), WOF_4 DERIVATIVES, 1-ETHYL-3-METHYLIMIDAZOLIUM BIFLUORIDE, PERFLUOROCARBOXYLIC ACIDS AND PERFLUOROCARBOXYLATES

PRAVEEN CHAUDHARY

Date of Defence: February 19, 2016

Dr. Michael Gerken Co-Supervisor	Professor	Ph.D.
Dr. Paul Hazendonk Co-Supervisor	Associate Professor	Ph.D.
Dr. Peter Dibble Thesis Examination Committee Member	Associate Professor	Ph.D.
Dr. Paul Hayes Thesis Examination Committee Member	Professor	Ph.D.
Dr. Adriana Predoi-Cross Thesis Examination Committee Member	Professor	Ph.D.
Dr. Carsten Jenne External Examiner University of Wuppertal, Germany	Professor	Ph.D.
Dr. Hans-Joachim Wieden Chair, Thesis Examination Committee	Associate Professor	Ph.D.

ABSTRACT

The Lewis acid chemistry of $[SF_3][MF_6]$ (M = Sb, As) salts with the nitrogen bases pyridine, acetonitrile, 1,10-phenanthroline and 4-dimethylaminopyridine (DAMP) is being explored, yielding 1:2 adducts for the mono-dentate bases and 1:1 adduct with the bidentate 1,10-phenanthroline. The crystal structures of α- and γ-$[SF_3][SbF_6]$ are characterized for the first time along with that of $[SF_3][AsF_6]$. Preliminary results for the deoxofluorination of two ketones, carboxylic acids and an alcohol are being presented using $[SF_3][MF_6]$ (M = Sb, As).

Chemistry of WOF_4 has been explored using SO_2, $[(CH_3)_4N][F]$ and a fluorinated aliphatic alcohol, CF_3CH_2OH. The products, i.e. $WOF_4 \cdot SO_2$, $[(CH_3)_4N][WOF_5]$ and $CH_3CN \cdot WOF_3(OCH_2CF_3)$ have been fully characterized by X-ray crystallography and Raman spectroscopy.

Crystal structures of perfluorinated carboxylic acids and carboxylates of environmental concern are reported for the first time.

The 1-ethyl-3-methylimidazolium bifluoride ($EMIMHF_2$) ionic liquid has been studied with solid-state MAS NMR spectroscopy at low temperature to explore its structural features.

ACKNOWLEDGEMENTS

I would like to thank my supervisor(s) Prof. Michael Gerken and Prof. Paul Hazendonk for providing me an opportunity to work in their laboratories. With their guidance and support, I handled both specialized areas of research, i.e., fluorine chemistry and NMR spectroscopy.

I would like to thank my committee members Profs. Peter Dibble, Paul Hayes, Adriana Predoi-Cross and the members of examination committee for their interest and investment of time.

I am thankful to Prof. Carsten Jenne for being my external examiner and investing his valuable time.

I would like to thank Tony Montina, NMR manager, as well as Michael Opyr for their support in running solid-state NMR experiments. Many thanks to Heinz Fischer for fixing the Raman low-temperature assembly unit time to time.

I would like to thank Alberta Ministry of Education and the University of Lethbridge for financial support. Again, many thanks to Alberta Innovates – Technology Futures for a Graduate Scholarship and the Len Bolger Scholarship. I would like to thank the Department of Chemistry and Biochemistry for the support in research.

Finally, I am thankful to my wife, my parents, my brother and my son for their support as I finished my studies.

TABLE OF CONTENTS

LIST OF TABLES

LIST OF FIGURES

LIST OF ABBREVIATION

General

ax	axial
eq	equatorial
Kel-F	chlorotrifluoroethylene
NMR	Nuclear Magnetic Resonance
TEA	triethylamine
br	broad
$EMIMHF_2$	1-ethyl-3-methylimidazolium bifluoride
C_5H_5N	pyridine
CH_3CN	acetonitrile
PFOA	perfluorooctanoic acid
PFDA	perfluorodecanoic acid
SPFO	sodium perfluorooctanoate
SPFB	sodium perfluorobutanoate

Nuclear Magnetic Resonance

δ	chemical shift in ppm
J	scalar coupling constant in Hertz
ppm	parts per million
TMS	tetramethylsilane
HFB	hexafluorobenzene
CP	cross polarization
DP	direct polarization
T_1	spin-lattice relaxation delay
T_2	spin-spin relaxation delay
MAS	magic angle spinning

X-ray Crystallography

a, b, c, α, β, γ	cell parameters
V	cell volume
λ	wavelength
Z	molecules per unit cell
mol. wt.	molecular weight
Wt. No.	isotopic molecular weight
μ	absorption coefficient
R_1	conventional agreement index
wR_2	weighted agreement index

Chapter-1

1. Introduction

1.1 Fluorine chemistry

Fluorine is a unique element because of its properties, such as the highest electronegativity of all elements in the periodic table and its relatively small size (van der Waal radius of 1.47 Å).[1,2] As a consequence, fluorine can impart special properties onto inorganic and organic compounds.

Fluorine forms ionic as well as covalent compounds depending on the electronegativity difference between the atoms involved in the bonding. If the electronegativity difference is large, an ionic fluoride is formed, e.g., NaF, CaF_2, etc. If the difference is small, the covalent character of the element–fluorine bond increases. Many covalent, molecular inorganic fluorine compounds are very reactive and unstable towards hydrolysis, e.g., XeF_2, SF_4, PF_5.[1]

Inorganic fluorine compounds have various applications. For example, low concentration of F^- (0.5 to 0.7 ppm in Lethbridge in the form of hydrofluorosilisic acid)[3] are added to the drinking water (fluoridation) and F^- is present in toothpaste (between 1000 and 1500 ppm in the form of NaF, SnF_2 or Na_2PO_3F) to improve dental health to strengthen the enamel.[4] In the semiconductor industry SF_6 has been used as an insulator and to create intricate circuitry patterns upon silicon wafers,[5] and Na_3AlF_6 is essential in the production of aluminium.[1] Inorganic fluorine compounds have also been used as reagents to introduce F into organic molecules, e.g., SF_4 and some of its derivatives have been used to convert –COOH to –C(O)F, –OH to –F and >C=O to $>CF_2$.[6] Inorganic fluorine compounds have also been instrumental to validate the VSEPR model introduced by Gillespie. For example,

the VSEPR model is correct in predicting the see-saw geometry of SF_4 and the linear geometry of XeF_2.[7]

In contrast to the reactivity of many inorganic molecular fluorine compounds, organic fluorine compounds generally exhibit great stability, since they contain very strong C–F bonds. The bond energy of a C–F bond is 485.7 kJ/mol which is significantly larger than that of a C–H bond, (around 337 kJ/mol).[9] Organofluorine compounds have a variety of applications because the fluoro substituent or fluorinated group, e.g., ($–CF_3$) increase the lipophilicity and metabolic stability.[10] The introduction of fluorine into organic substrates can result in more potent pharmaceutical compounds, and the use of fluorinated drugs is increasing rapidly. A good practical example of this type of application is the antibiotic drug, ciprofloxacin from Pfizer Inc. (scheme-I) in which the fluorine atom is introduced to have the polar as well as the directional effects. Another good example is Lipitor from NOVARTIS (scheme-I), a cholesterol lowering drug.[11]

(a) (b)

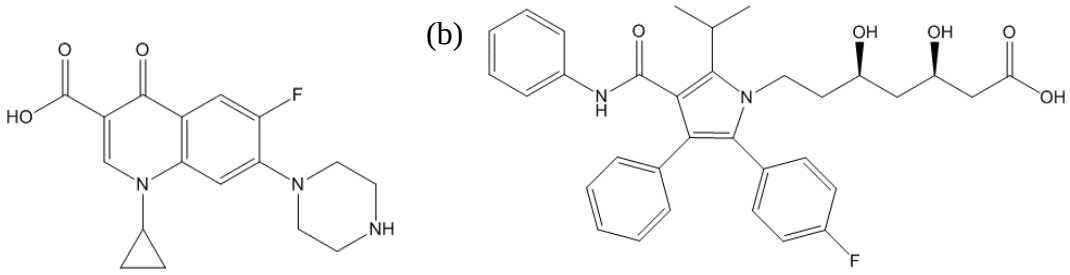

Scheme-I (a) Ciprofloxacin (b) Lipitor

Fluorinated pesticides are also extensively being used in agriculture. For example, Fluopicolide is used as a fungicide to control disease in potatoes by oomycetes, and Flamprop is used as an herbicide to control broadleaf weeds.[12]

The use of organofluorine compounds extents to the polymer field. Fluoropolymers are high-performance materials with many specific applications. Most widely known in the general public, Teflon (DuPont) coating is used on utensils for even heat distribution and for oil-free cooking. But at the same time, the compounds used as the polymerization aid in the generation of PTFE (polytetrafluoroethylene) can also cause environmental problems. Perfluorooctanoic acid (PFOA) is used to stabilize emulsion in the production of PTFE and is widely found in the environment due to its persistent nature.[13,14]

1.1.1 Nucleophilic fluorinating reagents

Approximately 30% of all agrochemicals and 20% of all pharmaceuticals contain fluorine.[15,16] Introduction of fluorine into the targeted organic compounds has found several applications in modern medicine, including diagnostic imaging, eye surgery, oxygen delivering systems, cancer therapy and respiratory medicine.[10] The Antibiotic 1-cyclopropyl-6-fluoro-4-oxo-7-(piperazin-1-yl)-quinoline-3-carboxylic acid (ciprofloxacin) (scheme-I), antibiotic fluoroquinolone (levofloxacin), and antitumor fluoronucleoside (tegafur) (scheme-II) are examples of the successful introduction of fluorine into organic molecules to obtain a pharmaceutically active compound.

(a) 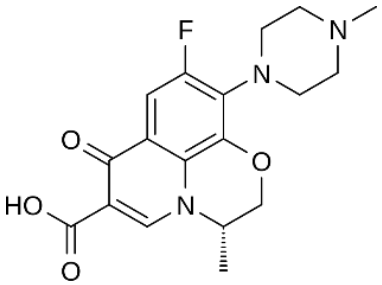

(b) 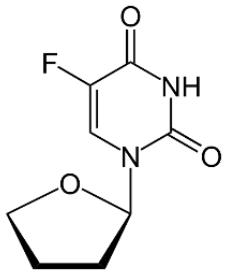

Scheme-II (a) Levofloxacin (b) Tegafur

Fluorine creates changes in the lipophilicity, acidity/basicity, dipole moment, overall reactivity, stability and the conformation of a compound. When substituting hydrogen, fluorine does not change the overall volume too dramatically (van der Waals radii for fluorine and hydrogen are 1.47 and 1.20 Å, respectively).[17,18] The higher amount of C–F bond energy (485.7 kJ/mol)[19] gives relative stability to C–F bonds against metabolic transformations. The replacement of hydrogen by fluorine can increase the lipid solubility of bioactive molecules.[20,21] This results in easier drug transport and good absorption rates in biological systems. As a consequence, the development of fluorination processes is essential for the synthesis of pharmaceutical and agricultural compounds and, hence, there is an ongoing demand for safe and efficient fluorinating reagents.

Among the different available techniques for fluorination (electrophilic fluorination, electrochemical fluorination and nucleophilic fluorination), nucleophilic fluorination is the most popular process because of the ease of handling of most of the reagents involved. The nucleophilic displacement of oxygen by fluorine, commonly known as deoxofluorination, is one of the most effective and routinely used approaches in medicinal chemistry.[22] Sometimes, the –OH group on these organic molecules can also be replaced by an –F group as required. Hydrogen fluoride (HF), some metal fluorides (e.g. CoF_3, KF), $[Bu_4N][F]$ and many sulfur fluorides make up the series of nucleophilic fluorinating reagents. Hydrogen fluoride has limited usage because of its toxic, corrosive properties and low reactivity. Its low reactivity is a result of strong H–F bond. Many ionic metal fluorides are hygroscopic in nature and water molecules can be strongly hydrogen bonded to these fluorides resulting in lower reactivity. Trimethyltin fluoride, Me_3SnF is also a representative of the nucleophilic fluorinating reagent series.[23] Alternatively, there

are many fluoro-sulfur compounds available on commercial scales (SF_4, DAST, Dexo-Fluor®, Fluolead™, XtalFluor-E®, XtalFluor-M®).

1.1.2 Fluoro-sulfur compounds as deoxofluorinating reagents

Sulfur tetrafluoride, SF_4, is one of the well-known binary sulfur fluorides and has been used as a fluorinating agent in the preparation of inorganic fluorine-containing compounds, such as IF_5, SeF_4, SnF_4, MoF_6 and UF_6 in high yields by fluorination of I_2O_5, SeO_2, SnS_2, MoO_3 and UO_3, respectively[24] and in synthesizing oxyfluorides.[25] More importantly, SF_4 has extensively been used as a deoxofluorinating reagent in organic chemistry for the conversion of $R_2C{=}O$ to R_2CF_2, –OH to –F and –COOH to $–CF_3$.[26] Since the gaseous, corrosive and toxic nature of SF_4 requires special equipment and techniques, a number of other sulfur-containing fluorinating reagents capable of selectively introducing fluorine in the target compounds have been developed. These fluorinating reagents are relatively easy to handle and do not require any special protocol for the fluorination process. Diethylamino sulfurtrifluoride, DAST (Et_2N-SF_3), Deoxo-Fluor® ($((CH_3O)_2(CH_2)_4N–SF_3$), Fluolead™ ((4-*tert*-butyl)(2,6-dimethyl)$C_6H_3SF_3$), XtalFluor-E® ($[Et_2N{=}SF_2][BF_4]$), and XtalFluor-M® (morpholinodifluorosulfinium tetrafluoroborate) as shown in scheme–III are some common commercially available fluoro-sulfur nucleophilic fluorinating reagents.

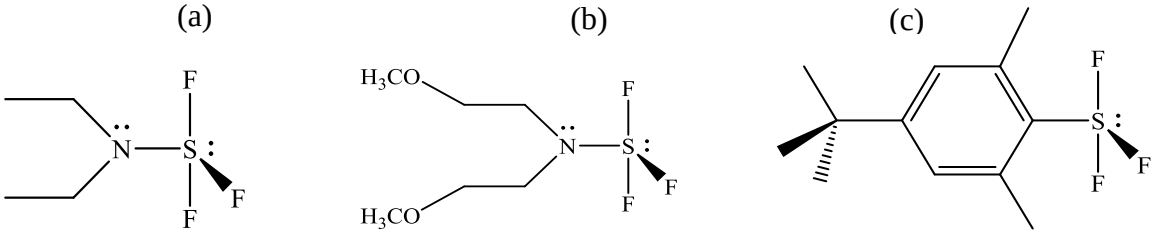

(d) (e)

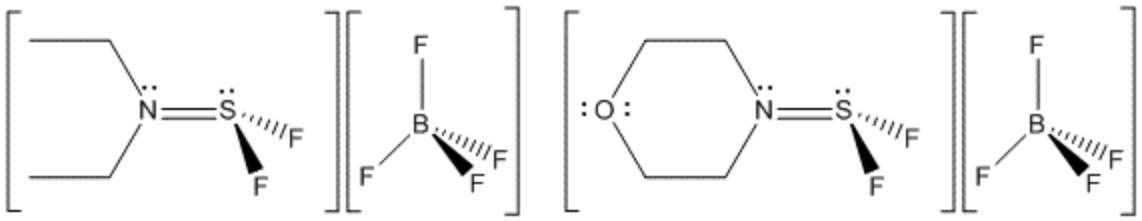

Scheme-III (a) DAST (b) Deoxo-Fluor® (c) Fluolead™ (d) XtalFluor-E® (e) XtalFluor-M®

DAST was originally developed as an alternative to SF_4. Its main advantage was its liquid form which is easier to handle and did not require special technique as is required in case of SF_4. DAST had a main disadvantage as well. At temperatures exceeding 90 °C, DAST decomposes in two stages. First, it decomposes to SF_4 and $(Et_2N)_2SF_2$ at 90 °C. After heating above 90 °C, $(Et_2N)_2SF_2$ can detonate. In the search for a safer alternative for DAST, Deoxo-Fluor® was synthesized. Deoxo-Fluor® ($(CH_3O)_2(CH_2)_4N\text{-}SF_3$) decomposes slowly with less heat evolution but the problem regarding its decomposition temperature (90 °C) remained the same. Upon use, both DAST and Deoxo-Fluor® generates HF, which is highly volatile and toxic. With the invention of Fluolead™ ((4-*tert*-butyl)(2,6-dimethyl)$C_6H_3SF_3$) (Ishikawa's reagent) in 2008, some improvement in the stability was achieved owing to the higher stability of C–S bonds but there is always the possibility of obtaining amides and esters side products. In 2010, two very useful and more selective fluorinating reagents namely XtalFluor-E® and XtalFluor-M®, were developed by Omegachem.[27] These two solid reagents are more stable than DAST as shown by differential scanning calorimetry and have shown the capability to selectively convert $R_2C{=}O$ to R_2CF_2, –COOH to –COF and –OH to –F.[27] The following mechanisms (scheme–IV) for the deoxofluorination reactions of carbonyl and hydroxyl groups by SF_4 in the presence of HF have been proposed in which SF_3^+ is the active species responsible for the deoxofluorination reaction.[70] The presence of SF_3^+ and HF_2^- in the SF_4-HF system was

demonstrated by conductivity measurements.[28]

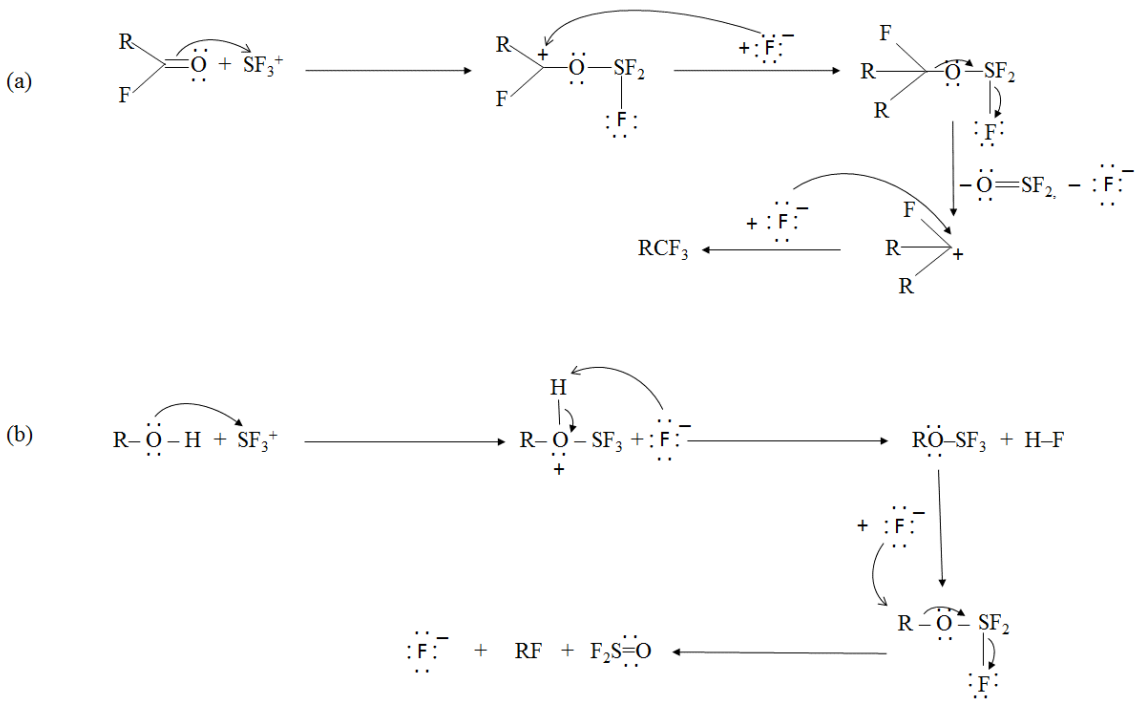

Scheme-IV Proposed mechanism for deoxofluorination process of (a) carbonyl group and (b) hydroxyl group by SF_4 in the presence of HF[28]

1.2 Sulfur tetrafluoride and $[SF_3][MF_6]$ (M = Sb, As) salts

1.2.1 Fluoride-ion donor properties of SF_4

Sulfur tetrafluoride, SF_4, is a corrosive and toxic gas at ambient temperature with a melting point of –121 °C and a boiling point of –38 °C. It readily forms HF upon contact with water. On one hand, SF_4 acts as a weak Lewis acid and can form Lewis acid-base adducts with F^- and nitrogen bases,[29] on the other hand, SF_4 can donate a fluoride ion towards strong Lewis acids such as BF_3, AsF_5, SbF_5 to form the corresponding SF_3^+ salts, e.g., $[SF_3][BF_4]$, $[SF_3][AsF_6]$ and $[SF_3][SbF_6]$ as shown in equation 1.1 and 1.2.[8]

$SF_4 + BF_3 \longrightarrow [SF_3][BF_4]$……..……....(1.1)

$SF_4 + MF_5 \longrightarrow [SF_3][MF_6]$ (M = Sb, As) ……..…….....(1.2)

In 1956, Bartlett and Robinson first reported that SF_4 can form solid complexes with a number of highly Lewis acidic inorganic fluorides, i.e., BF_3, AsF_5, and SbF_5, and noted the melting points of the resultant solids.[30] They suggested the possibility of $[F_3B \leftarrow :SF_4]$ Lewis acid-base interactions. Bartlett, Robinson found that the SF_4 adduct with BF_3 can be used to obtain pure SF_4 because of the reversibility of the formation reaction.[30] In 1958, Cotton and George carried out IR spectroscopic measurements on the $[F_3B \leftarrow :SF_4]$ adduct and presented arguments in favour of the ionic nature of the solid adduct based on the observation of BF_4^- bands. Since they were limited in carrying out their work in an air-free environment, they could not, however, conclusively prove their claim because of the highly hydrolytic nature of the BF_3–SF_4 reaction product, because it could form BF_4^- in the presence of moisture.[31] In 1961, Muetterties and coworkers filed a patent on the formation and use of a number of SF_4 adducts, i.e., $SF_4 \cdot BF_3$, $SF_4 \cdot SbF_5$, $SF_4 \cdot PF_5$ and $SF_4 \cdot AsF_3$. In the ^{19}F NMR spectrum of the SF_4–AsF_3 system at temperatures as low as –60 °C, only one type of fluorine resonance was observed, which was interpreted in terms of fluorine bridging between sulfur and arsenic.[32] An ^{19}F NMR study by Barr and Dunell on the SF_4 adduct with AsF_5, which is a much stronger Lewis acid than AsF_3, showed two distinct resonances in a 1:2 ratio confirming the ionic nature of the reaction product between SF_4 and AsF_5, i.e. $[SF_3][AsF_6]$.[33] Seel and Detmer studied the reaction between SF_4 and BF_3, AsF_5 and SbF_5 and looked at the thermal stability of the products. The sublimation temperature of $[SF_3][AsF_6]$ and $[SF_3][SbF_6]$ was reported as 90 °C and 253 °C, respectively. In addition, they studied the BF_3–SF_4 adduct by IR spectroscopy. The infrared band at 1050 cm^{-1} was attributed to the BF_4^- ion and the S–F stretching bands at 908 and 940 cm^{-1} were assigned to the SF_3^+ cation since they were significantly shifted to higher frequencies as compared to the S–F stretching bands of SF_4 (896 and 857 cm^{-1}). They also compared the BF_4^- band

of $[SF_3][BF_4]$ to the BF_4^- bands present in $[NH_4][BF_4]$ and $[Na][BF_4]$ salts to conclude the presence of BF_4^- ion. The $[SF_3][BF_4]$ adduct has a significant vapor pressure (approximately 100 mm Hg) at room temperature and dissociates into the original reactant components as determined by gas-phase IR spectroscopy. This dissociation can be utilized to get pure SF_4.[34] Gillespie and coworkers extended the vibrational characterization to Raman spectroscopy of $[SF_3][BF_4]$, $[SF_3][PF_6]$, $[SF_3][AsF_6]$ and $[SF_3][SbF_6]$ and interpreted the spectra in terms of SF_3^+ cation, BF_4^- and MF_6^- (where M = P, As, Sb) anions. Deviations of the observed spectra from those predicted for idealized ion symmetry were attributed to fluorine bridging between anions and cations.[8] For example, the Raman spectrum of $[SF_3][SbF_6]$ showed a band at 680 cm^{-1}, which can be assigned to the υ_3 mode of SbF_6^- anion with O_h symmetry although this mode is formally Raman inactive. They also observed splitting for υ_2 and υ_5 bands of SbF_6^- around 568 and 291 cm^{-1}. They attributed the splitting and the observation of formally inactive Raman bands as the consequence of lowering in symmetry due to the fluorine bridging between SbF_6^- and SF_3^+. Conductivity measurements on $[SF_3][BF_4]$ and $[SF_3][SbF_6]$ adducts in anhydrous HF yielded conductivities that are very similar to those of $[K][BF_4]$ and $[K][SbF_6]$ showing their dissociation in HF solution. Brownstein and Shamir carried out the Raman spectroscopic measurements of solutions of $[SF_3][BF_4]$, $[SF_3][PF_6]$ and $[SF_3][AsF_6]$ salts in anhydrous HF confirming the ionic formulations of these salts.[35] The Raman spectrum of the molten $[SF_3][SbF_6]$ salt at 250 °C also indicated the ionic form $[SF_3][SbF_6]$.[36]

In 1983, O'Brien and Desmarteau synthesized room-temperature unstable salts of SF_3^+ with SO_3F^- and $CF_3SO_3^-$ counter anions according to the reactions (1.3) to (1.5).

$$2SF_4 + ClOSO_2F \longrightarrow [SF_3][FSO_3] + SF_5Cl \text{ (–90 to –40 °C for 4h)} \quad \text{(1.3)}$$

$$2SF_4 + ClOSO_2CF_3 \xrightarrow{HF} [SF_3][CF_3SO_3] + SF_5Cl \text{ (–78 to –40 °C for 1 h)} \quad \text{(1.4)}$$

$2SF_4 + BrOSO_2CF_3 \longrightarrow [SF_3][CF_3SO_3] + SF_5Br$ (–70 to –10 °C for 3–6 h)……(1.5)

These salts were characterized by Raman spectroscopy which provided the characteristic S–F stretching frequencies of the SF_3^+ cation.[9]

Neil Bartlett and coworkers grew crystals of $[SF_3][BF_4]$ salt by sublimation and presented the first conclusive X-ray structural data of an SF_3^+ salt. In the crystal structure of $[SF_3][BF_4]$, the SF_3^+ cation forms three S···F contacts of 2 × 2.624(2) Å and 2.593(3) Å with fluorine atoms of three adjacent BF_4^- anions, increasing the coordination number of sulfur to six.[37] Bartlett et al. tried to grow $[SF_3][AsF_6]$ crystals by sublimation and obtained unit cell parameters for $[SF_3][AsF_6]$ (Orthorhombic *Cmc2₁* with the dimensions a = 20.375(3) Å, b = 8.508(3) Å, c = 11.224 (3) Å, and V = 1945.7 $Å^3$). The quality of the X-ray crystallographic data for $[SF_3][AsF_6]$ were poor[37] and did not allow for the localization of the fluorine atoms. Crystals of $[SF_3][SbF_6]$ could not be obtained. As a consequence, no conclusive structural information was obtained for $[SF_3][AsF_6]$ and $[SF_3][SbF_6]$ salts. Subsequently, Bartlett and coworkers also prepared the SF_3^+ salts with GeF_5^- and GeF_6^{2-} anions. The $[SF_3][GeF_5]$ salt was prepared by displacing BF_3 with GeF_4 in $[SF_3][BF_4]$ salt at –126 °C. The $[SF_3][GeF_5]$ salt is thermally unstable and dissociate to $[SF_3]_2[GeF_6]$ and GeF_4 at room temperature, except under liquid GeF_4. The formation of the $[SF_3][GeF_5]$ salt was verified by characteristic bands for SF_3^+ salts (945, 932, 914 cm^{-1} for $\upsilon(A_1)$ and 904, 887, 874 cm^{-1} for $\upsilon(E)$) in the Raman spectrum.[38] The $[SF_3]_2[GeF_6]$ salt was also prepared by reaction of SF_4 and GeF_4 in 2:1 molar ratio according to equation 1.7.

Dissociation

$SF_4 + GeF_4 \longrightarrow [SF_3][GeF_5] \rightleftharpoons [SF_3]_2[GeF_6] + GeF_4$……..(1.6)

$2SF_4 + GeF_4 \longrightarrow [SF_3]_2[GeF_6]$ ……..…….(1.7)

The $[SF_3]_2[GeF_6]$ salt readily sublimes at room temperature and the crystals of this material were obtained by the sublimation at 30–35 °C. $[SF_3]_2[GeF_6]$ crystallizes in the orthorhombic *Pmnn* space group. The SF_3^+ has C_{3v} symmetry with all S–F bonds of equal length (1.519(1) and 1.515(2) Å) within 3σ and all F–S–F angles equal (96.12(8)–96.23(10)°). The bridging contacts of fluorine bonded to germanium to sulfur (2.367(2) and 2.420(1) Å) are shorter than those found in the crystal structure of $[SF_3][BF_4]$ (2.593(3) and 2.624(2) Å).[39] Holloway and Rook synthesized $[SF_3][OsF_6]$ and $[SF_3][IrF_6]$ by a different approach.[40] They attempted the synthesis of MF_4S (M = Os or Ir) by the reaction of appropriate hexafluoride with ZnS or B_2S_3 at elevated temperatures (200 – 300 °C). However, by comparing the IR spectra of the reactants and the products, they concluded that instead of MF_4S, the reaction product was $[SF_3][MF_6]$ (M = Os or Ir) in addition to several by-products including a range of sulfur fluorides. In this reaction, OsF_6 and IrF_6 readily oxidatively fluorinates ZnS and B_2S_3. In solution ^{19}F NMR spectra of these compounds using anhydrous HF as solvent, a broad singlet characteristic to SF_3^+ cation at +31.0 ppm was observed.

The order of melting points of several SF_3^+ salts in decreasing order can be given as $[SF_3][SbF_6]$ (m.p. 253 °C) > $[SF_3][AsF_6]$ > $[SF_3][IrF_6]$ > $[SF_3][BF_4]$ > $[SF_3][PF_6]$ > $[(SF_3)_2][GeF_6]$> $[SF_3][AsF_4]$ (m.p. –20 °C).[40] Recently, the crystal structures of $[SF_3][SbF_6]$ and $[SF_3][AsF_6]$ have been predicted to be $P2_1/c$ and the unit cell parameters have been predicted based on molecular mechanics calculations,[41] but it is in contrast to the experimentally obtained unit cell data for $[SF_3][AsF_6]$.[37]

1.3 SF_3^+–nitrogen bases adducts

1.3.1 Introduction

Trifluorosulfonium salts such as $[SF_3][BF_4]$, $[SF_3][AsF_6]$ and $[SF_3][SbF_6]$ have been synthesized and analyzed using different techniques for a long time.[5,6,7,8] $[SF_3][AsF_6]$ and $[SF_3][SbF_6]$ salts with melting points of 90 and 253 °C, are of higher interest. In these SF_3^+ salts, sulfur is highly Lewis acidic.[37,42]

It had been postulated by Mews and coworkers that $[SF_3][BF_4]$ should react with NSF_3 to give $[F_3S–NSF_3][BF_4]$ which then converts to the observed product $F_5SN–SF_2$ after releasing BF_3 according to the equation 1.8.[43]

$$[SF_3][BF_4] + NSF_3 \longrightarrow [F_3S–NSF_3][BF_4] \longrightarrow [F_2SN–SF_4][BF_4] \xrightarrow{-BF_3} F_5SN–SF_2 \quad \ldots (1.8)$$

In the literature, the X-ray crystal structure of the $[SF_3(NSF_3)_2][AsF_6]$ salt was reported as the accidental decomposition product of $[F_4S{=}N–Xe{---}NSF_3][AsF_6]$ in an effort to grow crystals of $[F_4S{=}N–Xe{---}NSF_3][AsF_6]$ from NSF_3 at 0 °C.[44] This crystal structure shows the 1:2 adduct cation in contrast to the intermediate proposed by Mews.[43]

Mews and coworkers performed ^{19}F solution NMR spectroscopy of $[SF_3][AsF_6]$ with CH_3CN in 1:1 molar ratio using SO_2 as solvent at –30 °C. Based on the change of ^{19}F chemical shift from SF_3^+ in SO_2 (30.5 ppm) to 17.4 ppm when CH_3CN was added, the formation of the $[SF_3NCCH_3]^+$ adduct was proposed according to equation 1.9.[43]

$$[SF_3][AsF_6] + CH_3CN \underset{}{\overset{-30\ °C}{\rightleftharpoons}} [SF_3{\cdot}NCCH_3][AsF_6] \quad \ldots\ldots\ldots\ldots\ldots\ldots\ldots\ldots\ldots\ldots (1.9)$$

It was also stated that the proposed adduct decomposes according to the equation-1.10.[43]

$$[SF_3{\cdot}NCCH_3][AsF_6] \overset{-30\ ^\circ C}{\rightleftharpoons} [AsF_5{\cdot}NCCH_3](s) + SF_4\,(g) \quad \text{..... (1.10)}$$

Mews and coworkers also carried out the reactions of mono and di substituted SF_3^+ salts, i.e. $[(CF_3)SF_2][AsF_6]$ and $[(CF_3)_2SF][AsF_6]$ with CH_3CN in the presence of SO_2 according to equations 1.11 and 1.12 and proposed the formation of $[(CF_3)SF_2{\cdot}NCCH_3][AsF_6]$ and $[(CF_3)_2SF{\cdot}NCCH_3][AsF_6]$.

$$[(CF_3)SF_2][AsF_6] + CH_3CN \overset{-30\ ^\circ C}{\rightleftharpoons} [(CF_3)SF_2{\cdot}NCCH_3][AsF_6] \quad \text{.....(1.11)}$$

$$[(CF_3)_2SF][AsF_6] + CH_3CN \overset{-30\ ^\circ C}{\rightleftharpoons} [(CF_3)_2SF{\cdot}NCCH_3][AsF_6] \quad \text{.....(1.12)}$$

They observed a change of ^{19}F chemical shift for $[(CF_3)SF_2]^+$ in SO_2 from –54.7 ppm to –50.5 ppm when CH_3CN was added and a chemical shift change of –159.0 ppm to –78.5 ppm for $[(CF_3)_2SF_2]^+$ salt.[43] There are hardly any examples of trifluorosulfur cationic species in the pentacoordinate and difluorosulfur cationic species in the tetracoordinate state.[43,45]

Several reports have been published on the existence of the $[SF_3(C_5H_5N)_2]^+$ and $[SF_3(CH_3CN)_2]^+$ cationic species on the basis of results from mass spectrometry and molecular orbital calculations.[46,47,48,49] It was suggested that the formation of $[SF_3(C_5H_5N)_2]^+$ and $[SF_3(CH_3CN)_2]^+$ species should be possible by direct reaction of SF_3^+ species with pyridine and acetonitrile.

1.4 Tungsten oxide tetrafluoride, WOF_4

1.4.1 Introduction

Tungsten oxide tetrafluoride, WOF_4, was first synthesized by O. Ruff et al. in 1907.[50] They synthesized tungsten oxide tetrafluoride by the following two procedure as shown by reaction 1.13 and 1.14.

$$WOCl_4 + 4HF\ (\text{anhydrous}) \longrightarrow WOF_4 + 4HCl \quad \ldots\ldots\ldots\ldots\ldots\ldots\ldots\ldots\ldots\ldots\ldots\ldots (1.13)$$

$$WOCl_4 + 2PbF_2 \xrightarrow{\Delta} WOF_4 + 2PbCl_2 \quad \ldots\ldots\ldots\ldots\ldots\ldots\ldots\ldots\ldots\ldots\ldots\ldots\ldots\ldots (1.14)$$

Tungsten oxide tetrafluoride is a tetrameric compound represented by the formula WOF_4. It is a white crystalline solid, which melts at 104.7 °C. WOF_4 can be synthesized by many ways. It can be synthesized by the fluorination of WO_3 at 300 °C,[51] direct fluorination of W in the presence of O_2 at 300 °C,[52] slow hydrolysis of WF_6 [53] or by the reaction of $WOCl_4$ with HF.[54] Wilson and Christe synthesized WOF_4 by the reaction of silica with excess WF_6 in the presence of anhydrous HF (aHF) according to equation 1.15.[55]

$$2WF_6 + SiO_2 \xrightarrow{aHF} 2WOF_4 + SiF_4 \quad \ldots\ldots\ldots\ldots\ldots\ldots\ldots\ldots\ldots\ldots\ldots\ldots\ldots\ldots\ldots\ldots (1.15)$$

Excess amount of WF_6 avoids the formation of $[H_3O][WOF_5]$ and $[H_3O][W_2O_2F_9]$ salts. Pure WOF_4 can be obtained by the sublimation of this mixture under dynamic vacuum.

Initial X-ray crystallographic work by Edwards and Jones suggested an oxygen bridged cyclic tetrameric structure of WOF_4.[56] The W–O–W angle was given as 183°. Infrared spectroscopy of WOF_4 was carried out showing a band at 1055 cm^{-1}, which was assigned to the W–O stretch and a band at 650 cm^{-1}, which was assigned to a W–O–W stretch. In 1974, Alexander et al. showed the tetrameric WOF_4 structure does not contain oxygen bridges. In fact, it has fluorine bridges and they assigned W–F–W stretching mode at 550 cm^{-1}.[57] Another study was based on infrared and ^{19}F NMR spectroscopy of

$W^{18}OF_4$.[58] In the infrared spectrum, two W–O stretching bands were observed. One very sharp signal at 997 and a second weak signal at 1053 cm^{-1}. These wavenumbers corresponds to W–^{18}O and W–^{16}O stretches. In the ^{19}F NMR spectrum two signals were observed at low temperatures. T_1 relaxation times for the two signals were 3-4 min and 0.1 s, indicating two very different fluorine environments on WOF_4: a terminal fluorine and a bridging fluorine environment. At higher temperatures only one narrow line dominated the spectrum.

Tungsten oxide tetrafluoride is Lewis acidic. The tungsten center in WOF_4 can easily accept an electron pair from Lewis base. WOF_4 forms two different types of adducts with pyridine ($WOF_4 \cdot C_5H_5N$ and $WOF_4 \cdot 2C_5H_5N$).[59] The acidic character of WOF_4 has also been demonstrated by its reaction with CsF[8] or $ClOF_3$.[60]

Tungsten oxide fluorides form an important class of compounds being used in getting high purity metals, in organic synthesis as active halogenating agents and in catalysts.[61] Some enzymatic processes are also completed with the help of tungsten complexes in the living organism.[61] For example, tungsten-containing enzymes typically reduce carboxylic acids to aldehydes.[62] Tungsten is among one of the heavy metals known to be participating in the biological activities.[62]

Many derivatives of WF_6 have been prepared by replacement of a single fluorine atom with an RO^- ligand, such as CH_3O^-, $C_2H_5O^-$, $C_6H_5O^-$, $CF_3CH_2O^-$.[63,64,65,66,67] CH_3OWF_5 was prepared by the reaction of WF_6 and $CH_3OSi(CH_3)_3$ and was characterized by solution ^{19}F NMR spectroscopy.[68,69]

1.5 Solid-state NMR spectroscopy

(The following discussion is based on the NMR text books, Spin Dynamics (Levitt, M. H. 2001) and Understanding NMR Spectroscopy (Keeler, J. 2010), and articles about Hamiltonians of NMR by Smith et al. in Concept of Magnetic Resonance, 1992)

1.5.1 Solid-state NMR interaction tensors

The interaction associated with two magnetic field components ($\vec{\mathbf{I}}$ and $\vec{\mathbf{J}}$), either generated by two spins or by one spin and the externally applied magnetic field is written in the form of equation 1.16.

$$\hat{H} = C\,\hat{\mathbf{I}} \cdot \hat{\hat{\mathbf{M}}} \cdot \hat{\mathbf{J}} \qquad \text{.....(1.16)}$$

where, $\hat{\hat{M}}$ represents the spatial tensor in the form of a 3×3 matrix and 'C' is a constant.

(Suppose $\hat{\mathbf{I}}$ is a 1 × n matrix, $\hat{\hat{\mathbf{M}}}$ is an n × n matrix and $\hat{\mathbf{J}}$ is an n × 1 matrix. Thus the traces for the combination of A, B and C matrices can be given as,

$$Tr(\hat{\mathbf{I}} \cdot \hat{\hat{\mathbf{M}}} \cdot \hat{\mathbf{J}}) = Tr(\hat{\hat{\mathbf{M}}} \cdot \hat{\mathbf{J}} \cdot \hat{\mathbf{I}}) = Tr(\hat{\mathbf{J}} \cdot \hat{\hat{\mathbf{M}}} \cdot \hat{\mathbf{I}})).$$

This Hamiltonian can be rewritten as,

$$\hat{H} = C\,\hat{\hat{\mathbf{M}}} \cdot \hat{\mathbf{I}} \otimes \hat{\mathbf{J}}$$ **('⊗' is the outer product of $\hat{\mathbf{I}}$ with $\hat{\mathbf{J}}$)** .....(1.17)

$$\hat{H} = C\,\hat{\hat{\mathbf{M}}} \cdot \hat{\hat{\mathbf{X}}}$$ **('$\hat{\hat{\mathbf{X}}}$' is spin tensor representing the outer product of $\hat{\mathbf{I}}$ with $\hat{\mathbf{J}}$)** .....(1.18)

$\hat{\hat{\mathbf{M}}}$ and $\hat{\hat{\mathbf{X}}}$ tensors are rank 2 tensors and can be written in the form of following three irreducible Cartesian tensors $\hat{\hat{\mathbf{T}}}_{\mathbf{0}}^{\mathbf{0}}$(isotropic), $\hat{\hat{\mathbf{T}}}_{\mathbf{2}}^{\mathbf{0}}$ (anisotropy), $\hat{\hat{\mathbf{T}}}_{\mathbf{2}}^{\pm\mathbf{2}}$(asymmetry),

$$\hat{\hat{\mathbf{M}}} = \begin{bmatrix} m_{xx} & m_{xy} & m_{xz} \\ m_{yx} & m_{yy} & m_{yz} \\ m_{zx} & m_{zy} & m_{zz} \end{bmatrix} = M_{iso} \begin{bmatrix} 1 & 0 & 0 \\ 0 & 1 & 0 \\ 0 & 0 & 1 \end{bmatrix} + \begin{bmatrix} 0 & \alpha_{xy} & \alpha_{xz} \\ \alpha_{yx} & 0 & \alpha_{yz} \\ \alpha_{zx} & \alpha_{zy} & 0 \end{bmatrix} + \begin{bmatrix} \delta_{xx} & \delta_{xy} & \delta_{xz} \\ \delta_{yx} & \delta_{yy} & \delta_{yz} \\ \delta_{zx} & \delta_{zy} & \delta_{zz} \end{bmatrix}$$

$$\hat{\hat{\mathbf{T}}}_{\mathbf{0}}^{\mathbf{0}} \qquad\qquad \hat{\hat{\mathbf{T}}}_{\mathbf{2}}^{\mathbf{0}} \qquad\qquad \hat{\hat{\mathbf{T}}}_{\mathbf{2}}^{\pm\mathbf{2}}$$

.....(1.19)

The components of this simplification can be described as,

$M_{iso} = 1/2\ (m_{xx} + m_{yy} + m_{zz})$ ……..…...(1.20)

$\alpha_{uv} = 1/2\ (m_{uv} - m_{vu})$ ……..…..(1.21)

$\delta_{iso} = 1/2\ (m_{uv} + m_{vu} - 2m_{iso})$ ……..…(1.22)

$\hat{\hat{\mathbf{M}}}$, the spatial part, is always in the principal axis system (PAS) frame and $\hat{\hat{\mathbf{X}}}$, the spin part, is always in the lab frame at the starting point.

In the principal axis system (PAS), the tensor $\hat{\hat{\mathbf{M}}}$ can be written as,

$$\hat{\hat{\mathbf{M}}}\ \mathbf{(PAS)} = \begin{bmatrix} m_{xx} & 0 & 0 \\ 0 & m_{yy} & 0 \\ 0 & 0 & m_{zz} \end{bmatrix} = M_{iso} \begin{bmatrix} 1 & 0 & 0 \\ 0 & 1 & 0 \\ 0 & 0 & 1 \end{bmatrix} + \begin{bmatrix} 0 & 0 & 0 \\ 0 & 0 & 0 \\ 0 & 0 & 0 \end{bmatrix} + \begin{bmatrix} \delta_{xx} & 0 & 0 \\ 0 & \delta_{yy} & 0 \\ 0 & 0 & \delta_{zz} \end{bmatrix}$$

……..……...……...(1.23)

$M_{iso}\ (PAS) = 1/3\ (m_{xx} + m_{yy} + m_{zz})$ or $1/3\ \mathrm{Tr}\left\{\hat{\hat{\mathbf{M}}}\right\}$ ……..…(1.24)

$\delta_{uu}\ (PAS) = (m_{uu} - m_{iso})$ ……..…..…....(1.25)

To go from the principal axis system (PAS) frame to the Lab frame, first the components of the principal axis system are converted to the rotor frame components by using angle α, β, γ. The rotor frame components are then converted to the lab frame components using angles 0, θ_m, $\omega_r t$.

$$\text{PAS} \xrightarrow{(\alpha, \beta, \gamma)} \text{Rotor Frame} \xrightarrow{(0, \theta_m, \omega_r t)} \text{Lab Frame} \quad \text{…..……..…....(1.26)}$$

$\hat{\hat{\mathbf{X}}}$ is the Cartesian form of the spin tensor and is in the lab frame.

The different components for tensor $\hat{\hat{\mathbf{M}}}$ in the Cartesian system and in the principal axis system (PAS) can be written as mentioned in the following Table 1.1.

Table 1.1 Different components for tensor $\hat{\hat{\mathbf{M}}}$ in the Cartesian system and in the principal axis system (PAS)

Components in the Cartesian system	Components in the PAS system
$M_0^0 = -1/\sqrt{3}\,(M_{xx} + M_{yy} + M_{zz})$	$M_0^0(\text{PAS}) = -1/\sqrt{3}\,(\text{Tr}\{\hat{\hat{\mathbf{M}}}\})$
$M_1^0 = -i/\sqrt{2}\,(M_{xy} - M_{yx})$	$M_1^0(\text{PAS}) = 0$
$M_1^{\pm 1} = -1/2\,[M_{zx} - M_{xz} \pm i(M_{zy} - M_{yz})]$	$M_1^{\pm 1}(\text{PAS}) = 0$
$M_2^0 = -1/\sqrt{6}\,[3M_{zz} - (M_{xx} + M_{yy} + M_{zz})]$	$M_2^0(\text{PAS}) = \sqrt{3/2}\,(M_{zz} - 1/3\,\text{Tr}\{\hat{\hat{\mathbf{M}}}\})$
$M_2^{\pm 1} = \mp 1/2\,[M_{xz} + M_{zx} \pm i(M_{yz} + M_{zy})]$	$M_2^{\pm 1}(\text{PAS}) = 0$
$M_2^{\pm 2} = -1/2\,[M_{xx} - M_{yy} \pm i(M_{xy} - M_{yx})]$	$M_2^{\pm 2}(\text{PAS}) = 1/2\,(M_{xx} - M_{yy})$

This principal axis system (PAS) notation is converted to the rotor frame spherical tensor system using the Wigner Eckart theorem in the following way,

$$\hat{\hat{\mathbf{M}}}_l^{\boldsymbol{m}}(\text{RF}) = \sum_{-l}^{l} D_{m\,m'}^{l}(\alpha,\beta,\gamma)\hat{\hat{\mathbf{M}}}_l^{\boldsymbol{m'}}(\text{PAS}) \qquad \text{.....(1.27)}$$

where, $D_{m\,m'}^{l}(\alpha,\beta,\gamma) = e^{-i(m\alpha + m'\gamma)} d_{m\,m'}^{l}(\beta)$ .....(1.28)

These rotor frame (RF) components is converted to the lab frame (LF) tensor components using the Wigner Eckart theorem by taking $\alpha = 0$, $\beta = \theta_m$, $\gamma = \omega_r t$ in equation 1.29.

$$\hat{\hat{\mathbf{M}}}_l^{\boldsymbol{m}}(\text{LF}) = \sum_{-l}^{l} D_{m\,m'}^{l}(0,\theta_m,\omega_r t)\hat{\hat{\mathbf{M}}}_l^{\boldsymbol{m'}}(\text{RF}) \qquad \text{.....(1.29)}$$

The components X_l^m in the form of Cartesian components in Lab frame can be given according to the following Table 1.2.

Table 1.2 Components X_l^m in the form of Cartesian components in lab frame

Components in the Cartesian System
$X_0^0(\mathrm{LF}) = -1/\sqrt{3}\left(X_{xx} + X_{yy} + X_{zz}\right)$
$X_1^0(\mathrm{LF}) = i/\sqrt{2}\left(X_{xy} + X_{yx}\right)$
$X_1^{\pm 1}(\mathrm{LF}) = 1/2\left[X_{zx} - X_{xz}\right] \pm i(X_{zy} - X_{yz})$
$X_2^0(\mathrm{LF}) = -1/\sqrt{6}\left[3X_{zz} - \left(X_{xx} + X_{yy} + X_{zz}\right)\right]$
$X_2^{\pm 1}(\mathrm{LF}) = \mp 1/2\left[X_{xz} - X_{zx} \pm i\left(X_{zy} + X_{yz}\right)\right]$
$X_2^{\pm 2}(\mathrm{LF}) = 1/2\left[X_{xx} - X_{yy} \pm i\left(X_{xy} - X_{yx}\right)\right]$

The resultant Hamiltonian is obtained by,

$$\hat{H} = C\,\hat{\mathbf{M}} \cdot \hat{\mathbf{X}} = C\sum_{l=0}^{2}\sum_{m=-l}^{l}(-1)^m M_l^{-m}(LF)X_l^m(LF) \qquad \text{.....(1.30)}$$

1.5.2 Chemical shift (δ)

Suppose $\hat{\mathbf{I}}$ is the spin vector, $\hat{\boldsymbol{\sigma}}$ is the chemical shielding tensor and $\vec{B}$ is the static magnetic field. Thus the chemical shift Hamiltonian, $\hat{H}^{cs}$ can be written as,

$$\hat{H}^{cs} = \hbar\gamma \cdot \hat{\mathbf{I}} \cdot \hat{\boldsymbol{\sigma}} \cdot \vec{\mathbf{B}} \qquad \text{.....(1.31)}$$

For $\hat{\mathbf{I}} = \begin{bmatrix}\hat{I}_x & \hat{I}_y & \hat{I}_z\end{bmatrix}$ and $\vec{\mathbf{B}} = \begin{bmatrix}0\\0\\B_0\end{bmatrix}$, chemical shift Hamiltonian can be given as,

$$\hat{H}^{\mathbf{cs}} = \hbar\gamma \cdot \hat{\boldsymbol{\sigma}} \cdot \begin{bmatrix}0 & 0 & 0\\0 & 0 & 0\\\hat{I}_x B_0 & \hat{I}_y B_0 & \hat{I}_z B_0\end{bmatrix} \qquad \text{.....(1.32)}$$

Thus, following the procedure mentioned in section 1.5.1, the complete chemical shift Hamiltonian can be given as,

$$\hat{H}^{\mathbf{cs}} = C[\hat{\mathbf{X}}_{\mathbf{0}}^{\mathbf{0}}(\mathrm{LF})\hat{\boldsymbol{\sigma}}_{\mathbf{0}}^{\mathbf{0}}(\mathrm{LF}) + \hat{\mathbf{X}}_{\mathbf{2}}^{\mathbf{0}}(\mathrm{LF})\hat{\boldsymbol{\sigma}}_{\mathbf{2}}^{\mathbf{0}}(\mathrm{LF}) \qquad \text{.....(1.33)}$$

iso-term aniso-term

$$\widehat{H}^{\mathbf{cs}} = h\upsilon\left(\hat{I}_z B_0\right)[\sigma_{iso} + (1/4)\delta_{zz}[(3cos^2\theta_m - 1)[(3cos^2(\beta) - 1) + \eta sin^2(\beta)cos2\gamma] + (sin2\theta_m)[3\cos(\alpha + \omega_r t)\, sin2\beta - 2\eta sin\beta\{cos\beta cos2\gamma\cos(\alpha + \omega_r t) - \sin(\alpha + \omega_r t)sin2\gamma\}] + (sin^2\theta_m)[3\cos(\alpha + \omega_r t)\, sin^2\beta + \eta\{cos2\gamma(1 + cos^2\beta)\cos 2(\alpha + \omega_r t) + sin2\gamma cos\beta \sin(\alpha + \omega_r t)\}]] \quad \text{……..……..…..(1.34)}$$

After a complete rotor cycle, the sinosudal function $sin2\theta_m$ and $sin^2\theta_m$ in equation 34 becomes zero and the chemical shift expression becomes,

$$\widehat{H}^{\mathbf{cs}} = h\upsilon\left(\hat{I}_z B_0\right)[\sigma_{iso} + 1/4\,\delta_{zz}[(3cos^2\theta_m - 1)[(3cos^2(\beta) - 1) + \eta sin^2(\beta)cos2\gamma] \quad \text{……(1.35)}$$

The effect of the asymmetry parameter (η) on the shape of the solid-state NMR spectrum is shown in Figure 1.1.

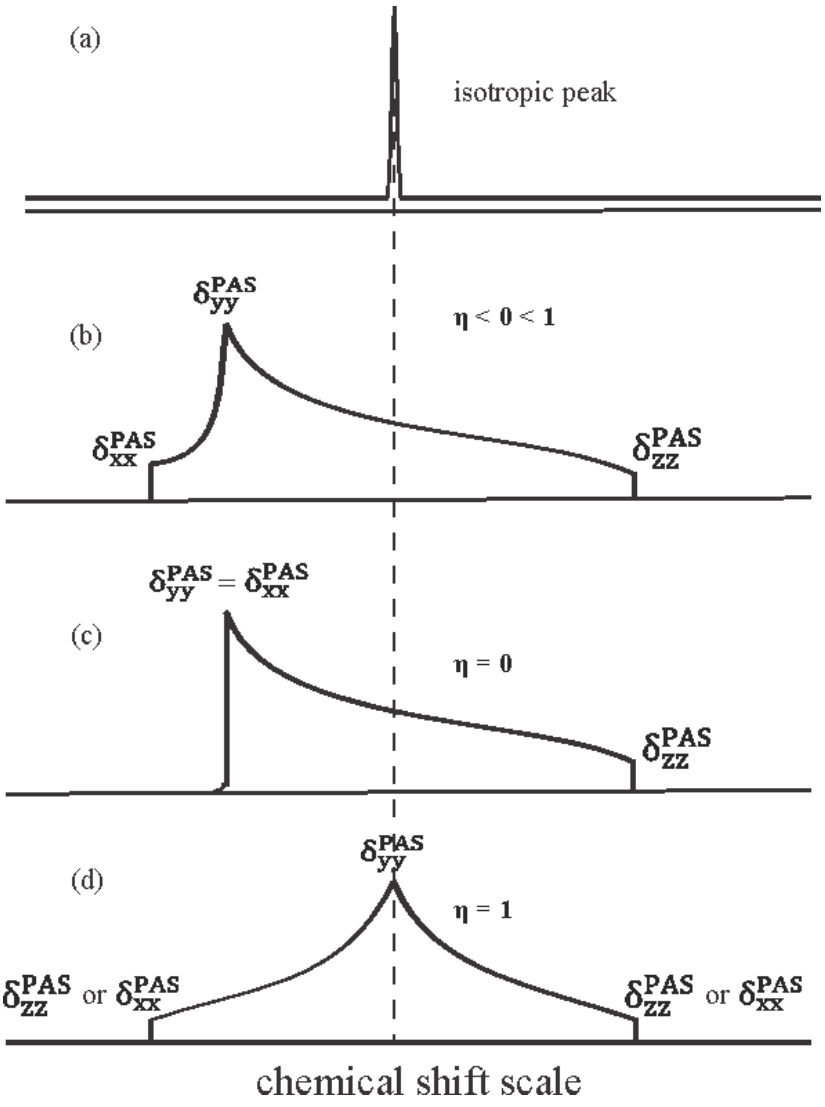

Figure 1.1. The NMR spectra of solids having chemical shielding interactions. a) The spectrum resulting from fast isotropic motion; b) the powder pattern resulting in the case of the asymmetry parameter being greater than zero and smaller than one; c) the powder pattern resulting in the case of the asymmetry parameter being equal to zero (axial symmetry); d) the powder pattern resulting in the case of the asymmetry parameter equal to one.[71]

1.5.3 Dipolar coupling

Dipolar coupling is the interaction of two nuclear spins through space. Because each nuclear spin is magnetic, it generates a magnetic field. Another nuclear spin in its proximity experiences this magnetic field and is affected by it. The same thing happens for the first

spin. This phenomenon may happen in the case of nuclear spins of the same type of nuclei (homonuclear dipolar coupling) or nuclear spins of different nuclei (heteronuclear dipolar coupling). Dipole-dipole interaction is directly proportional to the gyromagnetic ratios of the two interacting nuclei and inversely proportional to the cube root of the distance between them.

The energy between two dipoles ($\hat{\mathbf{I}}_i$ and $\hat{\mathbf{I}}_j$) with a separation r_{ij} is given by,

$$E_{DIP}(ij) = \sum_i^{spins} \sum_{j>i}^{spins} [\frac{\hat{\mathbf{I}}_i \cdot \hat{\mathbf{I}}_j}{{r_{ij}}^3} - 3\frac{(\hat{\boldsymbol{\mu}}_i \cdot r_{ij})(\hat{\boldsymbol{\mu}}_j \cdot r_{ij})}{{r_{ij}}^5}] \quad \text{.....(36)}$$

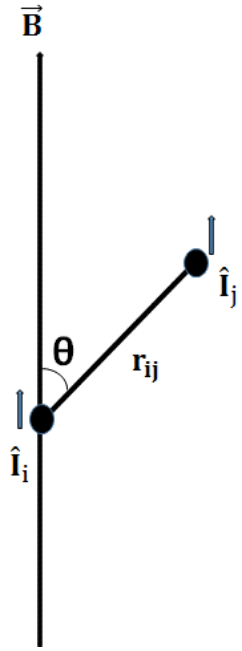

Figure 1.2. The orientation between spin $\hat{\mathbf{I}}_i$ and $\hat{\mathbf{I}}_j$ in the presence of static magnetic field $\vec{\mathbf{B}}$

The dipolar Hamiltonian (H_{DIP}) can be written in the form of above expression as,

$$\hat{H}(ij) = \sum_i^{spins} \sum_{j>i}^{spins} \frac{\mu_0}{4\pi} \frac{\gamma_i \gamma_j \hbar^2}{r_{ij}^3} \left[\hat{\mathbf{I}}_i \cdot \hat{\mathbf{I}}_j - 3\frac{(\hat{\boldsymbol{\mu}}_i \cdot \mathbf{r_{ij}})(\hat{\boldsymbol{\mu}}_j \cdot \mathbf{r_{ij}})}{{r_{ij}}^2}\right] \quad \text{.....(1.37)}$$

$$\hat{H}(ij) = \sum_i^{spins} \sum_{j>i}^{spins} \frac{\mu_0}{4\pi} \frac{\gamma_i \gamma_j \hbar^2}{r_{ij}^3} [\hat{\mathbf{I}}_i \cdot \hat{\mathbf{I}}_j - 3(\hat{\mathbf{I}}_i \cdot \mathbf{e_{ij}})(\hat{\mathbf{I}}_j \cdot \mathbf{e_{ij}})], \text{ where unit vector } \mathbf{e_{ij}} = \frac{\mathbf{r_{ij}}}{r_{ij}}$$

.....(1.38)

$$\hat{H}_{ij} = \sum_i^{spins} \sum_{j>i}^{spins} \frac{\mu_0}{4\pi} \frac{\gamma_i \gamma_j \hbar^2}{r_{ij}^3} [\hat{\mathbf{I}}_i \cdot \hat{\overline{\mathbf{1}}} \cdot \hat{\mathbf{I}}_j - 3(\hat{\mathbf{I}}_i \cdot \hat{\mathbf{e}} \cdot \hat{\mathbf{I}}_j)]$$, where $\hat{\mathbf{e}} = \mathbf{e_{ij}} \otimes \mathbf{e_{ij}}$

……..……..…..(1.39)

$$\hat{H}_{ij} = \sum_i^{spins} \sum_{j>i}^{spins} \frac{\mu_0}{4\pi} \frac{\gamma_i \gamma_j \hbar^2}{r_{ij}^3} [\hat{\mathbf{I}}_i (\hat{\overline{\mathbf{1}}} - 3\hat{\mathbf{e}}) \hat{\mathbf{I}}_j]$$ ……..……..….....(1.40)

$$\hat{H}_{ij} = \sum_i^{spins} \sum_{j>i}^{spins} \frac{\mu_0}{4\pi} \frac{\gamma_i \gamma_j \hbar^2}{r_{ij}^3} [\hat{\mathbf{I}}_i \cdot \hat{\overline{\mathbf{A}}} \cdot \hat{\mathbf{I}}_j],$$ ……..……..….....(1.41)

where, $\hat{\overline{\mathbf{A}}} = (\hat{\overline{\mathbf{1}}} - 3\hat{\mathbf{e}})$ is called the dipolar coupling tensor.

For a single spin pair, the dipolar Hamiltonian can be given as,

$$\hat{H}_{ij} = \frac{\mu_0}{4\pi} \frac{\gamma_i \gamma_j \hbar^2}{r_{ij}^3} [\hat{\mathbf{I}}_i \cdot \hat{\overline{\mathbf{A}}} \cdot \hat{\mathbf{I}}_j]$$ ……..……..….....(1.42)

where the elements of 3 × 3 matrix $\hat{\overline{\mathbf{A}}}$ are given by,

$$\left\langle u \left| \hat{\overline{\mathbf{A}}}_{\mathbf{ij}} \right| v \right\rangle = \delta_{uv} - 3e_u(j)e_v(i)$$. ……..……..….(1.43)

$$\hat{H}_{ij} = \frac{\mu_0}{4\pi} \frac{\gamma_i \gamma_j \hbar^2}{r_{ij}^3} [\hat{\overline{\mathbf{A}}} \cdot \hat{\overline{\mathbf{X}}}]$$, where $\hat{\overline{\mathbf{X}}} = \hat{\mathbf{I}}_i \otimes \hat{\mathbf{I}}_j$ ……..……..….....(1.44)

$$\hat{H} = C[\hat{\overline{\mathbf{A}}} \cdot \hat{\overline{\mathbf{X}}}]$$ ……..……..….....(1.45)

C is the dipolar coupling constant.

$$\hat{\overline{\mathbf{A}}}_{ij} = \begin{bmatrix} 1 - 3e_{xx} & -3e_{xy} & -3e_{xz} \\ -3e_{yx} & 1 - 3e_{yy} & -3e_{yz} \\ -3e_{zx} & -3e_{zy} & 1 - 3e_{zz} \end{bmatrix} \text{ or } \hat{\overline{\mathbf{A}}}(PAS, ij) = \begin{bmatrix} 1 & 0 & 0 \\ 0 & 1 & 0 \\ 0 & 0 & -2 \end{bmatrix}$$ ….……....(1.46)

The dipolar tensor is traceless. Hence, there will be no rank 0 component, and no off-diagonal elements, thus, there will be no rank 1 components. The spatial tensor in the principal axis system, $\hat{\overline{\mathbf{A}}}$ (PAS) can be given as,

$$\hat{\overline{\mathbf{A}}}(PAS) = 0 + 0 + \begin{bmatrix} 1 & 0 & 0 \\ 0 & 1 & 0 \\ 0 & 0 & -2 \end{bmatrix}$$ ……..……..….....(1.47)

The spin components in the Cartesian form can be given as,

$$\hat{\hat{\mathbf{X}}} = \hat{\mathbf{I}}_i \otimes \hat{\mathbf{I}}_j = [I_x, I_y, I_z] \otimes \begin{bmatrix} I_x \\ I_y \\ I_z \end{bmatrix} = \begin{bmatrix} I_x I_x & I_x I_y & I_x I_z \\ I_y I_x & I_y I_y & I_y I_z \\ I_z I_x & I_z I_x & I_z I_z \end{bmatrix} \quad \text{.....(1.48)}$$

Following the procedure mentioned in section 1.5.1, the dipolar coupling Hamiltonian can be written as,

$$\hat{H} = C(-1/4)[\{[(3cos^2\theta_m - 1)][(3cos^2\beta - 1) + 3sin2\theta_m sin2\beta \cos(\omega_r t + \gamma) + 3sin^2\theta_m sin^2\beta \cos(2\omega_r t + 2\gamma)]\}\{[3\hat{I}_z\hat{I}_z - (\hat{\mathbf{I}} \cdot \hat{\mathbf{I}})]\} \quad \text{.....(1.49)}$$

1.5.4 Magic angle spinning (MAS) technique

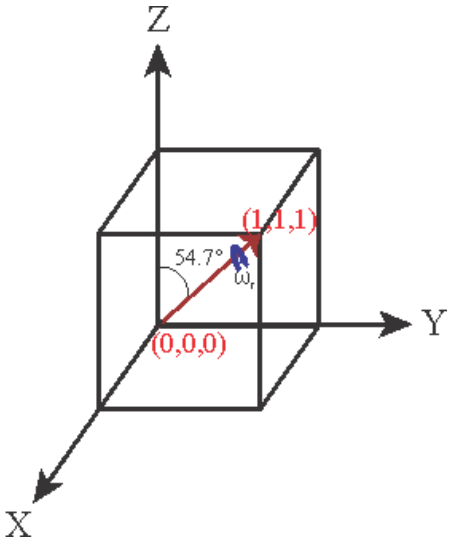

Figure 1.3. Magic Angle Spinning direction on the diagonal vector joining (0,0,0) and (1,1,1) coordinates in cubic symmetry at an angle of 54.7°

In solid-state NMR spectroscopy, all anisotropic interaction (CSA and dipolar coupling) terms depend on the orientation dependent trigonometric term $\frac{1}{2}(3\cos^2\theta - 1)$. It means that wherever this orientation term is involved, that part can be made zero by equating $\frac{1}{2}(3\cos^2\theta - 1)$ term zero. Equating $\frac{1}{2}(3\cos^2\theta - 1)$ to zero, yields the value of θ to 54.7°,

which is called the magic angle. If the sample is spun at 54.7° (with respect to the applied magnetic field) faster than the dipolar coupling strength, the homonuclear dipolar coupling can be reduced significantly and the isotropic value of the chemical shifts and possibly scalar couplings can be obtained. The dipolar coupling value, however, cannot be suppressed completely because of the presence of $(3\hat{I}_{1z}\hat{I}_{1z} - \hat{I}_1 \cdot \hat{I}_2)$ term, which leads to the flip-flop $(\frac{\hat{I}_+\hat{I}_- + \hat{I}_-\hat{I}_+}{2})$ term. This term cannot be averaged out completely.

1.5.5 Relaxation

Relaxation is the process in which the nuclear magnetization returns to its equilibrium state after the removal of an applied radiofrequency pulse. After a 90° pulse, the magnitude of z-magnetization (longitudinal magnetization), M_z increases gradually while the magnetization in the XY-plane (transverse magnetization) decreases. The longitudinal relaxation process of the net magnetization is called the spin-lattice relaxation and the time constant taken for this exponential decay is called spin lattice relaxation time (T_1) and the exponential decay of the net magnetization in the transverse plane is called the spin-spin relaxation and the time constant taken for this process is called transverse relaxation time (T_2). T_1 is a growing exponential of magnetization and T_2 is a decaying exponential of magnetization. These two processes can be written by the following formulas;

$M_z = M_o(1 - e^{-t/T_1})$ for T_1 relaxation ……....(1.50)

$M_z = M_o(e^{-t/T_2})$ for T_2 relaxation ……....(1.51)

Relaxation of spins occur due to the random magnetic field fluctuations (of same amplitude and same frequency range) in a certain given time. These random motions can be recognized by the auto correlation function, $B_x(t)$ which is defined by the same function

correlated with itself at different time points. The value for this autocorrelation function is zero for a long period of time and non-zero for a short period of time. The distribution of the magnetic field can be found by knowing its standard deviation $\overline{< B_x^2(t) >}$ i. e. by $\overline{< B_x^2(t) >} = 0$. The distribution of the magnetic field can be narrow or broad and it gives information about the amplitude of the field. Suppose at any time t, the auto correlation function is $B_x(t)$ and at time t+τ, the function is $B_x(t+\tau)$. Thus, fluctuations between these time intervals can be defined as,

$G(\tau) = \langle B_x(t) B_x(t+\tau) \rangle \neq 0$ for short period of time ……(1.52)

$= 0$ for long period of time.

The function G(t) is an exponential function and can be written by, $G(t) = < B_x^2(t) > e^{-t/\tau_c}$ where, τ_c is the correlation time or correlation time constant of decay. If there are fast fluctuations, the decay of this function is fast giving short correlation time and if the fluctuations are slow, the function decays slowly giving a long correlation time.

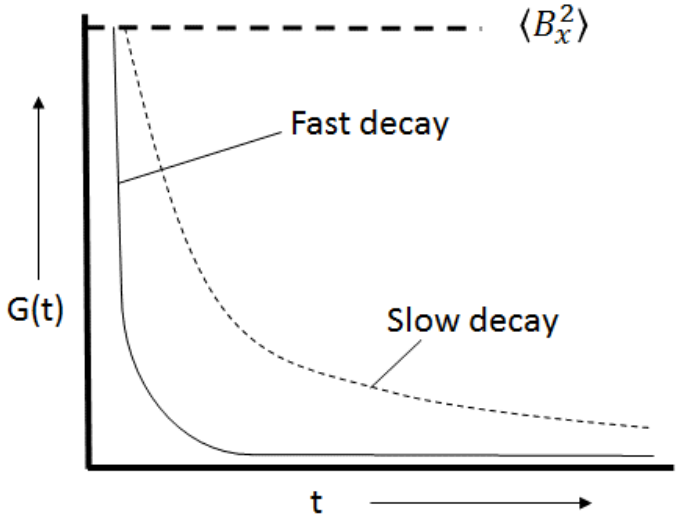

Figure 1.4. Variation of auto correlation function G(t) with time (t)

A fast rotating molecule experiences fast random fluctuations and thus has a short correlation time, relaxing at a fast rate, resulting in a broad spectrum (short τ_c). A slow rotating molecule experiences a larger correlation time, relaxing at a slow rate and thus giving narrow spectrum (long τ_c).

1.5.6 Spectral density function

The transitions between the energy states are given by the fluctuating transverse field. The probability of transition from one energy state to the other is given by the spectral density function J(ω), which is defined as,

$$J(\omega) = 2\int_0^{\infty} < B_x^2(t) > e^{-t/\tau_c}\, dt \qquad \text{.....(1.53)}$$

$$J(\omega) = 2< B_x^2(t) > \frac{\tau_c}{1+\omega^2\tau_c^2} \qquad \text{.....(1.54)}$$

J(ω) is a relaxation driver in terms of frequency. $< B_x^2(t) >$ is the strength of interactions. The term $\frac{\tau_c}{1+\omega^2\tau_c^2}$ is the frequency dependent term and is called the normalized spectral density function.

1.5.7 Spin-lattice relaxation (T_1)

This process is related to the rate of change of populations of the spins in the lower energy state (α) and higher energy state (β). When a radiofrequency radiation is applied, the equilibrium of spins is disturbed raising the number of spins in the higher energy state, and the magnetization vector of the spins is placed in the XY-plane. This magnetization vector returns back to the equilibrium state after the applied pulse is turned off; the number of spins are transferred back from the higher energy state to the lower energy state by the

dissipation of energy to the lattice. That is why the process is termed as spin-lattice relaxation process. In the T_1 process exchange of energy (loss of energy to the surroundings) takes place, thus it is analogous to a cooling process. The spin lattice relaxation time (T_1) is written in the form of following expression,

$$M_z(t) = M_0(1 - e^{-\frac{t}{T_1}}) \quad \text{.....(1.55)}$$

In terms of the correlation time (τ_c), the spin lattice relaxation (T_1) is written by the following expression,

$$T_1 = \frac{1}{\gamma^2 \langle B_x^2 \rangle} \left(\frac{1}{\tau_c} + \tau_c \omega^2\right) \quad \text{.....(1.56)}$$

Spin lattice relaxation time (T_1) gives information about the reorientation of the molecule in the lattice thus providing information about the rotational and translational motion. A relation between relaxation time and correlation time (figure 1.5) shows that the T_1 first decreases with the correlation time and increases again after a minimum. The first correlation follows when the correlation time is short i.e. the fast motional regime while the latter is true for the long correlation time i.e. slow motional regime (figure 1.6).

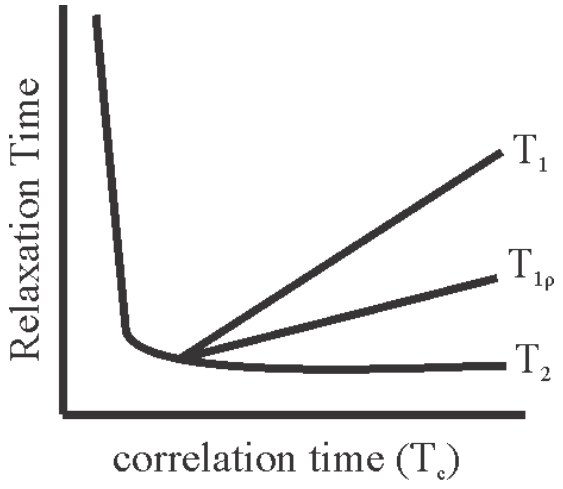

Figure 1.5. Variation of relaxation times with correlation time

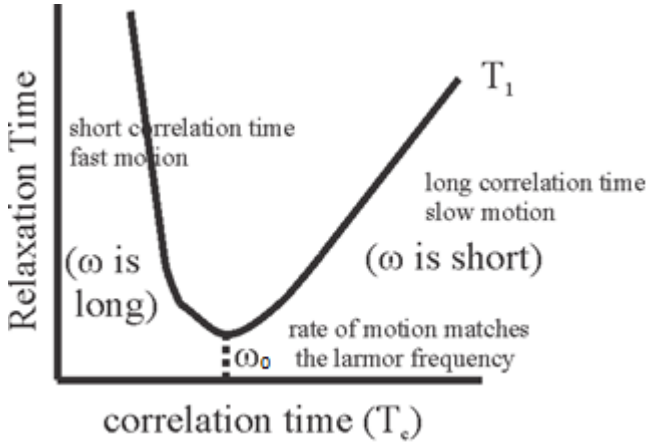

Figure 1.6. Dependence of relaxation time (T_1) on frequency (ω_0)

From the above equation 1.56, it follows that,

$$\frac{1}{\tau_c} \propto (\omega_0) \qquad \text{.....(1.57)}$$

(ω_0) is the static field strength for a particular nucleus. It means that if a control on the magnetic field strength is achieved, the different motional timescale regimes can be detected. In a $T_{1\rho}$ experiment, the power of the applied pulse field strength (ω_1 instead of (ω_0) can be controlled and the change of τ_c can be observed by varying the temperature to observe whether the motion is on the scale of ms and μs. In the solution state, the magnetic field is fixed in terms of a static instrument magnet field (MHz) and thus the motion on the nanosecond time scale can be observed by T_1 experiment. However, for the millisecond and microsecond timescale motion, a $T_{1\rho}$ experiment is performed.

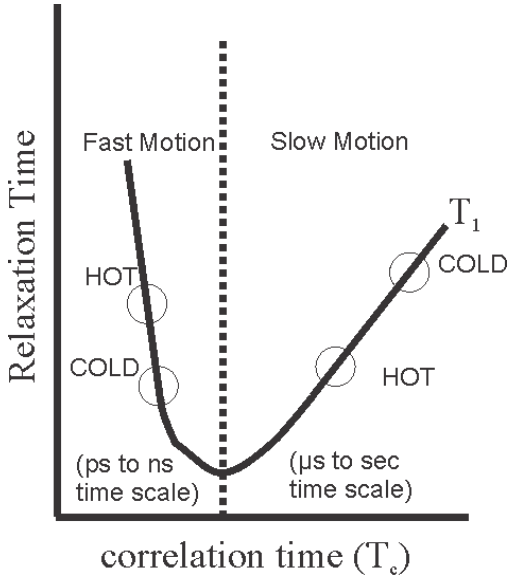

Figure 1.7 Dependence of relaxation time (T_1) on Temperature

The correlation time τ_c depends on temperature and the type of motional regime. For example, in the fast motional regime, if the given sample is warmed up, the fluctuations become faster, reducing the correlation time, increasing T_1. Cooling down the sample reduces fluctuations, increasing the correlation time and thus reducing T_1. The correlation time τ_c is also defined as the correlation time for fluctuations. In the solution state, τ_c is in the range of tens of picoseconds to several nanoseconds (Figure 1.7).

1.5.8 Spin-spin relaxation (T_2)

The decay rate of the net magnetization in the transverse plane is given by the equation 1.58. The overall transverse relaxation rate is equal to the sum of the dephasing rate due to field inhomogeneity and natural rate relaxation decay rate.

$$\frac{1}{T_2^*} = \frac{1}{T_2'} + \frac{1}{T_2} \qquad \text{.....(1.58)}$$

During the T_2 process, the total energy of the system remains constant. Mathematically, T_2 relaxation can be written as

$$M_z(t) = M_0 e^{\left(-\frac{t}{T_2}\right)} \quad \text{……...……....(1.59)}$$

This decaying process of magnetization in the transverse plane is usually governed mainly by the following four types of interaction,

1. Quadrupolar coupling interaction between nuclei and the electric field gradient (about 1–300 MHz)
2. Dipolar interactions such as among ^{1}H nuclei. (about 10–100 kHz)
3. CSA interactions such as for ^{13}C nuclei. (about 0.01–10 kHz)
4. Spin rotations which results in a local field such as in the case of heavy metals (mercury, lead etc.)
5. Relaxation due to the presence of paramagnetic species

1.5.9 T_1 relaxation in the rotating frame ($T_{1\rho}$)

If the tilted net magnetization spin vector is held in the XY-plane with the help of an applied radiofrequency pulse, the net magnetization spin vector decays slowly under the spin lock magnetic field (B_1). Under the spin lock, a transverse relaxation is happening since it has an analogy to T_1 relaxation being relaxed under the parallel applied magnetic field (in this case radio-frequency magnetic field, B_1 instead of static magnetic field, B_0). The mathematical expression for the $T_{1\rho}$ is given by the following equation.

$$M_z(t) = M_0 e^{\left(-\frac{t}{T_{1\rho}}\right)} \quad \text{……...……....(1.60)}$$

The pulse sequence for the $T_{1\rho}$ experiment is shown in the following figure 1.8.

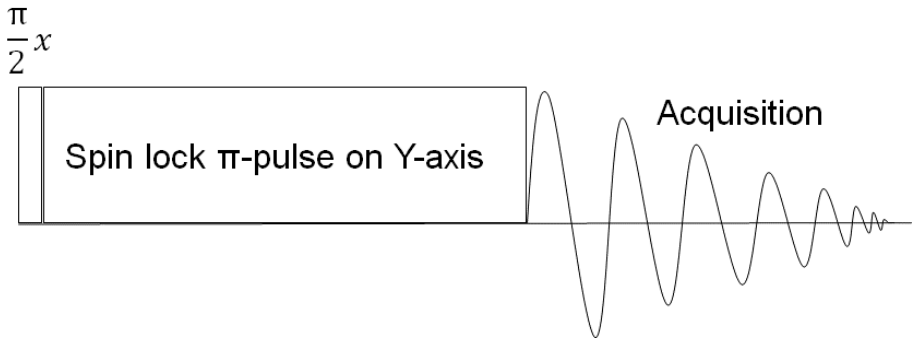

Figure 1.8. Pulse sequence for the $T_{1\rho}$ experiment

In terms of the spectral density function, $T_{1\rho}$ can be written in the form of the following formula,

$$T_{1\rho}^{-1} = (3/20)b^2\{J(0) + 10J(\omega^0) + 2J(2\omega^0) \quad \text{……...……...(1.61)}$$

1.5.10 Fluorine (^{19}F) solid-state NMR spectroscopy of solids containing both proton (^{1}H) and fluorine (^{19}F)

Fluorine-19 NMR spectroscopy is an ideal characterization technique to obtain structural information for fluorinated compounds. The reason is the high natural abundance (100%) of ^{19}F and its high gyromagnetic ratio, 25.181×10^7 rad $s^{-1}T^{-1}$ corresponding to a frequency of 470.322 MHz on a 500 MHz NMR spectrometer. The high chemical shift range (about 350 ppm) present the opportunity to obtain higher resolution in ^{19}F NMR spectra. The close resonance frequencies of ^{19}F and ^{1}H present a challenge in their separation (470.322 MHz for ^{19}F and 500 MHz for ^{1}H on a 500 MHz NMR instrument). To record high-resolution spectra high powers of the radio frequency field are required. There is a need of a highly sensitive filtering circuit, which can cleanly separate the frequency powers of ^{1}H and ^{19}F. The presence of strong heteronuclear coupling (between ^{1}H and ^{19}F) and strong homonuclear coupling (between two ^{19}F nuclei and between two ^{1}H nuclei) make the task

more difficult. Therefore, higher magic angle spinning speeds (>20 kHz) and special decoupling sequences are required such as XY-16 to remove strong heteronuclear coupling between ^{1}H and ^{19}F. Very efficient homonuclear decoupling can be achieved with sequences such as Lee-Goldburg. Moreover, the spinning of the fluorinated sample is a very difficult task except in case of stable fluorinated materials which have high melting points. In the case of unstable and sensitive fluorinated materials, very high rotor spinning speed cannot be applied without sufficiently cooling off the sample. If the material is air sensitive, special inserts of perfluorinated polymers are required to pack the materials and these inserts are then inserted in the rotor.[72]

1.5.11 Dipolar dephasing experiment

The basic principle behind the dipolar dephasing experiment is that an NMR signal should completely diphase or disappear in a certain definite dephasing delay depending on the distance between the observed nucleus and a dipolar coupled nucleus.

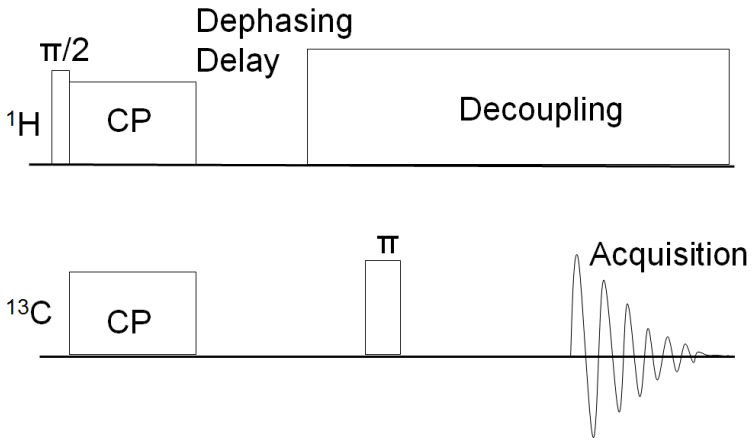

Figure 1.9. Dipolar Dephasing Pulse Sequence

If the signal does not dephase in that certain time period, it indicates some kind of dynamical feature of the compound. For example, if the motion is too fast as in the case of

methyl groups, the ^{13}C signal originating from it will be hardly suppressed by a dipolar-dephasing experiment. In this experiment, first the cross polarization is done from ^{1}H to ^{13}C. Then the signal is allowed to evolve under ^{1}H-^{13}C dipolar coupling for a fixed period of time as depicted in Figure 1.9. After this time period, the decoupling on the ^{1}H channel is turned on while the chemical shift evolution on ^{13}C channel is refocused with the application of a π-pulse. The FID is now acquired on the ^{13}C channel. If an appreciable amount of dipolar coupling is present between ^{13}C and ^{1}H atoms, the signal intensity will be appreciably suppressed depending on the amount of dipolar coupling while if dipolar coupling value is small, there will be a minute suppression in the signal intensity. If the value of dephasing time exceeds the value of expected dephasing time (calculated from distances obtained from X-ray crystallography), some kind of dynamics is expected in the compound.

References

1. Atkins, P.; Overton, T.; Rourke, J. Weller, M.; Armstrong, F. The Group 17 elements. *Inorganic Chemistry*, Fourth Edition; W. H. Freeman and Company: New York, 2005, pp 401.

2. Bondi, A. *J. Phys. Chem.*, **1964**, *68*, 441.

3. City of Lethbridge Home page, http://www.lethbridge.ca/living-here/water-wastewater/Pages/How-we-treat-our-water.aspx (accessed December 28, 2015).

4. Su, N.; Marek, C. L.; Ching, V.; Grushka, M. *J. Can. Dent. Assoc.* **2011**, *77*, b85.

5. Christophorou, L. G.; Olthoff, J. K.; VanBrunt, R. J. *IEEE Elect. Insul. Mag.* **1997**, *13*, 20.

6. Hasek, W. R.; Smith, W. C.; Engelhardt, V. A. *J. Am. Chem. Soc.* **1960**, 82, 543.

7. Gillespie, R. J. *Coor. Chem. Re*v. **2000**, *197*, 51.

8. Azeem, M.; Brownstein, M.; Gillespie, R. J. *Can. J. Chem.* **1969**, *47*, 4159.

9. O'Brien, B. A.; DesMarteau, D. D. *Inorg. Chem.* **1984**, *23*, 644.

10. Lowe, K. C. 'Perfluorochemicals in Medicine and Cell Biotechnology', *Fluorine in Medicine in the 21st Century*, Manchester: UMIST; 18-21 April, 1994; N. S. Faithfull, 'The Role of Perfluorochemicals in Improving Oxygenation – Intravascular and Respiratory Applications', *Fluorine in Medicine in the 21st Century*, Manchester: UMIST; 18-21 April, 1994.

11. Med Library Prescription Medication http://medlibrary.org/lib/rx/meds/ciprofloxacin-3/ (accessed December 28, 2015).

12. Gisi, U.; Chet, I.; Gullino, M. L. Novel tools to identify the mode of action of fungicides as exemplified with fluopicolide. *Recent Developments in Management of Plant Diseases*, 1; Springer: Netherlands **2010**, pp 21.

13. Alexander, J.; Auðunsson, A. G.; Benford, D.; Cockburn, A.; Cravedi, J.- P.; Dogliotti, E.; Domenico, A. D.; Fernández-Cruz, M. L.; Fink-Gremmels, J.; Fürst, P.; Galli, C.; Grandjean, P.; Gzyl, J.; Heinemeyer, G.; Johansson, N.; Mutti, A.; Schlatter, J.; Leeuwen, R.; Peteghem, C.; Verger, P. *J. Eur. Food Safety Authority* **2008**, *653*, 1.

14. Tsuji, M.; Inoue, T.; Shibata, O. *Colloids and Surfaces B: Biointerfaces* **2008**, *61*, 61.

15. Furuya, T.; Kamlet, A. S.; Ritter, T. *Nature*, **2011**, 473, 470.

16. Muller, K; Faeh, C.; Diederch, F. *Science* **2007**, *317*, 1881.

17. Bondi, A. *J. Phys. Chem.*, **1964**, *68*, 441.

18. Dikoiu, V. *Rev. Roum. Chim.*, **2007**, *52*, 3, 219.

19. O'Brien, B. A.; DesMarteau, D. D. *Inorg. Chem.* **1984**, *23*, 644.

20. Smart, B. E. *J. Fluorine Chem.*, **2001**, *109*, 3.

21. Parsch, J.; Engels, J. W. *J. Am. Chem. Soc.*, **2002**, *124*, 5664.

22. Grimley, J. *Chem. Eng. News*, ***2006,*** *84*, 49, 22.

23. a) (i) Herzog, A.; Liu, FQ; Roesky, H. W.; Demsar, A.; Keller, K.; Noltemeyer, M.; Pauer, F. *Organometallics* **1994**, *13*, 1251. (ii) Roesky, H. W.; Keller, K. *J. Fluorine Chem.* **1998**, *89*, 3. (iii) Edelson, B.S.; Stoltz, B.M. and Corey, E.J. *Tetrahedron Lett.* **1999**, *40*, 6729 b) Krause, E. *Ber. Dtsch. Chem. Ges*. **1918**, *51*, 1447.

24. Oppegard, A. L.; Smith, W. C.; Muetterties, E. L.; Engelhardt, V. A. *J. Am. Chem. Soc.* **1960**, 82, 3835.

25. Goettel, J. T.; Turnbull, D.; Gerken, M. *J. Fluorine Chem.* **2015**, *174*, 8.

26. Hasek, W. R.; Smith, W. C.; Engelhardt, V. A. *J. Am. Chem. Soc.* **1960**, 82, 543.

27. Heureux, A. L.; Beaulieu,F; Bennett, C.; Bill, D. R; Clayton, S.; LaFlamme, F; Mirmehrabi, M.; Tadayon, S; Tovell, D.; Couturier, M. *J. Org. Chem.* **2010**, *75*, 3401.

28. Baasner, B., Hagemann, H. and Tatlow, J. C. Organo-Fluorine Compounds Volume E 10 a-c, Thieme Stuttgart: NewYork, 2000.

29. (i) Chaudhary, P; Goettel, J. T.; Hazendonk, P.; Sowlati-Hashjin, S.; Mercier, H.P.A.; Gerken, M. *Chem. Eur. J.* **2015**, *21*, 1. (ii) Goettel, J. T.; Chaudhary, P.; Hazendonk, P.; Mercier, H. P. A.; Gerken, M. *Chem. Comm.* **2012**, *48*, 9120.

30. (i) Bartlett, N.; Robinson, P.L. *Chem. Ind. London.* **1956**, 1351. (ii) Bartlett, N.; Robinson, P. L. *J. Chem. Soc.* **1961**, 3417.

31. Cotton, F. A.; George, J. W. *J. Inorg. Nucl. Chem.* **1958**, *7*, 397.

32. Oppegard, A. L.; Smith, W. C.; Muetterties, E. L.; Engelhardt, V. A. *J. Am. Chem. Soc.* **1960**, 82, 3835.

33. Barr, M. R.; Dunell, B. A. *Can. J. Chem.* **1970**, *48*, 895.

34. Seel, V. F.; Detmer, O. *Z. Anorg. Allg. Chem.* **1959**, 301, 113.

35. Brownstein, M; Shamir, J. *Appl. Spec.* **1971**, *26*, 77.

36. Evan, J. A.; Long, D. A. *J. Chem. Soc. A* **1968**, 1688.

37. Gibler, D. D.; Adams, C. J.; Fischer, M.; Zalkin, A.; Bartlett, N. *Inorg. Chem.* **1972**, *11*, 2325.

38. Mallouk, T. E.; Bernard, D.; Bartlett, N. *Inorg. Chem.* **1984**, *23*, 3160.

39. Mallouk, T. E.; Rosenthal, G. L.; Müller, G.; Brusasco, R.; Bartlett, N. *Inorg. Chem.* **1984**, *23*, 3167.

40. Smith, W. C. *Angew. Chem., Int. Ed.* **1962**, *1*, 467.

41. Du, H-C; Wang, Z-K; Wang, Y.; Guo, J-Z *J. Chil. Chem. Soc.* **2014**, 59, 2322.

42. (i) Mallouk, T. E.; Bernard, D.; Bartlett, N. *Inorg. Chem.* **1984**, *23*, 3160 (ii) Mallouk, T. E.; Rosenthal, G. L.; Müller, G.; Brusasco, R.; Bartlett, N. *Inorg. Chem.* **1984**, *23*, 3167.

43. (i) Clifford, A. F.; Thompson, J. W. **1966**, *5*, 1424. (ii) Erhart, M.; Mews, R. *Z. Anorg. Allg. Chem.* **1992**, *615*, 117.

44. Smith, G. L; Mercier, H. P. A.; Schrobilgen, G. *Inorg. Chem.* **2011**, *50*, 12359.

45. Mews, R.; Henle, H. *J. Fluorine Chem.* **1979**, *14*, 495.

46. Cheung, Y. S.; Chen, Y. J.; Ng, C. Y.; Chiu, S. W.; Li, W. K. *J. Am. Chem. Soc.* **1995**, *117*, 9725.

47. Wong, P. S. H.; Ma, S.; Yang, S. S.; Cooks, R. G. *Am. Soc. Mass Spec.* **1997**, *8*, 68.

48. Gozzo, F. C.; Ifa, D. R.; Eberlin, M. N. *J. Org. Chem.* **2000**, *65*, 3920.

49. Sparrapan R., Mendes M. A., Eberlin M. N. *Int. J. Mass Spec.* **1999**, *182/183*, 369.

50. Ruff, O.; Eisner, F.; Heller, W. *Z. Anorg. Allgem. Chem.* **1907**, *52*, 256.

51. Cady, G. H.; Hargreaves, G. B. *J Chem. Soc.* **1961**, 1563.

52. Meinert, H.; Friedrich, L.; Kohl, W. *Z. Chem.* **1975**, *15*, 492.

53. Paine, R. T.; McDowell, R. S. *Inorg. Chem.* **1974**, *13*, 2367.

54. Burns, R. C.; O'Donnell, Waugh, A. B. *J. Fluorine Chem.* **1978**, *12*, 505.

55. Wilson, W. W.; Christe, K. O. *Inorg. Synth.* **1980**, *24*, 37.

56. Edwards, A. J.; Jones, G. R *J. Chem. Soc. (A)* **1968**, 2074.

57. Alexander, L. E.; Beattie, I. R.; Bukovszky, A.; Jones, P. J.; Marsden, C. J.; Schalkwyk, G. J. V. *J. Chem. Soc., Dalton Trans.* **1974**, 81.

58. Asprey, L. B.; Ryas, R. R.; Fukushima, E. *Inorg. Chem.* **1972**, *11*, 3122.

59. Arnaudt, L.; Bougon, R.; Ban, B.; Charpin, P.; Isabey, J.; Lance, M.; Nierlich, M.; Vigner, J. *Inorg. Chem.* **1989**, *28*, 257.

60. Bougon, R., Bui Huy T.; Charpin, P. *Inorg. Chem.* **1975**, *14*, 1822.

61. Abramenko, V. L.; Sergienko, V. S. *Russ. J. Inorg. Chem.* **2009**, *54*, *13*, 2031.

62. Lassner, Erik, Schubert, W. Tungsten and living organisms. *Tunsten: Properties, Chemistry, Technology of the element, Alloys and Chemical Compunds*; Springer: New York 1999, 409-411.

63. Quinones, G.S.; Hagele, G.; Seppelt, K *Chem. Eur. J.* **2004**, *10*, 4755.

64. Noble, A. M.; Winfield, J. M. *J. Chem. Soc. (A)* **1970**, 2574.

65. McFarlane, W.; Noble, A. M.; Winfield, J. M. *J. Chem. Soc. (A)* **1971**, 948.

66. Abramenko, V. L.; Sergienko, V. S. *Russ. J. Inorg. Chem.* **2009**, *54*, 2031.

67. Glavincevski, B.; Brownstein, S. *J. Inorg. Nucl. Chem.* **1981**, *43*, 1827.

68. Handy, L. B.; Brinckman, F. E. *Chem. Comm.* **1970**, *16*, 214.

69. Noble, A. M.; Winfield, J. M. *J. Chem. Soc. (A)* **1970**, 2574.

70. W. Dmowski in Houben-Weyl, Organo-Fluorine Compounds, Vol. E10a (Eds.: B. Baas-ner, H. Hagemann, J. C. Tatlow), Thieme, Stuttgart, **2000**, chapter 8.

71. Mason, J. *Solid State Magn. Res.* **1993**, *2*, 285.

72. Gerken, M.; Hazendonk, P.; Nieboer, J.; Schrobilgen, G. J. *J. Fluorine Chem.* **2004**, *125*, 1163.

Chapter-2

2. Experimental section

2.1 Standard techniques

The compounds used in the course of this work, except perfluorocarboxylic acids and carboxylates, are moisture- and air-sensitive; consequently all manipulations were carried out under rigorously anhydrous inert-atmosphere conditions. Glass and metal vacuum line systems, a dry-nitrogen-filled glove bag, and the oxygen- and moisture-free atmosphere of a Vacuum Atmospheres (Omni Lab) drybox were used.

Volatile materials that were non-corrosive towards glass in the absence of water were manipulated on a Pyrex-glass vacuum line equipped with grease-free 6-mm J. Young glass stopcocks equipped with PTFE barrels (Figure 2.1). Pressures inside the manifold were monitored using a Heise gauge (model CC, 0–1000 mmHg, beryllium/copper Bourdon tube, Dresser Instruments). The final vacuum was monitored by a Varian thermocouple gauge connected to the vacuum line between the liquid-nitrogen trap and the vacuum pump.

Volatile materials, which attacked glass, were handled on a metal vacuum line constructed from nickel and 316 stainless steel, and equipped with 316 stainless steel valves and fittings (Autoclave Engineers Inc.), PTFE, and FEP (Figure 2.2). Pressures were measured at ambient temperature using Baratron capacitance manometers (MKS, Type 626A, effective range 0 – 1000 mmHg) having inert wetted surfaces constructed of inconel, in conjunction with a digital readout.

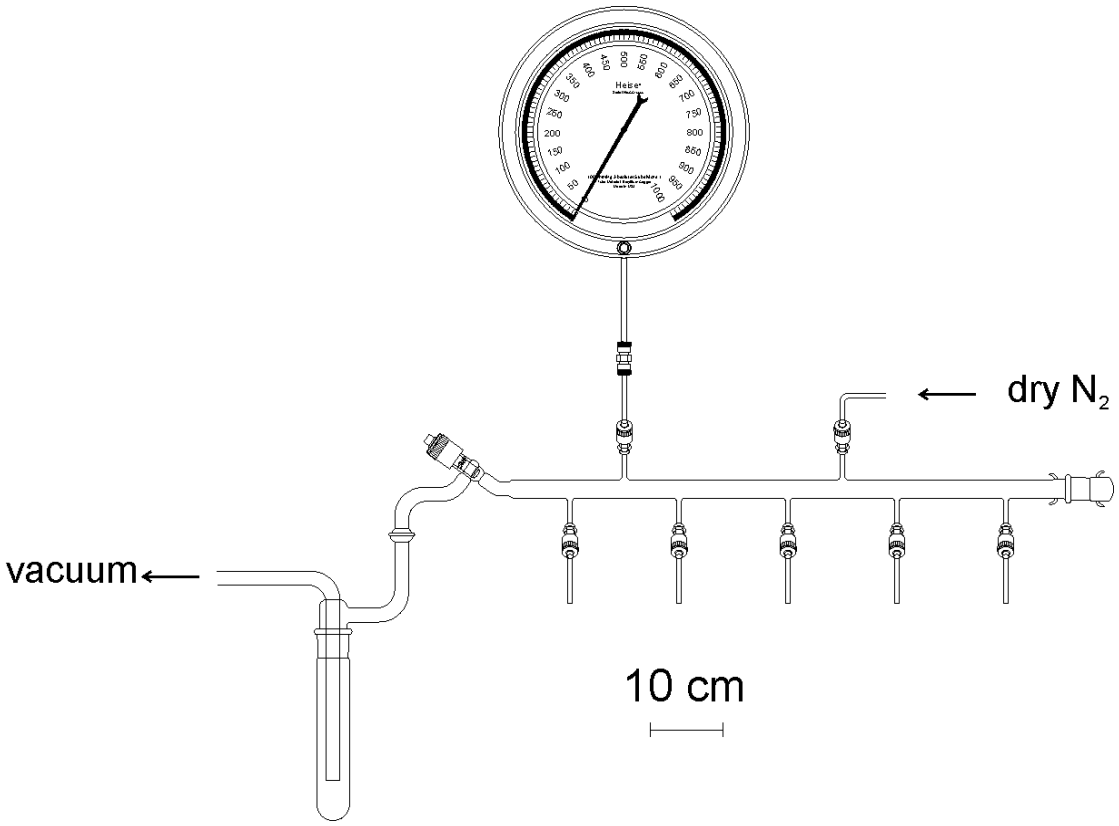

Figure 2.1 Glass vacuum line system equipped with J.Young PTFE / glass stop cocks and a Heise gauge (M.Sc. thesis from Jared Nieboer).[1]

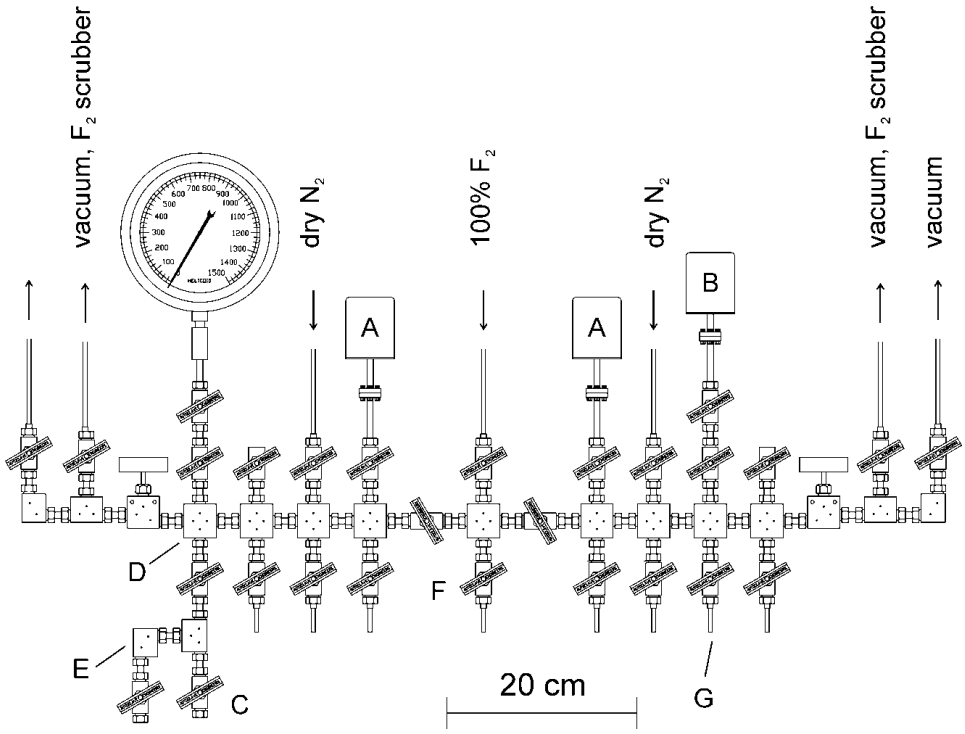

Figure 2.2 Metal vacuum system; (A) MKS type 626A capacitance manometer (0-1000 Torr), (B) MKS Model PDR-5B pressure transducers (0-10 Torr), (C) 3/8-in. stainless-steel high-pressure valves (Autoclave Engineers, 30VM6071), (D) 316 stainless-steel cross (Autoclave Engineers, CX6666), (E) 316 stainless-steel L-piece (Autoclave Engineers, CL6600), (F) 316 stainless steel T-piece (Autoclave engineers, CT6660), (G) $^{3}/_{8}$-in o.d., $^{1}/_{8}$-in. i.d. nickel connectors, (H) $^{1}/_{8}$-in o.d., $^{1}/_{8}$-in. i.d. nickel tube (M.Sc. thesis from Jared Nieboer).[1]

Vacuum on the glass (ca. 10^{-5} Torr) and metal lines (ca. 10^{-4} Torr) was attained by the use of Edwards two-stage direct-drive RV8 Edward vacuum pumps. Three vacuum pumps were used on a metal vacuum line, one for the rough vacuum and two for the fine vacuum on the two sides of the vacuum line. The rough pump was connected to a fluoride/fluorine trap consisting of a stainless-steel cylinder (75 cm length, 17 cm outer diameter) packed with soda lime absorbent (EMD, 4-mesh). Removal and disposal of volatile reactive fluorinated compounds was accomplished by pumping through and entrapment on a bed of soda lime followed by trapping of the volatile reaction products,

CO_2 and H_2O, in a glass liquid-nitrogen trap. The second vacuum pump provided the high vacuum source for the manifold and was cold trapped with a glass liquid-nitrogen trap.

All the preparative work involving SF_4, AsF_5, SbF_5, WOF_4 and anhydrous HF was carried out in ¼-in, ¾-in or 4-mm outer diameter FEP tubes which were heat-sealed at one end and connected through 45° flares to Kel-F or 37° flares to stainless steel valves. The FEP sample tubes were dried under dynamic vacuum overnight on a glass vacuum line prior to transfer on the metal line where they were checked for leaks, passivated with fluorine at 1 atm for 12 hours, re-evacuated and then back filled with dry N_2 before transferring to the dry box. Pyrex-glass reaction vessels were dried under dynamic vacuum overnight periodically flamed out by use of a Bunsen burner.

Nuclear magnetic resonance (NMR) spectra were recorded on samples prepared in 4-mm o.d. FEP tubes. The NMR tubing had one end heat sealed by pushing the end of the FEP tube into the hot end of a thin-walled 5-mm o.d. NMR tube and the other end was fused to a ¼-in. o.d. thick-walled FEP tubing which was heat-flared for direct attachment to a Kel-F valve (Figure 2.3(a)). The 4-mm sample tubes used for NMR spectroscopy were heat sealed under dynamic vacuum with a heat gun while the sample was frozen at –196 °C. All heat-sealed samples were stored submerged in liquid nitrogen (–196 °C) until they could be spectroscopically characterized. For NMR measurements, the 4-mm FEP tubes were inserted into standard 5-mm precision NMR tubes before insertion into the NMR probe.

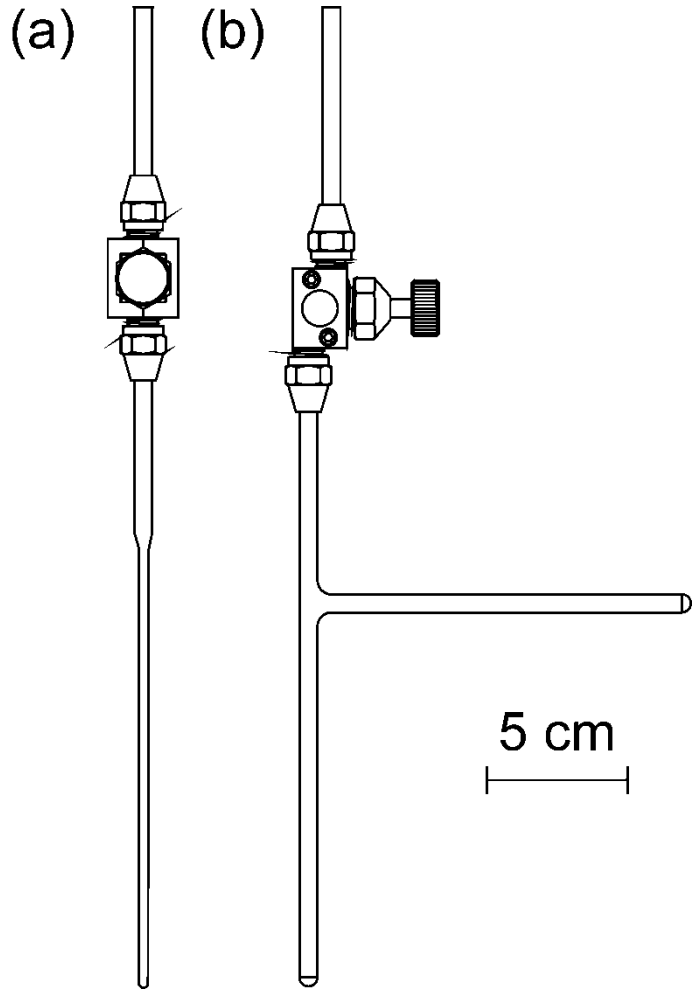

Figure 2.3 Common FEP reactors used to conduct experiments: (a) 4-mm o.d. reaction vessel equipped with a Kel-F valve. (b) ¼-in. o.d. FEP T-reactor equipped with Kel-F valve (M.Sc. thesis from Jared Nieboer).[1]

Raman spectra of solids that are stable at room temperature and which do not attack glass were recorded on samples in Pyrex-glass melting point capillaries. Before use, the melting point capillaries were heated under dynamic vacuum for 24 h at 200 °C and then stored in the drybox where they were loaded with the appropriate materials. The end of the loaded melting point capillary was temporarily sealed with Kel-F grease before removal from the drybox. The capillaries were then immediately heat-sealed with an oxygen-natural gas torch.

Vessels were attached to vacuum lines through thick-walled FEP tubing and ¼-in. PTFE Swagelok connectors or ¼-in. stainless-steel Ultra-Torr connectors fitted with viton rubber O-rings.

2.2 Preparation of inserts for solid-state NMR spectroscopy

Solid-state NMR spectra of imidazolium ionic liquids were recorded with the use of an FEP insert, which was prepared by using a 3.2-mm o.d. FEP tube through heat-sealing it at one end and then loading the required material in it inside the glove box. The filled inserts were plugged using an FEP plug and the plug was fused to the insert-walls outside of the dry box, permanently sealing the insert. This FEP insert was inserted in the 4-mm zirconia rotor before recording spectra at low temperature.

2.3 Purification of different materials

2.3.1 Purification of HF, SF_4, C_5H_5N, CH_3CN, AsF_5, SbF_5, WF_6 and 2,2,2-CF_3CH_2OH, 1,10-phenanthroline, 4-dimethylaminopyridine, 4-*tert*-butylcyclohexanone, 1,4-dioxaspiro[4.5]decan-8-one, cyclooctanol and pentafluorobenzoic acid

Anhydrous hydrogen fluoride (Air Products) was stored at room temperature in a nickel storage vessel equipped with a monel (Autoclave Engineers) valve. Hydrogen fluoride was dried over potassium hexafluoronickelate(VI) in a ¾-in o.d. FEP vessel (Figure 2.4), equipped with a stainless steel valve, prior to transfer to reaction vessels by vacuum distillation on the metal vacuum line through connections constructed of FEP.

Sulfur tetrafluoride (Ozark-Mahoning Co.) was purified by passing the gas through a column of activated charcoal. Traces of thionyl fluoride and sulfur hexafluoride were present in the sulfur tetrafluoride.

Pyridine (Sigma-Aldrich, 99.8%) was added to CaH_2 in a glass storage bulb equipped with a PTFE J. Young stopcock inside a glove bag. Then, the liquid was vacuum distilled from the original storage bulb onto fresh CaH_2 in a glass bulb equipped with a PTFE J. Young stopcock.

Antimony pentafluoride, SbF_5 (Ozark-Mahoning Co.) was purified by vacuum distillation in a PTFE and glass apparatus connected with PTFE Swagelok unions and stored in a glass U-tube equipped with PTFE J. Young stopcocks, which was kept in a desiccator. Subsequent transfers of SbF_5 were performed through a glass Y-piece with PTFE Swagelok connections.

Acetonitrile (Sigma-Aldrich) was purified according to the literature procedure.[2] CH_3CN was added to molecular sieves (4Å) in glass bulbs inside the glove bag, followed by vacuum distillation onto fresh molecular sieves in glass storage bulbs equipped with a PTFE J. Young stopcock.

WF_6 (Elf Atochem) was used as provided. 2,2,2-Trifluoroethanol (CF_3CH_2OH) was purchased from Sigma-Aldrich (≥99%) and dried over molecular sieves (4Å).

1,10-phenanthroline (Sigma-Aldrich) and 4-dimethylaminopyridine (Sigma-Aldrich) were used as received without any further purification.

Also, 4-*tert*-butylcyclohexanone (TCI Chemicals), 1,4-dioxaspiro[4.5]decan-8-one (TCI Chemicals), cyclooctanol (TCI Chemicals) and pentafluorobenzoic acid (Sigma-Aldrich) were used without any further purification.

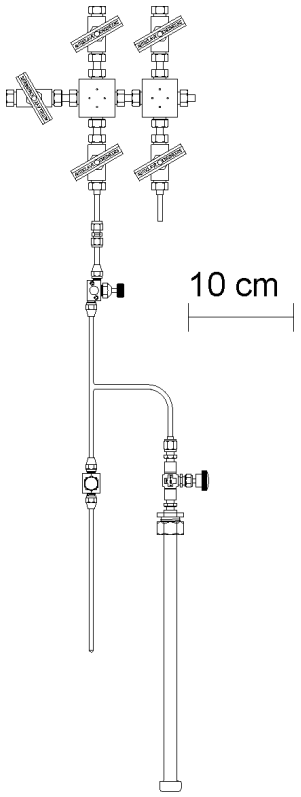

Figure 2.4 A ¾-in. o.d. FEP vessel equipped with a stainless steel valve and a FEP T-piece connection for distillation of HF to reactors (M.Sc. thesis from Jared Nieboer).[1]

2.3.2 Purification of perfluorooctanoic acid (PFOA), sodium perfluorooctanoate (SPFO), perfluorodecanoic acid (PFDA) and sodium perfluorobutyrate (SPFB)

Perfluorooctanoic acid, 96% and perfluorodecanoic acid, 98% were purchased from Sigma Aldrich SPFO, 98% and SPFB was purchased from SynQuest Laboratories Ltd. (USA). All of these chemicals were used without any further purification.

2.4 Synthesis of different fluorine containing compounds

2.4.1 Synthesis of AsF_5. Arsenic pentafluoride (AsF_5) was synthesized according to the given literature by reacting AsF_3 with F_2.[3]

2.4.2 Synthesis of WOF_4. The synthesis of WOF_4 was done according to the procedure described in the literature.[4] Quartz wool (0.2256 g; 3.735 mmol) was transferred to a ¾" FEP reactor having a Teflon coated magnetic stirring bar. WF_6 (15.958 mmol) and about 250 mL of anhydrous HF was distilled over quartz wool. The reactants were warmed up to room temperature and mixed with magnetic stirrer for 48 hrs. until all the quartz wool was dissolved. The excess anhydrous HF was pumped off from –90 °C to –10 °C. The resulted solid was sublimed between 55–60 °C under dynamic vacuum to collect the pure sublimed WOF_4 (0.9747 g).

2.4.3 Synthesis of $[SF_3][SbF_6]$ and $[SF_3][AsF_6]$ and scoping reactions for the use of $[SF_3][MF_6]$ (M = Sb, As) as deoxofluorinating reagents for 4-*tert-butyl*cyclohexanone, 1,4-dioxaspiro[4.5]decan-8-one, benzoic acid, pentafluorobenzoic acid, and cyclooctanol.

The $[SF_3][SbF_6]$ and $[SF_3][AsF_6]$ salts were prepared according to literature reports.[5,6,7]

2.4.3.1 Synthesis of $[SF_3][SbF_6]$. On a glass vacuum line, 0.362 g (1.67 mmol) of SbF_5 was transferred to a ¼-in o.d. vacuum-dried FEP reactor. Approximately 3.70 mmol SF_4 was vacuum distilled into the reactor at –196 °C. The reactor was slowly warmed up to –78 °C, and then to ambient temperature (20 °C) and properly agitated. The reactor was then agitated in warm water (32 °C) for the completion of reaction. The reactor was again transferred to an ethanol bath maintained at –78 °C. The excess SF_4 was removed on the vacuum line by slowly warming the reactor up to ambient temperature where a white $[SF_3][SbF_6]$ (0.447 g or 1.37 mmol) salt was obtained.

2.4.3.1.1 Crystal growth of $[SF_3][SbF_6]$. An amount of 0.012 g (0.037 mmol) of $[SF_3][SbF_6]$ was transferred to a ¼" FEP reactor. About ~2.0 mL of SO_2 was transferred to the reactor at –40 °C. After dissolving $[SF_3][SbF_6]$ in SO_2, the reactor was transferred to

cryobath at –70 °C. After the crystal growth the SO_2 was pumped off at about –50 °C. The crystals were mounted immediately after pumping off excess SO_2.

2.4.3.2 Synthesis of $[SF_3][AsF_6]$. On a steel vacuum line, approximately 2.11 mmol of SF_4 was vacuum distilled into a 4-mm o.d. FEP reactor. Approximately 1.90 mmol AsF_5 was vacuum distilled into the reactor. The reactor was slowly warmed to –78 °C and then to –40 °C by proper agitation for the completion of reaction. $[SF_3][AsF_6]$ was resulted as product in the form of a white salt. The excess SF_4 was removed by warming the reactor to ambient temperature (20 °C). The weight of white $[SF_3][AsF_6]$ salt was 0.445 g (1.60 mmol).

2.4.3.2.1 Crystal growth of $[SF_3][AsF_6]$. An amount of 0.021 g (0.76 mmol) of $[SF_3][AsF_6]$ was transferred to a ¼" FEP reactor. Then about ~ 2.5 mL of SO_2 was transferred to the reactor at –40 °C. After dissolving $[SF_3][AsF_6]$ in SO_2, the reactor was transferred to cryobath at –70 °C. After the crystal growth the SO_2 was pumped off at about –50 °C. The crystals were mounted immediately after pumping off excess SO_2.

2.4.3.3 Deoxofluorination of 4-*tert*-butylcyclohexanone at –20 °C. Inside the dry-box, 0.15 mmol (0.049 g) of $[SF_3][SbF_6]$ and 0.097 mmol (0.015 g) of 4-*tert*-butylcyclohexanone were taken into a 4-mm FEP reactor and approximately 0.006 g (0.04 mmol) of CsF was added to it. The reactor was hooked to the SO_2 line and excess SO_2 (~ 1.5 mL) was distilled to the reactor on a glass vacuum line. The reaction was allowed to take place at ambient temperature. The resultant product was monitored with the help of solution ^{19}F and ^{1}H NMR spectroscopy at –20 °C (for safe handling of SO_2).

2.4.3.4 Deoxofluorination of 1,4-dioxaspiro[4.5]decan-8-one. Inside the dry-box, 0.10 mmol (0.032 g) of $[SF_3][SbF_6]$ and 0.10 mmol (0.016 g) of 1,4-dioxaspiro[4.5]decan-8-one were taken into a 4-mm FEP reactor and 0.006 g (0.04 mmol) of CsF was added to it.

The reactor was attached to the CH_3CN line and excess CH_3CN (~ 2.0 mL) was distilled to the reactor on a glass vacuum line. The reaction was allowed to take place at –20 °C. The resultant product was monitored with the help of ^{19}F NMR spectroscopy at –20 °C.

2.4.3.5 Deoxofluorination of pentafluorobenzoic acid. Inside the dry-box, 0.063 mmol (0.020 g) of $[SF_3][SbF_6]$ and 0.059 mmol (0.012 g) of pentafluorobenzoic acid were taken into a 4-mm FEP reactor and 0.006 g (0.04 mmol) of CsF was added to it. The reactor was hooked to the SO_2 line and excess SO_2 (~ 1.9 mL) was distilled to the reactor on a glass vacuum line. The reaction was allowed to take place at ambient temperature. The resultant product was monitored with the help of ^{19}F NMR spectroscopy at –20 °C.

2.4.3.6 Deoxofluorination of benzoic acid. Inside the dry-box, 0.06 mmol (0.019 g) of $[SF_3][SbF_6]$ and 0.06 mmol (0.006 g) of benzoic acid were taken into a 4-mm FEP reactor and 0.006 g (0.04 mmol) of CsF was added to it. The reactor was hooked to the SO_2 line and excess SO_2 (~ 1.6 mL) was distilled to the reactor on a glass vacuum line. The reaction was allowed to take place at ambient temperature. The resultant product was monitored with the help of ^{19}F NMR spectroscopy at –20 °C.

2.4.3.7 Deoxofluorination of cyclooctanol. Inside the dry-box, 0.75 mmol (0.021 g) of $[SF_3][AsF_6]$ and 0.07 mmol (0.008 g) of cyclooctanol were taken into a 4-mm FEP reactor and 0.006 g (0.04 mmol) of CsF was added to it. The reactor was hooked to the SO_2 line and excess SO_2 (~ 1.9 mL) was distilled to the reactor on a glass vacuum line. The reaction was allowed to take place at ambient temperature. The resultant product was monitored with the help of ^{19}F NMR spectroscopy at –20 °C.

2.4.4 Synthesis of $[SF_3(N\text{-base})_2][MF_6]$·solvate (where M = Sb, As and N-base = C_5H_5N, CH_3CN), $[SF_3(Phen)][SbF_6]\cdot 2CH_2Cl_2$ and $[SF_2(DMAP)_2][SbF_6]_2\cdot CH_3CN$

2.4.4.1 Synthesis of $[SF_3(C_5H_5N)_2][SbF_6]\cdot nC_5H_5N$. The low-temperature stable yellow $[SF_3(C_5H_5N)_2][SbF_6]\cdot nC_5H_5N$ (where n = 0.15) salt was prepared by the reaction of 0.25 mmol (0.080 g) of $[SF_3][SbF_6]$ and 1.00 mL (16.7 mmol) neat C_5H_5N at –40 °C. Excess pyridine was removed up to –30 °C to get 0.149 g of the salt.

2.4.4.1.1 Crystal growth for $[SF_3(C_5H_5N)_2][SbF_6]\cdot C_5H_5N$. 0.149 g of $[SF_3(C_5H_5N)_2][SbF_6]$ was dissolved in 2.5 mL of CH_2Cl_2 and 0.5 mL of C_5H_5N inside a ¼ in. o.d. FEP tube equipped with a Kel-F valve and the solution was cooled to –70 °C for 12 h. The crystals were formed after 1 h. The solvent was slowly removed under dynamic vacuum at this temperature over a period of 12 h and yellow crystals of $[SF_3(C_5H_5N)_2][SbF_6]\cdot C_5H_5N$ in the form of needles were obtained.

2.4.4.1.2 Crystal growth for $[SF_3(C_5H_5N)_2][SbF_6]\cdot CH_3CN$. The product was synthesized by using 0.020 g of $[SF_3][SbF_6]$ using about 1.00 mL pyridine as solvent. After pumping off excess pyridine, the product was dissolved in 1.5 mL of CH_2Cl_2 and 0.5 mL of CH_3CN inside a ¼ in. o.d. FEP tube equipped with a Kel-F valve and the solution was cooled to –70 °C for 12 h. The crystals appeared after 1 h. The solvent was slowly removed under dynamic vacuum at this temperature over a period of 12 h and yellow crystals in the form of needle of $[SF_3(C_5H_5N)_2][SbF_6]\cdot CH_3CN$ were obtained.

2.4.4.1.3 Crystal growth for $[SF_3(C_5H_5N)_2][SbF_6]\cdot CH_2Cl_2$. The product was synthesized using about 0.030 g of $[SF_3][SbF_6]$ using 1.00 mL pyridine as solvent. After pumping off excess pyridine, the product was dissolved in 3.0 mL of CH_2Cl_2 inside a ¼ in. outer diameter (o.d.) FEP tube equipped with a Kel-F valve was cooled to –70 °C for 12 h. The crystal formation takes place after 2 h. All the solvent was slowly removed under dynamic

vacuum up to –30 °C over a period of approximately 9 h and yellow needle crystals were isolated.

2.4.4.2 Synthesis of $[SF_3(C_5H_5N)_2][AsF_6]\cdot nC_5H_5N$. The low temperature stable $[SF_3(C_5H_5N)_2][AsF_6]\cdot nC_5H_5N$ salt was prepared by the reaction of 0.11 mmol (0.030 g) of $[SF_3][AsF_6]$ and 0.45 mL (5.7 mmol) neat C_5H_5N at –40 °C. Excess pyridine was removed up to –30 °C to synthesize $[SF_3(C_5H_5N)_2][AsF_6]\cdot nC_5H_5N$.

2.4.4.2.1 Crystal growth for $[SF_3(C_5H_5N)_2][AsF_6]\cdot C_5H_5N$. The product was synthesized from about 0.020 g of $[SF_3][AsF_6]$ in ca. 1.0 mL pyridine as solvent. After pumping off excess pyridine, the product was dissolved in 2.0 mL of CH_2Cl_2 and 0.5 mL of CH_3CN inside a ¼ in. o.d. FEP tube equipped with a Kel-F valve and the solution was cooled to –70 °C for 12 h. The crystals appeared after 45 minutes. The solvent was slowly removed under dynamic vacuum at this temperature over a period of 12 h and yellow crystals of $[SF_3(C_5H_5N)_2][AsF_6]\cdot C_5H_5N$ were obtained.

2.4.4.2.2 Crystal growth for $[SF_3(C_5H_5N)_2][AsF_6]\cdot CH_2Cl_2$. The $[SF_3(C_5H_5N)_2][AsF_6]\cdot CH_2Cl_2$ crystals were grown by the following procedure. First the reaction of $SF_4\cdot C_5H_5N$ (1:1 adduct) was carried out with excess AsF_5 at –56 °C. After pumping off excess AsF_5, the product was dissolved in 4.0 mL of CH_2Cl_2 inside a ¼ in. o.d. FEP tube equipped with a Kel-F valve and was placed in the cryo-bath at –72 °C for crystal growth. After 14 h excess CH_2Cl_2 was pumped off from the reaction mixture to obtain the crystals of $[SF_3(C_5H_5N)_2][AsF_6]\cdot CH_2Cl_2$.

2.4.4.3 Synthesis of $[SF_3(CH_3CN)_2][SbF_6]$. The low temperature stable yellow $[SF_3(CH_3CN)_2][SbF_6]$ salt was prepared by the reaction of 0.19 mmol (0.062 g) of $[SF_3][SbF_6]$ and 0.60 mL (1.2 mmol) neat CH_3CN at –40 °C. Excess acetonitrile was pumped off to –30 °C to get 0.078 g of $[SF_3(CH_3CN)_2][SbF_6]$.

2.4.4.3.1 Crystals growth for $[SF_3(CH_3CN)_2][SbF_6]$. A solid sample of 0.078 g of $[SF_3(CH_3CN)_2][SbF_6]$ in 3.0 mL of CH_2Cl_2 inside a ¼ in. o.d. FEP tube equipped with a Kel-F valve was cooled to –70 °C for 12 h. Crystals appeared after 2 h. The solvent was slowly removed under dynamic vacuum up to –30 °C over a period of approximately 9 h and yellow needle crystals were isolated.

2.4.4.4 Synthesis of $[SF_3(CH_3CN)_2][AsF_6]$. The low-temperature stable $[SF_3(CH_3CN)_2][AsF_6]$ salt was prepared by the reaction of 0.13 mmol (0.036 g) of $[SF_3][AsF_6]$ with 0.45 mL (8.61 mmol) neat CH_3CN at –40 °C. Excess acetonitrile was pumped off to –30 °C.

2.4.4.5 Synthesis of $[SF_3(Phen)][SbF_6]\cdot 2CH_2Cl_2$. The low-temperature stable $[SF_3(Phen)]SbF_6$ salt was prepared by the reaction 0.089 mmol (0.029 g) of $[SF_3][SbF_6]$ and 0.083 mmol (0.015 g) of phenanthroline in the presence of 2.0 mL CH_3CN at –40 °C. Excess acetonitrile was pumped off up to –20 °C.

where, Phen = 1,10 Phenantholine

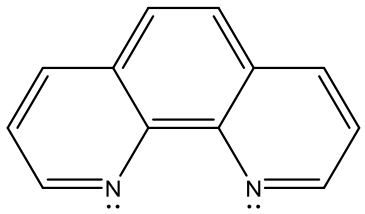

2.4.4.5.1 Crystal growth for $[SF_3(Phen)][SbF_6]\cdot 2CH_2Cl_2$. The synthesized material in section 2.4.4.5 was dissolved in 3.5 mL of CH_2Cl_2. The crystals appeared after 2 h. The solvent was slowly removed under dynamic vacuum up to –25 °C over a period of approximately 9 h and yellow needle crystals were isolated.

2.4.4.6 Synthesis of $[SF_2(DMAP)_2][SbF_6]_2\cdot CH_3CN$. The low temperature stable $[SF_2(DMAP)_2][SbF_6]_2$ salt was prepared by the reaction of 3.69×10^{-5} mol (0.012 g) of $[SF_3][SbF_6]$ with 0.046 g (0.038 mmol) of DMAP in 3.0 mL CH_3CN at –40 °C.

where, DMAP = 4-N,N'dimethylaminopyridine

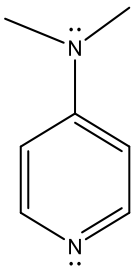

2.4.4.6.1 Crystal growth of $[SF_2(DMAP)_2][SbF_6]_2 \cdot CH_3CN$. The $[SF_2(DMAP)_2][SbF_6]_2 \cdot CH_3CN$ crystals were obtained by pumping off excess CH_3CN from the product as obtained in section 2.4.4.6 in the reactor to –35 °C. The resultant material was redissolved in 4.0 mL CH_2Cl_2 at –30 °C and kept in the cryo-bath at –72 °C for 14 h. The crystal growth took place after 1.5 h. The excess solvent was slowly pumped off under dynamic vacuum up to –35 °C over a period of approximately 8 h and yellow needle crystals were isolated.

2.4.4.6.2 Crystal growth of $[SF(DMAP)_4][SbF_6]_3 \cdot 2CH_3CN$. The low temperature stable $[SF(DMAP)_4][SbF_6]_3$ crystal was obtained by the reaction of 0.080 mmol (0.026 g) of $[SF_3][SbF_6]$ with 0.010 g (0.082 mmol) of DMAP in 3.9 mL CH_3CN at –40 °C inside a ¼ in. o.d. FEP tube equipped with a Kel-F valve. Excess acetonitrile was slowly pumped off to –28 °C. Dark yellow material having needle crystals was isolated.

2.4.5 Synthesis of $WOF_4 \cdot SO_2$, $[(CH_3)_4N][WOF_5]$ and $(CH_3CN)WOF_3(OCH_2CF_3)$

2.4.5.1 Synthesis of $WOF_4 \cdot SO_2$. To a ¼" FEP reactor, 0.783 mmol (0.216 g) of WOF_4 were transferred and excess SO_2 was transferred on top of it so that the solid, completely dissolves the WOF_4 at room temperature. The mixture was kept below –30 °C and all of excess SO_2 was pumped off up to –30 °C. The resultant $WOF_4 \cdot SO_2$ off-white solid was always kept below –30 °C to avoid the dissociation of $WOF_4 \cdot SO_2$ to WOF_4 and SO_2.

2.4.5.1.1 Crystal growth for $WOF_4 \cdot SO_2$. Approximately 0.054 mmol (0.015 g) of WOF_4 were transferred into a ¼" FEP reactor and 2.0 mL of SO_2 were transferred on top of it so that all of WOF_4 gets dissolved. The mixture was kept below –70 °C for 12 h and excess SO_2 was pumped off up to –30 °C. The resultant crystals were stored at –70 °C to avoid the dissociation of $WOF_4 \cdot SO_2$.

2.4.5.2 Synthesis of $[(CH_3)_4N][WOF_5]$. To the ¼" FEP reactor, 1.11 mmol (0.316 g) of WOF_4 were transferred and subsequently 1.15 mmol (0.107 g) of $[(CH_3)_4N][F]$ was added to the same reactor inside the dry box. Excess CH_3CN was transferred to the reactor and the temperature was kept cold (approximately –30 °C). The reaction mixture was mixed properly and excess CH_3CN was pumped off by warming up the reactor to –10 °C. The resultant $[(CH_3)_4N][WOF_5]$ (0.407 g) was obtained in the form of a white solid in a 99.0% yield.

2.4.5.2.1 Crystal growth for $[(CH_3)_4N][WOF_5]$. Approximately 0.041 mmol (0.015 g) of $[(CH_3)_4N][F]$ were transferred to the ¼" FEP reactor and excess anhydrous HF was transferred to the same reactor. The reactor was transferred to the cryo-bath to keep it cold (approx. –70 °C). After 12 h crystals grew and excess HF was pumped off at –30 °C. The resultant crystals were stored in the cryo-bath at –70 °C.

2.4.5.3 Synthesis of $(CH_3CN)W(O)F_3(OCH_2CF_3)$. A definite amount of WOF_4 (0.050 g or 0.18 mmol) was transferred in a ¼" FEP reactor and excess anhydrous CH_3CH_2OH (0.180 g or 1.79 mmol) was distilled over this WOF_4. The reaction mixture was warmed up to 20 °C. After pumping off excess CH_3CH_2OH up to ambient temperature for 12 h, a highly viscous liquid, $W(O)F_3(OCH_2CF_3)$ (0.097 g) results. Excess CH_3CN (~ 2.0 mL) was distilled over $WOF_3(OCH_2CF_3)$ and a solid product, $(CH_3CN)W(O)F_3(OCH_2CF_3)$ was obtained after puming off excess CH_3CN.

2.4.5.3.1 Crystal growth for (CH_3CN)$WOF_3(OCH_2CF_3)$. 0.015 g (or 0.054 mmol) of WOF_4 was transferred in a ¼" FEP reactor and then excess anhydrous CF_3CH_2OH (~ 1.0 mL, 14 mmol) was distilled on top of WOF_4. The reaction mixture was warmed up to 30 °C. After pumping off excess solvent up to ambient temperature for 12 h, excess CH_3CN (~ 1.0 mL) was distilled over $WOF_3(OCH_2CF_3)$ and excess CH_3CN was pumped off. The resultant solid was dissolved in about 2.0 ml of CH_2Cl_2 at ambient temperature and the reactor was transferred to cryo-bath maintained at –70 °C. Next day (after 12 h) after the crystal growth excess CH_2Cl_2 was pumped off up to –30 °C. The resultant crystals were stored at –70 °C.

2.5 Crystal growth for PFOA·H_2O, SPFO, PFDA·H_2O, and SPFB.

2.5.1 Crystal growth of PFOA·H_2O. 24 mmol (~ 1.0 g) of PFOA was dissolved in ~ 5.0 mL of 2,2,2-trifluoroethanol as solvent. The solvent was allowed to evaporate very slowly for five days. The resultant crystals were stored in the glass vial at ambient temperature.

2.5.2 Crystal growth for sodium perfluorooctanote (SPFO). 28 mmol (~ 1.2 g) of SPFO was dissolved in ~ 4.5 mL of anhydrous ethanol (99.5%). The ethanol was allowed to evaporate very slowly for three days. The resulted crystals were stored in the glass vial at ambient temperature.

2.5.3 Crystal growth for perfluorodecanoic acid as PFDA·H_2O. 2.9 mmol (~ 1.5 g) of PFDA was dissolved in ~ 6.0 mL of n-butanol as solvent. The solvent was allowed to evaporate very slowly for five days. The resulted crystals were stored in the glass vial at ambient temperature.

2.5.4 Crystal growth for sodium perfluorobutyrate (SPFB). 5.5 mmol (~ 1.5 g) of SPFB was dissolved in ~ 5.0 mL of ethanol as solvent. The ethanol was allowed to evaporate very

slowly for four days. The resulted crystals were stored in the glass vial at ambient temperature.

2.6 Low-temperature crystal mounting

A low-temperature crystal mounting technique was utilized for the thermally unstable and moisture-sensitive crystals. The FEP reactor containing crystals was cut open below the Kel-F valve under a flow of dry nitrogen while the lower part of the FEP reactor, which contained the crystals, was immersed in dry ice at –78 °C. The crystals were then quickly transferred from the chilled tube into an aluminum trough that was cooled by a flow of dry-nitrogen, which was passed through a 5-L Dewar of liquid nitrogen (Figure 2.5). The temperature of the trough had been adjusted to approximately –85 °C (except in case of α-$[SF_3][SbF_6]$ crystals) and had been measured with a copper-constantan thermocouple inserted midway into the stream ca. 2-mm above the trough. A crystal was selected under a microscope and mounted on a glass fibre using an inert perfluorinated polyether, Fomblin Z-25 (Ausimont Inc.) while being kept in the cold nitrogen stream. The polyether selected for crystal mounting was sufficiently viscous to adhere to the crystal, engulf it, and freeze quickly thereafter. The glass fibre had previously been attached using an epoxy to a metallic pin that was, in turn, mounted on a magnetic base, which was attached to a magnetic wand, while picking the crystal. The pin with the crystal was quickly (<30 s) transferred from the wand to the goniometer head of the X-ray instrument using cryotongs, which had been chilled with liquid nitrogen prior to use, and attached to the magnetic base on the goniometer head.

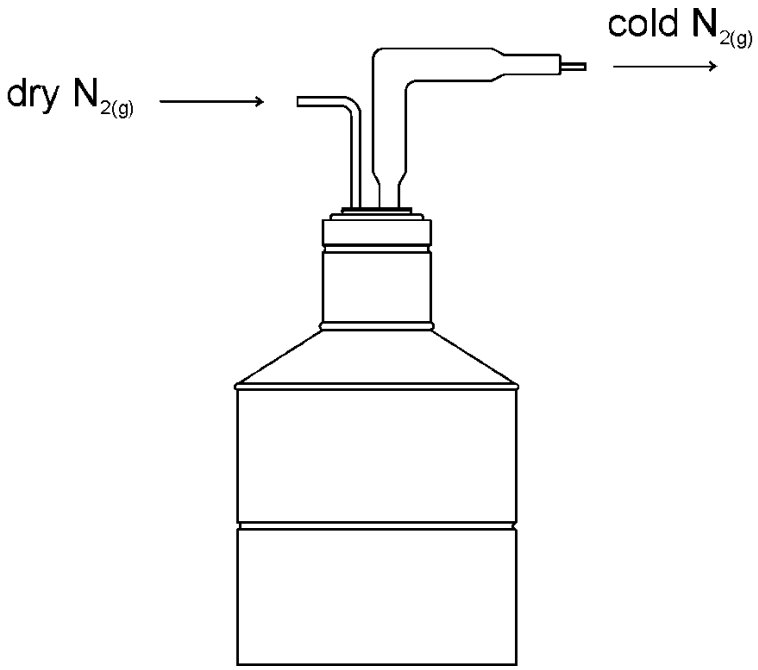

Figure 2.5 Crystal mounting apparatus consisting of a five-liter liquid nitrogen Dewar equipped with a rubber stopper, a glass dry nitrogen inlet and a silvered-glass cold nitrogen outlet with aluminum cold trough (M.Sc. thesis from Jared Nieboer).[1]

2.6.1 Collection of X-ray data

X-ray data was collected at –120 °C on a Bruker SMART APEX-II X-ray diffractometer, which was equipped with an Apex II 4K charge-coupled device (CCD) area detector, a Kryo-Flex low-temperature device, and a Mo Kα radiation (λ = 0.71073 Å) source with a graphite monochromator. The crystal-to-detector distance was 6.120 cm. A hemisphere of data was collected with 30 s exposure time.

2.6.2 Solution and refinement of structures

Calculations were performed using the *SHELXTL-plus v.6.14* package[8,9] for structure determination, refinement and molecular graphics. The *Xprep* program was used to confirm the unit cell dimensions and the crystal lattice. The crystal structure was solved using direct method. Successive difference Fourier syntheses revealed all lighter atoms. The structures

were minimized by least squares refinement based on the square of the structure factors, F^2 (equivalent to intensity). Atom positions were refined anisotropically and the extinction coefficient was calculated for the crystal structure. Both residual values, R_1 based on F and the weighted residual values wR_2 based on F^2, are available in the structure refinement tables along with the goodness of fit *GooF*. They represent the following equations:

$$R_1 = \frac{\sum \| Fo | - | Fc \|}{\sum | Fo |}$$ The conventional R-factor based upon the structure factor.

$$wR_2 = \sqrt{\frac{\sum [w(Fo^2 - Fc^2)^2]}{\sum [w(Fo^2)^2]}}$$ The weighted R-factor based on the square of the structure factors (observed and calculated, F^2 (based upon intensity).

$$GooF = \sqrt{\frac{\sum [w(Fo^2 - Fc^2)]}{(n-p)}}$$ The *GooF* is based upon intensity where n is the number of reflections, p is the number of parameters refined.

The X-ray crystallography data was collected for the following crystals listed in Table 2.1.

Table 2.1 List of the crystal materials with code number and data collection temperature

Code No.	Material	Temperature (°C)
MG11039	$[SF_3(C_5H_5N)_2][SbF_6]\cdot CH_2Cl_2$	–120
MG11042	$[SF_3(C_5H_5N)_2][SbF_6]\cdot CH_3CN$	–120
MG11047	$[SF_3(CH_3CN)_2][SbF_6]$	–120
MG11065	$[SF_3(C_5H_5N)_2][SbF_6]\cdot C_5H_5N$	–120
MG12041	$(CH_3CN)WOF_3(OCH_2CF_3)$	–120
MG12046	$[(CH_3)_4N][WOF_5]$	–120
MG12058	$[SF_3(C_5H_5N)_2][AsF_6]\cdot C_5H_5N$	–120
MG12082	$[SF_3(C_5H_5N)_2][AsF_6]\cdot CH_2Cl_2$	–120
MG12093	$[SF_2(DMAP)_2][SbF_6]_2\cdot CH_3CN$	–120
MG12109	$PFOA\cdot H_2O$	–120
MG13003	$[SF_3(Phen)][SbF_6]\cdot 2CH_2Cl_2$	–120
MG13021	$[SF(DMAP)_4]_2[SbF_6]_3\cdot 2CH_3CN$	–120
MG13025	SPFO	–120
MG13043	SPFB	–120
MG13061	$PFDA\cdot H_2O$	–120
MG13066	γ-$[SF_3][SbF_6]$	–130
MG14001	$[SF_3][AsF_6]$	–130
MG14016	$WOF_4\cdot SO_2$	–120
MG14022	α-$[SF_3][SbF_6]$	–40
MG14028	$EMIMHF_2$ (1-ethyl 3-methyl imidazolium hydrogenbifluoride)	–120

2.7 Raman spectroscopy:

All Raman spectra were recorded on a Bruker RFS 100 FT Raman spectrometer equipped with a quartz beam splitter, a liquid-nitrogen cooled Ge detector, and low-temperature accessory. The backscattered (180°) radiation was sampled. The useable Stokes range was 50-3500 cm^{-1} with a spectral resolution of 2 cm^{-1}. A Nd:Yag laser with a 1064-nm line was used for excitation of the sample. Spectra were recorded on solution samples in either 4-mm or ¼-in. FEP reactors using Laser powers of 150–200 mW. The spectra were collected between the temperature ranges 20 °C to –110 °C.

2.8 NMR spectroscopy

2.8.1 Solution-state NMR spectroscopy

All the solution-state NMR spectra were recorded on a 300 MHz Bruker Avance II NMR spectrometer. All the samples were contained in 4-mm FEP inliners and the NMR spectra were collected unlocked and were referenced externally. Fluorine-19 NMR spectra were referenced externally relative to neat $CFCl_3$ ($\delta(^{19}F) = 0$ ppm), while ^{1}H and ^{13}C NMR spectra were referenced relative to neat TMS ($\delta(^{13}C) = 0$ ppm; $\delta(^{1}H) = 0$ ppm) at room temperature.

2.8.2 Solid-state NMR spectroscopy

All the solid-state NMR spectra were recorded on a 500 MHz Varian-Inova NMR spectrometer. The imidazolium ionic liquid salt samples were contained in 3.2-mm o.d. FEP inserts and all NMR spectra were collected unlocked at low temperature and were referenced externally. Fluorine-19 NMR spectra were referenced externally relative to neat hexafluorobenzene ($\delta(^{19}F) = -166.4$ ppm), while ^{1}H and ^{13}C NMR spectra were referenced relative to adamantane, ($\delta(^{13}C) = -38.5$ ppm; $\delta(^{1}H) = 1.63$ ppm) at room temperature. A 4.0 µs excitation pulse was applied in acquiring ^{1}H direct polarization spectrum while for the ^{1}H-to-^{19}F, ^{19}F-to-^{1}H and ^{1}H-to-^{13}C cross polarizations, 5.0 µs pulse was used in chapter-7.

References:

1. Neiboer, J. The preparation and characterization of Tungsten and Molybdenum sulfide fluorides, M.Sc. Thesis, University of Lethbridge, 2007.

2. Winfield, J. M. *J. Fluorine Chem.* **1984**, *25*, 91.

3. Emara, A. A. A.; Lehmann, J. F.; Schrobilgen, G. J. *J. Fluorine Chem.* **2005**, *126*, 1373.

4. Wilson, W. W.; Christe, K. O.; Bougon, R. *Inorg. Synth.* **1980**, *24*, 37.

5. (i) Bartlett, N.; Robinson, P.L. Chem. Ind. London. 1956, 1351. (ii) Bartlett, N.; Robinson, P. L. *J. Chem. Soc.* **1961**, 3417.

6. Azeem, M.; Brownstein, M.; Gillespie, R.J. *Can. J. Chem.* **1969**, *47*, 4159.

7. Gillespie, R.J.; Moss, K.C. *J. Chem. Soc.* **1966**, 1170.

8. Bruker; Apex2 and Saint-plus. Bruker AXS Inc.: Madison, Wisconsin, USA, 2006.

9. Sheldrick, G. M.; 6.14 ed.; Bruker AXS Inc.: Madison, Wisconsin, USA, 2003.

Chapter-3

3. Structural characterization of $[SF_3][MF_6]$ (M = Sb, As) and their use in deoxofluorination reactions

3.1 Introduction

Sulfur tetrafluoride, SF_4, is known as a weak Lewis acid and for its fluoride-ion donor properties towards strong Lewis acids.[1,2] It forms a variety of different SF_3^+ salts, i.e., $[SF_3][SbF_6]$,[2,3] $[SF_3][AsF_6]$,[2,3] $[SF_3][IrF_6]$,[4] $[SF_3][BF_4]$,[2,3] $[SF_3][PF_6]$,[3] $[SF_3]_2[GeF_6]$,[5] $[SF_3][OsF_6]$,[4] and $[SF_3][AsF_4]$,[3] with the Lewis acids SbF_5, AsF_5, IrF_5, BF_3, PF_5, GeF_4, OsF_5, AsF_3, respectively. Among these, $[SF_3][AsF_6]$ and $[SF_3][SbF_6]$ are stable at ambient temperature under exclusion of moisture with melting points of 90 °C and 253 °C, respectively. The limitation of appropriate inert solvents for these salts makes it difficult to grow single crystals suitable for X-ray crystallography. Earlier attempts to grow single crystals of $[SF_3][SbF_6]$ through sublimation failed.[5(i)] Crystals of poor quality were obtained for $[SF_3][AsF_6]$ by the sublimation process, yielding only unit cell parameters.[5(i)] Previously, crystal structures for SF_3^+ salts were only reported for $[SF_3][BF_4]$,[2,3,5] and for $[SF_3]_2[GeF_6]$.[4]

Sulfur tetrafluoride has been found to exist in an equilibrium with SF_3^+ in anhydrous HF (equation 3.1) based on conductivity experiments.[1] This equilibrium is thought to be also operative in the presence of traces of HF. Since the presence of at least traces of HF are important in deoxofluorinating reactions using SF_4, SF_3^+ has been considered the reactive intermediate in the deoxofluorination reaction of SF_4, which can convert –COOH to $–CF_3$, >C=O to $>CF_2$ and –OH to –F functional groups.

$$SF_4 + HF \longrightarrow SF_3^+ + HF_2^- \quad \text{..... (3.1)}$$

The structures of $[SF_3][MF_6]$ (M = Sb, As) salts were studied in the present work because they are the only previously known SF_3^+ salts that are stable at room-temperature and, hence, could be used as storable reagents for deoxofluorination reactions.

3.2 Single-crystal X-ray structure determination of $[SF_3][SbF_6]$ and $[SF_3][AsF_6]$

Previously, three phases of $[SF_3][SbF_6]$ were identified by variable temperature solid-state ^{19}F MAS NMR and Raman spectroscopy between –25 and –125 °C, while only one phase was found for $[SF_3][AsF_6]$ in the same temperature range.[6] Attempts were made to grow crystals of $[SF_3][SbF_6]$ via sublimation,[5] anhydrous HF,[6] N-basic donor solvents such as CH_3CN and pyridine (Chapter-4) and SO_2(l). As previously reported, the sublimation process did not provide crystalline material. With anhydrous HF, crystals of $[SF_3](HF)][SbF_6]$ were obtained.[14] The use of nitrogen bases solvents resulted in adduct formation between SF_3^+ and nitrogen bases (See Chapter-4). Liquid SO_2 was found to be an excellent solvent for SF_3^+ salts as demonstrated by Mews et al. for $[SF_3][AsF_6]$.[11] Their report that no fluorine-oxygen exchange between SF_3^+ and SO_2 occurs at room temperature was confirmed in the present study by ^{19}F NMR and Raman spectroscopy. Crystals of $[SF_3][SbF_6]$ and $[SF_3][AsF_6]$ suitable for X-ray crystallography were obtained using this solvent.

3.2.1 X-ray crystallography of $[SF_3][SbF_6]$

In order to structurally characterize the three phases of $[SF_3][SbF_6]$, crystals were grown from liquid SO_2. Crystallization from liquid SO_2 at low temperatures furnished transparent crystals of $[SF_3][SbF_6]$ in the form of transparent needles. The crystals were manipulated at different temperatures depending on the phase of $[SF_3][SbF_6]$ salt. Good quality crystals

for γ-$[SF_3][SbF_6]$ and α-$[SF_3][SbF_6]$ were obtained by this method while material obtained for the β- modification was a single crystal.

Table 3.1 Selected crystallographic data for $[SF_3][SbF_6]$ and $[SF_3][AsF_6]$

	γ-$[SF_3][SbF_6]$	α-$[SF_3][SbF_6]$	$[SF_3][AsF_6]$
chem formula	SF_9Sb	SF_9Sb	SF_9As
crystal system	Monoclinic	Monoclinic	Orthorhombic
space group	$P2_1/n$	$P2_1/c$	$Cmc2_1$
a (Å)	7.6922(9)	5.555(8)	20.307(14)
b (Å)	10.5446(13)	11.698(16)	8.369(6)
c (Å)	8.0875(10)	11.026(15)	11.091(8)
β (°)	96.0122(12)	98.063(16)	90
V (Å^3)	652.38(14)	709.5(17)	1885(2)
Z	4	4	8
mol wt (g mol^{-1})	324.81	324.81	277.98
ρ_{calcd} (g cm^{-3})	3.307	3.041	2.939
T (°C)	–130	–40	–130
μ (mm^{-1})	4.67	4.29	5.87
R_1[a]	0.0133	0.0721	0.0193
wR_2[b]	0.0296	0.1973	0.0427

[a] R_1 is defined as $\Sigma||F_o| - |F_c||/\Sigma|F_o|$ for $I > 2\sigma(I)$. [b] wR_2 is defined as $[\Sigma[w(F_o^2 - F_c^2)^2]/\Sigma w(F_o^2)^2]^{½}$ for $I > 2\sigma(I)$.

3.2.1.1 γ-$[SF_3][SbF_6]$

The γ-$[SF_3][SbF_6]$ crystallizes in the monoclinic $P2_1/n$ space group with four formula units in the unit cell. Selected crystallographic data is mentioned in Table 3.1, while the bond lengths and bond angles are given in Table 3.2. A comparison with the known SF_3^+

structures is summarized in Table 3.3. The thermal ellipsoid plot of the crystallographic unit of γ-[SF_3][SbF_6] is shown in Figure 3.1.

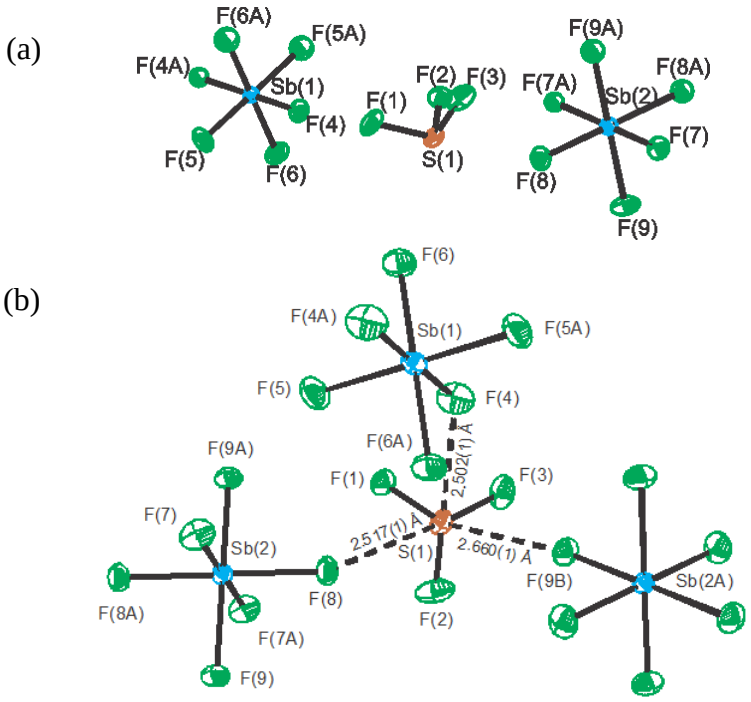

Figure 3.1(a) X-ray crystallographic structure of γ-[SF_3][SbF_6] (b) Extended view. Thermal ellipsoids are drawn at the 50% probability level.

Table 3.2 Bond lengths (Å), contacts (Å) and bond angles (°) for γ-[SF_3][SbF_6]

Bond lengths (Å)		Bond angles (°)	
S1-F1	1.5092(12)	F1-S1-F2	97.23(7)
S1-F2	1.5037(11)	F1-S1-F3	97.05(8)
S1-F3	1.5009(13)	F2-S1-F3	97.94(7)
S1···F6	2.502(1)	F4-Sb1-F5	90.25(5)
S1···F7	2.660(1)	F5-Sb1-F6	90.53(6)
S1···F8	2.517(1)	F4-Sb1-F6	90.63(5)
		F7-Sb2-F8	90.04(5)
Sb1-F4	1.8645(11)	F8-Sb2-F9	90.34(5)
Sb1-F5	1.8609(11)	F7-Sb2-F9	91.06(5)
Sb1-F6	1.8921(11)		
Sb2-F7	1.8815(10)		
Sb2-F8	1.8880(10)		
Sb2-F9	1.8567(10)		

The asymmetric unit contains one SF_3^+ cation located on a general position and two half SbF_6^- anions, which lie on crystallographic inversion centres. The SF_3^+ cation adopts a trigonal pyramidal geometry with approximate C_{3v} symmetry having S–F bond lengths of 1.5009(13), 1.5037(11) and 1.5092(12) Å which are in excellent agreement with the known SF_3^+ structures (Table 3.3).[2,3] The coordination sphere about S is expanded to hexacoordination by two short (2.502(1) and 2.517(1) Å) and one somewhat longer (2.660(1) Å) S···F contacts to adjacent SbF_6^- anions. The contacts avoid the location of the lone pair on sulfur. All of these long contacts are shorter than the sum of van der Waal's radii of sulfur and fluorine atoms (3.27 Å).[7]

Table 3.3 Bond lengths, contacts and bond angles for SF_3^+ in different compounds

	S–F bond length (Å)	S···F contacts (Å)	F–S–F bond angle (°)	Reference
$[SF_3]$ $[BF_4]$	1.499(2)	2.593(3)	97.62(7)	4
	1.495(2)	2.624(2)	97.39(12)	
$[SF_3]_2$ $[GeF_6]$	1.515(2)	2.420(1)	96.23(10)	5
	1.519(1)	2.367(2)	96.12(8)	
$[SF_3][AsF_6]$	1.503(3)	2.595(3)	97.16(18)	Present
	1.501(3)	2.566(3)	97.91(17)	work
	1.511(3)	2.558(3)	98.36(18)	
	1.502(3)	2.494(3)	97.56(17)	
	1.496(4)	2.983(3)	97.56(17)	
γ-$[SF_3][SbF_6]$	1.504(1)	2.660(1)	97.23(7)	Present
	1.501(1)	2.517(1)	97.05(8)	work
	1.509(1)	2.502(1)	97.94(7)	
α-$[SF_3][SbF_6]$	1.523(10)	2.519	98.3(6)	Present
	1.524(11)	2.587	95.8(6)	work
	1.533(10)	2.608	98.7(6)	

The F–S–F angles in the SF_3^+ cation are between 97.05(8) and 97.9(7)°. The F–S–F angle of the isoelectronic neutral PF_3 in the gas phase is essentially the same with 97.8(2)°,[15] evidencing that the anion-cation contacts in $[SF_3][SbF_6]$ do not significantly contribute to the size of F–S–F angle in the solid state. The F···S···F angles, on the other hand, vary significantly (80.13(4) to 108.67(4)°), because the weakness of the contacts makes these angles more susceptible to packing effects compared to the F−S−F angles. The fluorine contacts between SF_3^+ and SbF_6^- in this structure are similar to those found in $[SF_3][BF_4]$ (2.593(3) and 2.624(2) Å),[2,3] but significantly longer than those in $[SF_3]_2[GeF_6]$ (2.367(2) and 2.420(1) Å).[5] The short contacts in the latter salt is a result of the larger anionic charge and, therefore, the more ionic nature of the fluorine atoms in the GeF_6^{2-} anion. The Sb–F bond lengths in the SbF_6^- anion are within the expected range.[6] The fluorine atoms which form S···F contacts have longer Sb−F bonds (1.8921(11), 1.8815(10), 1.8880(10) Å) than those of the other Sb−F bonds (1.8609(11), 1.8645(11), 1.8567(10) Å). The difference in bond lengths and small deviations of the F−Sb−F angles from 90°, yield a distorted octahedral anion structure.

3.2.1.2 Factor group analysis of the Raman spectrum of γ-$[SF_3][SbF_6]$

Raman spectra of the three different phases of $[SF_3][SbF_6]$ had been recorded.[6] The X-ray crystal structures of the γ- phase of $[SF_3][SbF_6]$ enable the factor group analysis for this modification. Vibrational frequencies of $[SF_3][SbF_6]$ at –25 °C and –125 °C for the α- and γ- phases, respectively, are listed in Table 3.4. The free SF_3^+ cation and SbF_6^- anion are expected to adopt C_{3v} and O_h point symmetries, respectively, on the basis of the VSEPR model. Hence, the symmetry labels of the C_{3v} and O_h point groups are used in the discussion of the Raman spectra. In the Raman spectrum of γ-$[SF_3][SbF_6]$, all the four bands for ν_1, ν_2, ν_3 and ν_4 of SF_3^+ should be observed. Based on the factor group analysis (Table 3.5), $\nu_1(A_1)$

and ν_2 (A_1) should split into two Raman-active components whereas ν_3(E) and ν_4 (E) should show four splittings in the Raman spectrum of γ-[SF_3][SbF_6]. Experimentally, two components are observed for ν_1(A_1) (955 and 939 cm^{-1}), while no splitting was observed for ν_2(A_1) (527 cm^{-1}). For the ν_3(E) and ν_4 (E) modes two bands were observed (929 and 923 cm^{-1}), and (406 and 410 cm^{-1}), respectively as a consequence of the removal of degeneracy.

Table 3.4. Raman frequencies and their assignments for [SF_3][SbF_6][6]

Frequency (cm^{-1})		Assignments	
α-[SF_3][SbF_6]	γ-[SF_3][SbF_6]		
–25°C	–125°C	SF_3^+ (C_{3v})	SbF_6^- (O_h)
	955(20)		
946(79)	939(95)	$\nu_1(A_1)$, $\nu_s(SF_3)$	
928sh	929(15)	ν_3(E), $\nu_{as}(SF_3)$	
	923(23)		
669sh			$\nu_3(T_{1u})$, $\nu_{as}(SbF_6)$
652(100)	658(100)		$\nu_1(A_{1g})$, $\nu_s(SbF_6)$
643sh			
	598(6)		
	593(6)		
581sh	585(15)		$\nu_2(E_g)$, $\nu_{as}(SbF_6)$
	575(3)		
	557(8)		
552(46)	550(23)		
532(21)	527(14)	ν_2 (A_1), $\delta(SF_3)$	
411(12)	410(9)	ν_4(E), $\delta(SF_3)$	
406(12)	406(6)		
	288(25)		
283(57)	281(15)		$\nu_5(T_{2g})$, $\delta(SbF_6)$
	276sh		

Table 3.5. Correlation table for SF_3^+ cation for γ-$[SF_3][SbF_6]$

SF_3^+ free ion		Site symmetry	Factor group symmetry		
	C_{3v}	C_1	C_{2h}		
4T, $4\nu_1$, $4\nu_2$	A_1	A	A_g	ν_1, ν_2, $2\nu_3$, $2\nu_4$, 3R, 3T	RAMAN
			B_g	ν_1, ν_2, $2\nu_3$, $2\nu_4$, 3R, 3T	RAMAN
4R	A_2		A_u	ν_1, ν_2, $2\nu_3$, $2\nu_4$, 3R, 3T	IR
			B_u	ν_1, ν_2, $2\nu_3$, $2\nu_4$, 3R, 3T	IR
4T, 4R, $4\nu_3$, $4\nu_4$	E				
$\Gamma_{vib} = 2A_1 + 2E$					

Table 3.6 Correlation table for SbF_6^- anion for γ-$[SF_3][SbF_6]$

SbF_6^- free ion		Site symmetry	Factor group symmetry		
	O_h	C_i	C_{2h}		
$4\nu_1$	A_{1g}	A_g	A_g	$2\nu_1$, $4\nu_2$, $6\nu_5$, 3R, 3T	RAMAN
$4\nu_2$	E_g		B_g	$2\nu_1$, $4\nu_2$, $6\nu_5$, 3R, 3T	RAMAN
4R	T_{1g}		A_u	$6\nu_3$, $6\nu_4$, $6\nu_6$, 3R, 3T	IR
$4\nu_5$	T_{2g}	A_u	B_u	$6\nu_3$, $6\nu_4$, $6\nu_6$, 3R, 3T	IR
4T $4\nu_3$,$4\nu_4$	T_{1u}				
$4\nu_6$	T_{2u}				
$\Gamma_{vib} = A_{1g} + E_g + T_{2g} + 2T_{1u} + T_{2u}$					

Three bands, $\nu_1(A_{1g})$, $\nu_2(E_g)$, and ν_5 (T_{2g}) for SbF_6^- are expected in the Raman spectrum of γ-$[SF_3][SbF_6]$. The factor group analysis (Table 3.6) predicts four Raman-active components for $\nu_1(A_{1g})$, eight for $\nu_2(E_g)$ and twelve for ν_5 (T_{2g}). Two bands for of the A_1 mode (658 and 655 cm^{-1}) are observed. The E_g band is split into six components (551, 558, 598, 593, 585 and 575 cm^{-1}).

3.2.1.3 α-SF_3SbF_6

The α-phase of $[SF_3][SbF_6]$ crystallizes in the monoclinic space group $P2_1/c$ with four formula units per unit cell. Selected crystallographic data are given in Table 3.1. The bond lengths and bond angles are given in Table 3.7. The thermal ellipsoid plot of the crystallographic unit of α-$[SF_3][SbF_6]$ is shown in Figure 3.2.

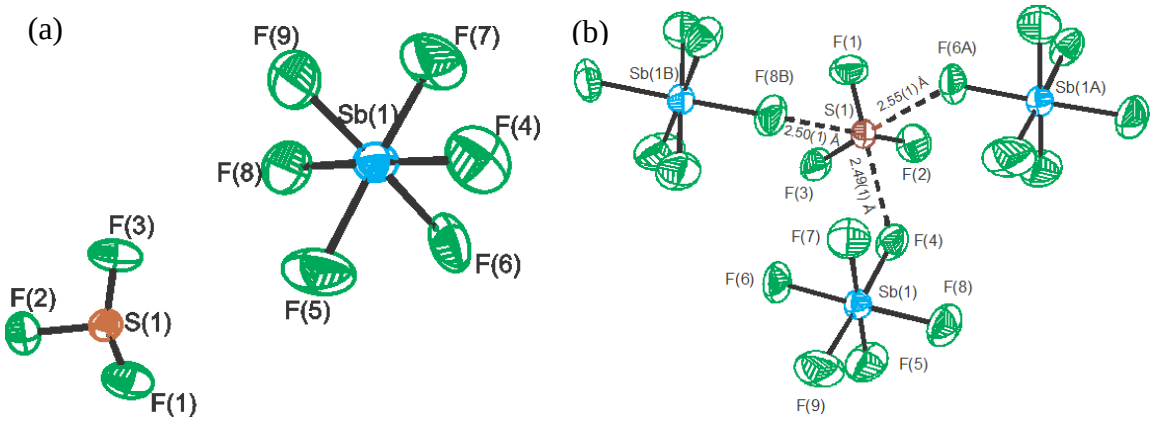

Figure 3.2 (a) X-ray crystallographic structure of α-$[SF_3][SbF_6]$ (b) Extended view. Thermal ellipsoids are drawn at the 50% probability level.

The deterioration of the crystal at −40 °C resulted in an incomplete data set and low accuracy of the metric parameters. The SF_3^+ cation adopts a trigonal pyramidal geometry with approximate C_{3v} symmetry having S–F bond lengths of 1.523(10), 1.524(11) and 1.533(10) Å. Three long contacts (2.519, 2.587 and 2.608 Å) from sulfur to the fluorine atoms bound to antimony make the coordination number of sulfur six. A comparison for the known $[SF_3]^+$ structures, i.e., $[SF_3][BF_4]$[2,3] and $[(SF_3)_2][GeF_6]$,[5] is summarized in the Table 3.3. The F–S–F angles in the SF_3^+ cation are 98.30(6), 95.80(6) and 98.70(6)° in agreement with the PF_3 angles as discussed in 3.2.1.1. The Sb–F bond lengths in the SbF_6^- anion are within the expected range.[6] As in the γ- phase, three S···F contacts are present between sulfur and fluorine of the adjacent SbF_6^- anion. The fluorine atoms which form S···F contacts exhibit longer Sb−F bonds (1.921(10) Å) compared to the Sb−F bonds (1.871(10) Å) without contacts to the cation. The difference in bond lengths and small deviations of the F−Sb−F angles from 90°, yield a distorted octahedral anion structure. The anion-cation packing in the α- and γ- modifications is similar to a distorted CsCl structure, with the SbF_6^- anions packed in a simple cubic fashion and the SF_3^+ cations in the cubic

holes. The anion-cation contacts result in displacing the cation from the center of the cubic hole.

Table 3.7. Bond lengths (Å) and bond angles (°) for α-[SF_3][SbF_6]

Bond lengths (Å)		Bond angles (°)	
S1-F1	1.523(10)	F1-S1-F2	98.3(6)
S1-F2	1.524(11)	F1-S1-F3	95.8(6)
S1-F3	1.533(10)	F2-S1-F3	98.7(6)
Sb1-F4	1.865(11)	F4-Sb1-F5	90.5(5)
Sb1-F5	1.870(9)	F5-Sb1-F6	88.6(4)
Sb1-F6	1.921(10)	F6-Sb1-F7	89.3(5)
Sb1-F7	1.871(10)	F7-Sb1-F8	91.4(5)
Sb1-F8	1.891(10)	F8-Sb1-F9	90.9(6)
Sb1-F9	1.881(10)	F9-Sb1-F4	91.1(6)
		F4-Sb1-F8	178.0(5)
		F5-Sb1-F7	177.7(5)
		F6-Sb1-F9	178.2(5)

3.2.1.4 Factor group analysis of α-[SF_3][SbF_6]

As for γ-[SF_3][SbF_6], the crystal structure of α-phase enabled a factor group analysis of the modification. In the Raman spectrum of SF_3^+ cation of α-[SF_3][SbF_6], the $\nu_1(A_1)$ is expected to split into two components based on the factor group analysis (Table 3.8) but no splitting was resolved for this band at 946 cm^{-1}. The $\nu_3(E)$ mode should show four splittings, however, the $\nu_3(E)$ band has only been observed as a shoulder at 928 cm^{-1}. The $\nu_2(A_1)$ mode comes at 532 cm^{-1} without splitting and $\nu_4(E)$ mode appears at 283 cm^{-1} although $\nu_2(A_1)$ and $\nu_4(E)$ should give two and four splittings, respectively.

Table 3.8. Correlation table for SF_3^+ cation for α-$[SF_3][SbF_6]$

SF_3^+ free ion		Site symmetry	Factor group symmetry		
C_{3v}		C_1	C_{2h}		
4T, $4\nu_1$, $4\nu_2$	A_1	A	A_g	ν_1, ν_2, $2\nu_3$, $2\nu_4$, 3R, 3T	RAMAN
			B_g	ν_1, ν_2, $2\nu_3$, $2\nu_4$, 3R, 3T	RAMAN
4R	A_2		A_u	ν_1, ν_2, $2\nu_3$, $2\nu_4$, 3R, 3T	IR
			B_u	ν_1, ν_2, $2\nu_3$, $2\nu_4$, 3R, 3T	IR
4T, 4R, $4\nu_3$, $4\nu_4$	E				
$\Gamma_{vib} = 2A_1 + 2E$					

Table 3.9. Correlation table for SbF_6^- anion for α-$[SF_3][SbF_6]$

SbF_6^- free ion		Site symmetry	Factor group symmetry		
O_h		C_1	C_{2h}		
$4\nu_1$	A_{1g}	A	A_g	ν_1,$2\nu_2$,$3\nu_3$,$3\nu_4$,$3\nu_5$,$3\nu_6$,3R,3T	RAMAN
			B_g	ν_1,$2\nu_2$,$3\nu_3$,$3\nu_4$,$3\nu_5$,$3\nu_6$,3R,3T	RAMAN
$4\nu_2$	E_g		A_u	ν_1, $2\nu_2$, $3\nu_3$, $3\nu_4$, $3\nu_5$, $3\nu_6$, 3R, 3T	IR
4R	T_{1g}		B_u	ν_1, $2\nu_2$, $3\nu_3$, $3\nu_4$, $3\nu_5$, $3\nu_6$, 3R, 3T	IR
$4\nu_5$	T_{2g}				
4T $4\nu_3$,$4\nu_4$	T_{1u}				
$4\nu_6$	T_{2u}				
$\Gamma_{vib} = A_{1g} + E_g + T_{2g} + 2T_{1u} + T_{2u}$					

The factor group analysis for SbF_6^- anion predicts the T_{1u} mode to be Raman active (Table 3.9) although the T_{1u} mode is Raman inactive for isolated octahedral species and the band is predicted to have twelve Raman-active components. The T_{1u} mode has been observed at 669 cm^{-1} as shoulder without splitting. The $\nu_1(A_{1g})$ mode should give two splitting. The $\nu_1(A_{1g})$ band of SbF_6^- anion comes at 652 cm^{-1} and the splitting appear in the form of shoulder at 643 cm^{-1} for this band. The $\nu_2(E_g)$ band should give four splitting, however, it gives two very broad contributions at 581 and 552 cm^{-1} due to lift in degeneracy. For the T_{2g} band at 283 cm^{-1}, no splitting shows up because of the broadness of the band although twelve splitting are expected for this band.

3.2.1.5 β-[SF_3][SbF_6]

Due to the poor quality of the crystal, a set of diffraction spots among the large number of observed reflections could be indexed with monoclinic cells. Refinement of the structures in the monoclinic space groups P$2_1/m$ and P$2/m$ resulted R_1 values below 2%. It was not possible to index all reflections, which might be the consequence of shattering of the crystal at –70 °C. In both crystal structure solutions, the sulfur in SF_3^+ is disordered while the SbF_6^- acquires the octahedral geometry. The unit cell parameters for the monoclinic P$2_1/m$ solution were: a = 5.3060(12) Å, b = 10.608(2) Å, c = 5.8862(14) Å and β = 92.787(2)° while for monoclinic P$2/m$, the unit cell parameters were: a = 5.309(7) Å, b = 5.309(7) Å, c = 5.287(8) Å and β = 92.80(1)°. Because of the multiple crystal nature of the material and some chemically strange bond lengths obtained from the refinement, doubts about the correct unit cell and structure remains.

3.2.2 X-ray crystallography of [SF_3][AsF_6]

In order to structurally characterize [SF_3][AsF_6], crystals were grown by dissolving [SF_3][AsF_6] in liquid SO_2. Crystallization from liquid SO_2 at –60 °C furnished transparent crystals of [SF_3][AsF_6] in the form of needles. These crystals were manipulated at low temperature, i.e., below –60 °C. The unit cell parameters of [SF_3][AsF_6] are in excellent agreement with those reported previously.[15] The [SF_3][AsF_6] salt crystallizes in the orthorhombic *Cmc*2_1 space group with two crystallographically unique cation-anion pairs (one full and one half) (Figure 3.3) having eight formula units in the unit cell. Selected crystallographic data has been given in Table 3.1. Bond lengths and bond angles are given in Table 3.10. The comparison of S–F bond length, S---F long distances and F–S–F bond angles among SF_3^+ salts is summarized in the Table 3.3.

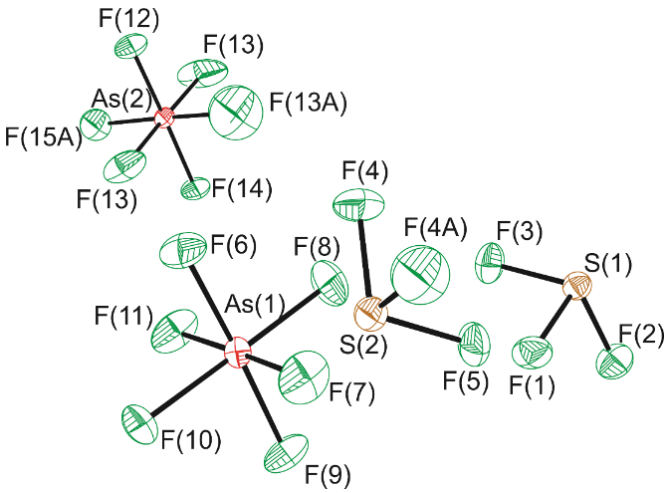

Figure 3.3 Thermal ellipsoid plots of the two independent $[SF_3][AsF_6]$ formula units in the X-ray crystal structure of $[SF_3][AsF_6]$. Thermal ellipsoids are drawn at 50% probability level.

The SF_3^+ cations adopt the expected trigonal pyramidal geometry with approximate C_{3v} symmetry having S–F bond lengths ranging from 1.496(4) to 1.511(3) Å, which are in good agreement with the S–F bond lengths found in $[SF_3][BF_4]$ (2.593(3) and 2.624(2)Å),[2,3] and in $[SF_3]_2[GeF_6]$ (2.367(2) and 2.420(1)Å)[5]. The S(2) atom has two close S···F contacts (2 × 2.494(3) Å) and one long S···F contact (2.983(3) Å) with adjacent anions. The coordination sphere of S(1) is also extended by three S···F contacts (2.558(3), 2.567(3) and 2.595(3) Å) with fluorine atoms of three AsF_6^- anions. These long distances increases the total coordination number of S(1) and S(2) to six. All of these contacts are shorter than the sum of van der Waal's radii (3.27 Å).[12] The fluorine contacts between SF_3^+ and AsF_6^- in this structure are similar to those found in $[SF_3][BF_4]$ (2.593(3) and 2.624(2) Å),[2,3] but significantly longer than those in $[SF_3]_2[GeF_6]$ (2.367(2) and 2.420(1) Å).[5] The environment about S(2) in $[SF_3][AsF_6]$ is rather unusual as the three S···F contacts are of similar length in all other known SF_3^+ salts (Table 3.3). The As–F bond lengths ranges from 1.690(3) to 1.732(2) Å. The S---F distance between F15 of As2 to S1 is 2.567(3) Å increasing the As2–F15 bond length to 1.709(3) Å while shortening the opposite As2–F13

bond length to 1.690(3) Å. F11 of As1 has a long contact with S1 (2.557(3) Å), thus the As1–F11 bond length becomes 1.732(2) Å while As1–F7 bond length becomes 1.729(3) Å. Similarly, F10 on As1 establishes a long contact with S1 (2.598 Å) making As1–F10 1.726(3) Å and shortening As1–F8 to 1.691(3) Å at the same time in a slightly distorted octahedral geometry of AsF_6^- anion in $[SF_3][AsF_6]$. The As–F bond lengths are of about the same size as were found for $[K][AsF_6]$ (1.712(1) Å).[8,9]

Table 3.10 Bond lengths (Å), contacts (Å) and bond angles (°) for $[SF_3][AsF_6]$

Bond lengths (Å)		Bond angles (°)	
S1-F1	1.503(3)	F1-S1-F2	97.16(18)
S1-F2	1.511(3)	F2-S1-F3	97.91(17)
S1-F3	1.501(3)	F1-S1-F3	98.36(18)
S2-F4	1.502(3)	F4-S2-F5	97.56(17)
S2-F5	1.496(4)	F6-As1-F7	90.48(12)
S1···F11	2.557(3)	F6-As1-F8	90.93(15)
S1···F15	2.567(3)	F6-As1-F9	177.56(19)
S1···F10	2.598(3)	F6-As1-F10	88.49(14)
S2···F7	2.494(2)	F6-As1-F11	89.65(11)
S2···F13	2.983(4)	F7-As1-F8	91.23(14)
		F7-As1-F9	89.76(11)
		F7-As1-F10	89.06(13)
As1-F8	1.691(3)	F7-As1-F11	178.54(16)
As1-F9	1.698(3)	F8-As1-F9	91.49(16)
As1-F10	1.726(3)	F8-As1-F10	179.35(14)
As1-F11	1.732(2)	F8-As1-F11	90.22(13)
As2-F12	1.694(4)	F9-As1-F10	89.09(16)
As2-F13	1.690(3)	F9-As1-F11	90.05(11)
As2-F14	1.711(3)	F10-As1-F11	89.49(13)
As2-F15	1.709(3)	F12-As2-F13	91.97(15)
		F12-As2-F14	178.7(2)
		F12-As2-F15	89.68(14)
		F13-As2-F14	88.95(15)
		F13-As2-F15	90.41(18)
		F15-As2-F14	89.40(14)

3.2.2.1 Factor group analysis of $[SF_3][AsF_6]$

The crystal structure of $[SF_3][AsF_6]$ allows for a factor group analysis. The observed vibrational Raman frequencies of $[SF_3][AsF_6]$ at ambient temperature are given in Table 3.11.[6] The recorded Raman frequencies are in agreement with those recorded by Azeem *et al.*[1]

Table 3.11 Assignment of Raman frequencies of $[SF_3][AsF_6]$[6]

Frequency (cm^{-1})	Assignment	
	SF_3^+ (C_{3v})	AsF_6^- (O_h)
960 (sh)		
945(81)	$\nu_1(A_1)$, $\nu_s(SF_3)$	
926(29)	$\nu_3(E)$, $\nu_{as}(SF_3)$	
715(20)		$\nu_3(T_{1u})$, $\nu_{as}(AsF_6)$
686(100)		$\nu_1(A_{1g})$, $\nu_{as}(AsF_6)$
587(23)		
563(32)		$\nu_2(E_g)$, $\nu_{as}(AsF_6)$
530(20)	$\nu_2(A_1)$, $\delta(SF_3)$	
411(22)	$\nu_4(E)$, $\delta(SF_3)$	
379(44)		$\nu_5(T_{2g})$, $\delta(AsF_6)$

In the X-ray crystal structure of $[SF_3][AsF_6]$, two different SF_3^+ cations and two AsF_6^- anions are present. One SF_3^+ and AsF_6^- are on the general position (C_1 site symmetry) and the other SF_3^+ and AsF_6^- are on the mirror planes (C_s symmetry). Thus, the factor group analysis is different for both pairs of SF_3^+ and AsF_6^-. The isolated SF_3^+ cation and AsF_6^- anion have molecular C_{3v} and O_h symmetries, respectively.

Table 3.12 Correlation table for the general position SF_3^+ cation in $[SF_3][AsF_6]$

SF_3^+ free ion		Site symmetry	Factor group symmetry	
C_{3v}		C_1	C_{2v}	
4T, $4\nu_1$, $4\nu_2$	A_1	A	A_1 ν_1, ν_2, $2\nu_3$, $2\nu_4$, 3R, 3T RAMAN	IR
			A_2 ν_1, ν_2, $2\nu_3$, $2\nu_4$, 3R, 3T RAMAN	
4R	A_2		B_1 ν_1, ν_2, $2\nu_3$, $2\nu_4$, 3R, 3T RAMAN	IR
			B_2 ν_1, ν_2, $2\nu_3$, $2\nu_4$, 3R, 3T RAMAN	IR
4T, 4R, $4\nu_3$, $4\nu_4$	E			
$\Gamma_{vib} = 2A_1 + 2E$				

Table 3.13 Correlation table for the SF_3^+ cation on the mirror plane in $[SF_3][AsF_6]$

SF_3^+ free ion		Site symmetry	Factor group symmetry	
C_{3v}		C_s	C_{2v}	
4T, $4\nu_1$, $4\nu_2$	A_1	A’	A_1 $2\nu_1$, $2\nu_2$, $2\nu_3$, $2\nu_4$ 2R, 4T RAMAN	IR
			A_2 $2\nu_3$, $2\nu_4$ 4R, 2T RAMAN	
4R	A_2	A”	B_1 $2\nu_3$, $2\nu_4$ 4R, 2T RAMAN	IR
			B_2 $2\nu_1$, $2\nu_2$, $2\nu_3$, $2\nu_4$ 2R, 4T RAMAN	IR
4T, 4R, $4\nu_3$, $4\nu_4$	E			
$\Gamma_{vib} = 2A_1 + 2E$				

Table 3.14 Correlation table for the general position AsF_6^- anion in $[SF_3][AsF_6]$

AsF_6^- free ion		Site symmetry	Factor group symmetry	
O_h		C_1	C_{2v}	
$4\nu_1$	A_{1g}	A	A_1 ν_1, $2\nu_2$, $3\nu_3$, $3\nu_4$, $3\nu_5$, $3\nu_6$, 3R,3T RAMAN	IR
			A_2 ν_1, $2\nu_2$, $3\nu_3$, $3\nu_4$, $3\nu_5$, $3\nu_6$, 3R,3T RAMAN	
$4\nu_2$	E_g		B_1 ν_1, $2\nu_2$, $3\nu_3$, $3\nu_4$, $3\nu_5$, $3\nu_6$, 3R,3T RAMAN	IR
4R	T_{1g}		B_2 ν_1, $2\nu_2$, $3\nu_3$, $3\nu_4$, $3\nu_5$, $3\nu_6$, 3R,3T RAMAN	IR
$4\nu_5$	T_{2g}			
4T $4\nu_3$,$4\nu_4$	T_{1u}			
$4\nu_6$	T_{2u}			
$\Gamma_{vib} = A_{1g} + E_g + T_{2g} + 2T_{1u} + T_{2u}$				

Table 3.15 Correlation table for the AsF_6^- anion on the mirror plane in $[SF_3][AsF_6]$

AsF_6^- free ion		Site symmetry	Factor group symmetry	
O_h		C_s	C_{2v}	
$4\nu_1$	A_{1g}	A’	A_1 $2\nu_1$, $4\nu_2$, $6\nu_5$, 18R, RAMAN	IR
			A_2 $6\nu_3$, $6\nu_4$, $6\nu_6$ 18T RAMAN	
$4\nu_2$	E_g		B_1 $6\nu_3$, $6\nu_4$, $6\nu_6$, 18T RAMAN	IR
4R	T_{1g}	A”	B_2 $2\nu_1$, $4\nu_2$, $6\nu_5$, 18R RAMAN	IR
$4\nu_5$	T_{2g}			
4T $4\nu_3$, $4\nu_4$	T_{1u}			
$4\nu_6$	T_{2u}			
$\Gamma_{vib} = A_{1g} + E_g + T_{2g} + 2T_{1u} + T_{2u}$				

The SF_3^+ cation has two A_1 normal modes of vibration (one stretching and one bending) as well as two doubly degenerate E modes (one stretching, one bending). All of these modes are Raman active. According to the factor group analysis for the SF_3^+ cation (Table 3.12) on the general position, each of $\nu_1(A_1)$ and $\nu_2(A_1)$ bands should split into four Raman-active components while $\nu_3(E)$ and $\nu_4(E)$ should split into eight. For the SF_3^+ cation situated on the mirror plane, the factor group analysis (Table 3.13) predicts the splitting of $\nu_1(A_1)$ and $\nu_2(A_1)$ into four while $\nu_3(E)$ and $\nu_4(E)$ should show eight splitting.

For the AsF_6^- anion, on the general position, six vibrational frequencies should be observed in the Raman spectrum $\nu_1(A_{1g})$. According to the factor group analysis (Table 3.14), $\nu_1(A_{1g})$ mode should split into four, $\nu_2(E_g)$ into eight while $\nu_3(T_{1u})$, $\nu_4(T_{1u})$, $\nu_5(T_{2g})$ and $\nu_6(T_{2u})$ is predicted to split into twelve splitting. The T_{1u} and T_{2u} modes should also be observable by Raman spectroscopy according to the factor group analysis Table 3.7 and 3.8. For the AsF_6^- anion on the mirror plane, $\nu_1(A_{1g})$ should show four and $\nu_2(E_g)$ frequency should show eight splitting while $\nu_3(T_{1u})$, $\nu_4(T_{1u})$ and $\nu_5(T_{2g})$ frequencies should show twelve splitting (Table 3.15).

In the experimental Raman spectrum of $[SF_3][AsF_6]$ (Table 3.11), all the observed vibrational bands are relatively broad and do not narrow appreciably upon cooling the sample. None of the predicted splittings for the SF_3^+ bands are resolved. This is likely the consequence of overlap, which contributes to the broadness of the Raman bands. In the case of AsF_6^- anion, the asymmetric T_{1u} mode is being assigned at 715 cm^{-1} as it is predicted to have a Raman active component (Table 3.6 and 3.8). The only observed splitting is that of the asymmetric anion stretching E_g mode into two components (587 and 563 cm^{-1}). As for the cation bands, almost all of the predicted splittings of the anion bands are not resolved, contributing to broadness.

3.3 Solution ^{19}F NMR spectroscopy and Raman spectroscopy of $[SF_3][MF_6]$ (M = Sb, As) salts using liquid SO_2 solvent

3.3.1 Solution ^{19}F NMR spectroscopy of $[SF_3][MF_6]$ (where M = Sb, As) salts using liquid SO_2 solvent

The chemical shifts from ^{19}F MAS NMR as well as solution NMR spectroscopy of $[SF_3][SbF_6]$ and $[SF_3][AsF_6]$ in liquid SO_2 and anhydrous HF solvent are summarized in Table 3.16. The chemical shift values for the SF_3^+ cation of $[SF_3][AsF_6]$ and $[SF_3][SbF_6]$ salts in liquid SO_2 solvent is close to the values obtained with solid-state ^{19}F MAS NMR spectroscopy. In the solution ^{19}F NMR spectrum of $[SF_3][AsF_6]$, a singlet is observed at +32.9 ppm for the SF_3^+ cation. The observation of one signal for the SF_3^+ cation shows the equivalency of fluorine atoms. For AsF_6^- anion a broad peak is observed at –58.5 ppm in liquid SO_2 solvent. The chemical shift for AsF_6^- anion in $[SF_3][AsF_6]$ is in good agreement with the literature where ^{19}F NMR spectrum was recorded in liquid SO_2 for $C_{60}(AsF_6)_x$ (–64.5 ppm).[10] The broadness of the AsF_6^- anion signal is due to the fast relaxing ^{75}As quadrupolar nucleus. The fast relaxation of ^{75}As nucleus removes the $^1J(^{75}As–^{19}F)$ scalar coupling information. Similarly, in ^{19}F solution NMR spectroscopy of $[SF_3][SbF_6]$ salt, only one signal is observed for the SF_3^+ cation. Because of the fast quadrupolar relaxation due to unsymmetrical fluorine environment about Sb, ^1J–coupling between ^{19}F and ^{121}Sb as well as ^{123}Sb were not observed in ^{19}F NMR spectra. Instead a broad peak resulted due to fast quadrupolar relaxation effect.

Table 3.16 ^{19}F NMR chemical shifts (δ) of $[SF_3][MF_6]$ (M = Sb, As) salts

Compound	Solvent	δ(^{19}F), ppm $[SF_3]^+$	δ(^{19}F), ppm $[MF_6]^-$ (M = Sb, As)	References
$[SF_3][AsF_6]$(s)	–	+32.9	–61.9	11
$[SF_3][AsF_6]$	SO_2(l)	+32.9	–58.5	6
$[SF_3][AsF_6]$	anhydrous HF	+28.8	–66.9	1c
$[SF_3][SbF_6]$(s)	–	+37.5	–115.6	11
$[SF_3][SbF_6]$	SO_2(l)	+34.5	–109.5	Present work
$[SF_3][SbF_6]$	anhydrous HF	+30.7	–123.2	1c

3.3.2 Raman spectrum of $[SF_3][MF_6]$ (M = Sb, As) salts in SO_2(l)

No change in the frequency position and band pattern of the SF_3^+ and MF_6^- signals was observed in the Raman spectrum of $[SF_3][MF_6]$ (M = Sb, As) in SO_2(l). The example of $[SF_3][SbF_6]$ in SO_2(l) is being demonstrated in Figure 3.5. For the confirmation of inertness of SO_2(l) towards $[SF_3][MF_6]$ (M = Sb, As) salts, the reaction between $[SF_3][MF_6]$ (M = Sb, As) salts and SO_2(l) was done at room temperature and then the Raman spectrum was recorded at –110 °C.

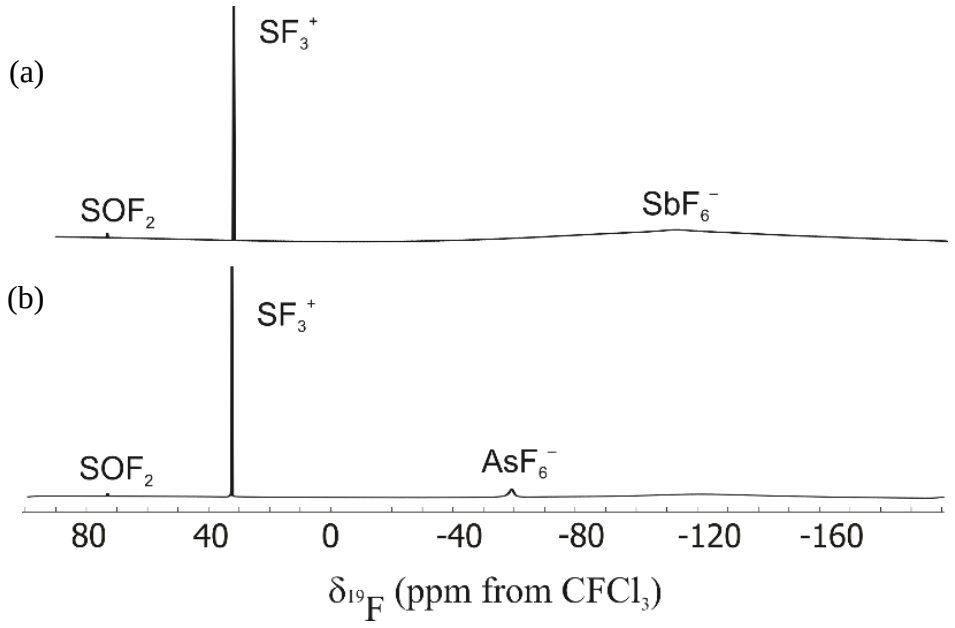

Figure 3.4 Solution ^{19}F NMR spectra of (a) $[SF_3][SbF_6]$ and (b) $[SF_3][AsF_6]$ salts in liquid SO_2

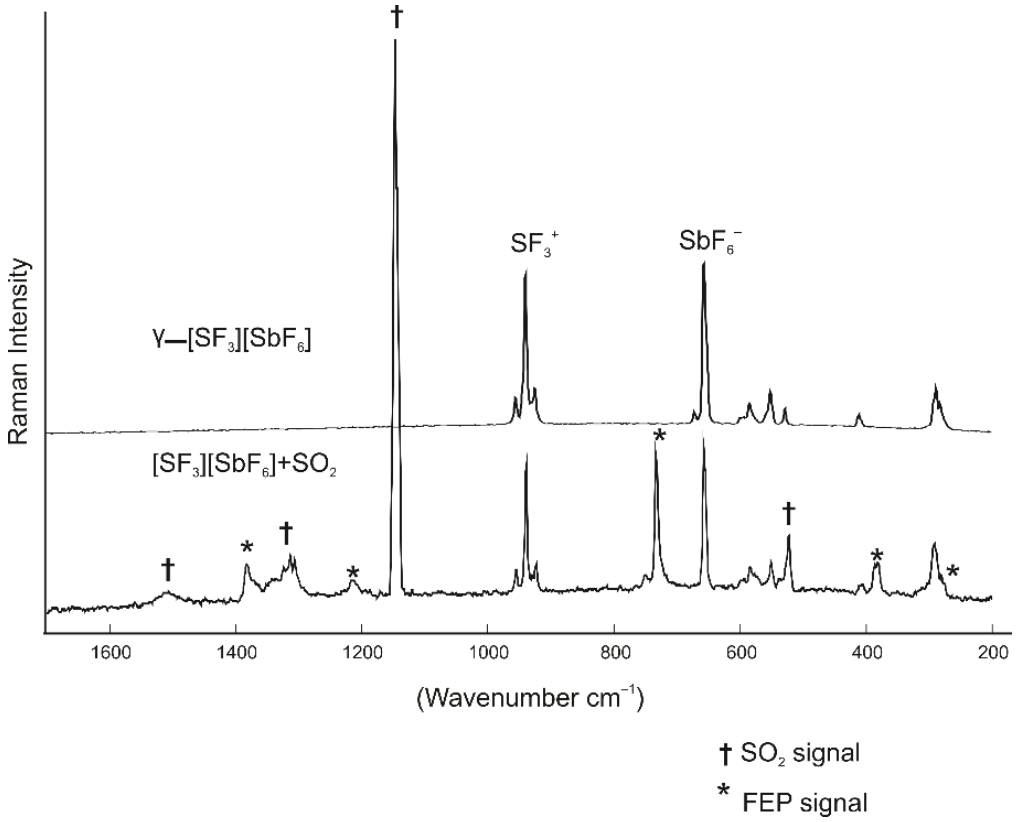

Figure 3.5 Raman spectrum of $[SF_3][SbF_6]$ in liquid SO_2 at –110 °C after getting them reacted at ambient temperature.

3.4 Scoping reactions for the use of $[SF_3][MF_6]$ (M=Sb, As) salts as deoxofluorinating reagents

A number of nucleophilic fluorinating reagents is available for deoxofluorination reactions in organic chemistry, ranging from SF_4 as the first fluorosulfur reagent (1958) to XtalFluor-E® and XtalFluor-M®, which are among the latest fluorosulfur nucleophilic reagents (2010). The ionic XtalFluor reagents have been shown to be stable in reactions at temperatures up to 205 °C.[12] The $[SF_3][MF_6]$ (M=Sb, As) salts have been known since 1956 and have a high melting point of 230 °C in the case of $[SF_3][SbF_6]$. Furthermore, the SF_3^+ cation is more electrophilic compared to SF_4 based on the positive charge situated on sulfur and the three highly electronegative substituents. Thus the reactions should proceed at lower temperature as compared to SF_4 or the $[Et_2NSF_2]^+$ cation which is part of XtalFluor-E®. Some of the results for the scoping reactions using $[SF_3][MF_6]$ (M=Sb, As) salts are presented in the following sections.

3.4.1 Reaction procedure for the nucleophilic fluorination reaction using $[SF_3][MF_6]$ (M=Sb, As) salts

Stoichiometric amounts or a slight excess of one of the $[SF_3][MF_6]$ (M=Sb, As) salts was combined with the organic compound and a substoichiometric amount of a F^- ion source such as anhydrous CsF or TMAF was added. This fluoride source presumably acts as a catalyst for the reaction. (The use of anhydrous HF in place of an ionic fluoride gave the product in low yield.) The fluorination reaction were carried out in solvents such as SO_2, CH_3CN or CH_2Cl_2. In the case of CH_3CN a low temperature of ca. –20 °C was maintained whereas with CH_2Cl_2 and SO_2, the reaction was carried out at ambient temperature. With CH_3CN, low temperature should be maintained all the time to avoid reaction involving CH_3CN. Deoxofluorination reactions using SF_3^+ salts were investigated for examples of

ketones (4-*tert*-butylcyclohexanone, 1,4-dioxaspiro[4.5]decan-8-one), carboxylic acids (pentafluorobenzoic acid, benzoic acid) and alcohol (cyclooctanol). These substrates have been used to evaluate the efficiency of XtalFluor-E®.[12]

3.4.2 Deoxofluorination of ketones

3.4.2.1 Deoxofluorination of 4-*tert*-butylcyclohexanone

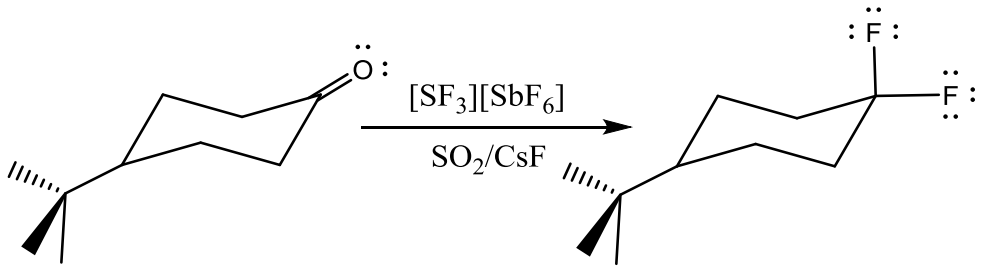

(3.2)

The deoxofluorination of a ketone to the respective difluoro compound (equation 3.2) was tested for 4-*tert*-butylcyclohexanone. For the reaction, $[SF_3][SbF_6]$ and 4-*tert*-butylcyclohexanone was taken in an approximately 1.5:1 ratio and CsF was added to the reaction mixture (ketone : CsF molar ratio; 1 : 0.4). The reaction was carried out either in excess liquid SO_2 or dry CH_2Cl_2 at ambient temperature in a thick wall ¼" FEP reactor which can handle the vapor pressure of the SO_2 and the pressure generated from SOF_2 and SF_4 gases. The production of 4-*tert*-butyl-1,1-difluorocyclohexane was monitored by ^{19}F NMR spectroscopy (Figure 3.6) and ^{1}H NMR spectroscopy (Figure 3.7).

In the $^{19}F\{^{1}H\}$ NMR spectrum, two doublets were observed for the reaction mixture consistent with the generation of 4-*tert*-butyl-1,1-difluorocyclohexane (–87.1 and –98.9 ppm with a $^{2}J(^{19}F–^{19}F)$ coupling constant of 237 Hz).[12] In the coupled ^{19}F NMR spectrum the $^{3}J(^{1}H–^{19}F)$ coupling value is 36 Hz was observed for the axial fluorine signal at –98.9 ppm, which shows closeness to the protons of the cyclohexane ring. These NMR parameters are in excellent agreement with those observed for 4-*tert*-butyl-1,1-

difluorocyclohexane.[12] Other signals at 73.6, 59.9 and –120.8 ppm were assigned to SOF_2, SF_4 and SbF_6^-, respectively. No $^1J(^{121}Sb–^{19}F)$ and $^1J(^{123}Sb–^{19}F)$ couplings were observed in case of SbF_6^-. The integration value for the two doublets of 4-*tert*-butyl-1,1-difluorocyclohexane is 1:1 while the integration value for SOF_2 with respect to one ^{19}F doublet of 4-*tert*-butyl-1,1-difluorocyclohexane signal was (26 : 1). This ratio is much larger than the expected ratio of 2:1. This may be due to the production of extra SOF_2 because of the reaction of SF_3^+ salt with moisture (Figure 3.4).

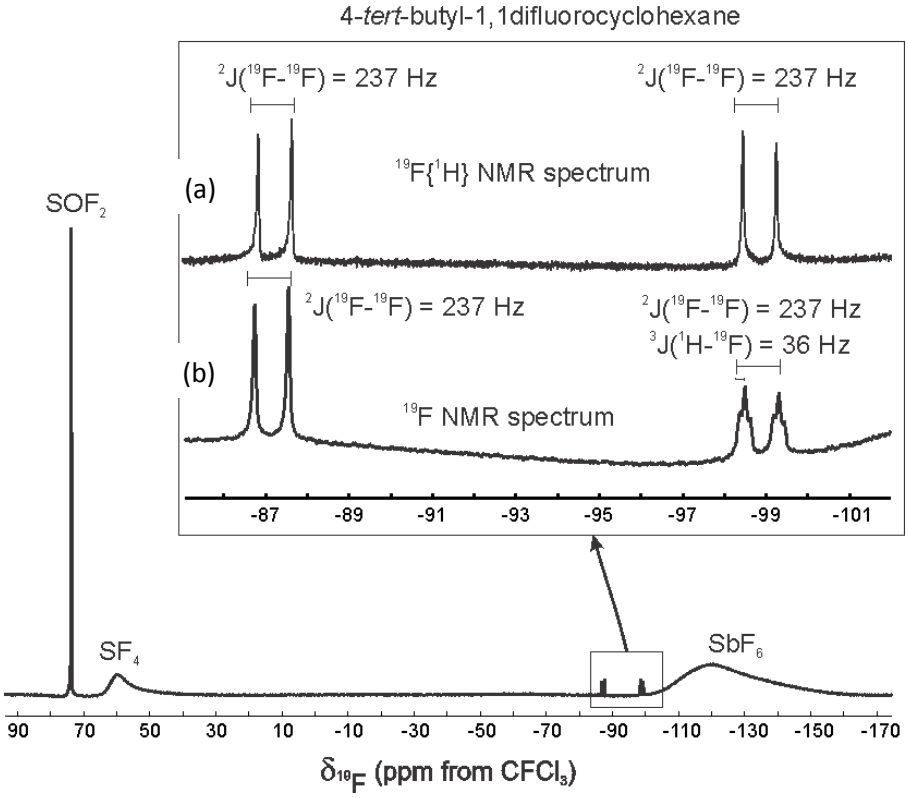

Figure 3.6 Solution-state ^{19}F NMR spectrum (a) $^{19}F\{^1H\}$ (b) ^{19}F with no decoupling of 4-*tert*-butylcyclohexanone in $[SF_3][SbF_6]$, CsF using liquid SO_2 (or CH_2Cl_2) as solvent at ambient temperature.

In the ^1H NMR spectrum, the signals of the 2nd, 3rd and 4th proton positions have been shifted at higher frequency due to the replacement of oxygen of the carbonyl group to the more electronegative fluorine. The protons at position 2 are shifted from 1.48 to 1.89

ppm, proton at position 4 is shifted from 1.36 to 1.48, protons at position 3 are shifted from 0.73 to 0.86 ppm. The protons of *t*-butyl group are shifted slightly from 0.21 to 0.23 ppm. These shifts also support the formation of 4-*tert*-butyl-1,1difluorocyclohexane.

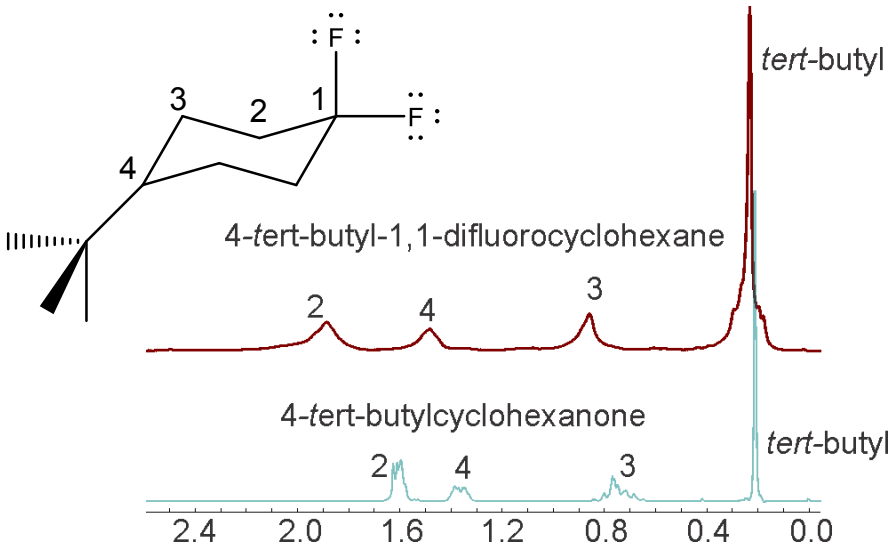

Figure 3.7 Overlap of solution-state ^{1}H DP NMR spectrum (a)grey color for 4-*tert*-butylcyclohexanone in CH_2Cl_2 and (b) brown color for 4-*tert*-butylcyclohexanone in $[SF_3][SbF_6]$, CsF using liquid CH_2Cl_2 as solvent at ambient temperature.

3.4.2.2 Deoxofluorination of 1,4-dioxaspiro[4.5]decan-8-one

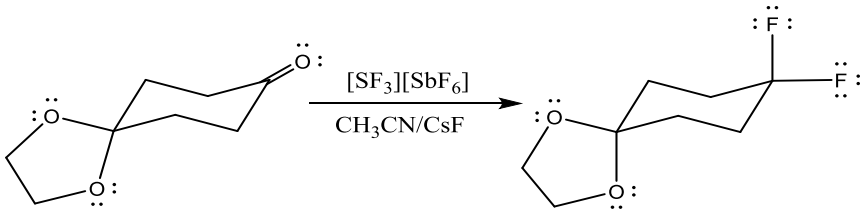

(3.3)

1,4-dioxaspiro[4.5]decan-8-one and $[SF_3][SbF_6]$ were allowed to react in 1:1 ratio using liquid CH_3CN solvent and CsF (ketone to CsF molar ratio of 1 : 0.4) at –20 °C. Doublets at –68.1 and –114.5 ppm ($^{2}J(^{19}F–^{19}F)$ = 9.1 Hz) in the ^{19}F NMR spectrum (Figure 3.8) indicate the production of 8,8-difluoro-1,4-dioxaspiro[4.5]decane as the product. The $^{2}J(^{19}F–^{19}F)$ coupling value is 9.1 Hz, which seems to be unexpectedly low. The yield of 8,8-difluoro-1,4-dioxaspiro[4.5]decane is low and significant amounts of HF (–180.4 ppm)

were produced as a side product. The singlet at 71.4 ppm represents SOF_2 and the triplets at 31.6 and 80.6 ppm represents SF_4 production. The multiplet signal at –122.6 ppm for SbF_6^- is a combination of sextet and octet resulted from $^1J(^{121}Sb–^{19}F)$ and $^1J(^{123}Sb–^{19}F)$. These coupling values are 1952 and 1046 Hz, respectively. The production of large amounts of HF suggests that the reactant 1,4-dioxaspiro[4.5]decan-8-one was wet and the residual moisture resulted in the production of HF. Presumably because of the moisture present in the reaction mixture and the small scale of this reaction, excess SOF_2 was also present and the integration value of one fluorine from 8,8-difluoro-1,4-dioxaspiro[4.5]decane to SOF_2 was 1 : 60.

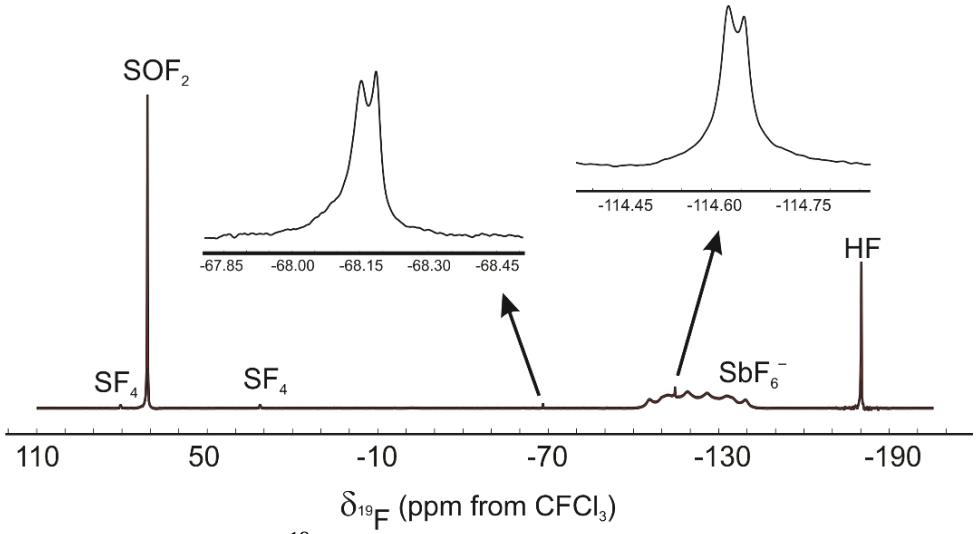

Figure 3.8 Solution-state ^{19}F NMR spectrum of 1,4-dioxaspiro[4.5]decan-8-one in $[SF_3][SbF_6]$, CsF using liquid CH_3CN as solvent at –30 °C.

3.4.3 Deoxofluorination of carboxylic acids (–COOH group) to acyl fluorides (–C(O)F group)

3.4.3.1 Deoxofluorination of pentafluorobenzoic acid

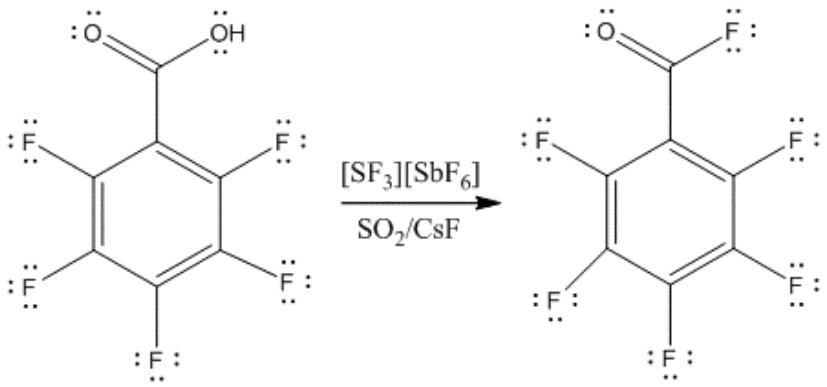

(3.4)

Pentafluorobenzoic acid and $[SF_3][SbF_6]$ were taken in a 1.1:1 ratio and CsF (carboxylic acid to CsF molar ratio of 1 : 0.7) using SO_2 solvent at ambient temperature. The production of pentafluorobenzoyl fluoride was confirmed by ^{19}F NMR spectroscopy (Figure 3.9). The triplet obtained at 35.1 ppm confirms the presence of –C(O)F group due to the coupling of fluorine of –C(O)F group to the two fluorine atoms in the ortho positions on the pentafluorobenzyl ring ($^3J(^{19}F–^1H)$ = 42.9 Hz). The multiplet at –133.7 ppm indicate two magnetically inequivalent ortho fluorines in pentafluorobenzoyl fluoride. The multiplets at –141.8 and –159.5 ppm represent the para and meta fluorines of pentafluorobenzoyl fluoride. The single peak at 74.6 ppm with isotopic shift for ^{34}S ($^1\Delta^{34}/^{32}S$ = –0.054 ppm) shows the presence of SOF_2 as a reaction product in agreement with the literature[16] while the broad signal at 35.1 ppm is indicative of excess SF_3^+ salt in the reaction mixture. The very broad signal at –121.1 ppm was observed for SbF_6^- anion. The integration values for the ortho, para and meta fluorine of pentafluorobenzoyl fluoride is 1.0 : 0.5 : 0.9 while for

SOF_2 is 3.4. The production of excess SOF_2 may be due to the reaction of excess $[SF_3][SbF_6]$ salt with traces of moisture present in the solvent.

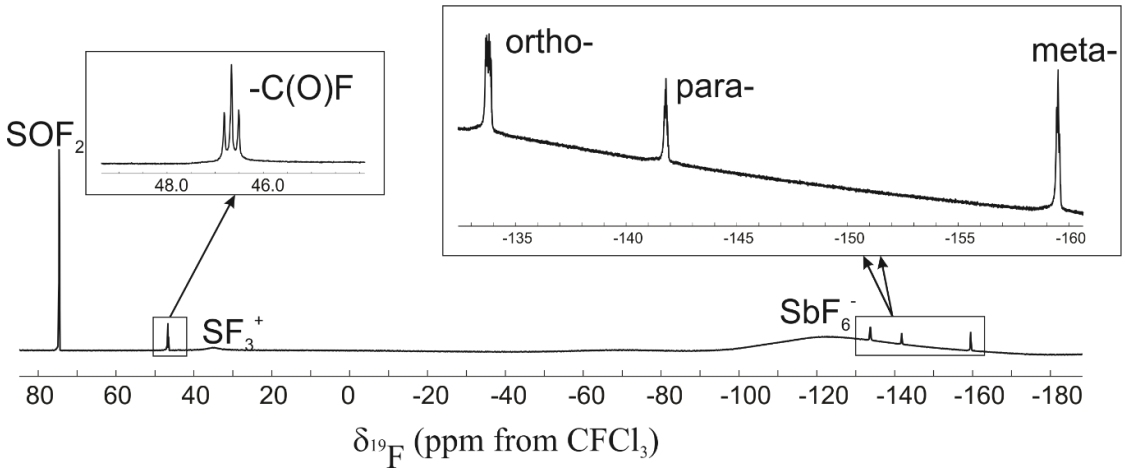

Figure 3.9 Solution-state ^{19}F NMR spectrum for production of pentafluorobenzoyl fluoride using $[SF_3][SbF_6]$, CsF in liquid SO_2 as solvent at ambient temperature.

3.4.3.2 Deoxofluorination of benzoic acid

Benzoic acid was combined with $[SF_3][SbF_6]$ in 1:1 ratio with CsF (carboxylic acid to CsF molar ratio of 1 : 0.7) using CH_3CN solvent at –20 °C. The singlet at 17.1 ppm in the ^{19}F NMR spectrum (Figure 3.10) can be assigned to the –C(O)F group of $C_6H_5C(O)F$, which is in agreement with the literature.[16] The singlet at 72.5 ppm represents the SOF_2 and the sextet and octet at –122.6 ppm represents the $^1J(^{121}Sb–^{19}F)$ and $^1J(^{123}Sb–^{19}F)$ coupling of the SbF_6^- anion signal. The coupling values for them were found to be 1935 Hz and 1049 Hz, respectively. These couplings have been observed in the HF solution of $NaSbF_6$ where the values for $^1J(^{121}Sb–^{19}F)$ and $^1J(^{123}Sb–^{19}F)$ were found to be 1945 ± 5 Hz and 1055 ± 5 Hz, respectively.[13] The integration value of –C(O)F signal with respect to SOF_2 (1.0 : 3.1) does not correlate well with the expected ratio of 1:2 and may be due to production of SOF_2 by the reaction of some SF_3^+ salt with the moisture in SO_2.

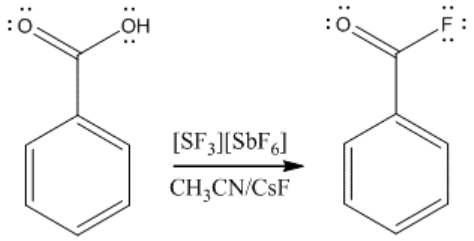

(3.5)

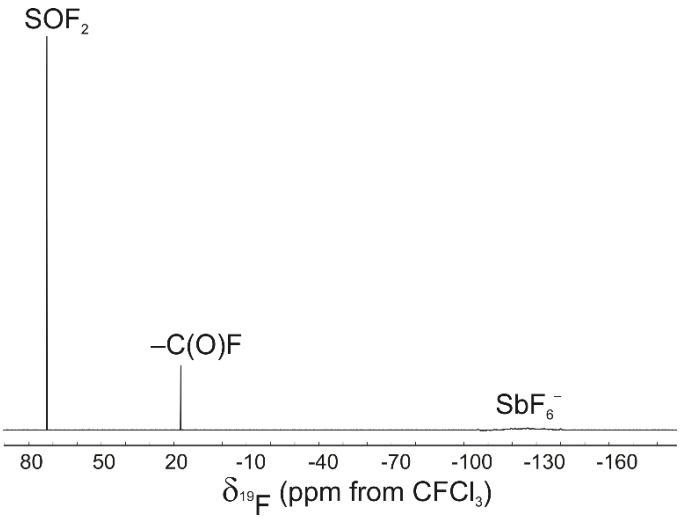

Figure 3.10 Solution-state ^{19}F NMR spectrum of benzoyl fluoride in $[SF_3][SbF_6]$, CsF using liquid CH_3CN as solvent at –20°C.

3.4.4 Deoxofluorination of alcohol

3.4..4.1 Deoxofluorination of cyclooctanol. Cyclooctanol was combined with $[SF_3][AsF_6]$ in a 1.1 : 1 ratio with CsF (alcohol to CsF molar ratio of 1 : 0.6) using liquid SO_2 as the solvent at ambient temperature. ^{19}F NMR spectroscopy (Figure 3.11) demonstrated the production of 1-fluorooctane as the product in the form of broad signal due to the viscous nature of the product in the form of oil at –158.5 ppm in agreement with the literature value (–159.0 ppm).[12] The $^3J(^1H–^{19}F)$ coupling was not observed because of the broadness of the resonance. The singlet at 74.9 ppm represents SOF_2 with characteristic sulfur isotopic peak and a broad signal at 63.3 ppm demonstrate the formation of SF_4. No $^1J(^{75}As–^{19}F)$ coupling was not observed because of the broad peak for AsF_6^- signal due to fast relaxation of the

quadrupolar ^{75}As nucleus. The integration value of 1-fluorooctane to SOF_2 was 5.1:1.0 and cannot be correlated. The reason may be the low solubility of SOF_2 in viscous solution.

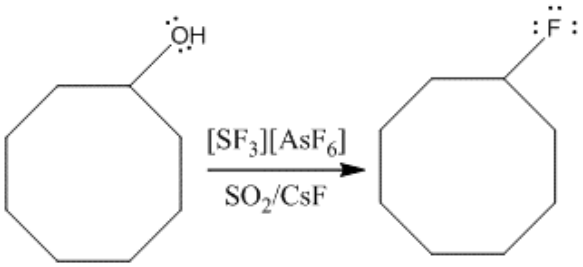

(3.6)

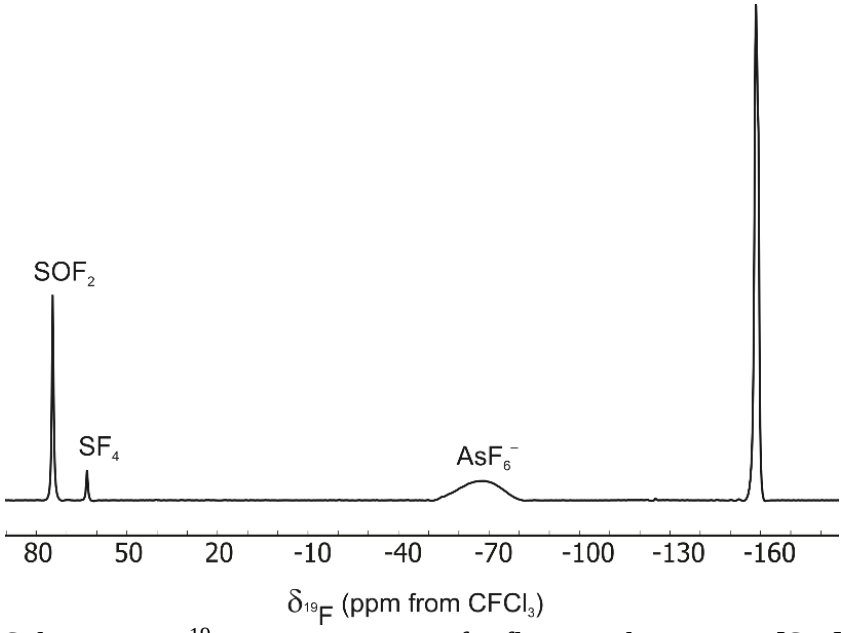

Figure 3.11 Solution-state ^{19}F NMR spectrum of 1-fluorocyclooctane in $[SF_3][AsF_6]$, CsF using liquid SO_2 as solvent at ambient temperature.

3.5 Conclusion and future directions

The crystal structures of two modifications of $[SF_3][SbF_6]$ (γ- and α-phases) and of $[SF_3][AsF_6]$ are being reported for the first time because of the difficulty present in the crystallization procedure. The scoping reactions for deoxofluorination of two ketones, two carboxylic acids and an alcohol have been carried out with $[SF_3][SbF_6]$ and $[SF_3][AsF_6]$ using SO_2, CH_3CN, and CH_2Cl_2 solvents. These reactions need to be further optimized and scaled up. Furthermore, the isolation of the products need to be done.

References

1. Azeem, M.; Brownstein, M.; Gillespie, R. J. *Can. J. Chem.* **1969**, *47*, 4159.

2. a. (i) Bartlett, N.; Robinson, P.L. *Chem. Ind. London.* **1956**, 1351. (ii) Bartlett, N.; Robinson, P. L. *J. Chem. Soc.* **1961**, 3417.
   b. Hasek, W. R.; Smith, W. C.; Engelhardt, V. A. *J. Am. Chem. Soc.* **1960**, 82, 543.

3. Oppegard, A. L.; Smith, W. C.; Muetterties, E. L.; Engelhardt, V. A. *J. Am. Chem. Soc.* **1960**, 82, 3835.

4. Holloway, J. H.; Rook, J. *J. Chem. Soc. Dalton Trans.* **1987**, 2285.

5. (i) Gibler, D. D.; Adams, C. J.; Fischer, M.; Zalkin, A.; Bartlett, N. *Inorg. Chem.* **1972**, *11*, 2325. (ii) Mallouk, T. E.; Bernard, D.; Bartlett, N. *Inorg. Chem.* **1984**, *23*, 3160 (iii) Mallouk, T. E.; Rosenthal, G. L.; Müller, G.; Brusasco, R.; Bartlett, N. *Inorg. Chem.* **1984**, *23*, 3167.

6. Chaudhary, P. Lewis-Acid and Fluoride-Ion Donor Properties of SF_4 and Solid-State NMR Spectroscopy of Me_3SnF, M.Sc. Thesis, University of Lethbridge, 2011.

7. Bondi, A. *J. Phys. Chem.*, **1964**, *68*, 441.

8. Johnson, J. P.; Murchie, M.; Passmore, J.; Mahmoud, T.; White, P. S.; Wong, C-M *Can. J. Chem.* **1987**, *65*, 2744.

9. (i) Peterkova, J.; Dusek, M.; Petricek, V.; Loub, J. *Acta Cryst.* **1998**, *B54*, 809.

   (ii) Smith, G. L.; Mercier, H. P. A.; Schrobilgen, G. *Inorg. Chem.* **2011**, *50*, 12359.

10. Datars, W. R.; Ummat, P. K. *Solid State Commun.* **1995**, *94*, 649.

11. Erhart, M.; Mews, R. *Z. Anorg. Allg. Chem.* **1992**, 615, 117.

12. Heureux, A. L.; Beaulieu,F; Bennett, C.; Bill, D. R; Clayton, S.; LaFlamme, F; Mirmehrabi, M.; Tadayon, S; Tovell, D.; Couturier, M. *J. Org. Chem.* **2010**, *75*, 3401.

13. Kidd, R. G; Matthews, R. W. *Inorg. Chem.* **1972**, *11*, 1156.

14. Kuster, R.; Drews, T.; Seppelt, K. *Inorg. Chem.* **2000**, *39*, 2784.

15. Morino, Y.; Kuchitsu, K.; Moritani, T. *Inorg. Chem.* **2000**, *8*, 867.

16. Gombler, W. *Z. Naturforsch.* **1985**, *40b*, 782.

Chapter-4

4. Synthesis and characterization of Lewis acid-base interactions between SF_3^+ and nitrogen bases

4.1 Introduction

Sulfur tetrafluoride is highly reactive in contrast to SF_6, which is inert because of its perfectly octahedral molecular geometry. Fluoride can be abstracted from SF_4 using strong Lewis acids such as BF_3, AsF_5, and SbF_5, yielding $[SF_3]^+$ salts. In the solid state, $[SF_3][SbF_6]$ and $[SF_3][AsF_6]$ were found to have contacts between sulfur and fluorine atoms of MF_6^- anion (M = Sb, As) that are significantly shorter than the sum of van der Waal's radii of sulfur and fluorine (See Chapter 3). In the case of γ-$[SF_3][SbF_6]$ and $[SF_3][AsF_6]$, the S---F contacts are as short as 2.502(1) and 2.494(3) Å, respectively. Such contacts have also been observed in solid $[SF_3][BF_4]$[1] and $[SF_3]_2[GeF_6]$.[2] These short contacts despite the relatively weakly coordinating nature of the MF_6^- anions (M = Sb, As) show the highly Lewis acidic nature of SF_3^+ cation. Recently, the weakly Lewis acidic SF_4 has conclusively been shown to form 1:1 Lewis acid-bases adducts with Lewis bases such as pyridine, 4-dimethylaminopyridine, 4-methylpyridine using low-temperature X-ray crystallography.[3] Because of the electron-poor nature of the SF_3^+ cation, Lewis acid-base adducts of the $[SF_3]^+$ cation with nitrogen bases are expected to be formed. Mews and coworker proposed the formation of $[SF_3(CH_3CN)][AsF_6]$ by the reaction of $[SF_3][AsF_6]$ with CH_3CN in SO_2 solvent at low-temperature (–30 °C) based on ^{19}F NMR chemical shifts which change from 30.5 ppm ($[SF_3][AsF_6]$ in SO_2) to 17.4 ppm up on addition of CH_3CN to the solution of $[SF_3][AsF_6]$ in SO_2.[4] Schrobilgen *et al.* have structurally characterized the 1:2 adduct of SF_3^+ and the N-base, $N{\equiv}SF_3$, by X-ray crystallography as the $[SF_3(NSF_3)_2][AsF_6]$ salt, which formed upon decomposition of $[F_4S{=}N{-}Xe{---}NSF_3][AsF_6]$ in an effort to grow

crystals of $[F_4S{=}N{-}Xe{---}NSF_3][AsF_6]$ from NSF_3 at 0 °C.[5] In addition, the $[SF_3(C_5H_5N)_2]^+$ and $[SF_3(CH_3CN)_2]^+$ cations have been detected by pentaquadrupole mass spectrometer (comprising of three Q1, Q3, Q5 mass analyzer quadrupoles and two Q2, Q4 reaction quadrupoles). These cationic adducts were generated by the reaction of the SF_3^+ cation, which was formed by electron ionization of SF_6 at 70 eV, with the nitrogen base in Q2.[6,7,8,9] These findings sparked the interest in synthesizing adducts of SF_3^+ in bulk and fully characterizing salts containing SF_3^+–nitrogen base adducts.

4.2 Results and discussion

4.2.1 Synthesis and properties of $[SF_3(C_5H_5N)_2][MF_6]$·solvent (M = Sb, As; solvent = CH_2Cl_2, C_5H_5N, CH_3CN), $[SF_3(CH_3CN)_2][MF_6]$ (M = Sb, As), and $[SF_3(phen)][SbF_6]\cdot 2CH_2Cl_2$

The $[SF_3(C_5H_5N)_2][MF_6]\cdot n C_5H_5N$ (M = Sb, As) salts were prepared by the reaction of $[SF_3][MF_6]$ salts with excess C_5H_5N at –40 °C according to equation 4.1. Excess pyridine was removed up to –30 °C under dynamic vacuum. The $[SF_3(C_5H_5N)_2][MF_6]\cdot n C_5H_5N$ salts were characterized by Raman in the solid state and NMR spectroscopy in solution. In the mass balance study, the molar ratio of $[SF_3][SbF_6]$ to pyridine was found to be 1 : 2.15, indicating the presence of additional, non-adducted pyridine in the solid, as observed by Raman spectroscopy and X-ray crystallography. This excess pyridine proved difficult to remove under dynamic vacuum even at 3 °C. These salts are of yellow color and are readily soluble in CH_2Cl_2, CH_3CN and SO_2, slightly soluble in THF and insoluble in toluene and $CFCl_3$. The $[SF_3(C_5H_5N)_2][SbF_6]\cdot n C_5H_5N$ salt is stable to 3 °C as shown by variable temperature Raman spectroscopy. Above 3 °C, the salt decomposes and turns to a brown-coloured

unidentified solid. The $[SF_3(C_5H_5N)_2][AsF_6]\cdot nC_5H_5N$ salt is stable only to –20 °C after which it turns to a brown color.

$$[SF_3][MF_6] + (2+n)\ C_5H_5N \xrightarrow{-40\ °C} [SF_3(C_5H_5N)_2][MF_6]\cdot nC_5H_5N \quad (M = Sb, As) \ldots.(4.1)$$

Crystallization of $[SF_3(C_5H_5N)_2][MF_6]$ (M = Sb, As) salts from CH_2Cl_2, and a C_5H_5N/CH_2Cl_2 solvent mixture at low-temperature furnished transparent crystals of $[SF_3(C_5H_5N)_2][MF_6]\cdot CH_2Cl_2$ and $[SF_3(C_5H_5N)_2][MF_6]\cdot C_5H_5N$ (M = Sb, As), respectively, in the form of needles. Crystal growth of $[SF_3(C_5H_5N)_2][SbF_6]$ from a mixture of CH_3CN and CH_2Cl_2 yielded crystals of $[SF_3(C_5H_5N)_2][SbF_6]\cdot CH_3CN$. It was observed that one solvent molecule is required for the crystallization of $[SF_3(C_5H_5N)_2][MF_6]$ salts. The solvent molecule is apparently required for efficient packing of the anions and cations in the solid state.

The $[SF_3(CH_3CN)_2][MF_6]$ salts are prepared by the reaction of $[SF_3][MF_6]$ (M = Sb, As) with excess CH_3CN at –40 °C according to equation 4.2. Excess acetonitrile was pumped off at –30 °C. These salts are of yellow colour and were characterized by Raman spectroscopy and X-ray crystallography in the solid state and ^{19}F NMR spectroscopy in solution. These salts are readily soluble in CH_2Cl_2 and SO_2, slightly soluble in THF and insoluble in toluene and $CFCl_3$. The $[SF_3(CH_3CN)_2][SbF_6]$ salt is stable to –20 °C based on Raman spectroscopy above which it turns into an unidentified brown solid.

$$[SF_3][MF_6] + 2CH_3CN \xrightarrow{-40\ °C} [SF_3(CH_3CN)_2][MF_6]\ (M = Sb, As) \quad \ldots\ldots\ldots\ldots(4.2)$$

The $[SF_3(phen)][SbF_6]\cdot 2CH_2Cl_2$ salt was prepared by the reaction of $[SF_3][SbF_6]$ salt and 1,10-phenanthroline in 1:1 ratio in CH_2Cl_2 solvent at –40 °C according to reaction equation 4.3. Excess CH_2Cl_2 was pumped off at –20 °C. This salt was characterized by Raman and solution NMR spectroscopy as well as by X-ray crystallography. This salt also is of yellow color and is readily soluble in CH_2Cl_2, CH_3CN and SO_2, slightly soluble in THF and insoluble in toluene and $CFCl_3$. Variable-temperature Raman spectroscopy shows that $[SF_3(phen)][SbF_6]\cdot 2CH_2Cl_2$ is stable to +15 °C. The chelating effect of bidentate 1,10-phenanthroline contributes to its stability at higher temperature compared to $[SF_3(C_5H_5N)_2][MF_6]$ and $[SF_3(CH_3CN)_2][MF_6]$ (M = Sb, As).

$$[SF_3][SbF_6] + \text{phen} + 2CH_2Cl_2 \xrightarrow[-40\ ^\circ C]{CH_2Cl_2} [SF_3(phen)][SbF_6]\cdot 2CH_2Cl_2 \quad \text{.....(4.3)}$$

where, phen = 1,10-Phenanthroline

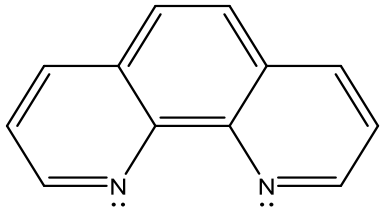

4.2.2 Synthesis and properties of $[SF_2(DMAP)_2][SbF_6]_2\cdot CH_3CN$ and crystal Growth of $[SF(DMAP)_4][SbF_6]_3\cdot 2CH_3CN$

The $[SF_2(DMAP)_2][SbF_6]_2\cdot CH_3CN$ salt was prepared by the reaction of $[SF_3][SbF_6]$ with DMAP in 1:1 ratio in excess CH_3CN at –40 °C according to reaction equation 4.4, followed by the removal of volatiles at –35 °C. This salt was characterized by X-ray crystallography and Raman spectroscopy in the solid state and by NMR spectroscopy in CH_3CN solvent. It is of intense yellow color and is readily soluble in CH_2Cl_2, CH_3CN and SO_2 and insoluble in toluene and $CFCl_3$. Surprisingly, no evidence for the $[SF_3(DMAP)_2]^+$ cation was observed by Raman and solution NMR spectroscopy at temperatures as low as –40 °C, even when using a

1:2 molar ratio of $[SF_3][SbF_6]$ to DMAP. The $[SF_3(DMAP)_2]^+$ cation is supposedly unstable and decomposes rapidly into $[SF_2(DAMP)_2]^{2+}$ and SF_4 (Eq 4.5). The stoichiometry of the products of the reaction equation 4.5 has been confirmed by ^{19}F NMR spectroscopy (vide infra).

$$2[SF_3][SbF_6] + 2DMAP \xrightarrow[-40\ °C]{CH_3CN} [SF_2(DMAP)_2][SbF_6]_2{\cdot}CH_3CN + SF_4 \quad \text{.....(4.4)}$$

where, DMAP = 4-dimethylaminopyridine 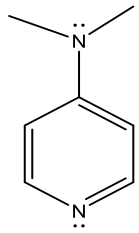

$$2[SF_3(DAMP)_2]^+ \longrightarrow [SF_2(DAMP)_2]^{2+} + SF_4 \quad \text{.....(4.5)}$$

Crystals of $[SF(DMAP)_4]_2[SbF_6]_3{\cdot}2CH_3CN$ were obtained by the reaction of $[SF_3][SbF_6]$ salt with DMAP in 1:2 ratio in excess CH_3CN at –40 °C, in an attempt to grow crystals of $[SF_2(DMAP)_2][SbF_6]_2$ from CH_3CN solvent. Excess acetonitrile was pumped off to –28 °C. The $[SF(DAMP)_4]^{3+}$ cation presumably forms in a ligand transfer reaction from $[SF_2(DAMP)_2]^{2+}$ according to equation 4.6.

$$3[SF_2(DAMP)_2]^{2+} \longrightarrow [SF(DAMP)_4]^{3+} + 2SF_4 + 2DMAP \quad \text{.....(4.6)}$$

4.2.3 X-ray Crystallography

4.2.3.1 X-ray crystallography of $[SF_3(C_5H_5N)_2][MF_6]$·solvent (M = Sb, As; solvent = CH_2Cl_2, C_5H_5N, CH_3CN).

The $[SF_3(C_5H_5N)_2][MF_6]·CH_2Cl_2$, $[SF_3(C_5H_5N)_2][MF_6]·C_5H_5N$ (M = Sb, As) and $[SF_3(C_5H_5N)_2][SbF_6]·CH_3CN$ salts were characterized by single-crystal X-ray diffraction. It was observed that $[SF_3(C_5H_5N)_2][MF_6]$ (M = Sb, As) salts crystallized with a solvent of crystallization such as C_5H_5N, CH_3CN and CH_2Cl_2. The two $[SF_3(C_5H_5N)_2][MF_6]·CH_2Cl_2$ salts with M = Sb, As were found to be isostructural, crystallizing in the monoclinic *C*2/*c* space group with four formula units in the unit cell. The two $[SF_3(C_5H_5N)_2][MF_6]·C_5H_5N$ (M = Sb, As) salts were also isostructural, crystallizing in the monoclinic *C*2/*c* space group with eight formula units of in the unit cell. The $[SF_3(C_5H_5N)_2SbF_6]·CH_3CN$ salt crystallizes in triclinic $P\bar{1}$ space group with two formula units of $[SF_3(C_5H_5N)_2SbF_6]·CH_3CN$ in the unit cell. The structural units in the X-ray crystal structures of $[SF_3(C_5H_5N)_2][SbF_6]·CH_2Cl_2$, $[SF_3(C_5H_5N)_2][SbF_6]·C_5H_5N$ and $[SF_3(C_5H_5N)_2][SbF_6]·CH_3CN$ salts are shown in Figures 4.1, 4.2 and 4.3, respectively. A summary of the refinement results and other crystallographic data has been given in Table 4.1. Selected bond lengths, contact distances, and bond angles are given in Tables 4.2, 4.3 and 4.4.

Table 4.1. Crystallographic data for $[SF_3(C_5H_5N)_2][MF_6]\cdot CH_2Cl_2$ (M = Sb, As), $[SF_3(C_5H_5N)_2][MF_6]\cdot C_5H_5N$ (M = Sb, As), $[SF_3(C_5H_5N)_2][SbF_6]\cdot CH_3CN$, and $[SF_3(CH_3CN)_2][SbF_6]$.

Chemical formula	$[SF_3(C_5H_5N)_2][SbF_6]\cdot CH_2Cl_2$	$[SF_3(C_5H_5N)_2][AsF_6]\cdot CH_2Cl_2$	$[SF_3(C_5H_5N)_2][SbF_6]\cdot CH_3CN$	$[SF_3(C_5H_5N)_2][SbF_6]\cdot C_5H_5N$	$[SF_3(C_5H_5N)_2][AsF_6]\cdot C_5H_5N$
Crystal system	Monoclinic	Monoclinic	Triclinic	Monoclinic	Monoclinic
Space group	*C2/c*	*C2/c*	*P –1*	*C2/c*	*C2/c*
a (Å)	10.9125(14)	10.836(3)	7.6726(19)	26.913(4)	26.694(11)
b (Å)	12.6405(16)	12.472(3)	9.059(2)	8.5679(11)	8.517(3)
c (Å)	14.3435(19)	14.118(3)	14.157(4)	18.443(2)	17.978(7)
α (°)	90	90	71.383(3)	90	90
β (°)	108.040(10)	107.463(3)	78.418(3)	125.151(10)	124.422(5)
γ (°)	90	90	79.548(3)	90	90
Z	4	4	2	8	8
Formula weight (g mol^{-1})	567.94	392.53	524.06	562.12	515.28
Calcd density (g cm^{-3})	1.5826	1.8328	1.8497	2.0690	1.9541
T (°C)	–120	–120	–120	–120	–120
μ (mm^{-1})	3.855	4.384	3.396	2.085	2.244
R_1[a]	0.0240	0.0474	0.0402	0.0263	0.0326
wR_2[b]	0.0548	0.1389	0.1094	0.0714	0.0655

[a] R_1 is defined as $\Sigma||F_o| - |F_c||/\Sigma|F_o|$ for $I > 2\sigma(I)$. [b] wR_2 is defined as $[\Sigma[w(F_o^2 - F_c^2)^2]/\Sigma w(F_o^2)^2]^{½}$ for $I > 2\sigma(I)$.

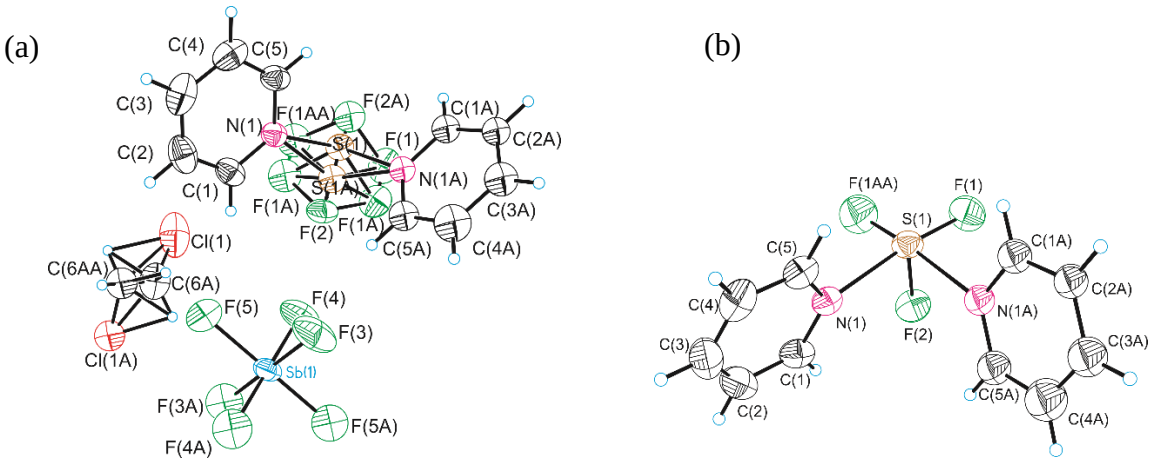

Figure 4.1 The thermal ellipsoid plots of (a) structural unit in the X-ray crystal structure of $[SF_3(C_5H_5N)_2][SbF_6]\cdot CH_2Cl_2$ in the crystal of $[SF_3(C_5H_5N)_2][SbF_6]\cdot CH_2Cl_2$ and (b) one component of the disordered $[SF_3(C_5H_5N)_2]^+$ cation. Thermal ellipsoids are drawn at the 50% probability level.

Table 4.2 Bond lengths (Å) and bond angles (°) for $[SF_3(C_5H_5N)_2][MF_6]\cdot CH_2Cl_2$ (M = Sb, As)

Bond lengths (Å) and bond angles (°)			
$[SF_3(C_5H_5N)_2][SbF_6]\cdot CH_2Cl_2$		$[SF_3(C_5H_5N)_2][AsF_6]\cdot CH_2Cl_2$	
S1-F1	1.614(4)	S1-F1	1.617(6)
S1-F2	1.573(4)	S1-F2	1.566(4)
S1-F1A	1.608(4)	S1-F1A	1.620(4)
S1-N1	2.106(2)	S1-N1	2.098(2)
S1-N1A	2.124(2)	S1-N1A	2.106(2)
Sb1-F3	1.8585(13)	As1-F3	1.706(3)
Sb1-F4	1.8651(13)	As1-F4	1.713(3)
Sb1-F5	1.8633(16)	As1-F5	1.707(3)
F1-S1-F2	89.47(18)	F1-S1-F2	90.6(3)
F2-S1-F1A	90.10(17)	F2-S1-F1A	90.5(4)
F1-S1-F1A	90.86(13)	F1-S1-F1A	90.5(3)
N1-S1-N1A	90.30(9)	N1-S1-N1A	90.67(18)
F3-Sb1-F4	90.68(7)	F3-As1-F5	90.25(16)
F3-Sb1-F5	90.11(8)	F4-As1-F5	90.35(18)
F4-Sb1-F5	90.17(8)	F3-As1-F4	90.47(19)

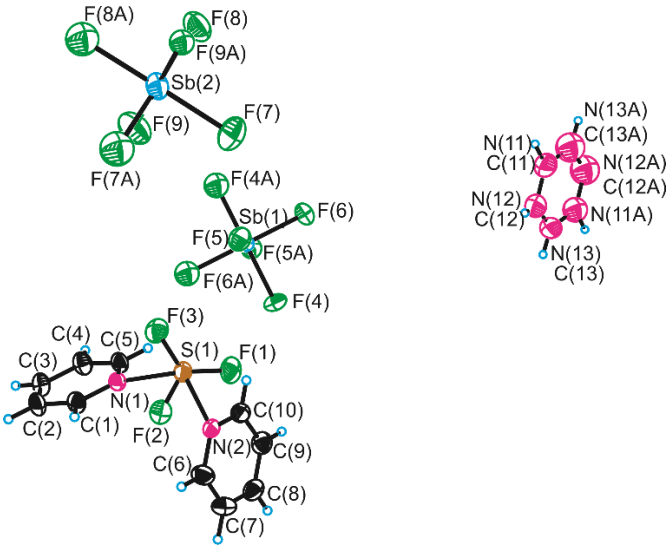

Figure 4.2 Thermal ellipsoid plot of the $[SF_3(C_5H_5N)_2][SbF_6]\cdot C_5H_5N$ structural unit in the crystal of $[SF_3(C_5H_5N)_2][SbF_6]\cdot C_5H_5N$. Thermal ellipsoids are drawn at the 50% probability level.

Table 4.3 Bond lengths (Å) and bond angles (°) for $[SF_3(C_5H_5N)_2][MF_6]\cdot C_5H_5N$ (M = Sb, As)

Bond lengths (Å) and bond angles (°)			
$[SF_3(C_5H_5N)_2][SbF_6]\cdot C_5H_5N$		$[SF_3(C_5H_5N)_2][AsF_6]\cdot C_5H_5N$	
S1-F1	1.6000(12)	S1-F1	1.628(4)
S1-F2	1.5609(12)	S1-F2	1.584(4)
S1-F3	1.6288(13)	S1-F3	1.564(4)
S1---N1	2.1421(16)	S1---N1	2.154(5)
S1---N2	2.0613(16)	S1---N2	2.052(5)
Sb1-F4	1.8758(11)	As1-F7	1.719(4)
Sb1-F5	1.8712(12)	As1-F8	1.715(3)
Sb1-F6	1.8794(12)	As1-F9	1.704(3)
Sb2-F7	1.8761(12)	As2-F4	1.718(3)
Sb2-F8	1.8732(12)	As2-F5	1.705(4)
Sb2-F9	1.8721(12)	As2-F6	1.708(3)
F1-S1-F2	90.08(7)	F1-S1-F2	90.8(2)
F1-S1-F3	90.75(7)	F1-S1-F3	88.5(2)
F2-S1-F3	88.64(7)	F2-S1-F3	89.8(2)
N1-S1-N2	89.40(6)	N1-S1-N2	88.46(19)
F4-Sb1-F5	90.05(6)	F7-As1-F8	90.08(17)
F4-Sb1-F6	90.06(6)	F7-As1-F9	90.08(18)
F5-Sb1-F6	91.38(6)	F9-As1-F8	90.27(17)
F7-Sb2-F8	89.92(6)	F4-As2-F5	89.83(17)
F7-Sb2-F9	89.73(6)	F4-As2-F6	90.19(16)
F8-Sb2-F9	90.48(6)	F5-As2-F6	89.86(17)

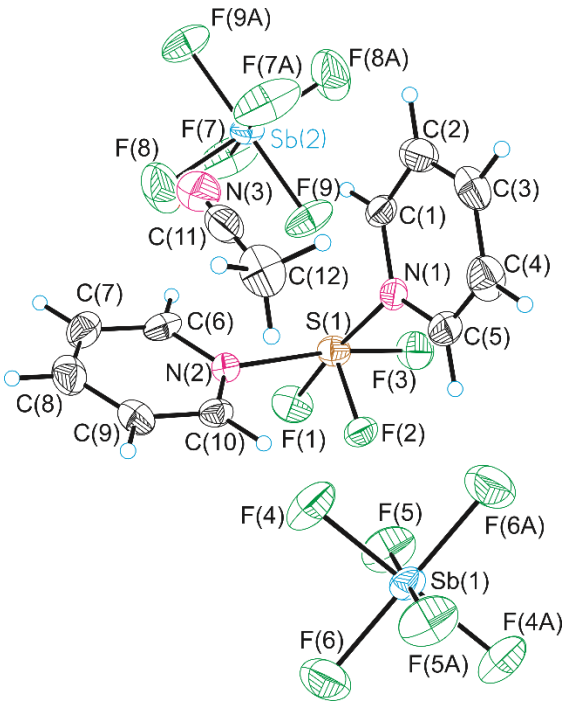

Figure 4.3 Thermal ellipsoid plot of the $[SF_3(C_5H_5N)_2][SbF_6]\cdot CH_3CN$ structural unit in the crystal of $[SF_3(C_5H_5N)_2][SbF_6]\cdot CH_3CN$. Thermal ellipsoids are drawn at the 50% probability level.

Table 4.4 Bond lengths (Å) and bond angles (°) for $[SF_3(C_5H_5N)_2][SbF_6]\cdot CH_3CN$

Bond lengths (Å)		Bond angles (°)	
S1-F1	1.627(3)	F1-S1-F2	88.68(17)
S1-F2	1.559(3)	F2-S1-F3	90.06(16)
S1-F3	1.600(3)	F1-S1-F3	90.85(18)
S1-N1	2.062(4)	N1-S1-N2	89.52(16)
S1-N2	2.143(4)		
Sb1-F4	1.865(3)	F4-Sb1-F5	90.64(16)
Sb1-F6	1.868(3)	F4-Sb1-F6	90.08(18)
Sb1-F5	1.875(3)	F5-Sb1-F6	90.36(17)
Sb2-F7	1.855(3)	F7-Sb2-F8	90.10(2)
Sb2-F8	1.855(4)	F7-Sb2-F9	90.54(16)
Sb2-F9	1.876(3)	F8-Sb2-F9	90.42(19)

In $[SF_3(C_5H_5N)_2][MF_6]\cdot CH_2Cl_2$ (M = Sb, As), the $[SF_3(C_5H_5N)_2]^+$ cation and the CH_2Cl_2 molecule are positionally disordered along a C_2 axis (50:50% disorder). The disorder in the $[SF_3(C_5H_5N)_2]^+$ cation was modeled by defining two orientations of the SF_3 moieties in which the axial fluorine atom points to opposite sides. A disorder in the two pyridine moieties of the $[SF_3(C_5H_5N)_2]^+$ cation could not be resolved. The disorder in the CH_2Cl_2 molecule was modelled by defining two positions for carbon (and as a consequence two positions for the hydrogen atoms). The two chlorine atoms in CH_2Cl_2 were not split in the disorder model and were taken as the pivot points. In $[SF_3(C_5H_5N)_2][MF_6]\cdot C_5H_5N$ (M = Sb, As), the cation was ordered, while the solvent C_5H_5N molecule, which is situated on a crystallographic inversion centre, exhibits a six-fold rotational disorder along the axis perpendicular to the molecular plane. The crystal structure of $[SF_3(C_5H_5N)_2][SbF_6]\cdot CH_3CN$ is the only structure in this series that does not exhibit any disorder.

The $[SF_3(C_5H_5N)_2]^+$ cation adopts a square pyramidal molecular geometry in all of the above mentioned salts in accord with an AX_3Y_2E VSEPR geometry having six electron pairs about sulfur. Two fluorine atoms and the two pyridine molecules are located in the equatorial position while one fluorine occupies the axial position, *trans* to the lone pair. In Table 4.5, selected metric parameters of the $[SF_3(C_5H_5N)_2]^+$ cation are compared with those of other square pyramidal sulfur species, the SF_5^- anion and the $[SF_3(NSF_3)_2]^+$ cation. The F–S–F angles about sulfur in the $[SF_3(C_5H_5N)_2]^+$ cation are quite close to 90°. Such angles reflect a substantial geometry change of the SF_3 moiety upon adduct formation with pyridine (γ-$[SF_3][SbF_6]$ 97.23(7), 97.05(8), 97.94(7)°), $[SF_3][AsF_6]$ (97.16(18), 97.91(17), 98.36(18), 97.56(17)°), and $[SF_3][BF_4]$ (97.62(7), 97.39(12)°). In the $[SF_3(C_5H_5N)_2]^+$ cation, the axial S–F bond length is significantly shorter than the equatorial S–F bond lengths ($[SF_3(C_5H_5N)_2][SbF_6]\cdot CH_2Cl_2$: F_{ax} 1.573(4), F_{eq} 1.608(4)/1.614(4) Å;

$[SF_3(C_5H_5N)_2][AsF_6]\cdot CH_2Cl_2$: F_{ax} 1.566(4), F_{eq} 1.617(4)/1.620(4) Å; $[SF_3(C_5H_5N)_2][SbF_6]\cdot C_5H_5N$: F_{ax} 1.5609(12), F_{eq} 1.6000(12)/1.6288(13) Å; $[SF_3(C_5H_5N)_2][AsF_6]\cdot C_5H_5N$: F_{ax} 1.584(4), F_{eq} 1.628(4)/1.564(4) Å; $[SF_3(C_5H_5N)_2][SbF_6]\cdot CH_3CN$: F_{ax} 1.559(3), F_{eq} 1.600(3)/1.627(3) Å). The same has been observed for the SF_5^- anion in $[Rb][SF_5]$ salt[10] with the axial and equatorial bond lengths being 1.559(15) Å and 1.707(14)/1.729(13) Å, respectively. Upon complexation of the SF_3^+ cation by pyridine, all S−F bond lengths are elongated, reflecting more ionic S−F bonds upon donation of electron density to sulfur (γ-$[SF_3][SbF_6]$: 1.501(1) to 1.509(1) Å; $[SF_3][AsF_6]$: 1.501(3) to 1.510(3) Å; $[SF_3(C_5H_5N)_2]^+$: 1.559(3) to 1.729(13) Å). When compared to the adduct with a much weaker Lewis base, NSF_3, the axial and equatorial bond lengths are longer in the $[SF_3(C_5H_5N)_2]^+$ than the corresponding axial and equatorial bond lengths found in $[SF_3(NSF_3)_2][AsF_6]$ salt (1.511(1), 1.520(1) and 1.519(1) Å) (Table 4.5), also reflecting the larger electron donating power of pyridine than NSF_3.[11]

Table 4.5 Comparison of distances and angles in different fluorosulfur(IV) compounds

Compound	Distance (Å)		Distance (Å)	Distance (Å)	Angle(s) (°)		Angle(s) (°)	Ref[a]
	$S–F_{ax}$	$S–F_{eq}$	S···N	S···F	$F_{ax}–S–F_{eq}$	$F_{eq}–S–F_{eq}$	$N_1–S–N_2$	
$[Rb][SF_5]$	1.559(15)	1.707(14) 1.729(13)						33
$[SF_3(NSF_3)_2][AsF_6]$	1.511(1)	1.519(1) 1.520(1)	2.511(2) 2.554(2)	2.558(2)	96.2(1) 96.8(1)	96.3(1)	96.3(1)	31
$[SF_3(CH_3CN)_2][SbF_6]$	1.505(2)	1.5104(16) 1.5104(16)	2.458(3) 2.458(3)	2.616(3)	96.38(7) 96.38(7)	94.90(14)	101.3(4)	PW
$[SF_3(Py)_2][SbF_6]\cdot CH_2Cl_2$	1.573(4)	1.614(4) 1.608(4)	2.106(2), 2.124(2)	3.324(9)	89.5(2) 90.1(2)	90.9(2)	90.30(9)	PW
$[SF_3(Py)_2][AsF_6]\cdot CH_2Cl_2$	1.566(4)	1.617(4) 1.620(4)	2.087(4) 2.094(4)	3.417(5)	90.5(3) 90.5(3)	90.5(3)	90.68(18)	PW
$[SF_3(Py)_2][SbF_6]\cdot CH_3CN$	1.559(3)	1.627(3) 1.600(3)	2.143(4) 2.063(5)	3.056(4)	88.7(2) 90.1(2)	90.9(2)	89.52(16)	PW
$[SF_3(Py)_2][SbF_6]\cdot C_5H_5N$	1.5609(12)	1.6000(12) 1.6288(13)	2.1421(16) 2.0613(16)	3.304(9)	88.65(7) 90.09(7)	90.76(8)	89.40(6)	PW
$[SF_3(Py)_2][AsF_6]\cdot C_5H_5N$	1.564(4)	1.584(4) 1.628(4)	2.154(5) 2.052(5)	3.252(5)	88.5(2) 89.8(2)	90.8(2)	88.46(19)	PW
$[SF_3(Phen)][SbF_6]\cdot 2CH_2Cl_2$	1.554(2)	1.613(3) 1.601(3)	2.140(3) 2.111(3)	3.015(3)	89.7(1) 88.9(1)	93.7(1)	78.37(12)	PW
$[SF_2(DMAP)_2][SbF_6]_2\cdot CH_3CN$	1.701(4) 1.701(4)		1.724(5) 1.724(5)	4.297			100.4(3)	PW
$[SF(DMAP)_4]_2[SbF_6]_3\cdot 2CH_3CN$	1.594(8)		2×1.878(7) 2×1.924(7)	3.500			90.0(3)	PW

[a]PW-Present Work

The coordination of the two pyridine ligands to sulfur is slightly unsymmetrical (the S---N distances for $[SF_3(C_5H_5N)_2][SbF_6]\cdot CH_2Cl_2$ and $[SF_3(C_5H_5N)_2][AsF_6]\cdot CH_2Cl_2$ are 2.106(2)/2.124(2) Å and 2.098(2)/2.106(2) Å, respectively). For the structures that incorporate a pyridine and acetonitrile of crystallization, the asymmetry is somewhat more pronounced: 2.1421(16)/2.0613(16) Å ($[SF_3(C_5H_5N)_2][SbF_6]\cdot C_5H_5N$), 2.154(5)/2.052(5) Å ($[SF_3(C_5H_5N)_2][AsF_6]\cdot C_5H_5N$), and 2.062(4)/2.143(4) Å ($[SF_3(C_5H_5N)_2][SbF_6]\cdot CH_3CN$). A significant asymmetry of S---N distances has been predicted by computational means for the isolated cation in the gas phase with distances of 2.28 and 2.44 Å.[7] All of these S---N distances are shorter than the sum of van der Waal's radii of sulfur and nitrogen (3.35 Å)[12] and considerably shorter than what has been found in $SF_4\cdot NC_5H_5$ adduct[3] (2.5138(18) Å) indicating a strong coordination of C_5H_5N with SF_3^+ cation in $[SF_3(C_5H_5N)_2][MF_6]\cdot$Solvent. This is expected due to SF_3^+ being more Lewis acidic than SF_4. The shortest S···F cation-anion distances in the $[SF_3(C_5H_5N)_2][MF_6]$ (M = Sb, As) salts are longer or close to the limit of the sum of the van der Waal's radii, i.e., 3.27 Å,[12] (3.324(9) Å, in $[SF_3(C_5H_5N)_2][SbF_6]\cdot CH_2Cl_2$ and 3.417(5) Å in $[SF_3(C_5H_5N)_2][AsF_6]\cdot CH_2Cl_2$), indicating well separated anions and cations in these structures. With two dative bonds from the nitrogen of C_5H_5N, the coordination sphere about sulfur in $[SF_3(C_5H_5N)_2][MF_6]\cdot CH_2Cl_2$ (M = Sb, As) and $[SF_3(C_5H_5N)_2][MF_6]\cdot C_5H_5N$ (M = Sb, As) salts is expanded increasing the total coordination number of sulfur to five and sufficiently saturated that no further donation of electron density is needed. The MF_6^- (M = Sb, As) anion in these salts have approximate octahedral geometries.

4.2.3.2 X-ray crystallography of $[SF_3(CH_3CN)_2][SbF_6]$

The $[SF_3(CH_3CN)_2][SbF_6]$ salt crystallizes in the orthorhombic space group *Pnma* with four formula units of $[SF_3(CH_3CN)_2][SbF_6]$ in the unit cell. A summary of the refinement results and other crystallographic data has been given in Table 4.6. Selected bond lengths, contact distances, and angles are given in Table 4.7. Unlike the $[SF_3(C_5H_5N)_2]^+$ salts, the $[SF_3(CH_3CN)_2]^+$ salt crystallizes without any solvent of crystallization. In the crystal structure of $[SF_3(CH_3CN)_2][SbF_6]$ (Figure 4.4), the $[SF_3(CH_3CN)_2]^+$ cation lies on a crystallographic mirror plane and has a distorted square pyramidal geometry. Two fluorine atoms of $[SF_3(CH_3CN)_2]^+$ cation are in the equatorial position (S–F distance, 2 × 1.5104(16) Å) along with two CH_3CN molecules (S---N distance, 2 × 2.458(3) Å), which are shorter than the sum of van der Waal's radii of sulfur and nitrogen (3.35 Å)[12], while one of the fluorine is in the axial position with the S–F bond length of 1.505(2) Å. These S–F bond lengths are of the same size as those present in γ-$[SF_3][SbF_6]$ (1.501(1) to 1.509(1) Å) showing the small effect of the CH_3CN coordination. The F–S–F angles in $[SF_3(CH_3CN)_2]^+$ cation (94.90(14), 2×96.38(7)°) are somewhat smaller than those in γ-$[SF_3][SbF_6]$ salt (97.05(8), 97.23(7) and 97.94(7)°) as a result of the coordination of two CH_3CN molecules. In addition to two dative bonds with the nitrogen of CH_3CN, the coordination sphere about S in $[SF_3(CH_3CN)_2]^+$ is expanded by a S···F contact to one fluorine atom of an adjacent SbF_6^- anion (2.616(3) Å), which is significantly shorter than the sum of van der Waal's radii (3.27 Å).[12] As a result, the total coordination number about sulfur becomes six. The long sulfur-fluorine contact between $[SF_3(CH_3CN)_2]^+$ and SbF_6^-, i.e., 2.616(3) Å, in this structure is about the same length as those found in γ-$[SF_3][SbF_6]$ (2.660(1), 2.517(1) and 2.502(1) Å). In the SbF_6^- anion, one of the Sb–F distance (1.891(2) Å) is significantly

longer than the other Sb–F distances (1.8280(18) to 1.861(2) Å) because of the stronger interaction of this fluorine atom towards sulfur.

The S–F bond lengths and the S–N interactions are different in $[SF_3(CH_3CN)_2][SbF_6]$ compared to those in the $[SF_3(C_5H_5N)_2][SbF_6]$·Solvent structures. The S–F bond lengths in the $[SF_3(C_5H_5N)_2][SbF_6]\cdot C_5H_5N$ crystal structures (1.5609(12), 1.6000(12) and 1.6288(13) Å) are longer as compared to the S–F bond lengths in the $[SF_3(CH_3CN)_2][SbF_6]$ (2×1.5104(16) and 1.505(2) Å) and the S---N bond lengths are shorter ($[SF_3(C_5H_5N)_2][SbF_6]\cdot C_5H_5N$: 2.1421(16) to 2.0613(16) Å) as a result of the stronger Lewis basicity of C_5H_5N compared to that of CH_3CN. As a consequence of the weaker electron donating effect of CH_3CN, the sulfur has one additional S···F contact in the CH_3CN adduct, which has also been observed in the crystal structure of $[SF_3(NSF_3)_2][AsF_6]$.

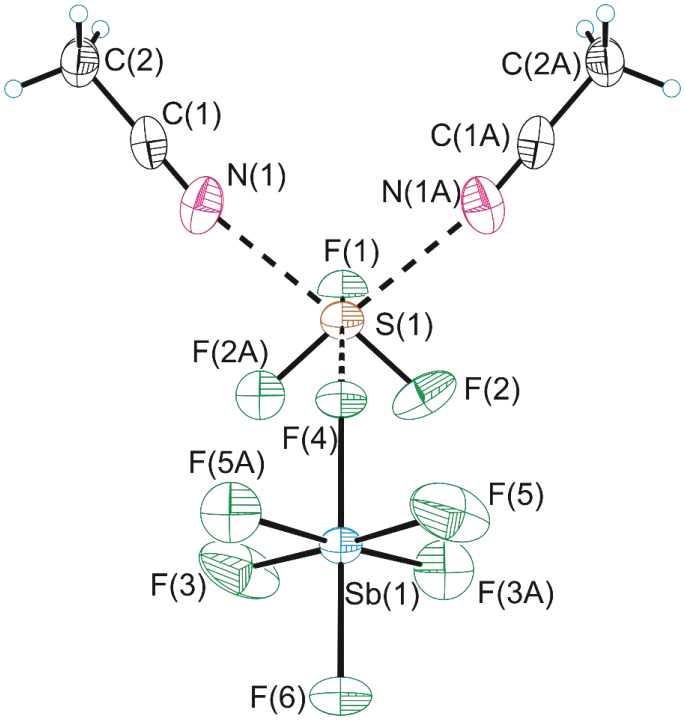

Figure 4.4 Thermal ellipsoid of the cation anion pair in the X-ray crystal structure of $[SF_3(CH_3CN)_2][SbF_6]$. Thermal ellipsoids are drawn at the 50% probability level.

Table 4.6. Crystallographic data for $[SF_3(CH_3CN)_2][SbF_6]$ and $SF_3(Phen)][SbF_6]\cdot 2CH_2Cl_2$, $[SF_2(DMAP)_2][SbF_6]_2\cdot CH_3CN$ and $[SF(DMAP)_4][SbF_6]_3\cdot 2CH_3CN$ salts

Chemical formula	$[SF_3(CH_3CN)_2][SbF_6]$	$[SF_3(Phen)][SbF_6]\cdot 2CH_2Cl_2$	$[SF_2(DMAP)_2][SbF_6]_2\cdot CH_3CN$	$[SF(DMAP)_4][SbF_6]_3\cdot 2CH_3CN$
Crystal system	Orthorhombic	Monoclinic	Monoclinic	Monoclinic
space group	*Pnma*	$P2_1/c$	*C*2/*c*	*C*2/*c*
a (Å)	13.560(13)	7.6726(19)	12.806(8)	16.0316(18)
b (Å)	12.727(13)	9.059(2)	10.699(7)	17.4013(19)
c (Å)	6.999(7)	14.157(4)	22.056(15)	19.832(2)
α (°)	90	90	90	90
β (°)	90	94.5460(10)	107.463(3)	107.4588(14)
γ (°)	90	90	90	90
Z	4	4	4	4
Formula weight (g mol^{-1})	406.91	684.922	814.948	1868.852
Calcd density (g cm^{-3})	2.1634	1.9658	1.8038	2.2667
T (°C)	–120	–120	–120	–120
μ (mm^{-1})	3.805	1.891	3.193	2.333
R_1[a]	0.0252	0.0426	0.0497	0.0808
wR_2[b]	0.0811	0.0882	0.0933	0.1552

[a] R_1 is defined as $\Sigma||F_o| - |F_c||/\Sigma|F_o|$ for $I > 2\sigma(I)$. [b] wR_2 is defined as $[\Sigma[w(F_o^2 - F_c^2)^2]/\Sigma w(F_o^2)^2]^{½}$ for $I > 2\sigma(I)$.

Table 4.7 Bond lengths (Å) and bond angles (°) for $[SF_3(CH_3CN)_2][SbF_6]$

Bond Lengths (Å)		Bond Angles (°)	
S1-F1	1.505(2)	F1-S1-F2	96.38(7)
S1-F2	1.5104(16)	F1-S1-F2A	96.38(7)
S1-F2A	1.5104(16)	F2-S1-F2A	94.90(14)
S1-N1	2.458(3)	N1-S1-N1A	101.3(4)
S1-N1A	2.458(3)	N1-C1-C2	179.5(3)
Sb1-F3	1.8280(18)	F3-Sb1-F5	90.24(12)
Sb1-F4	1.891(2)	F3-Sb1-F6	90.55(7)
Sb1-F5	1.8410(17)	F5-Sb1-F6	91.55(7)
Sb1-F6	1.861(2)	F4-Sb1-F5	89.14(6)
		F3-Sb1-F4	88.78(6)

4.2.3.3 X-ray crystallography of $[SF_3(phen)][SbF_6]\cdot 2CH_2Cl_2$

The $[SF_3(phen)][SbF_6]\cdot 2CH_2Cl_2$ crystallizes in the monoclinic space group $P2_1/c$ with four formula units in the unit cell. A summary of the refinement results and other crystallographic data has been given in Table 4.6. Selected bond lengths and bond angles are given in Table 4.8. The structural unit in the X-ray crystal structure of $[SF_3(phen)][SbF_6]\cdot 2CH_2Cl_2$ is shown in Figure 4.5. In the crystal structure of $[SF_3(phen)][SbF_6]\cdot 2CH_2Cl_2$, the $[SF_3(phen)]^+$ cation is square pyramidal with two equatorial S–F bonds (1.601(3) and 1.613(3) Å), two S---N coordinate bonds (2.140(3) and 2.111(3) Å), and one axial S–F bond length of 1.554(2) Å. The S–F bond lengths in the $[SF_3(phen)]^+$ cation are longer than those present in γ-$[SF_3][SbF_6]$ (1.501(1) to 1.509(1) Å). The angles about sulfur are close to 90°, as found for the $[SF_3(C_5H_5N)_2]^+$ cation, although the bidentate nature of 1,10-phenanthroline constrains the N−S−N angle in the equatorial plane (Table 4.5). The closest S···F cation anion distance is 3.015(3) Å, which is close to the sum of van der Waal's radii of sulfur and fluorine (3.27 Å).[12] This very weak contact

does not have any significant influence on the cation geometry, as indicated by the bond angles in the $[SF_3(phen)]^+$ cation.

Table 4.8 Bond lengths (Å) and bond angles (°) for $[SF_3(phen)][SbF_6]\cdot 2CH_2Cl_2$

Bond lengths (Å)		Bond angles (°)	
S1-F1	1.613(3)	F1-S1-F2	88.90(13)
S1-F2	1.554(2)	F2-S1-F3	89.71(14)
S1-F3	1.601(3)	F1-S1-F3	93.72(15)
S1-N1	2.140(3)	N1-S1-N2	78.37(12)
S1-N2	2.111(3)		
Sb1-F4	1.860(3)	F4-Sb1-F5	92.40(13)
Sb1-F5	1.861(3)	F4-Sb1-F6	89.10(13)
Sb1-F6	1.871(2)	F4-Sb1-F7	177.13(14)
Sb1-F7	1.866(3)	F4-Sb1-F8	91.84(15)
Sb1-F8	1.852(3)	F4-Sb1-F9	88.41(14)
Sb1-F9	1.877(3)	F8-Sb1-F9	179.55(14)

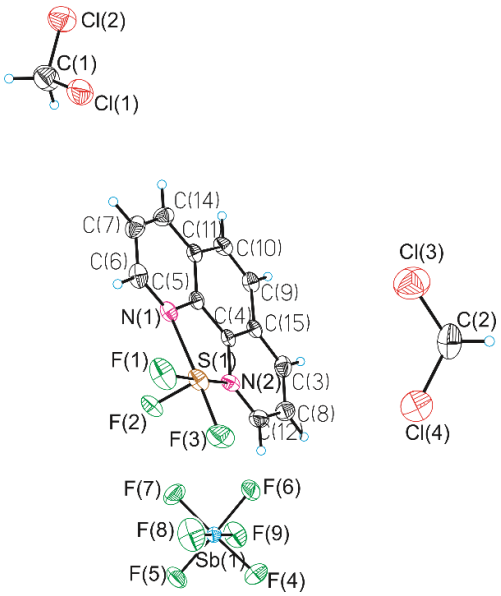

Figure 4.5 The thermal ellipsoid of the structural unit in the X-ray crystal structure of $[SF_3(phen)][SbF_6]\cdot 2CH_2Cl_2$ in the crystal of $[SF_3(phen)][SbF_6]\cdot 2CH_2Cl_2$. Thermal ellipsoids are drawn at the 50% probability level.

4.2.3.4 X-ray crystallography of $[SF_2(DMAP)_2][SbF_6]_2{\cdot}CH_3CN$ and $[SF(DMAP)_2][SbF_6]_3{\cdot}2CH_3CN$

4.2.3.4.1 X-ray crystallography of $[SF_2(DMAP)_2][SbF_6]_2{\cdot}CH_3CN$. The $[SF_2(DMAP)_2][SbF_6]_2$ salt co-crystallizes with a CH_3CN solvent molecule, in the form of $[SF_2(DMAP)_2][SbF_6]_2{\cdot}CH_3CN$, which crystallizes in the monoclinic *C*2/*c* space group with four formula units in the unit cell. The structural unit in the X-ray crystal structure of $[SF_2(DMAP)_2][SbF_6]_2{\cdot}CH_3CN$ is shown in Figure 4.6. The crystallographic data are given in Table 4.6. Selected bond lengths and angles are given in Table 4.9. In the crystal structure of $[SF_2(DMAP)_2][SbF_6]_2{\cdot}CH_3CN$, the $[SF_2(DMAP)_2]^{2+}$ cation crystallizes in a see-saw geometry with two symmetry–related fluorine atoms in the axial positions with S–F bond lengths of 1.701(4) Å, which are much longer than those present in γ-$[SF_3][SbF_6]$ (1.504(1), 1.501(1) and 1.509(1) Å) despite of the additional positive charge of the $[SF_2(DMAP)_2]^{2+}$ cation. These axial S–F bond lengths is similar what was found for bis(imidazole)sulfur difluoride, $[(C_3H_3N_2)_2SF_2)]$, (1.709(2) and 1.693(2) Å)[13] whereas longer than those present in solid SF_4 (1.647(5) and 1.675(5) Å). Two DMAP molecules occupy the equatorial position with the S–N bond lengths of 1.724(5) Å. The S−N bonds represent strong covalent bonding between sulfur and nitrogen, unlike the weaker bonds in the cationic adducts of SF_3^+ and nitrogen bases. In bis(imidazole)sulfur difluoride, the S−N bonds are shorter (1.700(2) and 1.690(3) Å) than those present in the $[SF_2(DMAP)_2]^{2+}$ cation. The lone pair is in the equatorial plane of the distorted trigonal bipyramidal geometry in accord with the VSEPR model. The axial F7−S1−F7A bond angle of 175.4(3)° deviates somewhat from the linearity due to the lone pair – bond pair repulsion. The F−S−F bond angle is 173.86(12)° in case of bis(imidazole)sulfur difluoride. The closest S···F distance in $[SF_2(DMAP)_2][SbF_6]_2{\cdot}CH_3CN$ is 4.297 Å which is much longer than the sum of van der

Waal's radii of sulfur and fluorine (3.27 Å),[10] indicating well separated $[SF_2(DMAP)_2]^+$ cation and SbF_6^- anion.

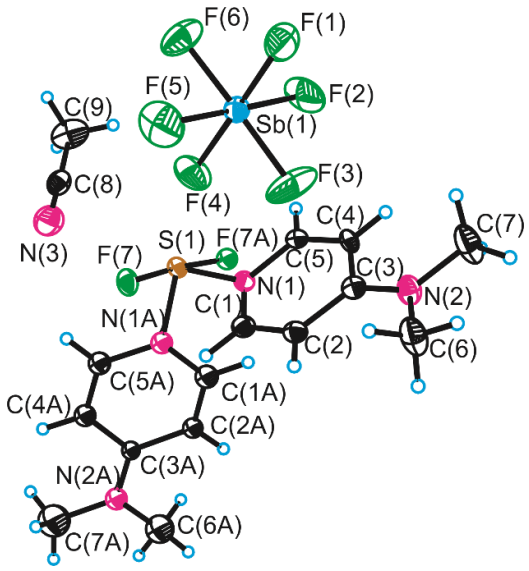

Figure 4.6 The thermal ellipsoid of the structural unit in the X-ray crystal structure of $[SF_2(DMAP)_2][SbF_6]_2{\cdot}CH_3CN$ in the crystal of $[SF_2(DMAP)_2][SbF_6]_2{\cdot}CH_3CN$. Thermal ellipsoids are drawn at the 50% probability level.

Table 4.9 Bond lengths (Å) and bond angles (°) for $[SF_2(DMAP)_2][SbF_6]_2{\cdot}CH_3CN$

Bond lengths (Å)		Bond angles (°)	
S1-F7	1.701(4)	F7-S1-F7A	175.4(3)
S1-F7A	1.701(4)		
S1-N1	1.724(5)	N1-S1-N1A	100.4(3)
S1-N1A	1.724(5)		
Sb1-F1	1.863(4)	F1-Sb1-F2	91.1(2)
Sb1-F2	1.868(4)	F2-Sb1-F3	89.7(2)
Sb1-F3	1.862(4)	F2-Sb1-F4	90.4(2)
Sb1-F4	1.867(4)	F3-Sb1-F4	89.5(2)
Sb1-F5	1.877(5)	F4-Sb1-F5	88.8(2)
Sb1-F6	1.869(5)	F6-Sb1-F5	87.8(2)

4.2.3.4.2 X-ray crystallography of $[SF(DMAP)_4][SbF_6]_3{\cdot}2CH_3CN$. The $[SF(DMAP)_4]_2[SbF_6]_3{\cdot}2CH_3CN$ crystallizes in the monoclinic space group *C2/c* with four

formula units in the unit cell. The crystallographic data is given in Table 4.6. The structural unit in the X-ray crystal structure of $[SF(DMAP)_4][SbF_6]_3{\cdot}2CH_3CN$ is shown in Figure 4.7 and the bond lengths and angles are given in Table 4.10. In the crystal structure of $[SF(DMAP)_4][SbF_6]_3{\cdot}2CH_3CN$, the $[SF(DMAP)_4]^{3+}$ cation adopts a square pyramidal VSEPR geometry. The fluorine on sulfur is disordered with respect to a crystallographic C_2 axis and was refined by taking into account a 50% occupancy. The fluorine atom is in the axial position with S–F bond length of 1.594(8) Å, which is longer than the S–F bond length present in γ-$[SF_3][SbF_6]$ (1.504(1), 1.501(1) and 1.509(1) Å). Four DMAP molecules are in the equatorial position. The S–N bond lengths of 2×1.878(7) Å and 2×1.924(7) Å are strong covalent bonds, but longer than the S−N bonds in the $[SF_2(DMAP)_2]^{2+}$ cation. The N–S–N bond angles are 90.0(3)° giving the structure a square shape in the equatorial plane. The shortest S···F distance (3.500 Å) between $[SF(DMAP)_4]^{3+}$ cation and SbF_6^- anion in $[SF(DMAP)_4][SbF_6]_3{\cdot}2CH_3CN$ is longer than the sum of the van der Waal's radii of sulfur and fluorine i.e. 3.27 Å,[12] separating the $[SF(DMAP)_4]^{3+}$ cation and SbF_6^- anion completely. In the crystal structure, the lone pair on sulfur is situated trans to the axial fluorine to avoid any repulsion between lone pair and bond pair.

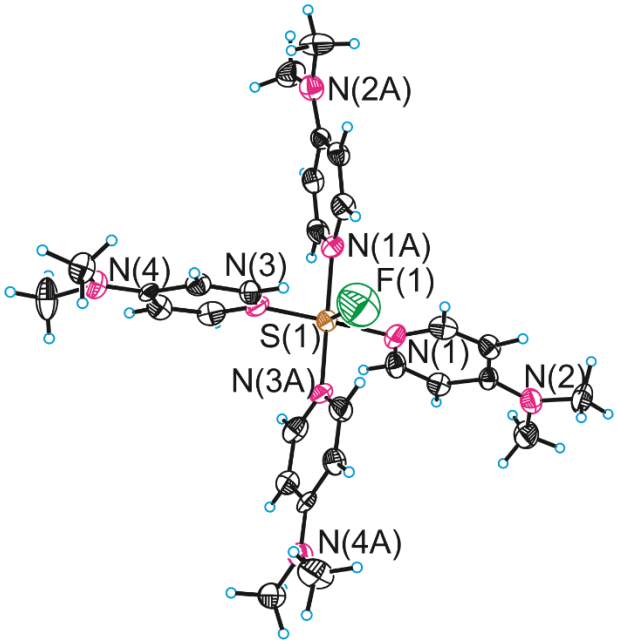

Figure 4.7 The thermal ellipsoid of the structural unit of $[SF(DMAP)_4]^{3+}$ cation in the X-ray crystal structure of $[SF(DMAP)_4][SbF_6]_3 \cdot 2CH_3CN$. Thermal ellipsoids are drawn at the 50% probability level.

Table 4.10 Bond lengths (Å) and bond angles (°) for $[SF(DMAP)_4][SbF_6]_3 \cdot 2CH_3CN$

Bond lengths (Å)		Bond angles (°)	
S1-F1	1.594(8)		
		F1-S1-N1	88.7(4)
S1-N1	1.924(7)	N1-S1-N3	90.0(3)
S1-N3	1.878(7)	F1-S1-N3	89.8(4)
Sb1-F2	1.986(11)	F3-Sb1-F6	91.6(3)
Sb1-F3	1.861(6)	F5-Sb1-F6	94.2(8)
Sb1-F4	1.907(9)	F3-Sb1-F5	167.8(5)
Sb1-F5	1.80(2)	F4-Sb1-F5	88.7(7)
Sb1-F6	1.822(6)	F2-Sb1-F6	79.0(5)
Sb2-F8	1.846(9)	F2-Sb1-F3	84.9(4)
Sb2-F9	1.873(5)	F2-Sb1-F4	85.2(5)
Sb2-F10	1.853(5)	F2-Sb1-F5	85.7(6)
Sb2-F11	1.855(10)	F5-Sb1-F7	107.1(9)
		F8-Sb2-F9	89.8(2)
		F9-Sb2-F10	90.3(2)
		F10-Sb2-F11	88.8(3)
		F9-Sb2-F11	90.2(2)

4.2.4 Raman spectroscopy

4.2.4.1 Raman spectroscopy of $[SF_3(C_5H_5N)_2][MF_6]$·solvent (M = Sb, As; solvent = CH_2Cl_2, C_5H_5N and $[SF_3(C_5H_5N)_2][SbF_6]$·CH_3CN

The Raman spectra of $[SF_3(C_5H_5N)_2][MF_6]$·$n$$C_5H_5N$ (M = Sb, As) salts at –110 °C (with n = 0.15 determined by mass balance in case of $[SF_3(C_5H_5N)_2][SbF_6]$·$n$$C_5H_5N$ salt) are depicted in Figure 4.8 along with the spectrum of neat C_5H_5N[14] and the vibrational frequencies for $[SF_3(C_5H_5N)_2][SbF_6]$·$n$$C_5H_5N$, $[SF_3(C_5H_5N)_2][AsF_6]$·$n$$C_5H_5N$, $[SF_3(C_5H_5N)_2][SbF_6]$·CH_3CN, $[SF_3(C_5H_5N)_2][SbF_6]$·CH_2Cl_2, and $[SF_3(C_5H_5N)_2][AsF_6]$·CH_2Cl_2 are listed in Table 4.11, 4.12, 4.13, 4.14 and 4.15, respectively.

After the formation of the adducts between $[SF_3][MF_6]$ (where M = Sb, As) salts and C_5H_5N, shifts in the Raman frequencies for the SF_3^+ moiety, and C_5H_5N are expected to be observed. In the case of $[SF_3(C_5H_5N)_2][SbF_6]$·C_5H_5N, the symmetric SF_3 stretching band (ν_s) is shifted to 816 cm^{-1} for $[SF_3(C_5H_5N)_2]^+$ cation as compared to 939 cm^{-1} for $[SF_3]^+$ cation in $[SF_3][SbF_6]$, while in the case of $[SF_3(C_5H_5N)_2][AsF_6]$·C_5H_5N salt, the $\nu_s(SF_3)$ appears at 812 cm^{-1} for $[SF_3(C_5H_5N)_2]^+$ cation in comparison to 945 cm^{-1} for $[SF_3]^+$ cation in $[SF_3][AsF_6]$. Similar $\nu_s(SF_3)$ frequencies are observed for $[SF_3(C_5H_5N)_2][SbF_6]$·CH_2Cl_2 (815 cm^{-1}), $[SF_3(C_5H_5N)_2][AsF_6]$·CH_2Cl_2 (818 cm^{-1}) and $[SF_3(C_5H_5N)_2][SbF_6]$·CH_3CN (808 and 828 cm^{-1}). Upon complexation of $[SF_3][MF_6]$ (M = Sb, As) salts with C_5H_5N, the S–F bond lengths in the $[SF_3(C_5H_5N)_2]^+$ cations become longer as observed in the crystal structures, which is paralleled by a decrease of the S–F bond strength. Several Raman signals associated with the C_5H_5N part of the adduct are significantly shifted compared to those of the free pyridine. One set of signals, however, is unshifted indicating the presence of some unadducted pyridine in the resultant salt. For

example, the most intense band in the Raman spectrum of free pyridine comes at 990 cm^{-1}, which corresponds to the symmetric C_5N ring breathing mode. This band shifts to higher frequency upon complexation of C_5H_5N with $[SF_3][MF_6]$ (M = Sb, As) salts, i.e., to 1018 cm^{-1} in case of $[SF_3(C_5H_5N)_2][SbF_6]\cdot C_5H_5N$ and 1022 cm^{-1} in case of $[SF_3(C_5H_5N)_2][AsF_6]\cdot C_5H_5N$. Similar frequencies were observed for the C_5N breathing mode (1020 cm^{-1}) in $[SF_3(C_5H_5N)_2][SbF_6]\cdot CH_2Cl_2$, $[SF_3(C_5H_5N)_2][AsF_6]\cdot CH_2Cl_2$ (1019 cm^{-1}) and $[SF_3(C_5H_5N)_2][SbF_6]\cdot CH_3CN$ (1018 cm^{-1}). A strong shift in the $\nu_s(C_5N)$ mode of C_5H_5N in $[SF_3(C_5H_5N)_2][MF_6]\cdot C_5H_5N$ (M = Sb, As) salts shows that C_5H_5N is strongly bonded with $[SF_3][MF_6]$ (M = Sb, As). The C_5N ring breathing mode for C_5H_5N in case of the strong $BF_3\cdot NC_5H_5$ adduct was shifted to 1026 cm^{-1} in comparison to the free pyridine C_5N mode at 990 cm^{-1},[15] whereas it was shifted to 1003 cm^{-1} in case of weak $SF_4\cdot C_5H_5N$ adduct[16] and to 1016 cm^{-1} for the $WSF_4\cdot C_5H_5N$ adduct.[17] The signals from the C_5N ring breathing mode shows splitting likely from vibrational coupling of the C_5H_5N molecules in the adduct at 1010, 1032 and 1038 cm^{-1} for $[SF_3(C_5H_5N)_2][SbF_6]\cdot nC_5H_5N$, 1022 and 1031 cm^{-1} for $[SF_3(C_5H_5N)_2][AsF_6]\cdot nC_5H_5N$ salt, 1032 and 1041 cm^{-1} for $[SF_3(C_5H_5N)_2][SbF_6]\cdot CH_3CN$, 1012, 1032 and 1038 cm^{-1} for $[SF_3(C_5H_5N)_2][SbF_6]\cdot CH_2Cl_2$ and at 1006, 1034 and 1041 cm^{-1} for $[SF_3(C_5H_5N)_2][AsF_6]\cdot CH_2Cl_2$. Upon complexation of pyridine with BF_3, a shift of the C–C stretching mode from 1581 to 1631 cm^{-1} has been observed.[12(b)] A similar shift from 1581 to 1607 cm^{-1} was observed for $[SF_3(C_5H_5N)_2][SbF_6]\cdot nC_5H_5N$, to 1604 cm^{-1} in case of $[SF_3(C_5H_5N)_2][AsF_6]\cdot nC_5H_5N$, to 1608 cm^{-1} in case of $[SF_3(C_5H_5N)_2][SbF_6]\cdot CH_2Cl_2$, to 1609 cm^{-1} in case of $[SF_3(C_5H_5N)_2][AsF_6]\cdot CH_2Cl_2$ and to 1608 cm^{-1} in case of $[SF_3(C_5H_5N)_2][SbF_6]\cdot CH_3CN$ in the current study. The stretching frequencies of the C–H vibrations of pyridine are also shifted upon complex formation, e.g., the signal at 3088 cm^{-1} in free pyridine is shifted to

3116 cm^{-1} for $[SF_3(C_5H_5N)_2][SbF_6]\cdot nC_5H_5N$, to 3111 cm^{-1} for $[SF_3(C_5H_5N)_2][AsF_6]\cdot nC_5H_5N$, to 3116 cm^{-1} in case of $[SF_3(C_5H_5N)_2][SbF_6]\cdot CH_2Cl_2$, to 3107 cm^{-1} in case of $[SF_3(C_5H_5N)_2][AsF_6]\cdot CH_2Cl_2$ and to 3113 cm^{-1} in case of $[SF_3(C_5H_5N)_2][SbF_6]\cdot CH_3CN$. A similar shift to 3124 cm^{-1} in the C–H stretching frequency was observed for C_5H_5N in $BF_3\cdot NC_5H_5$ adduct.

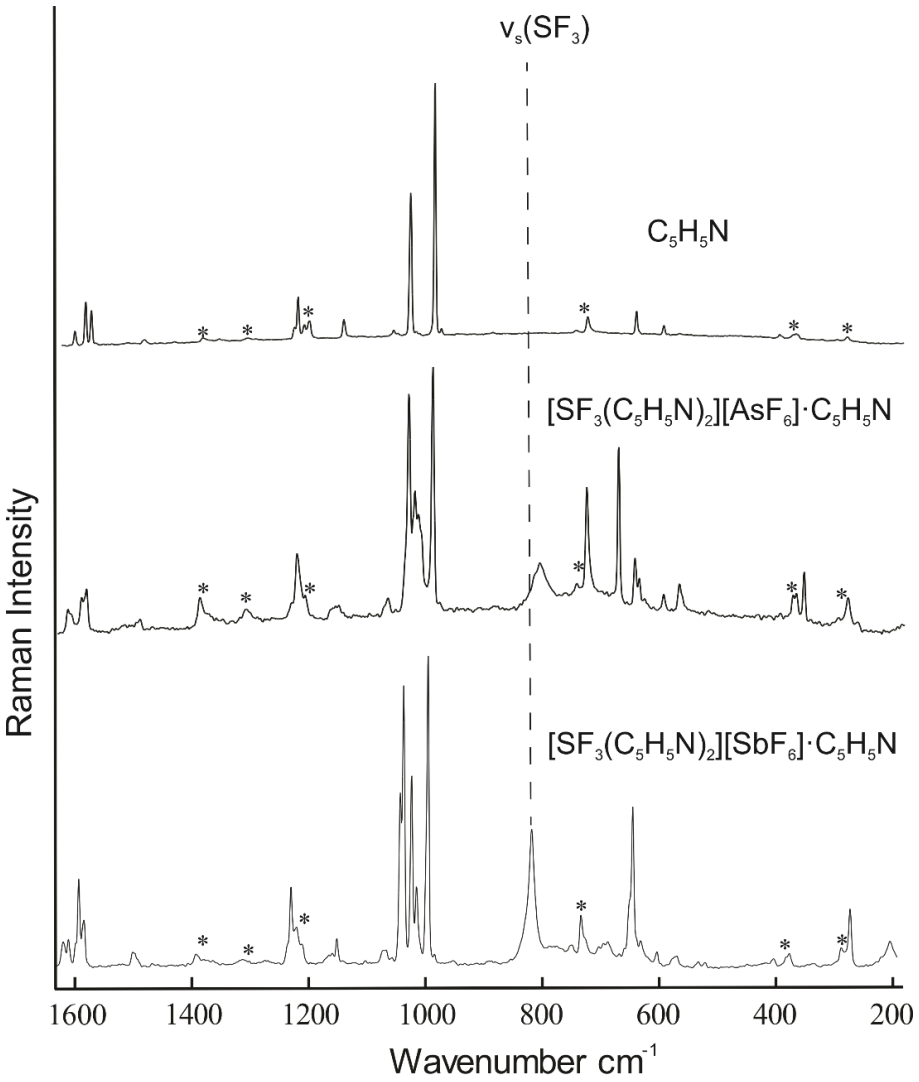

Figure 4.8 Raman spectrum of C_5H_5N, $[SF_3(C_5H_5N)_2][AsF_6]\cdot C_5H_5N$, $[SF_3(C_5H_5N)_2][SbF_6]\cdot C_5H_5N$ at –110 °C. Asterisks (*) denote bands arising from the FEP sample tube.

Table 4.11 Raman frequencies (relative intensities), cm^{-1} of SF_3SbF_6, C_5H_5N and $[SF_3(C_5H_5N)_2][SbF_6]\cdot nC_5H_5N$ at –110 °C together with their tentative assignments.

Vibrational frequencies			Assignments		
C_5H_5N	$[SF_3][SbF_6]$[a]	$[SF_3(C_5H_5N)_2][SbF_6]\cdot nC_5H_5N$[b]	C_5H_5N	$[SF_3][SbF_6]$[a]	$[SF_3(C_5H_5N)_2][SbF_6]\cdot nC_5H_5N$[b]
3173(1)		3143(3)			
3156(1)		3116(4)			
3143(3)		3099(10)			
3088(5)		3087(19)			
		3078(21)	ν(C-H)		ν(C-H)
3070(2)		3071(24)			
3060(sh)		3061(31)			
3055(39)		3057(32)			
3033(5)		3033(6)			
3020(5)		3020(4)			
2987(2)			overtones and		
2954(2)			combination		
2917(1)			bands		
		1607(10)			
1599(5)		1599(10)			
1581(9)		1587(9)	ν(C=C)		ν(C=C)
		1581(29)			
1571(7)		1572(17)	ν(C=N)		ν(C=N)
		1514(2)			
1481(3)		1489(7)			
		1458(3)			
1383(1)					
		1354(4)			
1228(3)		1229(9)			
1222(18)		1222(27)	δ(C-H)		δ(C-H)
1211(2)					
1203(5)		1204(9)			
		1162(7)			
		1152(6)			
1145(2)		1145(11)			
		1097(4)			
		1067(7)			
1060(2)		1062(7)			
		1038(52)			in-plane ring-def
1031(75)		1032(91)			$\nu_s(C_5N$ ring)
		1018(62)	in-plane		
		1010(27)	ring-def		
990(100)		991(100)	$\nu_s(C_5N$ ring)		
980(1)		980(6)			
	955(39)				
	939(95)			$\nu(SF_3)$	
	929(15)				
	923(23)	816(45)			$\nu(SF_3)$
		755(8)			

		751(9)			
		748(9)			
		726(11)			
		703(8)			out-of-plane C-H def.
		695(9)			
		688(10)			
	671(29)	668(6)		$\nu(SbF_6)$	$\nu(SbF_6)$
		660(8)			
650(5)	650(100)	652(22)			
		645(52)			
	634(8)	633(10)	in-plane ring-def		in-plane ring-def
604(3)	617(8)	605(7)			
		589(3)			
	580(17)	580(4)		$\delta(SbF_6)$	$\delta(SbF_6)$
		577(5)			
578(1)		571(5)			
	552(20)	553(2)			
		540(33)			
	533(sh)	535(4)			
	529(13)	523(4)		$\delta(SF_3)^+$	$\delta(SF_3)^+$
		513(18)			
		411(4)		$\delta_{sciss}(SF_3)^+$	$\delta_{sciss}(SF_3)^+$
408(1)	410(11)	407(5)	out-of-plane ring def		& out-of-plane
381(2)		381(6)			ring def
313(1)	301(8)			$\delta(SbF_6)$	$\delta(SbF_6)$
294(1)					
		279(20)			
		212(10)			

[a] The Raman spectrum was recorded in a glass NMR tube at –110 °C. [b] The Raman spectrum was recorded in a ¼–in FEP tube at –110 °C. Signals observed at 294(8), 1213(15) cm^{-1} in the spectrum of $[SF_3(C_5H_5N)_2][SbF_6]\cdot nC_5H_5N$ are overlapped with the bands of FEP sample tube. [c] Signals observed at 387(5), 733(18), 1303(4), 1382(6) cm^{-1} represents FEP. [d] Pyridine bands have been assigned based on references 19–23. [e] $[SF_3][SbF_6]$ bands have been assigned based on references 2c.

Table 4.12 Raman frequencies (relative intensities), cm^{-1} of $[SF_3][AsF_6]$, C_5H_5N and $[SF_3(C_5H_5N)_2][AsF_6]\cdot nC_5H_5N$ at –110 °C together with their tentative assignments.

Vibrational frequencies			Assignments		
C_5H_5N	$[SF_3][AsF_6]$[a]	$[SF_3(C_5H_5N)_2][AsF_6]\cdot nC_5H_5N$[b]	C_5H_5N	$[SF_3][AsF_6]$[a]	$[SF_3(C_5H_5N)_2][AsF_6]\cdot nC_5H_5N$[b]
3173(1)					
3156(1)					
3143(3)		3111(6)			
		3105(13)			
		3090(21)			
3088(5)		3084(26)	ν(C-H)		ν(C-H)
		3060(35)			
3070(2)		3039(8)			
3060(sh)		3036(6)			
3055(39)		3032(6)			
3033(5)		3026(6)			
3020(5)					
2987(2)			overtones and		
2954(2)			combination		
2917(1)			bands		
		1604(9)			
1599(5)		1600(8)	ν(C=C)		ν(C=C)
1581(9)		1582(14)			
1571(7)		1574(17)	ν(C=N)		ν(C=N)
		1490(2)			
1481(3)		1484(3)			
1383(1)		1368(5)			
1228(3)		1229(9)			
1222(18)			δ(C-H)		δ(C-H)
1211(2)		1206(11)			
1203(5)		1155(5)			
1145(2)		1150(5)			
1060(2)		1067(8)			
1031(75)		1031(92)			
		1022(53)			
		1016(43)	in-plane ring-def		in-plane ring-def
990(100)		992(100)	$\nu_s(C_5N$ ring)		$\nu_s(C_5N$ ring)
980(1)					
	960(sh)				
	945(81)	822(13)		ν(SF_3)	ν(SF_3)
	926(29)	812(19)			
		749(3)			
	686(100)	679(64)		ν(AsF_6)	ν(AsF_6)
650(5)		652(19)			
		645(13)			
		633(10)			
604(3)		604(6)			

	587(23)			$\delta(AsF_6)$	$\delta(AsF_6)$
578(1)		577(11)			
	563(32)				
	530(20)				
	529(13)	528(1)		$\delta(SF_3)^+$	$\delta(SF_3)^+$
		411(4)		$\delta_{sciss}(SF_3)^+$	$\delta_{sciss}(SF_3)^+$
408(1)	411(22)	407(5)	out-of-plane ring def		& out-of-plane ring def
381(2)	379(44)	381(13)			
		368(22)			
313(1)	301(8)			$\delta(AsF_6)$	$\delta(AsF_6)$
294(1)		278(3)			

[a] The Raman spectrum was recorded in a glass NMR tube at –110 °C. [b] The Raman spectrum was recorded in a ¼–in FEP tube at –110 °C. Signals observed at 733(51), 1219(29) cm^{-1} in Raman spectrum of $[SF_3(C_5H_5N)_2][AsF_6]\cdot nC_5H_5N$ are overlapped with the bands of FEP sample tube. [c] Signals observed at 294(11), 387(13), 1305(5), 1383(13) cm^{-1} in Raman spectrum are of FEP sample tube. [d] Pyridine bands have been assigned based on references 19–23. [e] $[SF_3][AsF_6]$ bands have been assigned based on references 2c.

Table 4.13. Raman frequencies (relative intensities), cm^{-1} of $[SF_3][SbF_6]$, C_5H_5N and $[SF_3(C_5H_5N)_2][SbF_6]\cdot CH_3CN$ at –110 °C together with their tentative assignments.

Vibrational frequencies			Assignments		
C_5H_5N	$[SF_3][SbF_6]$[a]	$[SF_3(C_5H_5N)_2][SbF_6]\cdot CH_3CN$[b]	C_5H_5N	$[SF_3][SbF_6]$[a]	$[SF_3(C_5H_5N)_2][SbF_6]\cdot CH_3CN$[b]
3173(1)					
3156(1)		3158(2)			
3143(3)		3146(2)			
3088(5)		3080(22)	ν(C-H)		ν(C-H)
3070(2)		3061(24)			
3060(sh)					
3055(39)					
3033(5)					
3020(5)					
		2999(18)			
2987(2)		2950(20)	overtones and		
2954(2)		2936(42)	combination		
2917(1)		2292(6)	bands		
		2248(46)			
		1608(12)			
1599(5)		1599(8)	ν(C=C)		ν(C=C)
1581(9)		1583(18)			
1571(7)		1574(18)	ν(C=N)		ν(C=N)
		1514(2)			
1481(3)		1489(4)			
		1455(6)			
1383(1)					
		1307(1)			
1228(3)			δ(C-H)		δ(C-H)
1222(18)					
1211(2)					
1203(5)		1162(6)			
1145(2)		1149(6)			
1060(2)		1067(8)			
		1041(53)	in-plane ring-def		in-plane ring-def
1031(75)		1032(73)			
		1018(100)			$\nu_s(C_5N$ ring)
990(100)		992(68)	$\nu_s(C_5N$ ring)		
980(1)		980(6)			
	955(39)				
	939(95)			$\nu(SF_3)$	
	929(15)	828(14)			$\nu(SF_3)$
	923(23)	808(33)			
		697(6)			
	671(29)	671(14)			
650(5)	650(100)	647(86)		$\nu(SbF_6)$	$\nu(SbF_6)$

	634(8)				
604(3)	617(8)	605(4)			
	580(17)	575(6)		$\delta(SbF_6)$	$\delta(SbF_6)$
578(1)					
	552(20)				
	533(sh)				
	529(13)	528(1)		$\delta(SF_3)^+$	$\delta(SF_3)^+$
				$\delta_{sciss}(SF_3)^+$	$\delta_{sciss}(SF_3)^+$
408(1)	410(11)	397(4)	out-of-plane		& out-of-plane
381(2)		351(4)	ring def		ring def
313(1)	301(8)			$\delta(SbF_6)$	$\delta(SbF_6)$
294(1)		279(37)			
		220(9)			

[a] The Raman spectrum was recorded in a glass NMR tube at –110 °C. [b] Signals observed at 384(14), 1219(23), 1375(12) cm^{-1} in the Raman spectrum of $[SF_3(C_5H_5N)_2][SbF_6]\cdot CH_3CN$ are overlapped with FEP signals. [b] Signals observed at 293(8), 733(25), 1307(1) cm^{-1} are of FEP. [d] Pyridine bands have been assigned based on references 19-23. [e] $[SF_3][SbF_6]$ bands have been assigned based on references 2c.

Table 4.14 Raman frequencies (relative intensities), cm^{-1} of $[SF_3][SbF_6]$, C_5H_5N and $[SF_3(C_5H_5N)_2][SbF_6]\cdot CH_2Cl_2$ at –110 °C together with their tentative assignments.

Vibrational frequencies			Assignments		
C_5H_5N	$[SF_3][SbF_6]$[a]	$[SF_3(C_5H_5N)_2][SbF_6]\cdot CH_2Cl_2$[b]	C_5H_5N	$[SF_3][SbF_6]$[a]	$[SF_3(C_5H_5N)_2][SbF_6]\cdot CH_2Cl_2$[b]
3173(1)					
3156(1)		3149(6)			
3143(3)		3116(6)			
3088(5)		3095(28)	ν(C-H)		ν(C-H)
3070(2)		3078(36)			
3060(sh)		3061(39)			
3055(39)					
3033(5)		3038(11)			
3020(5)					
2987(2)		2978(8)	overtones and		overtones and
2954(2)			combination		combination
2917(1)			bands		bands
		1608(15)			
1599(5)		1599(8)	ν(C=C)		ν(C=C)
1581(9)		1581(26)			
1571(7)		1574(19)	ν(C=N)		ν(C=N)
		1510(1)			
1481(3)		1489(6)			
		1418(1)			
1383(1)					
1228(3)			δ(C-H)		δ(C-H)
1222(18)					
1211(2)					
1203(5)		1153(5)			
1145(2)					
1060(2)		1068(6)			
		1038(56)			in-plane
1031(75)		1032(87)	in-plane		ring-def
		1020(100)	ring-def		$\nu_s(C_5N$ ring)
		1012(26)			
990(100)		992(80)	$\nu_s(C_5N$ ring)		$\nu_s(C_5N$ ring)
980(1)					
	955(39)				
	939(95)			$\nu(SF_3)$	
	929(15)	815(36)			$\nu(SF_3)$
	923(23)				
		750(5)			
	671(29)	702(19)			$\nu_s(CCl_2)$
650(5)	650(100)	653(23)		$\nu(SbF_6)$	
	634(8)	646(93)			$\nu(SbF_6)$
604(3)	617(8)	605(6)			
	580(17)	575(6)		$\delta(SbF_6)$	$\delta(SbF_6)$
578(1)					
	552(20)				
	533(sh)	537(1)			

	529(13)	526(1)		$\delta(SF_3)$	$\delta(SF_3)$
	410(11)	411(11)		$\delta_{sciss}(SF_3)$	$\delta_{sciss}(SF_3)$
408(1)		408(11)	out-of-plane		& out-of-plane
381(2)			ring def		ring def
313(1)		381(11)			
	301(8)			$\delta(SbF_6)$	
294(1)		292(10)			
		279(20)			
		216(9)			

[a] The Raman spectrum was recorded in a glass NMR tube at –110 °C. [b] Signals observed at 387(24), 1217(25) cm^{-1} in the Raman spectrum of $[SF_3(C_5H_5N)_2][SbF_6]\cdot CH_2Cl_2$ are overlapped with FEP signals. [c] Signals from the FEP sample tube were observed at 292(10), 733(54), 1304(6), 1383(15) cm^{-1}. [d] Pyridine bands have been assigned based on references 19-23. [e] $[SF_3][SbF_6]$ bands have been assigned based on references 2c.

Table 4.15 Raman frequencies (relative intensities), cm^{-1} of $[SF_3][AsF_6]$, C_5H_5N and $[SF_3(C_5H_5N)_2][AsF_6]\cdot CH_2Cl_2$ at –110 °C together with their tentative assignments.

Vibrational frequencies			Assignments		
C_5H_5N	$[SF_3][AsF_6]$[a]	$[SF_3(C_5H_5N)_2][AsF_6]\cdot CH_2Cl_2$[b]	C_5H_5N	$[SF_3][AsF_6]$[a]	$[SF_3(C_5H_5N)_2][AsF_6]\cdot CH_2Cl_2$[b]
3173(1)		3120(10)			
3156(1)		3113(10)	ν(C-H)		ν(C-H)
3143(3)		3106(21)			
3088(5)		3077(31)			
3070(2)					
3060(sh)					
3055(39)					
3033(5)					
3020(5)					
2987(2)			overtones and		
2954(2)			combination		
2917(1)			bands		
		1625(7)			
1599(5)		1609(13)	ν(C=C)		ν(C=C)
1581(9)					
1571(7)		1574(9)	ν(C=N)		ν(C=N)
1481(3)		1490(7)			
1383(1)					
1228(3)					
1222(18)			δ(C-H)		δ(C-H)
1211(2)		1162(5)			
1203(5)		1153(5)			
1145(2)		1150(5)			
1060(2)		1069(4)			
		1041(38)	in-plane		in-plane
			ring-def		ring-def
1031(75)		1034(58)			
		1020(100)			
		1006(33)			
990(100)			$\nu_s(C_5N$ ring)		$\nu_s(C_5N$ ring)
980(1)					
	960(sh)	882(20)			
	945(81)	844(26)		ν(SF_3)	ν(SF_3)
	926(29)	818(17)			
		701(19)			$\nu_s(CCl_2)$
	686(100)	682(65)		ν(AsF_6)	ν(AsF_6)
650(5)		672(29)			
		647(31)			
		636(18)			
604(3)					
	587(23)	580(11)		δ(AsF_6)	δ(AsF_6)
		575(10)			
578(1)					

	563(32)				
	530(20)	535(20)			
	529(13)	517(14)		$\delta(SF_3)^+$	$\delta(SF_3)^+$
				$\delta_{sciss}(SF_3)^+$	$\delta_{sciss}(SF_3)^+$
408(1)	411(22)	411(1)	out-of-plane ring def		& out-of-plane ring def
381(2)	379(44)	369(18)			
313(1)	301(8)			$\delta(AsF_6)$	$\delta(AsF_6)$
294(1)		278(4)			
		256(3)			
		212(8)			

[a] The Raman spectrum was recorded in a glass NMR tube at –110 °C. [b] Signals observed 1217(21) cm^{-1} in the Raman spectrum of $[SF_3(C_5H_5N)_2][AsF_6]\cdot CH_2Cl_2$ are overlapped with FEP signals. [c] The signals from the FEP sample tube were observed at 294(13), 387(13), 733(31), 1307(4), 1383(8) cm^{-1}. [d] Pyridine bands have been assigned based on references 19-23. [e] $[SF_3][AsF_6]$ bands have been assigned based on references 2c.

4.2.4.2 Raman spectroscopy of $[SF_3(Phen)][SbF_6]\cdot 2CH_2Cl_2$

The vibrational frequencies of $[SF_3(Phen)][SbF_6]\cdot 2CH_2Cl_2$ are listed in Table 4.16 together with their tentative assignments while the Raman spectrum is shown in Figure 4.9. The symmetric SF_3 stretch is situated at 832 cm^{-1} indicating similar coordination strength of 1,10-phenanthroline with SF_3^+ cation in $[SF_3(Phen)][SbF_6]$ as compared to the C_5H_5N coordination with SF_3^+ cation in $[SF_3(C_5H_5N)_2][SbF_6]\cdot nC_5H_5N$ for which the symmetric SF_3 stretch is at 812 cm^{-1}. The 1,10–phenanthroline ring stretching mode, also shifts from 1034 to 1057 cm^{-1} upon adduct formation. This band has been shifted to 1050 cm^{-1} in case of $[Ag(phen)]^+$ complex.[17] The A_{1g} stretching mode of SbF_6^- has been shifted insignificantly from 650 to 646 cm^{-1}. The same difference in the magnitude of the Raman shift of SbF_6^- was found in $[SF_3(C_5H_5N)_2][SbF_6]\cdot nC_5H_5N$ salt indicating a similar lack of cation-anion interaction in $[SF_3(Phen)][SbF_6]\cdot 2CH_2Cl_2$ salt as is present in $[SF_3(C_5H_5N)_2][SbF_6]\cdot nC_5H_5N$ salt.

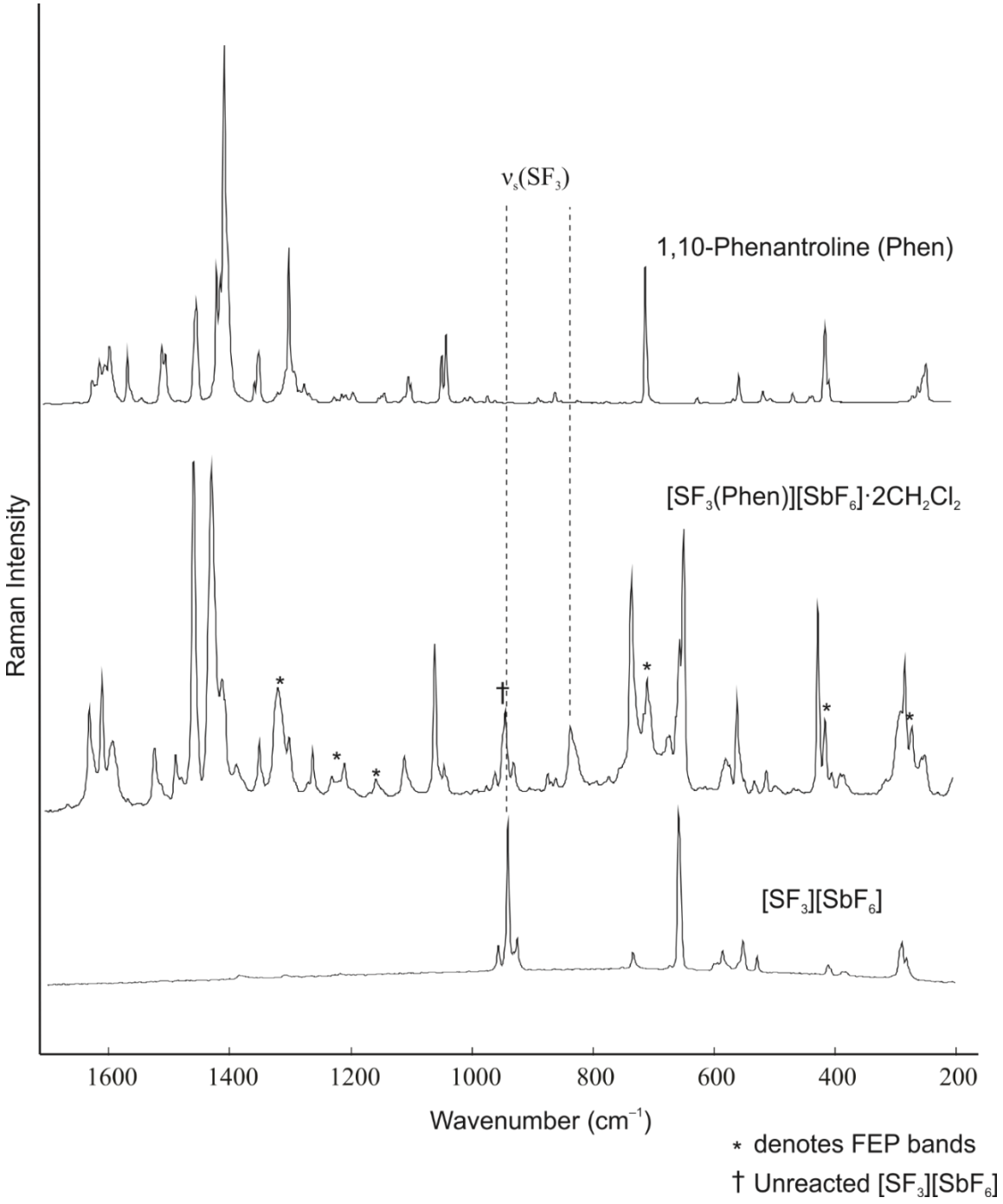

Figure 4.9 Raman spectrum of $[SF_3][SbF_6]$, $[SF_3(Phen)][SbF_6]\cdot 2CH_2Cl_2$ and 1,10-phenanthroline (Phen) solids at –110 °C. Asterisks (*) denote bands arising from the FEP sample tube.

Table 4.16 Raman frequencies (relative intensities), cm^{-1} of $[SF_3][SbF_6]$, 1,10-Phenanthroline (Phen) and $[SF_3(Phen)][SbF_6]\cdot 2CH_2Cl_2$ at –110 °C together with their tentative assignments.

Vibrational frequencies			Assignments		
1,10-phenanthroline	$[SF_3][SbF_6]$[a]	$[SF_3(Phen)][SbF_6]\cdot 2CH_2Cl_2$[b]	1,10-phenanthroline	$[SF_3][SbF_6]$[a]	$[SF_3(Phen)][SbF_6]\cdot 2CH_2Cl_2$[b]
3180(1)					
3118(1)					
		3105(16)			
3096(1)		3086(26)			
		3077(24)	ν(C-H)		ν(C-H)
3070(2)		3072(22)			
3065(14)		3027(10)			
3046(10)					
3030(5)					
2993(3)		2998(10)	overtones and		overtones and
2970(1)		2922(6)	combination		combination
1619(6)		1625(37)	bands		bands
1607(12)		1604(44)	ν(C=C)		ν(C=C)
1598(11)					
1590(16)		1587(29)	ν(C=N)		ν(C=N)
1561(14)		1518(28)			
1504(16)					
1498(14)		1484(26)			
1446(28)		1454(100)	ν(C-N)		ν(C-N)
1414(38)		1424(98)			
1408(35)		1406(46)			
1401(100)					
1351(6)					
1344(15)		1345(29)			
1313(4)					
1294(44)		1296(3)			δ(C-H)
1285(10)					
1277(3)					
1269(5)		1257(28)			
1260(3)		1226(20)			
1219(2)			δ(C-H)		δ(C-H)
1207(2)		1205(23)			
1200(2)					
1188(3)		1153(19)			
1146(2)					
1140(3)					
1137(3)					
1097(7)		1106(25)			
1093(5)		1057(54)			
1042(13)		1040(23)			
1034(20)		1034(20)	in-plane ring-def		in-plane ring-def

1004(2)			$\nu_s(C_5N$ ring)		
965(2)					
	955(39)				
	939(95)	832(34)		$\nu_s(SF_3)$	$\nu_s(SF_3)$
	929(15)				
	923(23)				
883(2)		870(20)			
		865(36)			
855(3)		856(20)			
		823(28)			
					$\nu_s(CCl_2)$
705(38)		706(46)			
	671(29)	671(31)		$\nu(SbF_6)$	$\nu(SbF_6)$
	650(100)	651(54)			
619(2)	634(8)	646(84)			
609(1)	617(8)				
	580(17)	576(25)			
561(2)	563(32)	570(22)			
551(8)		558(40)		$\delta(SbF_6)$	$\delta(SbF_6)$
	530(20)	544(19)			
511(3)	529(13)	528(19)		$\delta(SF_3)$	$\delta(SF_3)$
500(2)		509(22)			
462(2)		492(18)			
434(2)		424(63)		$\delta(SF_3)$	$\delta(SF_3)$
429(2)					
408(22)	410(11)	412(35)		$\delta_{sciss}(SF_3)$	$\delta_{sciss}(SF_3)^+$
402(6)		401(20)	out-of-plane		out-of-plane
			ring def		ring def
		381(20)			
	301(8)	312(19)			
265(3)	286(22)			$\delta(SbF_6)$	$\delta(SbF_6)$
256(5)	274(12)	281(50)			
247(7)		252(24)			
242(12)		247(26)			

[a] The Raman spectrum was recorded in a glass NMR tube at –110 °C. [b] Signals observed at 292(37) and 1316(43) cm^{-1} in the Raman spectrum of $[SF_3(Phen)][SbF_6]\cdot 2CH_2Cl_2$ are overlapped with FEP signals. [c] Signals from the FEP sample tube were observed at 388(20), 733(71), 1215(18), 1383(23) cm^{-1}. [d] 1,10-phenanthroline bands have been assigned based on references 24-25. [e] $[SF_3][SbF_6]$ bands have been assigned based on references 2c. Signals from unreacted $[SF_3][SbF_6]$ were obtained at 926(23), 939(37) and 955(20) cm^{-1}.

4.2.4.3 Raman spectroscopy of $[SF_3(CH_3CN)_2][MF_6]$ (M = Sb, As) salts

The Raman spectra for the $[SF_3(CH_3CN)_2][MF_6]$ (M = Sb, As) salts are shown in Figure 4.10 along with the Raman spectrum of CH_3CN. The vibrational frequencies of $[SF_3(CH_3CN)_2][SbF_6]$ and $[SF_3(CH_3CN)_2][AsF_6]$ are listed in Table 4.18 and 4.19, respectively. After adduct formation between $[SF_3][MF_6]$ (M = Sb, As) and CH_3CN, diagnostic shifts of vibrational bands in the S–F stretching region of SF_3^+ cation and of the C–N stretching mode of CH_3CN are expected. The most intense band in the S–F stretching region of the $[SF_3(CH_3CN)_2][MF_6]$ in the Raman spectra appears at 900 cm^{-1} and can be assigned to $\nu_s(SF_3)$ mode. This frequency is significantly lower than that of $[SF_3][MF_6]$ (M = As: 945 cm^{-1}, M = Sb: 939 cm^{-1}). In addition to this band a number of other bands appear in this region. The band at 927 ($[SF_3(CH_3CN)_2][SbF_6]$) / 926 ($[SF_3(CH_3CN)_2][AsF_6]$) has been tentatively assigned to the ν(C-C) mode of adducted CH_3CN. A factor group analysis table (Table 4.17) was constructed for the SF_3^+ group in $[SF_3(CH_3CN)_2][SbF_6]$ to predict splitting of SF_3^+ vibrational bands because of the solid-state structure. The analysis predicts two Raman active components for ν_1 and ν_2 while four components are expected for ν_3 and ν_4 in the Raman spectra of $[SF_3(CH_3CN)_2][SbF_6]$. The large number of vibrational bands in the S–F stretching (besides the band at 900 cm^{-1}) likely arise from factor group splitting of $\nu_s(SF_3)$ mode and the asymmetric SF_3 stretching modes with their respective splitting. The Raman spectrum was recorded repeating the same reaction twice to verify that all the bands belong to $[SF_3(CH_3CN)_2][SbF_6]$.

Table 4.17 Factor group analysis table for SF_3 group in $[SF_3(CH_3CN)_2][SbF_6]$

SF_3^+ cation symmetry	Site symmetry	Crystal symmetry		
C_{3v}	C_s	D_{2h}		
4T, 4ν_1, 4ν_2	A_1	A_{1g}	ν_1, ν_2, ν_3, ν_4, R, 2T	RAMAN
		B_{1g}	ν_3, ν_4, 2R, T	RAMAN
	A’	B_{2g}	ν_1, ν_2, ν_3, ν_4, R, 2T	RAMAN
4R	A_2	B_{3g}	ν_3, ν_4, 2R, T	RAMAN
		A_{1u}	ν_3, ν_4, 2R, T	
	A”	B_{1u}	ν_1, ν_2, ν_3, ν_4, R, 2T	IR
4T, 4R, 4ν_3, 4ν_4	E	B_{2u}	ν_3, ν_4, 2R, T	IR
		B_{3u}	ν_1, ν_2, ν_3, ν_4, R, 2T	IR
$\Gamma_{vib} = 2A_1 + 2E$				

The Raman frequency of the $\nu_s(SF_3)$ of $[SF_3(CH_3CN)_2][MF_6]$ (M = Sb, As) salts is much larger compared to those in $[SF_3(C_5H_5N)_2][MF_6]\cdot C_5H_5N$ (M = Sb, As) salts because of lesser donor strength of CH_3CN compared to C_5H_5N. This comparison is also reflected in terms of the differences in the S–F bond lengths (Table 4.5). The C–N stretching mode of CH_3CN shifts from 2248 (neat CH_3CN) to 2271 cm^{-1} for $[SF_3(CH_3CN)_2][SbF_6]$ salt while to 2266 cm^{-1} for $[SF_3(CH_3CN)_2][AsF_6]$ salt. This is even a smaller complexation shift than that observed in the weakly coordinated $WSF_4\cdot CH_3CN$ complex (2286 cm^{-1}).[28] The Raman stretching frequencies for SbF_6^- and AsF_6^- shift slightly from 647 to 650 cm^{-1} for SbF_6^- and 680 to 683 cm^{-1} for AsF_6^-. The C–H stretch gets shifted by 10 cm^{-1} to 2946 cm^{-1} for $[SF_3(CH_3CN)_2][SbF_6]$ salt while to 2955 cm^{-1} for $[SF_3(CH_3CN)_2][AsF_6]$ salt as compared to 2936 cm^{-1} in free CH_3CN. This 10 cm^{-1} shift is the same as has been observed for weakly coordinated $WSF_4\cdot CH_3CN$ adduct.[18]

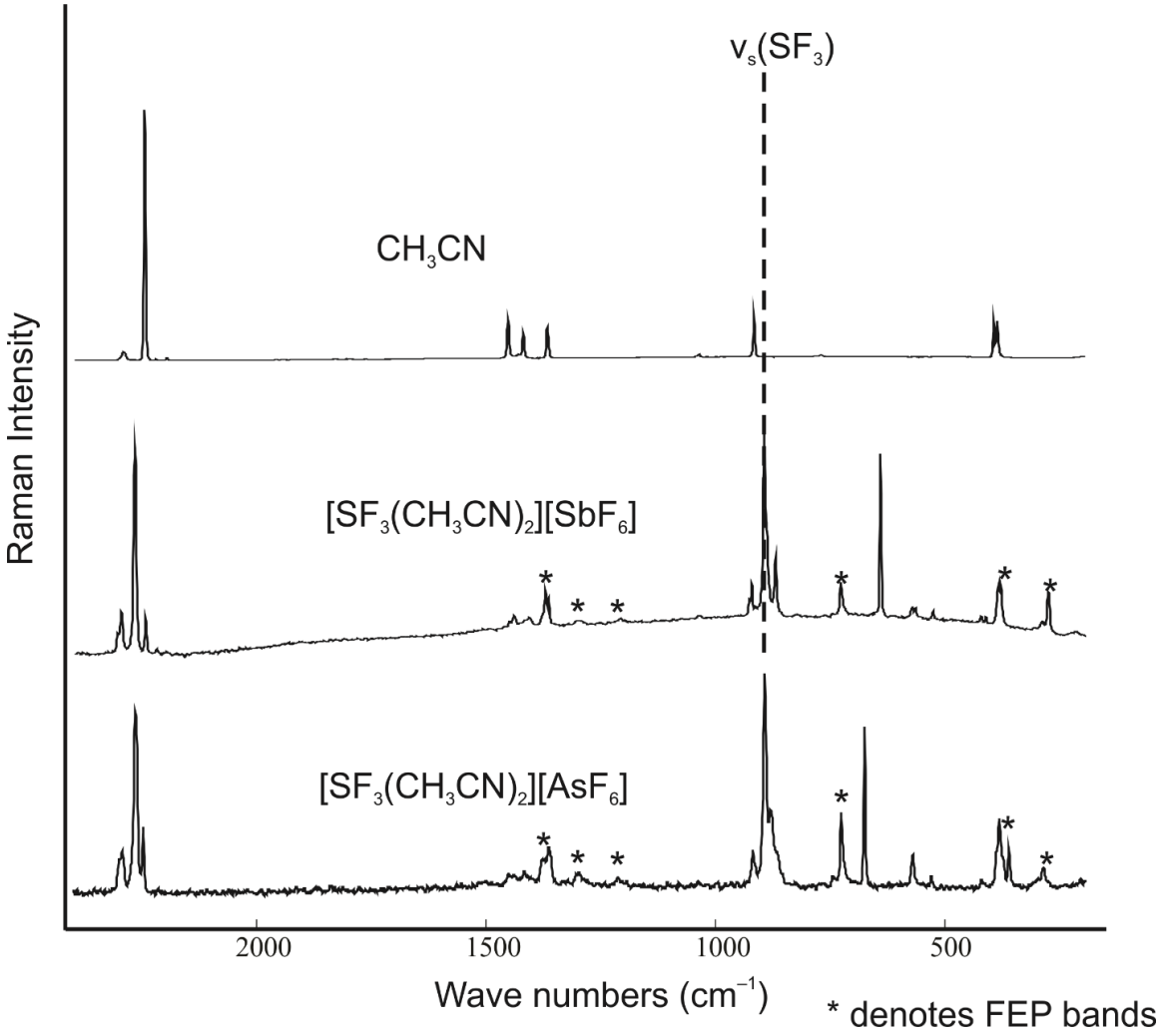

Figure 4.10 Raman spectrum of $[SF_3][SbF_6]$, $[SF_3(CH_3CN)_2][SbF_6]$, $[SF_3(CH_3CN)_2][AsF_6]$ salts and CH_3CN at –110 °C. Asterisks (*) denote bands arising from the FEP sample tube.

Table 4.18 Raman frequencies (relative intensities), cm^{-1} of $[SF_3][SbF_6]$, CH_3CN and $[SF_3(CH_3CN)_2][SbF_6]$ at –110 °C together with their tentative assignments.

Vibrational frequencies			Assignments		
CH_3CN	$[SF_3][SbF_6]$[a]	$[SF_3\cdot(CH_3CN)_2][SbF_6]$[b]	CH_3CN	$[SF_3][SbF_6]$[a]	$[SF_3\cdot(CH_3CN)_2][SbF_6]$[b]
3001(43)		3012(7)			
		3007(13)	$\nu_s(CH_3)$		$\nu_s(CH_3)$
		3000(12)			
2936(90)		2951(44)			
		2946(83)			
2909(1)		2936(19)			
2888(2)		2890(2)			
2850(2)		2875(2)	combination		combination
2817(1)		2843(2)	bands		bands
2732(4)		2734(2)			
2451(1)					
		2309(10)			
2294(3)		2301(19)	$\nu(C\equiv N)$		$\nu(C\equiv N)$
2249(1)		2271(100)			
2248(100)		2248(17)			
2225(1)					
2201(1)					
1456(13)		1454(2)			
1423(8)		1445(4)	CH_3		CH_3
		1412(4)	deformation		deformation
1370(11)		1377(17)			
		1371(13)			
		1305(1)			
		1215(1)[f]			
1040(1)	955(39)				
	939(95)	932(8)		$\nu_s(SF_3)$	
920(15)	929(15)	927(15)			
	923(23)				
		920(4)			
		900(88)			$\nu_s(SF_3)$
		894(sh)			
		876(29)			
774(1)		733(15)[f]			
	671(29)				
	650(100)	647(79)		$\nu(SbF_6)$	$\nu(SbF_6)$
	634(8)				
	617(8)				
	580(17)	577(5)		$\delta(SbF_6)$	$\delta(SbF_6)$
	552(20)	570(2)			
	533(sh)	532(3)		$\delta(SF_3)$	$\delta(SF_3)$
	529(13)				
		427(2)			
	410(11)	417(2)		$\delta_{sciss}(SF_3)$	$\delta_{sciss}(SF_3)$
397(14)		390(11)			
389(14)		385(19)[f]			

[a] The Raman spectrum was recorded in a glass NMR tube at –110 °C. [b] Signals observed at 385(19) and 1377(17) cm^{-1} in the Raman spectrum of $[SF_3(CH_3CN)_2][SbF_6]$ are overlapped with FEP signals. [c] Signals from the FEP sample tube were observed at 733(15), 1215(1), 1305(1) cm^{-1}. [d] Acetonitrile bands have been assigned based on references 26. [e] $[SF_3][SbF_6]$ bands have been assigned based on references 2c.

Table 4.19 Raman frequencies (relative intensities), cm^{-1} of $[SF_3][AsF_6]$, CH_3CN and $[SF_3(CH_3CN)_2][AsF_6]$ at –110 °C together with their tentative assignments.

Vibrational frequencies			Assignments		
CH_3CN	$[SF_3][AsF_6]$[a]	$[SF_3\cdot(CH_3CN)_2][AsF_6]$[b]	CH_3CN	$[SF_3][AsF_6]$[a]	$[SF_3\cdot(CH_3CN)_2][AsF_6]$[b]
3001(43)		3022(9)			
		3016(11)	$\nu_s(CH_3)$		$\nu_s(CH_3)$
		2999(18)			
2936(90)		2955(57))			
2909(1)					
2888(2)					
2850(2)			combination		
2817(1)			bands		
2732(4)					
2451(1)		2301(16)			
2294(3)		2294(20)	$\nu(C\equiv N)$		$\nu(C\equiv N)$
2249(1)		2264(83)			
2248(100)		2248(30)			
2225(1)					
2201(1)		1457(9)			
1456(13)		1442(9)			
1423(8)		1421(11)	CH_3		CH_3
			deformation		deformation
1370(11)		1369(21)			
1040(1)	960(sh)				
	945(81)			$\nu_s(SF_3)$	
920(15)	926(29)	926(20)			
		921(13)			
		900(100)			$\nu_s(SF_3)$
		886(38)			
		872(20)			
		860(9)			
774(1)					
	686(100)	683(74)		$\nu(AsF_6)$	$\nu(AsF_6)$
	587(23)	578(18)		$\delta(AsF_6)$	$\delta(AsF_6)$
	563(32)				
	530(20)	538(7)		$\delta(SF_3)$	$\delta(SF_3)$
	529(13)				
		430(6)			
397(14)	410(22)	397(20)		$\delta_{sciss}(SF_3)$	$\delta_{sciss}(SF_3)$
389(14)		390(34)			

[a] The Raman spectrum was recorded in a glass NMR tube at –110 °C. [b] Signals observed at 385(19) and 1381(16) cm^{-1} in the Raman spectrum of $[SF_3(CH_3CN)_2][AsF_6]$ are overlapped with FEP signals. [c] Signals from the FEP sample tube were observed at 733(37), 1215(7), 1305(11) cm^{-1}. [d] Acetonitrile bands have been assigned based on references 26. [e] $[SF_3][AsF_6]$ bands have been assigned based on references 2c.

4.2.4.4 Raman spectroscopy of $[SF_2(DMAP)_2][SbF_6]_2 \cdot CH_3CN$

The vibrational frequencies of $[SF_2(DMAP)_2][SbF_6]_2 \cdot CH_3CN$ are listed in Table 4.20 and the Raman spectrum is shown in Figure 4.11. In the case of $[SF_2(DMAP)_2][SbF_6]_2 \cdot CH_3CN$, the S–F stretch is at 922 cm^{-1}, at a higher frequency in comparison to that of the $[SF_3(Nitrogen\text{-}base)_2]^+$ salts. This is the result of increased positive ionic charge of this fluorosulfur cation. The DMAP breathing C_5N mode is at 1016 cm^{-1}. This mode has been shifted from 998 to 1009 cm^{-1} in the case of $SF_4 \cdot DMAP$ adduct.[3] Signals attributable to CH_3CN were also observed. The C–N stretching mode appears at the same place as was found in uncomplexed CH_3CN, i.e., at 2248 cm^{-1} indicating the presence of free CH_3CN. The Sb–F stretching frequency for SbF_6^- shifts from 650 to 646 cm^{-1} indicating a very weak interaction between $[SF_2(DMAP)_2]^{2+}$ cation and SbF_6^- anion.

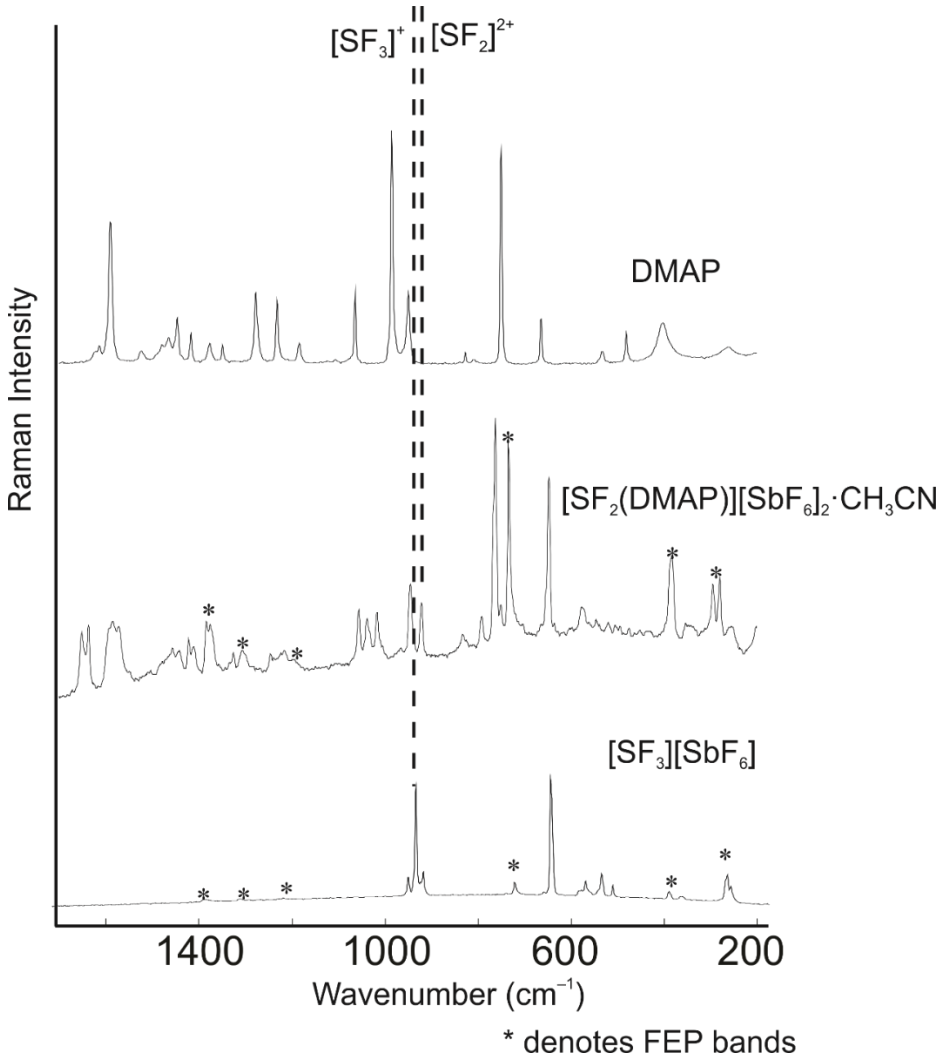

Figure 4.11 Raman spectrum of $[SF_3][SbF_6]$, $[SF_2(DMAP)_2][SbF_6]_2{\cdot}CH_3CN$ and DMAP solids at –110 °C. Asterisks (*) denote bands arising from the FEP sample tube.

Table 4.20 Raman frequencies (relative intensities), cm^{-1} of $[SF_3][SbF_6]$, DMAP and $[SF_2(DMAP)_2][SbF_6]_2 \cdot CH_3CN$ at –110 °C together with their tentative assignments.

Vibrational frequencies			Assignments		
DMAP	$[SF_3][SbF_6]$[b]	$[SF_2(DMAP)_2][SbF_6]_2 \cdot CH_3CN$[b]	DMAP	$[SF_3][SbF_6]$[a]	$[SF_2(DMAP)_2][SbF_6]_2 \cdot CH_3CN$[b]
3089(16)					
3085(16)		3101(8)			
3078(14)		3084(8)	$\nu_s(CH_3)$		$\nu_s(CH_3)$
3070(12)					
3034(13)		3034(6)			
2999(33)		3001(22)			
2941(16)		2945(52)			
2922(18)		2936(35)			
2910(20)			overtones and		overtones and
2870(41)			combination		combination
2856(17)			bands		bands
2843(8)		2859(41)			
2833(8)		2820(6)			
2810(27)		2809(8)			
		2256(29)			
		2248(19)			
		2084(10)			
		2028(6)			
		1653(29)			
		1642(20)			
1621(3)		1636(25)			
1614(5)					
1590(59)		1592(46)	ν(C=C)		ν(C=C)
		1574(23)			
1523(3)		1482(6)			ν(C=N)
1478(7)		1466(8)	ν(C=N)		
1465(9)		1462(8)			
1446(17)		1445(10)			
1437(2)		1421(10)			
1417(11)		1414(10)			
1376(8)		1375(10)			
1349(7)		1324(6)	$\delta(CH_3)$		$\delta(CH_3)$
1277(29)		1282(8)			
1231(26)		1247(8)			
1184(7)		1063(12)			
1064(29)		1056(23)	in-plane ring-		in-plane ring-
		1037(16)	def		def
1031(75)		1016(25)			$\nu_s(C_5N$ ring)
985(100)			$\nu_s(C_5N$ ring)		
949(29)	955(39)	943(34)			
	939(95)			$\nu_s(SF_3)$	
	929(15)	922(12)			$\nu_s(SF_2)$
	923(23)				
		831(8)			

		791(14)		
		766(60)		
		762(100)		
750(92)		751(32)		
		705(6)		
664(20)		664(8)		
	671(29)			
	650(100)	646(75)	$\nu(SbF_6)$	$\nu(SbF_6)$
	634(8)	635(8)		
	617(8)			
	580(17)	577(8)	$\delta(SbF_6)$	$\delta(SbF_6)$
		571(8)		
	552(20)	546(8)	$\delta(SbF_6)$	$\delta(SbF_6)$
532(4)	533(sh)	538(16)		
481(11)	529(13)			
	410(11)		$\delta(SF_3)$	$\delta_{sciss}(SF_3)$
402(16)		353(8)		
	301(8)			
263(3)	286(22)	279(31)	$\delta(SbF_6)$	$\delta(SbF_6)$
	274(12)	256(12)		

[a] The Raman spectrum was recorded in a glass NMR tube at –110 °C. [b] Signal observed at 382(25) cm^{-1} in the Raman spectrum of $[SF_2(DMAP)_2][SbF_6]_2 \cdot CH_3CN$ is overlapped with FEP signals. [c] Signals from the FEP sample tube were observed at 294(16), 733(48), 1307(6), 1382(10) cm^{-1}. [d] DMAP bands have been assigned based on references 27. [e] $[SF_3][SbF_6]$ bands have been assigned based on references 2c.

Table 4.21 Comparison of S–F stretching vibrational frequency

Compounds	S–F stretching frequency, υ (cm^{-1})
γ-$[SF_3][SbF_6]$	939
$[SF_3][AsF_6]$	945
$[SF_3(Py)_2][SbF_6]\cdot CH_2Cl_2$/$[SF_3(Py)_2][AsF_6]\cdot CH_2Cl_2$	816/818
$[SF_3(Py)_2][SbF_6]\cdot CH_3CN$	808, 828
$[SF_3(Py)_2][SbF_6]\cdot C_5H_5N$/$[SF_3(Py)_2][AsF_6]\cdot C_5H_5N$	815/812
$[SF_3(CH_3CN)_2][SbF_6]$/$[SF_3(CH_3CN)_2][AsF_6]$	900/900
$[SF_3(Phen)][SbF_6]\cdot 2CH_2Cl_2$	832
$[SF_2(DMAP)_2][SbF_6]_2\cdot CH_3CN$	922

A comparison of S–F stretching vibrational frequencies of different fluorosulfur cationic species is presented in Table 4.21. The S–F stretching frequency for $[SF_3][SbF_6]$ is present at 939 cm^{-1}. In the case of $[SF_3(C_5H_5N)_2][SbF_6]\cdot CH_2Cl_2$, $[SF_3(C_5H_5N)_2][SbF_6]\cdot CH_3CN$ and $[SF_3(C_5H_5N)_2][SbF_6]\cdot C_5H_5N$, the S–F stretch is shifted to 816, 808 and 815 cm^{-1}. The decrease in stretching frequency is a consequence of the weakening of the S−F bonds in the trifluorosulfur cationic species. This is also supported by the fact that the S–F bond lengths has been increased when SF_3^+ has formed adducts with nitrogen bases (Table 4.5). Similar shifts in Raman frequencies have been observed for $[SF_3(C_5H_5N)_2][AsF_6]\cdot CH_2Cl_2$ (818 cm^{-1}) and $[SF_3(C_5H_5N)_2][AsF_6]\cdot C_5H_5N$ (812 cm^{-1}) as compared to $[SF_3][AsF_6]$ (945 cm^{-1}) for the same reason. In case of $[SF_3(Phen)][SbF_6]\cdot 2CH_2Cl_2$ the Raman signal for the symmetric SF_3 stretch has been shifted to 832 cm^{-1} as compared to 939 cm^{-1} in γ-$[SF_3][SbF_6]$. However, in the case of $[SF_3(CH_3CN)_2][MF_6]$ where M = Sb, As, the S–F stretch is at 900 cm^{-1}. The difference in the SF_3 stretching frequency is directly related to the donor strengths of different nitrogen bases (Table 4.5). The higher the donor strength of the nitrogen base, the shorter the S–N distance, the longer the S–F distance and lower the value of the Raman frequency. In case of $[SF_2(DMAP)_2][SbF_6]_2\cdot CH_3CN$, the value of

the Raman frequency is high i.e. 922 cm^{-1} although DMAP is a stronger base. This is due to an increase in the positive charge on fluorosulfur species from +1 to +2.

4.2.5 ^{19}F NMR spectroscopy

4.2.5.1 ^{19}F NMR spectroscopy of $[SF_3(C_5H_5N)_2][MF_6]\cdot C_5H_5N$ (M = Sb, As), $[SF_3(CH_3CN)_2][MF_6]$ (M = Sb, As), and $[SF_3(phen)][SbF_6]\cdot 2CH_2Cl_2$

The ^{19}F NMR chemical shifts for $[SF_3][SbF_6]$ and $[SF_3][AsF_6]$ salts show a marked solvent dependence in solution. The ^{19}F NMR chemical shifts for $[SF_3][SbF_6]$ and $[SF_3][AsF_6]$ salts in pyridine, acetonitrile and SO_2 solvents are tabulated in Table 4.22. Dissolving the $[SF_3][MF_6]$ (M = Sb, As) salts in a nitrogen-base solvents such as C_5H_5N or CH_3CN results in low frequency ^{19}F chemical shifts between 18.5 and 16.8 ppm in comparison to the values for $[SF_3][MF_6]$ (M = Sb, As) salts in SO_2(l) (31.5, 32.9 ppm), which is an inert solvent for $[SF_3][MF_6]$ (M = Sb, As) salts. Donation of the electron lone pair from nitrogen bases to the SF_3^+ cation renders the S–F bond more ionic by increasing the electron density on sulfur, predicting increased shielding of the fluorine environments. Fast exchange between axial and equatorial fluorine environments result in the observation of only one ^{19}F resonance (except for $[SF_3(phen)][SbF_6]\cdot 2CH_2Cl_2$), even at temperatures as low as –40 °C.

Table 4.22 ^{19}F NMR chemical shifts (δ) of ionic species in different $[SF_3]^+$ and $[SF_2]^{2+}$ salts with different nitrogen bases at –30 °C

Compound	Solvent	Chemical Shift (ppm), δ $[SF_3]^+$	$^2J(^{19}F–^{19}F)$ (Hz)	Chemical Shift (δ), ppm $[MF_6]^–$ (M = Sb, As)	$^1J(^{19}F–^nM)$ (Hz) (^nM = $^{121}Sb/^{123}Sb$ /^{75}As)
$[SF_3][SbF_6]$	SO_2(l)	31.5 (s)	–	–109.5	–
$[SF_3][AsF_6]$	SO_2(l)	32.9 (s)	–	–58.5	–
$[SF_3(C_5H_5N)_2][SbF_6]\cdot C_5H_5N$	C_5H_5N	18.5 (s)	–	–121.3	Overlap
$[SF_3(C_5H_5N)_2][AsF_6]\cdot C_5H_5N$	C_5H_5N	18.5 (s)	–	–64.4	930
$[SF_3(CH_3CN)_2][SbF_6]$	CH_3CN	16.8 (s)	–	–123.3	Overlap
$[SF_3(CH_3CN)_2][AsF_6]$	CH_3CN	18.8 (s)	–	–64.8	933
$[SF_3(Phen)][SbF_6]\cdot CH_2Cl_2$	CH_2Cl_2	27.3 (*d*), 60.3 (*t*)	6.8	–116.7	1950/1013
$[SF_2(DMAP)_2][SbF_6]_2\cdot CH_3CN$	CH_3CN	52.6 (s)	–	–123.0	1946/930

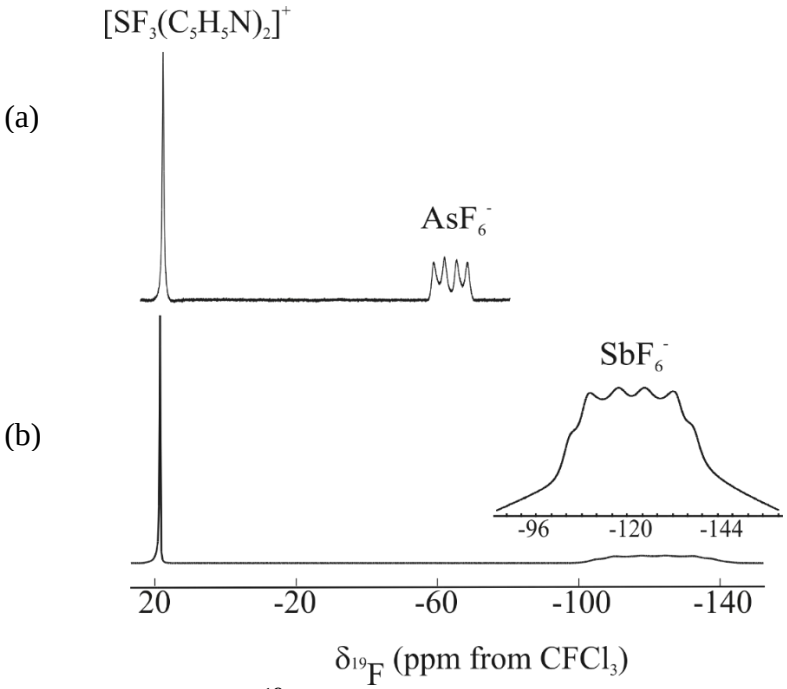

Figure 4.12 Solution-state ^{19}F NMR spectrum of (a) $[SF_3(C_5H_5N)_2][AsF_6]$ and (b) $[SF_3(C_5H_5N)_2][SbF_6]$ in liquid C_5H_5N at –30 °C.

The exchange generally results in relatively sharp ^{19}F cation resonances. The ^{19}F NMR spectrum of $[SF_3(CH_3CN)_2][AsF_6]$ is the exception where a broad singlet is observed at 18.8 ppm ($\Delta\upsilon_{1/2}$ = 912 Hz). This broadening is a result of slowing down the exchange between the cation fluorine environments likely as a consequence of strong cation anion contacts. The AsF_6^- is somewhat more fluorobasic than SbF_6^- and the sulfur in $[SF_3(CH_3CN)_2]^+$ is more electrophilic than in $[SF_3(C_5H_5N)_2]^+$. Therefore, the cation-anion interactions are the most severe in the $[SF_3(CH_3CN)_2][AsF_6]$ among the salts in this chapter. For all adduct salts, coupling of ^{19}F with the quadrupolar nuclei ^{75}As and $^{121}Sb/^{123}Sb$ were observed.

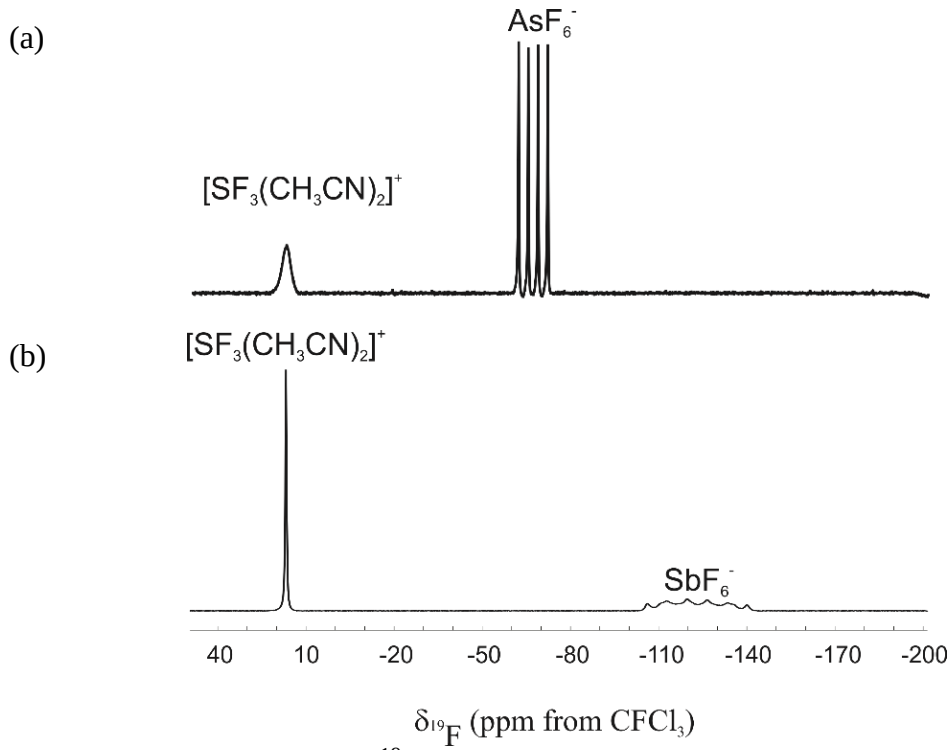

Figure 4.13 Solution-state ^{19}F NMR spectrum of (a) $[SF_3(CH_3CN)_2][AsF_6]$ and (b) $[SF_3(CH_3CN)_2][SbF_6]$ in liquid CH_3CN at –30 °C.

The dissociation of the nitrogen-base from the $[SF_3(\text{Nitrogen-base})_2]^+$ adduct with subsequent rapid exchange with the nitrogen base solvent is hypothesized to be the mechanism of exchange of the axial and equatorial fluorine environments. This mechanism would go via a trigonal bipyramidal electron group geometry, which can scramble the axial and equatorial fluorine environments via the Berry pseudo rotation. The use of the chelating ligand 1,10-phenanthroline was expected to increase the kinetic stability of the adduct between SF_3^+ cation and the nitrogen base. The ^{19}F NMR spectrum of $[SF_3(Phen)][SbF_6]$ salt in CH_3CN solvent gave rise to resonances at 22.7 and 56.1 ppm in a 2:1 ratio for the equatorial and axial fluorine environments, respectively, at –35 °C while in CH_2Cl_2 solvent the resonances are at 27.3 and 60.3 ppm for the equatorial and axial fluorine at –40 °C, respectively. In CH_2Cl_2 solvent, coupling was revealed. The axial fluorine is a triplet and the equatorial fluorine a doublet with a $^2J(^{19}F–^{19}F)$ coupling constant of 6.8 Hz in CH_2Cl_2 solvent. Production of SF_4 may be the result of residual moisture in CH_2Cl_2 because no SF_4 signal was observed in well dried CH_3CN solvent (Figure 4.14). A two-dimensional $^{19}F–^{19}F$ magnitude COSY experiment clearly showed a correlation between the resonances at 27.3 and 60.3 ppm of $[SF_3(Phen)]^+$ in the form of cross peaks. Furthermore, the same sign of the $^2J(^{19}F–^{19}F)$ coupling constant for $[SF_3(Phen)]^+$ and SF4 was confirmed by 2D $^{19}F–^{19}F$ COSY45 experiment (Figure 4.16). The high resolution in the COSY45 showed the same leaning behaviour of the doublet and triplet for $[SF_3(Phen)]^+$ in correspondence with the leaning behaviour of the two triplets for SF_4. This behaviour prove the same sign of $^2J(^{19}F–^{19}F)$ coupling for $[SF_3(Phen)]^+$ and SF_4. The ^{19}F signal for SbF_6^- is at –123.3 ppm in the form of a broad pattern because of fast relaxation of the quadrupolar $^{121,123}Sb$ nuclei.

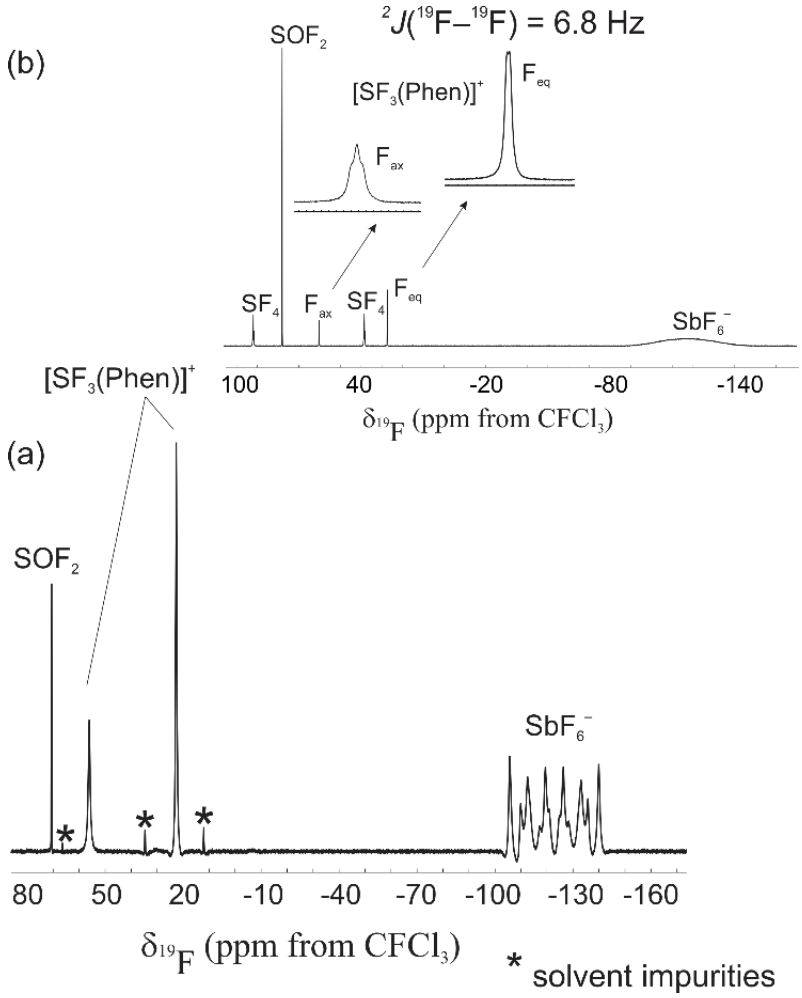

Figure 4.14 (a) Solution-state ^{19}F NMR spectrum of 1:1 ratio of $[SF_3][SbF_6]$ and 1,10-phenanthroline in liquid CH_3CN at –35 °C (b) in liquid CH_2Cl_2 at –40 °C. The production of SF_4 in (b) is a result of the presence of moisture in CH_2Cl_2.

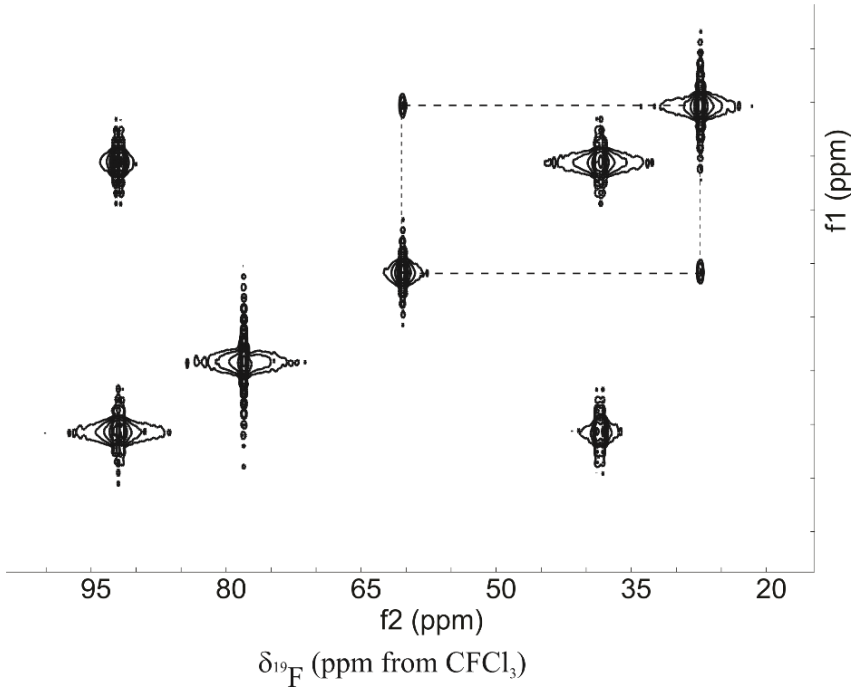

Figure 4.15 Solution-state ^{19}F–^{19}F COSY NMR spectrum of 1:1 ratio of $[SF_3][SbF_6]$ and 1,10-phenanthroline in liquid CH_2Cl_2 at –40 °C.

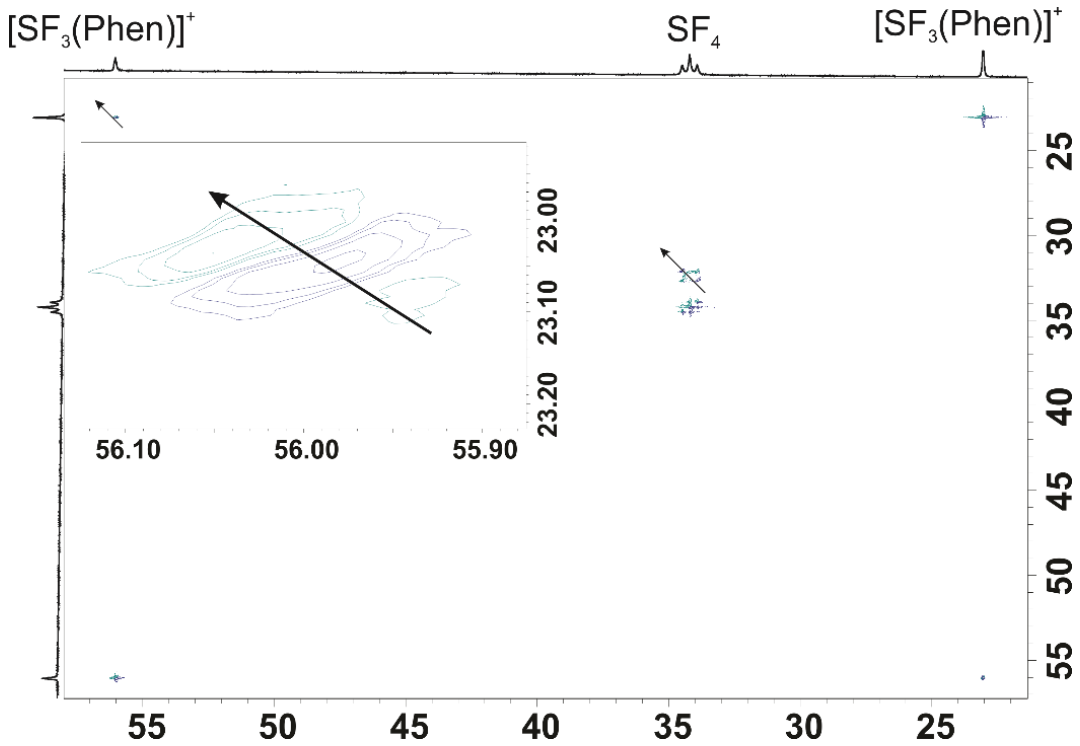

Figure 4.16 Solution-state ^{19}F–^{19}F COSY45 NMR spectrum of 1:1 ratio of $[SF_3][SbF_6]$ and 1,10-phenanthroline in liquid CH_2Cl_2 at –40 °C.

4.2.5.2 ^{19}F NMR spectroscopy of $[SF_2(DMAP)_2][SbF_6]_2 \cdot CH_3CN$

The ^{19}F NMR chemical shift for the $[SF_2(DMAP)_2]^{2+}$ cation, as the product of the reaction of $[SF_3][SbF_6]$ salt with DMAP in a 1:1 ratio in CH_3CN, is a singlet at 52.6 ppm due to the presence of only one fluorine environment. The chemical shift for this fluorosulfur (IV) cation has moved to higher frequency due to an increase in the positive ionic charge, i.e. +2, in comparison to the $[SF_3(C_5H_5N)_2]^+$ cation, which results in less polar S–F bonding. The SbF_6^- anion signal is at –123.0 ppm with the values for $^1J(^{121}Sb–^{19}F)$ and $^1J(^{123}Sb–^{19}F)$ 1946 and 930 Hz as obtained by deconvolution, in agreement with the literature.[7] The stoichiometry of the dismutation reaction (Eq 4) was confirmed by integrating the resonance at 52.6 ppm with respect to the two triplet resonances for SF_4 at 32.8 and 84.2 ppm. The integration shows 0.98:1.06:1.00 ratio for the resonances at 32.8, 52.6 and 84.2 ppm confirming the equimolar ratio of $[SF_2(DMAP)_2]^{2+}$ and SF_4.

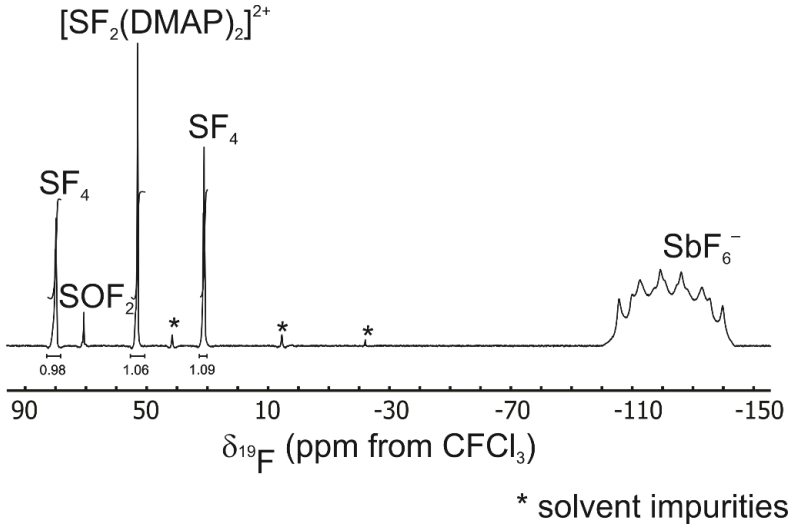

Figure 4.17 Solution-state ^{19}F NMR spectrum of 1:1 ratio of $[SF_3][SbF_6]$ and 4-dimethylamino pyridine (DMAP) in liquid CH_3CN at –30 °C.

4.3 Conclusion and future directions

A series of adducts between $[SF_3][MF_6]$ (M = Sb, As) and nitrogen bases was studied and conclusively characterized. The 1:2 adducts using C_5H_5N and CH_3CN were found to be stable at low temperature. For the bidentate ligand 1,10-phenanthroline, a 1:1 adduct was obtained. The synthesis and conclusive characterization of $[SF_3(N\text{-base})][MF_6]$ (M = Sb, As) is still pending. The reactions of the $[SF_3(N\text{-base})_x]^+$ cation with highly Lewis acidic materials such as AsF_5 and SbF_5 can be studied to synthesize $[SF_2(N\text{-base})_x]^{2+}$ compounds. In the future, the nitrogen bases can be replaced with oxygen bases to study $[SF_3(O\text{-base})][MF_6]$ and $[SF_3(O\text{-base})_2][MF_6]$ (M = Sb, As) compounds to better understand the reactive intermediate species in the deoxofluorination reactions of carbonyl compounds.

References

1. Gibler, D. D.; Adams, C. J.; Fischer, M.; Zalkin, A.; Bartlett, N. *Inorg. Chem.* **1972**, *11*, 2325.

2. (i) Mallouk, T. E.; Bernard, D.; Bartlett, N. *Inorg. Chem.* **1984**, *23*, 3160 (ii) Mallouk, T. E.; Rosenthal, G. L.; Müller, G.; Brusasco, R.; Bartlett, N. *Inorg. Chem.* **1984**, *23*, 3167

3. Chaudhary, P.; Goettel, J. T.; Hazendonk, P.; Sowlati-Hashjin, S.; Mercier, H.P.A.; Gerken, M. *Chem. Eur. J.* **2015**, *21*, 6247.

4. Erhart, M.; Mews, R. *Z. Anorg. Allg. Chem.* **1992**, 615, 117.

5. Smith, G. L; Mercier, H. P. A.; Schrobilgen, G. *Inorg. Chem.* **2011**, *50*, 12359.

6. Cheung, Y. S.; Chen, Y. J.; Ng, C. Y.; Chiu, S. W.; Li, W. K. *J. Am. Chem. Soc.* **1995**, *117*, 9725.

7. Wong, P. S. H.; Ma, S.; Yang, S. S.; Cooks, R. G. *Am. Soc. Mass Spec.* **1997**, *8*, 68.

8. Gozzo, F. C.; Ifa, D. R.; Eberlin, M. N. *J. Org. Chem.* **2000**, *65*, 3920.

9. Sparrapan R., Mendes M. A., Eberlin M. N. *Int. J. Mass Spec.* **1999**, *182/183*, 369.

10. Bittner, J.; Fuchs, J.; Seppelt, K. *Z. Anorg. Allg. Chem.* **1988**, *557*, 182.

11. Smith, G. L; Mercier, H. P. A.; Schrobilgen, G. *Inorg. Chem.* **2009**, *48*, 7714.

12. Bondi, A. *J. Phys. Chem.* **1964**, *68*, 441. (b) Datars, W. R.; Ummat, P. K. *Solid State Commun.* **1995**, *94*, 649.

13. Syvret, R. G. *Inorg. Chem.* **1999**, *38*, 4784.

14. Chaudhary, P. **M.Sc. Thesis 2011**, University of Lethbridge.

15. Marzocchi, M. P.; Migliorini, M. G. *Spectrochim. Acta A* **1973**, *29*, 1643.

16. Nieboer, J.; Yu, X.; Chaudhary, P.; Mercier, H. P. A.; Gerken, M. *Z. Anorg. Allg. Chem.* **2012**, *638*, 520.

17. Muniz-Miranda, M. *J. Phys. Chem. A* **2000**, *104*, 7803.

18. Nieboer, J.; Hillary, W.; Yu, X.; Mercier, H. P. A.; Gerken, M. *Inorg. Chem.* **2009**, *48*, 11251.

19. Miller, T. M.; Viggiano, A. A.; Dolbier, W. R.; Sergeeva, T. A.; Friedman, J. F. *J. Phys. Chem. A.* **2007,** *111*, 1024.

20. Cohen, B.; Hoover, T. R.; Pered, R. D. *Inorg. Nucl. Chem.* **1966**, *28*, 919.

21. Cohen, B.; MacDiarmind, A. G. *Angew. Chem., Int. Ed.* **1963**, *75*, 207.

22. Muetterties, E. L. *J. Am. Chem. Soc.* **1960**, *82*, 1082.

23. Padma, D. K. *J. Fluorine Chem.* **1974**, *4*, 441.

24. Reiher, M.; Brehm, G.; Schneider, S. *J. Phys. Chem. A* **2004**, *108*, 734.

25. Miranda, M. M. *J. Phys. Chem. A* **2000**, *104*, 7803.

26. Marzocchi, M. P.; Migliorini, M. G. *Spectrochim. Acta A* **1973**, *29*, 1643.

27. Sundaraganesan, N.; Kalaichelvan, S.; Meganathan, C.; Joshua, B. D.; Cornard, J. *Spectrochim. Acta* **2008**, *71*, 898.

28. Janzen, A. F. *Coord. Chem. Rev.* **1994** *130*, 355.

Chapter-5

5. Synthesis and characterization of $WOF_4 \cdot SO_2$, $[(CH_3)_4N][WOF_5]$, and $CH_3CN \cdot WOF_3(OCH_2CF_3)$

5.1 Introduction

Tungsten oxytetrafluoride, WOF_4, is a moderately strong Lewis acid and can accept electrons from weak as well as strong nitrogen bases such as CH_3CN and C_5H_5N. The adducts of WOF_4 with C_5H_5N, i.e. $WOF_4 \cdot nC_5H_5N$ (n = 1, 2) show characteristic W=O stretching frequencies of 996 cm^{-1} ($WOF_4 \cdot C_5H_5N$) and 969 cm^{-1} ($WOF_4 \cdot 2C_5H_5N$) in the Raman spectra compared to 1056 cm^{-1} for WOF_4. The ^{19}F chemical shift of these adducts (63.9 ppm for $WOF_4 \cdot C_5H_5N$ with $^1J(^{183}W–^{19}F)$ of 67 Hz; 63.6 ppm for $WOF_4 \cdot 2C_5H_5N$ with $^1J(^{183}W–^{19}F)$ of 67 Hz) appear at lower frequency compared to that of WOF_4 (70.5 ppm) in CH_2Cl_2 solvent.[1,2] X–ray crystallography showed the octahedral geometry of $WOF_4 \cdot C_5H_5N$ and pentagonal bipyramidal geometry of $WOF_4 \cdot 2C_5H_5N$.[1,2] The adduct formation of WOF_4 with CH_3CN was identified solely based on the ^{19}F NMR spectroscopy results where a change in the chemical shift was observed for WOF_4 upon addition of one equivalent of CH_3CN from 69.0 ppm to 66.9 ppm with $^1J(^{183}W–^{19}F)$ of 68 Hz using chloroform as solvent.[10] The Lewis acidity of WOF_4 is also reflected by its tetrameric fluorine bridged structure in the solid state and in CH_2Cl_2 solvent.[1] The tetramer gets converted to monomeric $WOF_4 \cdot CH_3CN$ in CH_3CN solvent. Furthermore, WOF_4 was found to be soluble in liquid SO_2. The observation of a narrow singlet at –73.9 ppm with $^1J(^{183}W–^{19}F)$ coupling constant of 64 Hz at 28 °C[4] suggests the monomeric nature of WOF_4 in SO_2.

Due to the Lewis acidic nature of WOF_4, F^- ion addition to WOF_4 results in the formation of WOF_5^- salts. The known WOF_5^- compounds are summarized in Table 5.1 with their characterization methods.

Table 5.1 Known WOF_5^- compounds and their characterization techniques

WOF_5^- salts	Vibrational spectroscopy	NMR spectroscopy	X-ray diffractometry	Elemental analysis (EA)	Ref
$[NO][WOF_5]$	Raman	Solution ^{19}F NMR	Powder X-ray Diffraction		7
$[NF_4][WOF_5]$	IR & Raman	Solution ^{19}F NMR		EA	6,19
$[EMIM][WOF_5]$[a]	IR & Raman			EA	5
$[As(Ph)_4][WOF_5]$			X-ray crystallography (Disordered structure)	EA	8

[a] [EMIM] is 1-ethyl 3-methylimidazolium cation

WOF_5^- salts have been prepared in several ways. For example, Hagiwara et al. reported the synthesis of the WOF_5^- salt of 1-ethyl 3-methyl imidazolium (EMIM), i.e. $[EMIM][WOF_5]$, by the reaction of $[EMIM][(HF)_{2.3}F]$ with WOF_4 and characterized it by Raman spectroscopy.[5] Similarly, Wilson and Christe synthesized $[NF_4][WOF_5]$ by the reaction of $[NF_4][HF_2]$ with WOF_4 in the presence of HF and characterized it by IR, Raman and solution ^{19}F NMR spectroscopy.[6] Charpin et al. synthesized $[NO][WOF_5]$ by the decomposition of $[NO]_2[WOF_6]$, which was synthesized by the reaction of FNO and WOF_4, and characterized $[NO][WOF_5]$ by Raman and NMR spectroscopy, as well as by powder X-ray diffraction.[7] However, the only X-ray crystal structure known thus far for WOF_5^- salt is of tetraphenylarsonium oxo-pentafluoro-tungstenate ($[As(Ph)_4][WOF_5]$) which exhibits a 50:50% disorder between oxygen and the axial fluorine on tungsten[8] and therefore no ordered structure of the WOF_5^- with accurate metric parameters is known prior to this work to clearly predicting the accurate distances to axial oxygen and fluorine. The $[As(Ph)_4][WOF_5]$ salt was synthesized by stirring 3.38 mmol of $[As(Ph)_4][Cl_5W{\equiv}N{-}CCl_3]$

with 24 mmol of AgF in 30 ml of CH_3CN and 0.06 g of water.[6] A ^{19}F and ^{129}Xe solution NMR study showed that WOF_4 and XeF_2 form an adduct.[9] A doublet for the terminal fluorine atoms on W and a quintet for the bridging fluorine atom was observed in the ^{19}F solution NMR spectrum. ^{19}F solution NMR spectroscopy data of the known WOF_5^- systems and $FXeFWOF_4$ adduct are summarized in Table 5.2.

Table 5.2 ^{19}F solution NMR spectroscopy of known WOF_5^- salts and $FNgFWOF_4$ (Ng = Xe, Kr) adducts

WOF_5^- salts	Solvent system	Temperature (°C)	δ (ppm)	$^2J(^{19}F–^{19}F)$	$^1J(^{183}W–^{19}F)$	Ref
$[NO][WOF_5]$	HF/ClF_3	10	+49.2 –145.7	57.5	70/55	7
$[WOF_5]^-$	$HF/WOCl_4$	RT	53.7 –104.0	55	72	3
$XeF_2{\cdot}WOF_4$	SO_2ClF	–124	69.7 –166.8	55	–	18
$KrF_2{\cdot}WOF_4$	SO_2ClF	–121	67.9 –26.1	48	–	18
$[WOF_5]^-$	CH_3CN	RT	48.4 –83.5	51.9	–	20

The value for the H–F bond dissociation enthalpy, (i.e., 568 kJ/mol at 25°C) is among one of the highest known bond enthalpies. Thus, HF formation as the driving force has been utilized for substituting one or more fluorides from WF_6 with the $^-OCH_2CF_3$ nucleophilic ligand.[10] $F_5W(OCH_2CF_3)$ and cis-$F_4W(OCH_2CF_3)_2$ were prepared from WF_6 and CF_3CH_2OH in 1:1 and 1:2 stoichiometry and have been characterized by solution ^{19}F NMR and Raman spectroscopy. Cis-$F_4W(OCH_2CF_3)_2$ was also characterized by X-ray crystallography.[10] A number of other substituents have been introduced in WF_6, i.e. the $^-$OR groups with R = $–CH_3$, $–C_2H_5$ and $–C_6H_5$.[11,12,13,14] Instead of utilizing the alcohol, Noble and Winfield synthesized monosubstituted $F_5W(OR)$ (R = $–CH_3$, $–C_2H_5$ and $–C_6H_5$)

compounds by the reaction of WF_6 with dialkyl and diaryl sulphites.[13] They were also able to obtain a series $WF_{6-n}(OR)_n$ (R = CH_3, C_2H_5, C_6H_5) to a maximum of four substituted fluorine atoms (n = 4) by reacting WF_6 with methylalkoxy and methylphenoxy silanes.[11] They also obtained $WF_4(OCH_3)_2$ by the reaction of $WF_5(OCH_3)$ with $[(CH_3O)_2SO]$. All of the WF_6 derivatives were identified by ^{19}F NMR spectroscopy.

5.2 Results and discussion

5.2.1 Synthesis and properties of $WOF_4{\cdot}SO_2$, $[(CH_3)_4N][WOF_5]$, and $CH_3CN{\cdot}WOF_3(OCH_2CF_3)$

5.2.1.1 Synthesis and properties of $WOF_4{\cdot}SO_2$

The $WOF_4{\cdot}SO_2$ adduct was synthesized by the reaction of WOF_4 with excess SO_2 at low-temperature (–30 °C) according to the reaction equation 5.1. The resultant $WOF_4{\cdot}SO_2$ adduct is a white solid which is highly soluble in SO_2. Reaction (1) is reversible and neat WOF_4 was recovered after pumping off SO_2 to ambient temperature.

$$WOF_4 + SO_2 \underset{}{\overset{-30\ ^\circ C}{\rightleftharpoons}} WOF_4{\cdot}SO_2 \quad \text{..... (5.1)}$$

The ^{19}F solution NMR spectroscopy of WOF_4 was performed using excess SO_2 as solvent at –60 °C. A single fluorine resonance at 74.9 ppm with tungsten satellites ($^1J(^{183}W–^{19}F)$ = 65.4 Hz) was observed due to equivalent fluorine environments about tungsten. This signal compares well with the literature value (73.9 ppm).[4]

5.2.1.2 Synthesis and properties of $[(CH_3)_4N][WOF_5]$

Tetramethylammonium oxypentafluorotungstate, $[(CH_3)_4N][WOF_5]$, was synthesized by reacting a 1:1 molar ratio of $[(CH_3)_4N][F]$ and WOF_4 at –30 °C in CH_3CN solvent and subsequently removing CH_3CN under dynamic vacuum as well as allowing the resultant

white solid to warm up to room temperature. The $[(CH_3)_4N][WOF_5]$ salt is highly soluble in CH_3CN.

$$[(CH_3)_4N][F] + WOF_4 \xrightarrow[CH_3CN]{-30\ ^\circ C} [(CH_3)_4N][WOF_5] \quad \text{.....(2)}$$

The ^{19}F NMR spectrum of $[(CH_3)_4N][WOF_5]$ was recorded in CH_3CN solvent (Table 5.2). The ^{19}F NMR spectrum using CH_3CN solvent shows a doublet at 48.2 ppm for the four equivalent equatorial fluorine atoms and a quintet at –82.8 ppm for axial fluorine (Figure 5.1). The observed $^2J(^{19}F–^{19}F)$ and $^1J(^{183}W\text{-}^{19}F)$ are in agreement with the literature value obtained for WOF_5^- anion.[7,20] The observed solvent dependence (see Table 5.2 and 5.3) of the chemical shift corresponding to the axial fluorine indicates strong $F_{ax}\cdots$solvent interactions if solvents such as HF are used.

Table 5.3 ^{19}F NMR spectroscopy data for $[N(CH_3)_4][WOF_5]$

Chemical shift (ppm)	Species	Solvent	Scalar-coupling(J) (Hz)	Assignment(s)
48.2	F_{eq}	CH_3CN	52.1/71.5	$^2J(^{19}F\text{-}^{19}F)/^1J(^{183}W\text{-}^{19}F_{eq})$
–82.8	F_{ax}	CH_3CN	52.1/52.7	$^2J(^{19}F\text{-}^{19}F)/^1J(^{183}W\text{-}^{19}F_{ax})$

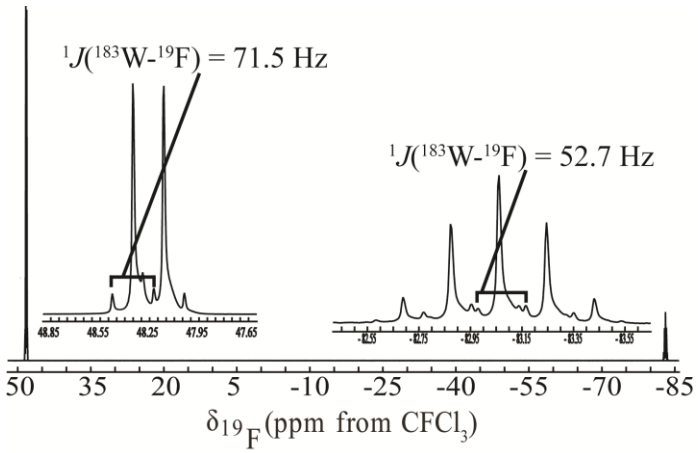

Figure 5.1. ^{19}F NMR spectrum of $[N(CH_3)_4][WOF_5]$ in CH_3CN solvent

Comparing the ^{19}F chemical shifts of the four equatorial fluorine atoms in WOF_4 adducts, the trend of decreasing ^{19}F chemical shifts with increasing donor strength of the Lewis base is observed ($WOF_4 \cdot SO_2$: 74.9 ppm, $WOF_4 \cdot C_5H_5N$: 63.9 ppm[4], $WOF_4 \cdot F^-$: 48.2 ppm).

5.2.1.3 Synthesis and properties of $CH_3CN \cdot WOF_3(OCH_2CF_3)$

Tungsten oxytetrafluoride, WOF_4, was reacted with excess CF_3CH_2OH at ambient temperature in the absence of a solvent. Exclusively, the monosubstituted $W(O)F_3(OCH_2CF_3)$, a colorless translucent liquid at room temperature, was obtained and characterized by Raman and ^{19}F solution NMR spectroscopy. The state of matter of the related $F_5W(OCH_2CF_3)$ has also been found to be liquid at room temperature.[10]

$$WOF_4 + CF_3CH_2OH \longrightarrow W(O)F_3(OCH_2CF_3) + HF \quad \text{.....(5.3)}$$

The ^{19}F solution NMR spectroscopy indicated the formation of $W(O)F_3(OCH_2CF_3)$. The ^{19}F solution NMR spectrum of $W(O)F_3(OCH_2CF_3)$ was recorded using excess CF_3CH_2OH as solvent and is shown in Figure 5.3. The chemical shifts and the coupling constants are given in Table 5.4. The ^{19}F AX_2 NMR spectrum comprises a doublet at 22.3 ppm with a $^2J(^{19}F–^{19}F)$ coupling of 79.2 Hz and with tungsten satellites ($^1J(^{183}W–^{19}F)$ = 72.6 Hz) for the two equivalent *cis*-fluorine and a triplet at 15.6 ppm with tungsten satellites ($^1J(^{183}W–^{19}F)$ = 49.6 Hz) for one *trans*-fluorine. The ^{19}F NMR spectrum is in agreement with a monomeric square pyramidal structure (Fig. 5.2). The size of the $^1J(^{183}W–^{19}F)$ value is in agreement with the literature value obtained for mono substituted WF_6 products and for WOF_5^- anion.[8]

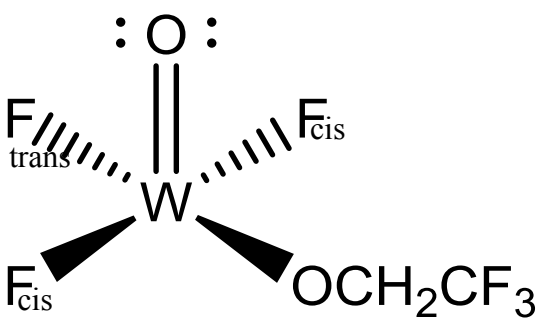

Figure 5.2 Wedge and dash diagram of $W(O)F_3(OCH_2CF_3)$

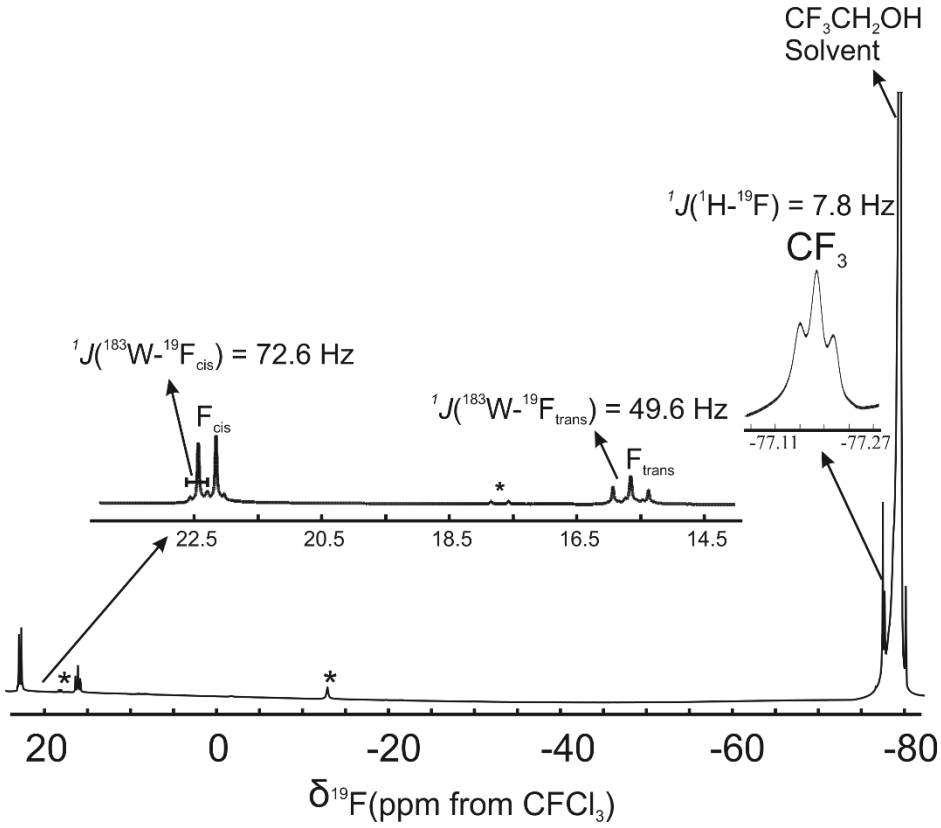

Figure 5.3 ^{19}F NMR spectrum of $W(O)F_3(OCH_2CF_3)$, *represents impurities

Table 5.4 ^{19}F chemical shifts for $W(O)F_3(OCH_2CF_3)$

Chemical shift (ppm)[a]	Species	Scalar-coupling(*J*) (Hz)	Assignment(s)
22.3(d)	$^{19}F_{cis}$	79.2/72.6	^2J (^{19}F-^{19}F)/^1J (^{183}W-$^{19}F_{cis}$)
15.6(t)	$^{19}F_{trans}$	79.2/49.6	^2J (^{19}F-^{19}F)/^1J (^{183}W-$^{19}F_{trans}$)
–77.1(t)	$-CF_3$	7.8	^3J(^1H-^{19}F)

[a] d-doublet, t-triplet

Reacting $W(O)F_3(OCH_2CF_3)$ with excess CH_3CN at ambient temperature yielded the $CH_3CN{\cdot}WOF_3(OCH_2CF_3)$ adduct. The resultant adduct is a white solid and is soluble in CH_2Cl_2, from which the crystals of $CH_3CN{\cdot}W(O)F_3(OCH_2CF_3)$ were grown.

$$W(O)F_3(OCH_2CF_3) + CH_3CN \longrightarrow CH_3CN{\cdot}W(O)F_3(OCH_2CF_3) \quad \text{.....(4)}$$

5.2.2 X-ray crystallography

5.2.2.1 X-ray crystallography of $WOF_4{\cdot}SO_2$

Crystals of $WOF_4{\cdot}SO_2$ were grown from SO_2 at low temperature (–70 °C). $WOF_4{\cdot}SO_2$ crystallizes in monoclinic space group $P2_1/c$ with four formula units per unit cell (Table 5.5). The structural unit of $WOF_4{\cdot}SO_2$ crystal structure is shown in Figure 5.4 while the bond lengths and bond angles are given in Table 5.6. In the crystal structure of $WOF_4{\cdot}SO_2$ adduct, the SO_2 molecule is joined to WOF_4 with a weak coordinate W···O bond. The $WOF_4{\cdot}SO_2$ adduct has a six coordinate W center with four fluorine atoms in the equatorial plane and the two oxygen atoms on the axial position, one strong covalent W1–O1 bond with a bond length of 1.658(5) Å, and a weak co-ordinate W1–O2 bond with a bond length of 2.381(5) Å. The O1–W1–O2 angle is essentially linear (179.2(2)°). The W–F bond lengths in $WOF_4{\cdot}SO_2$ range from 1.841(4) to 1.859(4) Å. A meaningful comparison of bond lengths and angles with those of WOF_4 (determined in 1968 at ambient temperature) and $WOF_4{\cdot}C_5H_5N$ (determined in 1988 at 22 °C) is not possible because of the large uncertainties in the metric parameters of these two structures. The monomeric structure of $WOF_4{\cdot}SO_2$ indicates the monomerization of the $(WOF_4)_4$ tetramer upon dissolution in SO_2.

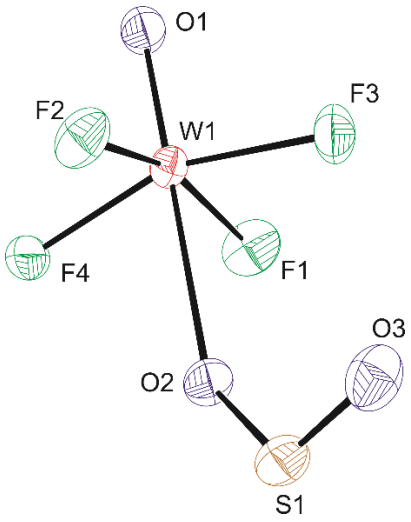

Figure 5.4 Thermal ellipsoid plot of the structural unit of $WOF_4 \cdot SO_2$ in the crystal structure of $WOF_4 \cdot SO_2$ at 50% probability level.

Table 5.5 Crystallographic data for $WOF_4 \cdot SO_2$, $CH_3CN \cdot WOF_3(OCH_2CF_3)$ and $[(CH_3)_4N][WOF_5]$

Chemical formula	$WOF_4 \cdot SO_2$	$[(CH_3)_4N][WOF_5]$	$CH_3CN \cdot WOF_3(OCH_2CF_3)$
Crystal system	Monoclinic	Tetragonal	Monoclinic
Space group	$P2_1/c$	$P4/n$	$P2_1/c$
a (Å)	7.7097(15)	8.205(3)	8.1236(12)
b (Å)	7.2274(14)	8.205(3)	12.7219(19)
c (Å)	10.244(2)	6.989(2)	8.9834(13)
α (°)	90	90	90
β (°)	90.530(2)	90	97.386(2)
γ (°)	90	90	90
Z	4	2	4
Formula weight (g mol^{-1})	339.91	369.00	396.94
Calcd density (g cm^{-3})	3.956	2.604	2.864
T (°C)	–120	–120	–120
μ (mm^{-1})	20.629	12.311	12.618
R_1[a]	0.0310	0.0209	0.0325
wR_2[b]	0.0479	0.0391	0.0646

[a] R_1 is defined as $\Sigma||F_o| - |F_c||/\Sigma|F_o|$ for $I > 2\sigma(I)$. [b] wR_2 is defined as $[\Sigma[w(F_o^2 - F_c^2)^2]/\Sigma w(F_o^2)^2]^{½}$ for $I > 2\sigma(I)$.

Table 5.6 Bond lengths (Å) and bond angles (°) of $WOF_4 \cdot SO_2$ adduct

Bond lengths (Å)		Bond angles (°)	
W1-O1	1.658(5)	O1-W1-F1	100.2(2)
W1-O2	2.381(5)	O1-W1-F2	101.2(2)
		O1-W1-F3	100.6(2)
W1-F1	1.859(4)	O1-W1-F4	101.3(2)
W1-F2	1.841(4)	O1-W1-O2	179.2(2)
W1-F3	1.842(4)	F1-W1-F2	158.58(18)
W1-F4	1.855(4)	F1-W1-F3	87.65(18)
		F1-W1-F4	86.62(18)
S1-O2	1.446(5)	F2-W1-F3	89.52(17)
S1-O3	1.410(5)	F2-W1-F4	88.12(18)
		F3-W1-F4	157.99(18)
		F1-W1-O2	79.30(17)
		F2-W1-O2	79.30(17)
		F3-W1-O2	79.99(17)
		F4-W1-O2	78.07(17)
		S1-O2-W1	141.3(3)
		O3-S1-O2	117.6(3)

5.2.2.2 X-ray crystallography of $[(CH_3)_4N][WOF_5]$

Crystals of $[(CH_3)_4N][WOF_5]$ were grown from anhydrous HF at low temperature (–70 °C). $[(CH_3)_4N][WOF_5]$ crystallizes in the tetragonal space group *P*4*/n* with two formula units per units cell (Table 5.4). The structural unit of $[(CH_3)_4N][WOF_5]$ crystal is shown in Figure 5.5 while the bond lengths and bond angles are given in Table 5.7. The WOF_5^- is a distorted octahedron with the axial W–F bond (1.943(6) Å), which is trans to the W–O bond, being longer than the crystallographically equivalent equatorial W–F bonds (1.859(3) Å). This elongation is a consequence of the trans influence of the W–O bond that has significant double bond character (W1–O1 = 1.675(8) Å).

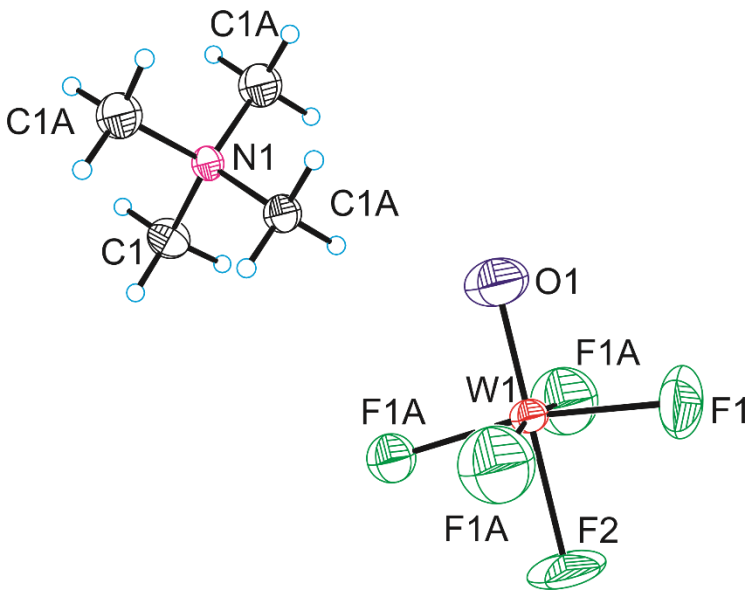

Figure 5.5 Thermal ellipsoid plot of the structural unit of $[(CH_3)_4N][WOF_5]$ in the crystal structure of $[(CH_3)_4N][WOF_5]$ at 50% probability level.

The O1–W1–F2 angle in the $[WOF_5]^-$ anion is 180.0°. The W1–O1 bond length (1.675(8) Å) is longer than the W1–O1 bond length ((1.658(5) Å)) found in $WOF_4 \cdot SO_2$ (section 5.3.1) reflecting the higher Lewis basicity of naked F^- versus SO_2. The equatorial W–F bond lengths (1.859(3) Å) are comparable to those in $[(Ph)_4As][WOF_5]$ (1.852(7) Å)[8] and $WOF_4 \cdot SO_2$ (1.841(4) to 1.859(4) Å). The average of the W–F2 and W=O bond lengths in $[(CH_3)_4N][WOF_5]$ (1.809 Å) is comparable to the average bond length of 1.822(13) Å for $[(Ph)_4As][WOF_5]$, which exhibits a 50:50% disorder between these axial atoms. The O1–W1–F2 angle (180.0°) in $[WOF_5]^-$ anion of $[(CH_3)_4N][WOF_5]$ is perfectly linear and is comparable to the O–W–F1 angle in $[(Ph)_4As][WOF_5]$ (180.0°)[7] and O1–W–O2 angle in $WOF_4 \cdot SO_2$ (179.2(2)°) in section 5.2.2.1.

Table 5.7 Bond lengths (Å) and Bond angles (°) in $[(CH_3)_4N][WOF_5]$

Bond lengths (Å)		Bond angles (°)	
W1-O1	1.675(8)	O1-W1-F1	95.74(11)
W1-F1	1.859(3)	O1-W1-F1	95.74(11)
W1-F1	1.859(3)	O1-W1-F1	95.74(10)
W1-F1	1.859(3)	O1-W1-F1	95.74(11)
W1-F1	1.859(3)	O1-W1-F2	180.0
W1-F2	1.943(6)		
N1-C1	1.496(4)	F1-W1-F1	89.43(2)
N1-C1	1.496(4)	F1-W1-F1	89.43(2)
N1-C1	1.496(4)	F1-W1-F1	89.43(2)
N1-C1	1.496(4)	F1-W1-F1	168.5(2)
		F1-W1-F1	168.5(2)
		F1-W1-F1	89.43(2)
		F1-W1-F2	84.26(11)
		F1-W1-F2	84.26(10)
		F1-W1-F2	84.26(10)
		F1-W1-F2	84.26(10)
		C1-N1-C1	109.8(3)
		C1-N1-C1	109.30(17)
		C1-N1-C1	109.30(17)

5.2.2.3 X-ray crystallography of $CH_3CN{\cdot}WOF_3(OCH_2CF_3)$

Crystals of $CH_3CN{\cdot}WOF_3(OCH_2CF_3)$ were grown using CH_2Cl_2 solvent. The $CH_3CN{\cdot}WOF_3(OCH_2CF_3)$ crystallizes in monoclinic space group $P2_1/c$ with four formula units per unit cell (Table 5.4). The structural unit of the $CH_3CN{\cdot}WOF_3(OCH_2CF_3)$ crystal structure is shown in Figure 5.6 while the bond lengths and bond angles are given in Table 5.8. The $WOF_3(OCH_2CF_3)$ moiety adopts a square pyramidal geometry as predicted by ^{19}F NMR spectroscopy for $WOF_3(OCH_2CF_3)$ (Figure 5.2) with F1,F2, F3 and O2 atoms in the equatorial plane about tungsten while O1 in the axial position. The CH_3CN molecule coordinates trans to the W=O bond with an almost linear O1–W1–N1 angle (178.7(2)°),

expanding the coordination number of tungsten to six. The W1–O1 bond length (1.686(2) Å) is the same size as that for $[(CH_3)_4N][WOF_5]$ (1.675(8) Å). The equatorial W–F bond lengths in $CH_3CN{\cdot}WOF_3(OCH_2CF_3)$ (1.860(9) to 1.871(4) Å) are the same within 3σ as those in WOF_5^- anion.

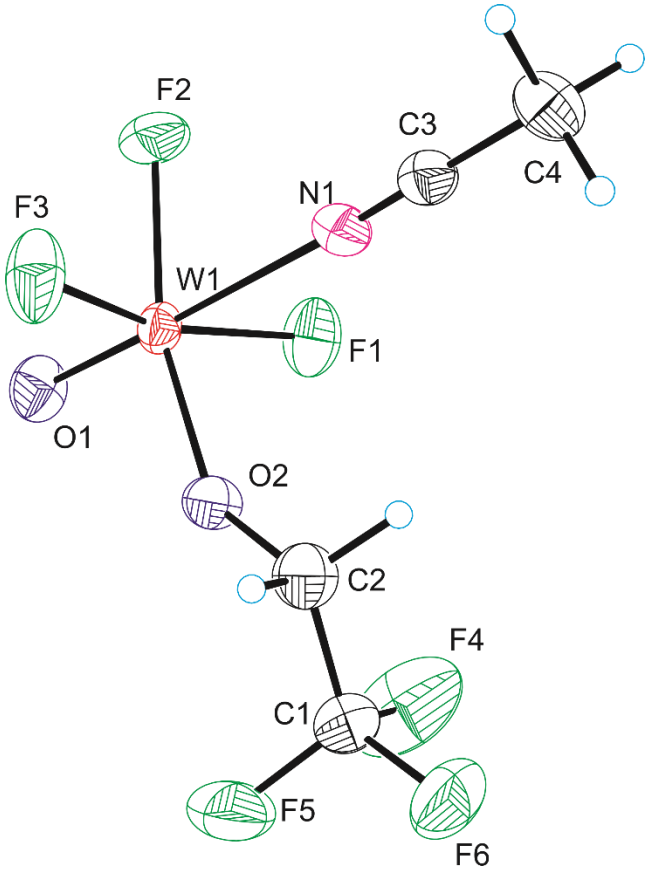

Figure 5.6 Thermal ellipsoid plot of the structural unit of $CH_3CN{\cdot}WOF_3(OCH_2CF_3)$ in the X–ray structure of $CH_3CN{\cdot}WOF_3(OCH_2CF_3)$

Table 5.8 Bond lengths (Å) and bond angles (°) for $CH_3CN{\cdot}WOF_3(OCH_2CF_3)$

Bond lengths (Å)		Bond angles (°)	
W1-O1	1.686(5)	O1-W1-O2	98.6(2)
W1-O2	1.844(5)	O1-W1-N1	178.7(2)
W1-F1	1.871(4)		
W1-F2	1.863(4)	O1-W1-F1	99.1(2)
W1-F3	1.860(4)	O1-W1-F2	99.2(2)
W1-N1	2.343(6)	O1-W1-F3	99.1(2)
C1-F4	1.325(9)		
C1-F5	1.315(9)	O2-W1-F1	90.9(2)
C1-F6	1.326(9)	O2-W1-F2	162.2(2)
C1-C2	1.464(10)	O2-W1-F3	91.6(2)
C3-C4	1.447(10)		
N1-C3	1.130(8)	F1-W1-F2	84.9(2)
C2-O2	1.397(8)	F1-W1-F3	161.1(2)
		F2-W1-F3	86.9(2)

5.2.3 Raman spectroscopy

5.2.3.1 Raman spectroscopy of $WOF_4{\cdot}SO_2$ adduct

The Raman spectrum of $WOF_4{\cdot}SO_2$ together with that of solid WOF_4, i.e. $(WOF_4)_4$, is shown in Figure 5.7 and the Raman frequencies are listed in Table 5.10. After the adduct formation of WOF_4 with SO_2, the W=O stretch shifts from 1057 to 1041 cm^{-1}. Based on the crystal structure of $WOF_4{\cdot}SO_2$, a factor group analysis was performed for WOF_4 (Table 5.9). The factor group splitting of this mode into two Raman-active components was predicted and observed (1041 and 1048 cm^{-1}). This shift reflects a weakening of the axial W=O bond length in $WOF_4{\cdot}SO_2$ adduct. Similarly, the frequency of the symmetric WF_4 stretch shifts from 726 to 701/711 cm^{-1}. The splitting of this band into two Raman active components is predicted by the factor group analysis. The WF_4 asymmetrical stretching mode is predicted to split into four bands in the Raman spectrum, but only two bands are resolved (660 to 645 cm^{-1}). Solid SO_2 shows the asymmetric stretching frequency at 1351

and 1341 cm^{-1}, symmetric stretch with a spilt at 1148 and 1144 cm^{-1}, and the bending mode at 523 and 537 cm^{-1}.[15] After adduct formation, the SO_2 stretching frequencies appear at lower frequency ($\nu_s(SO_2)$: 1142/1136 cm^{-1} and $\nu_{as}(SO_2)$: 1126 cm^{-1}) while the bending mode is shifted to higher frequency (534 cm^{-1}).

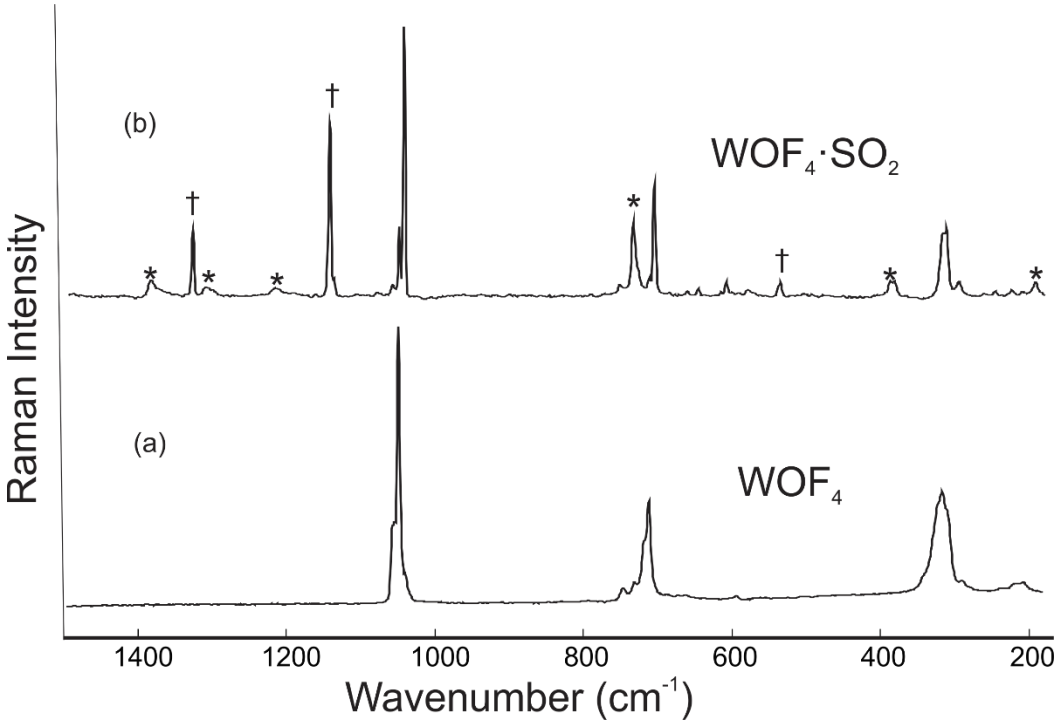

Figure 5.7. Raman spectra of (a) WOF_4 and (b) $WOF_4 \cdot SO_2$ adduct recorded in FEP reactor at –110 °C. '*' denotes the FEP signals and '†' denotes the SO_2 bands.

Table 5.9 Factor group analysis table for WOF_4 in $WOF_4 \cdot SO_2$

Local symmetry	Site symmetry		Factor group symmetry		
C_{4v}	C_1		C_{2h}		
$4\upsilon_1, 4\upsilon_2, 4\upsilon_3$	A_1	A	A_g	$\upsilon_1, \upsilon_2, \upsilon_3, \upsilon_4, \upsilon_5, \upsilon_6, 2\upsilon_7, 2\upsilon_8, 2\upsilon_9$	Raman
	A_2		B_g	$\upsilon_1, \upsilon_2, \upsilon_3, \upsilon_4, \upsilon_5, \upsilon_6, 2\upsilon_7, 2\upsilon_8, 2\upsilon_9$	Raman
$4\upsilon_4, 4\upsilon_5$	B_1		A_u	$\upsilon_1, \upsilon_2, \upsilon_3, \upsilon_4, \upsilon_5, \upsilon_6, 2\upsilon_7, 2\upsilon_8, 2\upsilon_9$	IR
$4\upsilon_6$	B_2		B_u	$\upsilon_1, \upsilon_2, \upsilon_3, \upsilon_4, \upsilon_5, \upsilon_6, 2\upsilon_7, 2\upsilon_8, 2\upsilon_9$	IR
$4\upsilon_7, 4\upsilon_8, 4\upsilon_9$	E				

Table 5.10 Raman frequencies (relative intensities), cm^{-1} of WOF_4, SO_2 and $WOF_4 \cdot SO_2$ at –110 °C together with their assignments.

Vibrational frequencies			Assignments
SO_2[a]	$(WOF_4)_4$[b]	$WOF_4 \cdot SO_2$[c]	
1351(3) 1340(4)		1326(24)	$\nu_{as}(SO_2)$
1148(100) 1144(69)		1142(63) 1136(54)	$\nu_s(SO_2)$
	1057(100)	1048(27) 1041(100)	$\nu(W=O)$
	743(14) 726(51)	711(9) 701(43)	$\nu_s(WF_4)$ (A_1)
	704(1) 668(1) 660(7)	660(5) 645(5)	$\nu_{as}(WF_4)$ (E)
		608(5)	$\nu_{as}(WF_4)$ (B_1)
	561(1)	578(2)	
539(2) 523(10)	518(3)	534(4)	$\delta(SO_2)$
	329(18) 317(30) 312(34)	316(21) 312(27)	$\delta(WOF_4)$ (E)
	263(1)	294(8)	$\delta(WOF_4)$ (B_1)
	240(4)	246(5)	
	216(6)	224(3)	
	205(7)	191(6)	
	120(8)	123(6)	

[a] Crystalline SO_2 assignment has been done at –78 °C in reference 9.[b,c] The Raman spectrum were recorded in a ¼–in FEP reactor at –110 °C. Signals from the FEP sample tube were observed at 294(8), 386(9), 733(29), 751(7), 1216(6), 1309(7), 1383(9) cm^{-1}. WOF_4 bands have been assigned based on references 7, 16, 17 and 18. Unreacted $(WOF_4)_4$ bands appeared at 1056(7) and 727(10) cm^{-1}.

5.2.3.2 Raman spectroscopy of $[(CH_3)_4N][WOF_5]$

The Raman spectrum of $[(CH_3)_4N][WOF_5]$ is shown in Figure 5.8 and the Raman frequencies for $[(CH_3)_4N][WOF_5]$ are tabulated in Table 5.11. The W=O stretching frequency for $[(CH_3)_4N][WOF_5]$ is 985 cm^{-1}. This is in agreement with the literature value

of W=O stretching frequency of WOF_5^- anion in $[EMIM][WOF_5]$[7] (982 cm^{-1}) and $[NF_4][WOF_5]$[3,15] (996 cm^{-1}). This represents a dramatic decrease in W=O stretching frequency compared to WOF_4 (1056 cm^{-1}).[16] The adduct of WOF_4 with the much weaker Lewis base SO_2 results in a much smaller change in the ν_s(W=O) frequency (1041 cm^{-1}). The equatorial WF_4 stretching bands appear at 681 and 587 cm^{-1} in the Raman spectrum. This is in agreement what has been observed for $[NO][WOF_5]$[7] (684 cm^{-1} for equatorial fluorine and 591 cm^{-1} for axial fluorine) and $[NF_4][WOF_5]$ (690 cm^{-1} for equatorial fluorine and 613 cm^{-1} for axial fluorine).[3,15] The WOF_4 bending frequency appears at 323 cm^{-1}. For $[NO][WOF_5]$[6], this frequency is 327 cm^{-1} while for $[NF_4][WOF_5]$ is 329 cm^{-1}.[3,15]

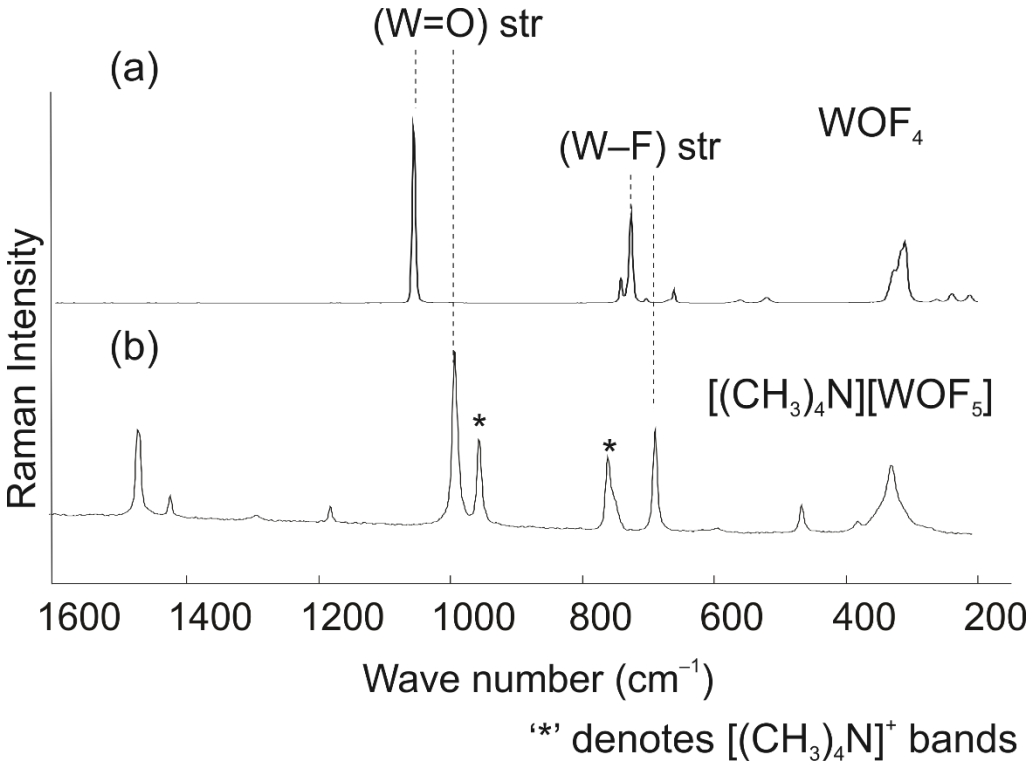

Figure 5.8. Raman spectra of (a) WOF_4 and (b) $[(CH_3)_4N][WOF_5]$ in glass melting point capillaries at ambient temperature. $[(CH_3)_4N]^+$ bands also appear at 3041, 2992, 2964, 2818, 1466, 1417, 1174, 948, 753, and 374 cm^{-1} in $[(CH_3)_4N][WOF_5]$.

Table 5.11. Raman spectroscopic data for $[N(CH_3)_4][WOF_5]$ at ambient temperature

	vibrational frequencies				
$(WOF_4)_4$ [a]	$[WOF_5^-]$ frequencies in $[(CH_3)_4N][WOF_5]$ [b]	$[WOF_5^-]$ frequencies in [EMIM][WOF_5]	$[WOF_5^-]$ frequencies in $[NF_4][WOF_5]$	$[WOF_5^-]$ frequencies in [NO][WOF_5]	Assignment (C_{4v})
1056(100)	985(100)	982(vs)	996(100)	1001(100)	ν_s(W=O) (A_1)
742(14)					
726(51)					
704(1)	681(57)	679(vs)	690(54)	684(35)	$\nu_s(WF_4)$ (A_1)
670(1)					
661(7)					
562(1)	587(2)		613(49)	591(40)	$\nu_{as}(WF_4)$ (B_1)
521(3)	459(15)		446(16)		
328(18)	323(38)	324(s)	329(68)	327(59)	$\delta(WOF_4)$ (E)
317(30)					
311(34)					

[a] WOF_4 is a tetramer in solid state. [b] $[(CH_3)_4N]^+$ bands also appear at 3041, 2992, 2964, 2818, 1466, 1417, 1174, 948, 753, and 374 cm^{-1} in $[(CH_3)_4N][WOF_5]$.

5.2.3.3 Raman spectroscopy of $CH_3CN{\cdot}WOF_3(OCH_2CF_3)$

The Raman spectra for solid WOF_4, $W(O)F_3(OCH_2CF_3)$ and $CH_3CN{\cdot}WOF_3(OCH_2CF_3)$ are shown in Figure 5.9 and the Raman frequencies are given in Table 5.12. For $W(O)F_3(OCH_2CF_3)$, with a square pyramidal geometry, there is a significant difference in the W=O stretching frequency to that of solid WOF_4 (ν_s(W=O) 1028 cm^{-1} for $W(O)F_3(OCH_2CF_3)$; ν_s(W=O) 1056 cm^{-1} for WOF_4). The $\nu_s(WF_2\text{-cis})$ symmetrical stretching bands appear at 701 and 711 cm^{-1} in $W(O)F_3(OCH_2CF_3)$, as compared to the WF_4 symmetrical stretching in neat WOF_4 (726 cm^{-1}). The W=O stretching frequency is further shifted to 1001 cm^{-1} upon coordination of CH_3CN trans to the W=O bond. This shift (1001 cm^{-1}) towards lower frequency in W=O stretch of $CH_3CN{\cdot}W(O)F_3(OCH_2CF_3)$ is a consequence of donation of electron density from CH_3CN to W, resulting in a more ionic W–O bond. The WF_2 stretching mode for $CH_3CN{\cdot}WOF_3(OCH_2CF_3)$ (659 cm^{-1}) is also shifted to lower frequency upon CH_3CN coordination. For $W(O)F_3(OCH_2CF_3)$, the CH_2 stretching and bending modes are between 2964 to 3013 cm^{-1} and 1174 to 1444 cm^{-1}, respectively. These ranges have been shifted to 2953 to 3005 cm^{-1} and 1129 to 1441 cm^{-1} for stretching and bending modes in case of $CH_3CN{\cdot}WOF_3(OCH_2CF_3)$, respectively.

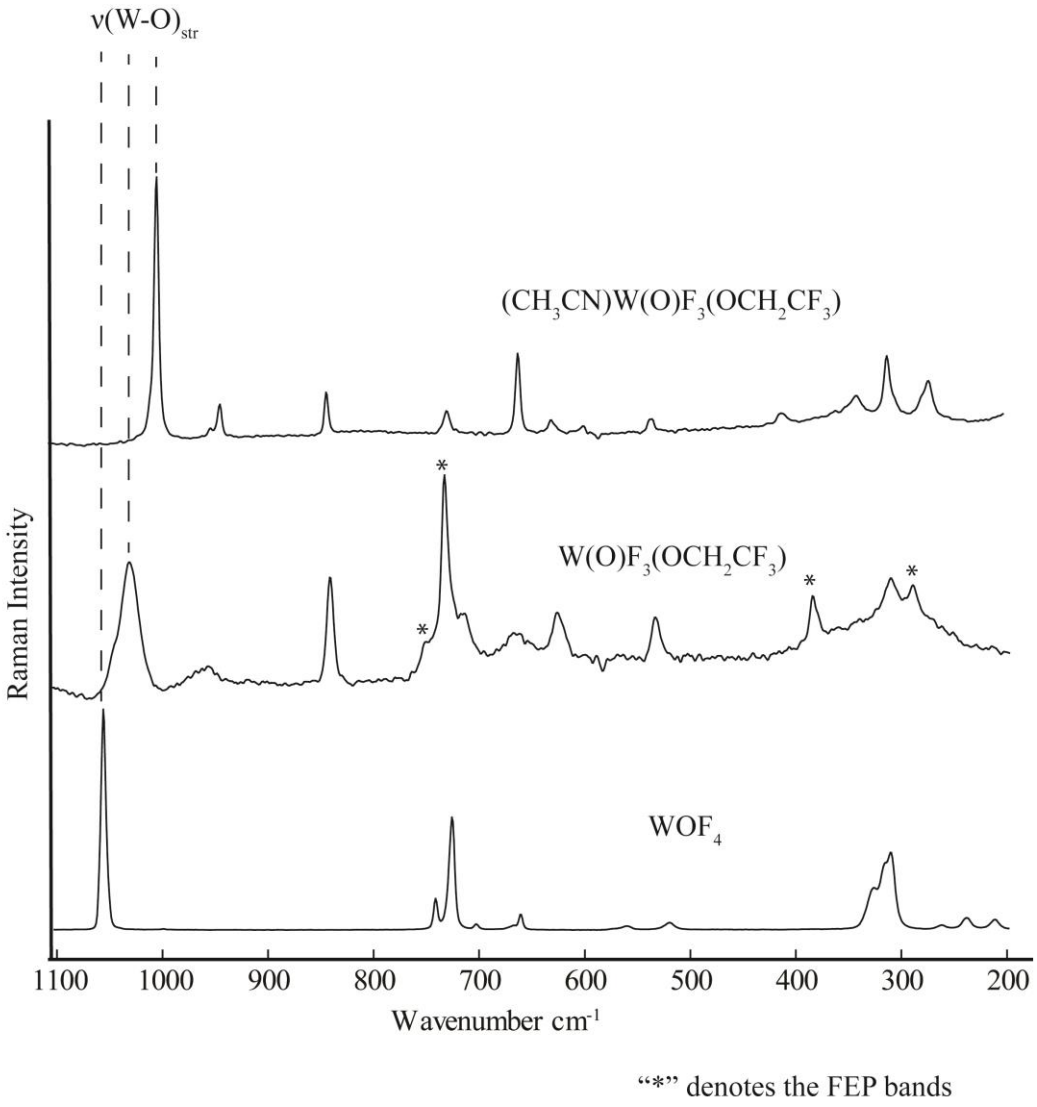

Figure 5.9 Comparison of the Raman spectra of WOF_4, $W(O)F_3(OCH_2CF_3)$ and $CH_3CN{\cdot}WOF_3(OCH_2CF_3)$ at ambient temperature.

Table 5.12 Raman frequencies (relative intensities), cm^{-1} of WOF_4, $W(O)F_3(OCH_2CF_3)$ and $CH_3CN{\cdot}WOF_3(OCH_2CF_3)$ at room temperature together with their assignments.

Vibrational frequencies				Assignments
$(WOF_4)_4$[a]	CH_3CN	$W(O)F_3(OCH_2CF_3)$[b]	$CH_3CN{\cdot}WOF_3$ (OCH_2CF_3)[c]	
		3013(11)		
	2999(52)	2996(11)	3005(3)	$\nu_{as}(CH_2+CH_3)$
		2964(34)	2964(14)	$\nu_s(CH_2+CH_3)$
	2936(90)		2953(35)	
	2817(3)			
	2732(5)	2874(3)		
	2293(4)		2317(33)	
	2248(100)		2291(26)	
	1453(16)	1444(14)	1441(3)	CH_3+ CH_2 deformation
	1423(10)	1400(2)		
	1371(12)		1366(9)	
			1290(3)	
		1174(14)	1129(5)	
1056(100)	1040(1)	1029(69)	1001(100)	$\nu_s(W{=}O)$ (A_1)
	919(15)	955(8)	950(3)	
			941(12)	
		840(54)	840(15)	
742(14)				
726(51)			726(8)	$\nu_s(WF_4)$ (A_1) /$\nu_s(WF_2)$ (A_1)
670(1)		667(8)	659(30)	$\nu_{as}(WF_4)$ /$\nu_{as}(WF_2)$
661(7)		626(23)	627(5)	
			597(3)	CF_3 def
562(1)		534(20)	532(5)	$\nu_s(WF_4)$ (B_1) /$\nu_s(WF_2)$ (B_1)
	397(14)			
	390(14)		410(5)	$\delta(WOF_4)$ (E) + (C-C) deformation
328(18)			339(9)	
317(30)				
311(34)		312(17)	310(23)	$\delta(WOF_4)$ (B_1) /$\delta(WOF_2)$ (B_1)
263(1)			271(14)	
240(4)				

[a] The Raman spectrum was recorded in a glass melting point capillary at ambient temperature. [b] The Raman spectrum was recorded in a ¼–in FEP tube. Signals from the FEP sample tube were observed at 291(11), 386(20), 733(100), 1285(17), 1379(17) cm^{-1}. [c]The Raman spectrum was recorded in a glass melting point capillary at ambient temperature. [d] $(WOF_4)_4$ bands have been assigned based on references 7, 16, 17 and 18. CH_3CN bands have been assigned based on references 21.

5.3 Conclusion

For the first time, the $WOF_4 \cdot SO_2$ adduct was identified in the solid state and conclusively characterized by X-ray crystallography and Raman spectroscopy. The identification of this SO_2 solvate in the solid state suggests its presence in SO_2 solution.

There has been a lack of a high-quality X-ray structure of WOF_5^- salts in literature and the only crystal structure known to date is $[As(Ph)_4][WOF_5]$. The crystal structure of $[As(Ph)_4][WOF_5]$ possess a 50:50% disorder between axial oxygen and fluorine on tungsten.[7] The first X-ray structure of WOF_5^- in the form of $[(CH_3)_4N][WOF_5]$ salt without any disorder and more accurate metric parameters has been presented in the given chapter.

Attempts to derivatize WOF_4 with CF_3CH_2OH, yielded only the mono-substituted $WOF_3(OCH_2CF_3)$ compound which was identified by ^{19}F NMR spectroscopy as a monomeric compound in CF_3CH_2OH solvent. The CH_3CN adduct of $WOF_3(OCH_2CF_3)$, i.e. $CH_3CN \cdot WOF_3(OCH_2CF_3)$, was structurally characterized by X-ray crystallography.

References

1. Edwards, A. J.; Jones, G. R *J. Chem. Soc. (A)* **1968**, 2074.

2. Arnaudt, L.; Bougon, R.; Ban, B.; Charpin, P.; Isabey, J.; Lance, M.; Nierlich, M.; Vigner, *Inorg. Chem.* **1989**, *28*, *2*, 257.

3. Buslaev, Y. A.; Kokunov, Y. V.; Bochkareva, V. A. *Zh. Strukt. Khim.* **1972**, *13*, 611.

4. Tebbe, F. N.; Muetterties, E. L. *Inorg. Chem.* **1968**, *7*, 172.

5. Matsumoto, K.; Hagiwara, R. *J. Fluorine Chem.* **2005**, *126*, 1095.

6. Wilson W. W.; Christe, K. O. *Inorg. Chem.* **1981**, *20*, 4139.

7. Bougon, R.; Huy, T. B.; Charpin, P. *Inorg. Chem.* **1975**, *14*, 1822.

8. Massa, W.; Hermann, S.; Dehnicke, K. *Z. Anorg. Allg. Chem.* **1982**, *493*, 33.

9. Holloway, J. H.; Schrobilgen, G. J. *Inorg. Chem.* **1980**, *19*, 2632.

10. Dimitrov, A.; Seidel, S.; Seppelt, K. *Eur. J. Inorg. Chem.* **1999**, *952*, 95.

11. Dimitrov, A.; Seidel, S.; Seppelt, K. *Eur. J. Inorg. Chem.* **1999**, *952*, 95.

12. McFarlane, W.; Noble, A. M.; Winfield, J. M. *J. Chem. Soc. (A)* **1971**, 948.

13. Noble, A. M.; Winfield, J. M. *J. Inorg. Phys. Theor.* **1970**, 501.

14. Handy, B. L.; Brinckman, F. E. *Chem. Comm.* **1970,** 214.

15. Anderson, A.; Savoie, R. *Can. J. Chem.* **1965**, *43*, 2271.

16. Alexander, L. E.; Beattie, R.; Bukovszky, A.; Jones, P. J.; Marsden, C. J.; Schalkwyk, G. J. *J. Chem. Soc. Dalton* **1974**, 81.

17. Matsumoto, K.; Hagiwara, R. *J. Fluorine Chem.* **2005**, *126*, 1095.

18. Holloway, J. H.; Schrobilgen, G. J. *Inorg. Chem.* **1981**, *20*, 3363.

19. Beuter, V. A.; Sawodny, W. *Z. Anorg. Allg. Chem.* **1976**, *427*, 37.

20. Nieboer, J.; Haiges, R.; Hillary, W.; Yu, X.; Richardt, T.; Mercier, H. P. A.; Gerken, M. *Inorg. Chem.* **2012**, *51*, 6350.

21. Vorob'eva, G. A.; Timonin, S. P. *J. Appl. Spec.* **1973**, *18*, 629.

Chapter-6

6. Structural characterization of perfluorocarboxylic acids and carboxylates of environmental concern

6.1 Introduction

Perfluoroorganocompounds are synthetic materials being used for many applications, e.g. the use of polytetrafluoroethylene in our daily life from greaseless screws to the non-stick black coating on the cookwares. Perfluorooctanoic acid (PFOA) and its salts are used as polymerization aid in the polymerization process of fluoropolymers.[1] In spite of their usefulness, PFOA and its salts have posed environmental concern due to their non-biodegradability and bioaccumulative property in the environment.[2] For example, researchers have linked exposure of 3-30 mg/l of PFOA and its salts, to inhibition of the thyroid hormone biosynthesis genes, birth defects (causes ovary degeneration in females), liver damage (ammonium salt of PFOA increased the weight of rat liver, and may induce peroxisomal fatty acid oxidation and impose oxidative stress through the alteration of cellular oxidative homeostasis in the liver), cancer (peroxisome proliferation is a key carcinogenic mechanism) and suppression of immunity (PFOA affects the lysozyme activity).[2]

Important perfluoroalkanoic acids and their salts are perfluorooctanoic acid (PFOA), sodium perfluorooctanoate (SPFO), perfluorodecanoic acid (PFDA) and sodium perfluorobutyrate (SPFB).[3,4] Perfluorooctanoic acid, PFOA, is highly stable solid at 25 °C with a low vapor pressure of 1.65×10^{-2} mm Hg (Screening Assessment Report, Health Canada, August 2012)[2]. Its vapor pressure increases close to its melting point (52–54 °C).[5,6] PFOA is readily soluble in $CDCl_3$, D_2O and $(CH_3)_2CO$ and 2,2,2-trifluoroethanol.

The sodium salt of perfluorooctanoic acid has been used as emulsifier to stabilize perfluorocarbon emulsions and is also one of the salt of environmental concern. It is a white powder having a melting point of 280 °C. This compound has been studied earlier in the form of inclusion complex with β-cyclodextrin using solid-state NMR techniques.[7] Perfluorodecanoic acid (PFDA) is another member of long chain perfluoroalkanoic acid. It is a white powder having a melting point of 78 °C. Its usage includes as commercial wetting agent and flame retardant.[6,8] Sodium perfluorobutyrate is white powder having melting point of 248 °C.[5,6,7]

Perfluorinated materials are preferred over hydrocarbon analogues because of the higher surface activity in the stabilization of emulsions, e.g. the critical micelle concentration (cmc) of SPFO is 0.032 M[9] as compared to 0.4 M of sodium octanoate.[10.11,12,13,14] PFOA, SPFO, and SPFB have been studied by solution-state NMR spectroscopy,[9,15] molecular orbital calculations,[11] viscometry,[12] differential scanning calorimetry (DSC),[5,7] thermogravimetric analysis (TGA),[5,7] and powder X-ray diffraction[5,7] as well as in the form of their inclusion complexes with other materials such as with β-cyclodextrin by solid-state NMR spectroscopy.[5,7] Even after being so thoroughly studied, the solid-state information of these materials is limited because of the unavailability of exact structural parameters. To determine the exact dipolar coupling constant values between carbon and fluorine and between two fluorine atoms in space for solid-state NMR studies, it is necessary to have the X-ray characterization done for this compound. The single-crystal X-ray characterization of these perfluorinated materials has never been reported because of the difficulty associated with the crystallization of these materials. Here, we report the first X-ray crystallographic characterization for perfluorooctanoic acid (PFOA) as its hydrate PFOA·H_2O, sodium perfluorooctanoate (SPFO), perfluorodecanoic

acid (PFDA) as PFDA·H_2O and sodium perfluorobutyrate (SPFB). Perfluorodecanoic acid (PFDA) was chosen in search for any sign of a different conformation of the long perfluoro chain in the perfluoroalkanoic acids. Because of today's trend for using short chain perfluorocompounds as a replacement for the long chain ones, SPFB was chosen for the X-ray crystallography study.

6.2 X-ray crystal structure of perfluorooctanoic acid monohydrate (PFOA·H_2O)

A sample of PFOA was used as received (Sigma-Aldrich), which was shown to contain H_2O based on its infrared spectrum. Infrared spectroscopy on PFOA shows the presence of water by the observation of the broad O–H stretching bands at 3540 and 3464 cm^{-1}. Data obtained from thermogravimetric analysis (TGA) and differential scanning calorimetry (DSC) verifies the presence of water in the crystal lattice of PFOA. In the thermogravimetric analysis of PFOA, weight loss was observed at 100 °C due to the loss of water molecules associated with PFOA while in DSC measurement, the corresponding endothermic transition was observed at 110 °C reflecting the thermal phase transition.[13]

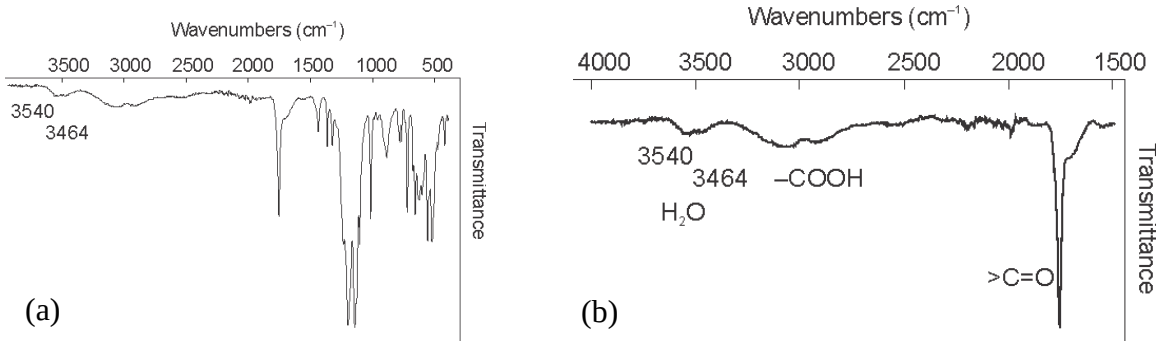

Figure 6.1 Infrared spectrum of perfluorooctanoic acid (a) complete spectrum (b) narrow range

Several attempts were made to grow crystals of PFOA from CH_2Cl_2, D_2O, and liquid SO_2 but these were unsuccessful. Crystals of PFOA·H_2O were obtained from its solution in 2,2,2-trifluoroethanol suggesting that PFOA usually exists in its monohydrated form as PFOA·H_2O. Efforts were made to get the anhydrous form of PFOA, instead of the monohydrate, by drying it completely under dynamic vacuum at 50 °C but water removal under vacuum remained unsuccessful since PFOA sublimed under dynamic vacuum above 50 °C.[5] In the search for getting PFOA·nH_2O (n>1), crystal growth was attempted by dissolving PFOA·H_2O in excess D_2O, but crystals obtained from D_2O had the same unit cell as PFOA·H_2O as determined by X-ray crystallography. It should be noted that these crystals were of substantially poorer quality than grown from those CF_3CH_2OH.

PFOA·H_2O crystallizes in the monoclinic $P2_1/c$ space group with four formula unit of PFOA·H_2O in the unit cell. The thermal ellipsoid plot of PFOA·H_2O is shown in Figure 6.2(a). The concise crystal data for PFOA·H_2O has been given in Table 6.1. The bond lengths and bond angles are given in Table 6.2.

Usually, carboxylic acids form hydrogen bonded dimers and crystallize without water molecules.[16] In contrast, in PFOA·H_2O, water molecules were found between PFOA units in the crystal structure. Each water molecule is hydrogen bonded to two PFOA molecules resulting in a layered structure. The PFOA chains are aligned along the *a*-axis. The packing diagram of PFOA·H_2O (Figure 6.2b) shows two types of layers in the *bc*-plane of PFOA·H_2O. One is the fluorophilic layer generated by the regular arrangement of perfluoro chains and the other is the hydrophilic layer composed of the carboxylic acid groups and water. Such a layered structure was also observed for carboxylic acids (Fig 6.2c). The distance between the two opposite perfluoro chains (–CF_3 group to –CF_3 group) in the fluorophilic layer is 4.245(3) Å in perfluorooctanoic acid monohydrate while for

octanoic acid (Figure 6.2c) the distance between the two opposite alkyl chains (–CH_3 group to –CH_3 group) in the hydrophobic layer is 3.896(4) Å. The distance between two adjacent perfluorooctanoic molecules is 5.573(4) Å while the distance is 4.379(4) Å in case of octyl chains in octanoic acid. The reason being larger size and higher electronegativity of fluorine atom in comparison to hydrogen atom.

The three conformations found in hydrocarbons are syn, anti and gauche, of which the anti-configuration is the most stable conformation in hydrocarbon chains. But in the case of perfluorocarbons, a distorted anti conformation is preferred (Scheme-I) due to the electronic repulsion of fluorine atoms.[16] As a consequence, the perfluoro chains usually adopt a helical structure as observed for PFOA. The distorted anti conformation of the perfluorooctyl chain in PFOA·H_2O is in accordance with the results found on the basis of ^{19}F–^{19}F COSY,[15] ^{19}F–^{19}F NOESY NMR study,[15] AM-1 calculation which predict an anti conformation up to the perfluorocarbon chain length of eight.[15] The ^{19}F solid-state study of PFOA on its inclusion complex with β-cyclodextrin demonstrated the acquisition of anti and gauche arrangements of PFOA in the complex with heating and cooling of the sample.[5]

Table 6.1. Crystallographic data for perfluorooctanoic acid (PFOA) as PFOA·H_2O, perfluorodecanoic acid (PFDA) as PFDA·H_2O, sodium perfluorooctanoate (SPFO), and sodium perfluorobutyrate (SPFB)

Chemical formula	$C_8F_{15}O_3H_2$	$C_{10}F_{19}O_3H_2$	$C_8F_{15}O_2Na$	$C_4F_7O_2Na$
Crystal system	Monoclinic	Monoclinic	Monoclinic	Monoclinic
Space group	$P2_1/c$	$P2_1/c$	$P2_1/c$	$C2/c$
a (Å)	22.752(14)	27.035(10)	22.43(4)	25.99(2)
b (Å)	5.309(3)	5.396(2)	5.878(11)	6.113(5)
c (Å)	11.026(7)	10.944(4)	9.626(17)	9.181(7)
α (°)	90	90	90	90
β (°)	91.215(8)	95.350(4)	95.472(18)	99.069(8)
γ (°)	90	90	90	90
Z	4	4	4	8
Formula weight (g mol^{-1})	432.10	532.12	452.05	236.02
Calcd density (g cm^{-3})	2.155	2.223	2.291	1.048
T (°C)	–120	–120	–120	–120
μ (mm^{-1})	0.290	0.300	0.318	0.326
R_1[a]	0.0366	0.0808	0.0417	0.0476
wR_2[b]	0.0728	0.1849	0.0610	0.0891

[a] R_1 is defined as $\Sigma||F_o| - |F_c||/\Sigma|F_o|$ for $I > 2\sigma(I)$. [b] wR_2 is defined as $[\Sigma[w(F_o^2 - F_c^2)^2]/\Sigma w(F_o^2)^2]^{½}$ for $I > 2\sigma(I)$.

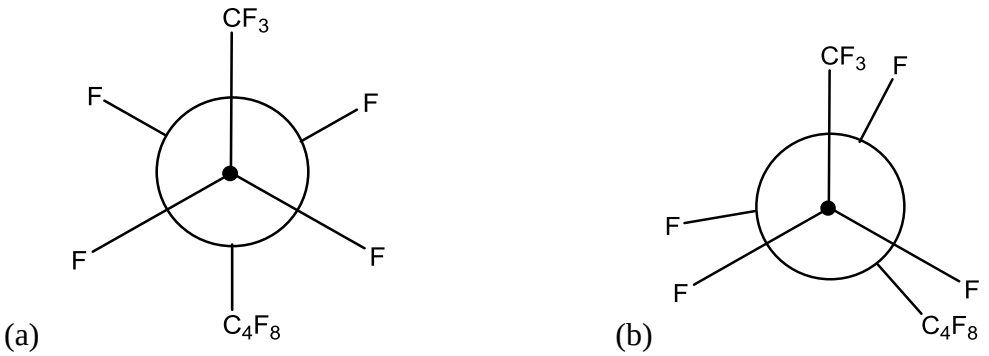

(Scheme – I)

Two types of conformational Newman projections of perfluoro chains of PFOA (a) anti conformation (b) distorted anti conformation.

For the comparison of hydrogen bonding strength in the carboxylic acid monohydrates, the available structures in the literature were hydrated 4-bromo-6-oxotetrahydro-3H,8H-pyrano[3,4-d]pyrrolo[1,2-c][1,3]oxazole-8-carboxylic acid[17] and hydrated 11-aminoundecanoic acid.[18] The comparison with hydrated hydrogenated acid was done due to the lack of availability of the crystal structure hydrated perfluoroalkanoic acid in literature. The hydrogen bonding between the perfluorooctanoic acid and the water molecule is significantly stronger than in the two cited structures. The RO···O distance in PFOA·H_2O is 2.503(2) Å, which is smaller than the RO···O distance of 2.794(3) Å found for 4-bromo-6-oxotetrahydro-3H,8H-pyrano[3,4-d]pyrrolo[1,2-c][1,3]oxazole-8-carboxylic acid monohydrate[19] and 2.786(8) Å found for hydrated 11-aminoundecanoic acid.[18] The carbon-fluorine bond lengths are in the expected range of 1.309(3) to 1.347(2) Å. The C–C–C bond angles vary from 113.10(15) to 115.06(17)° in the helical structure.

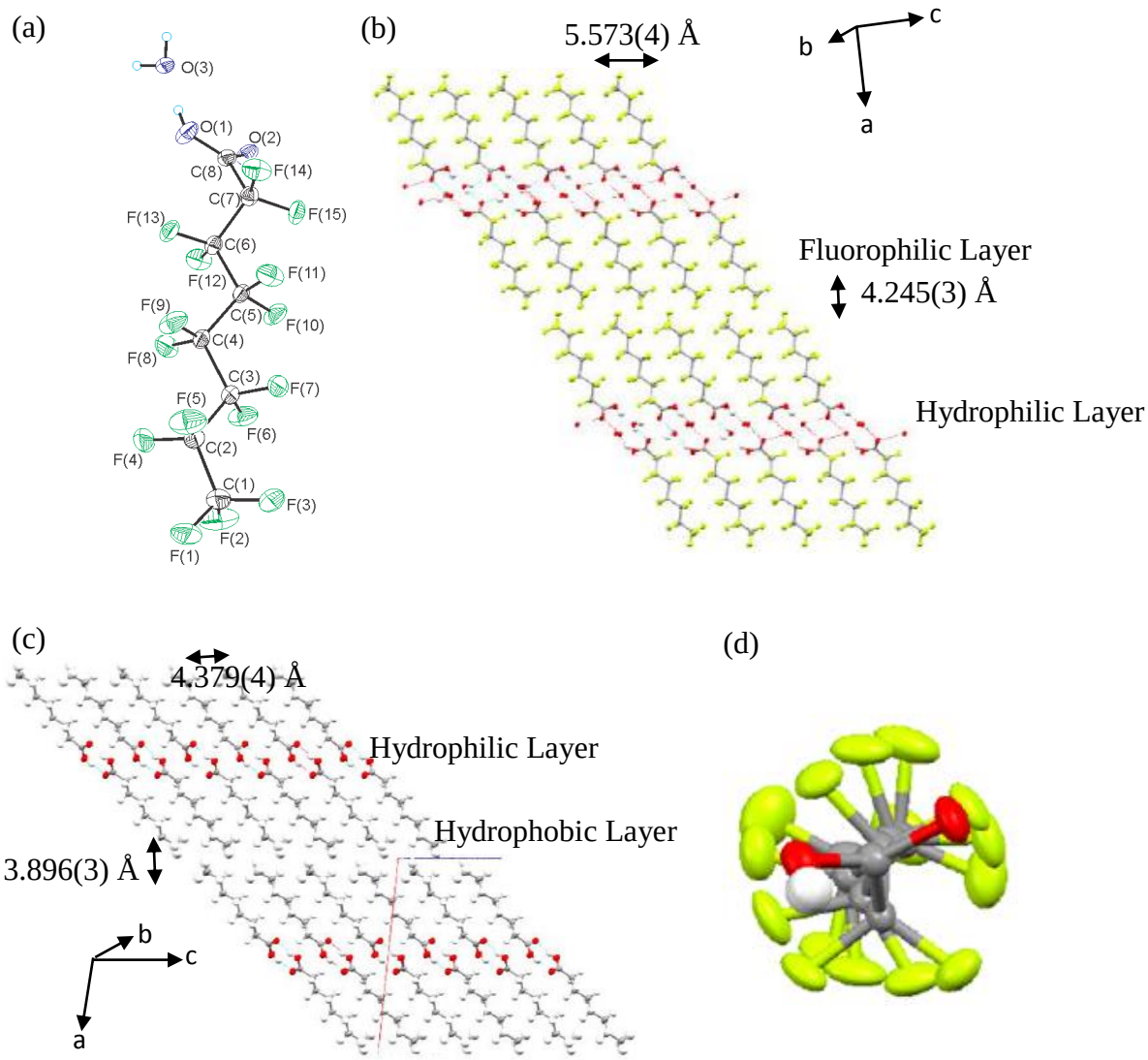

Figure 6.2 (a) Thermal ellipsoid plot of PFOA·H_2O at 50% probability level in the crystal structure of PFOA·H_2O (b) Arrangement of fluorophilc perfluoro chains having hydrophilic channel in PFOA·H_2O which includes water molecules between two perfluorooctanoic molecules and a distance of 4.245(3) Å between two opposite perfluoro chains and a distance of 5.573(4) Å (c) Arrangement of hydrophobic alkyl chains having hydrophilic channel octanoic acid. The distance between two opposite alkyl chains is 3.896(3) Å and the distance between two octanoic acid units is 4.379(4) Å (d) helical view of PFOA unit in PFOA·H_2O.

Table 6.2 Bond lengths and bond angles for PFOA·H_2O

Bond lengths (Å)		Bond angles (°)	
C1-F1	1.316(3)	C1-C2-C3	115.06(17)
C1-F2	1.314(3)	C2-C3-C4	114.23(15)
C1-F3	1.309(3)	C3-C4-C5	113.63(15)
C2-F4	1.336(2)	C4-C5-C6	114.36(14)
C2-F5	1.333(3)	C5-C6-C7	114.48(15)
C3-F6	1.342(2)	C6-C7-C8	113.10(15)
C3-F7	1.333(2)		
C4-F8	1.337(2)	C7-C8-O1	111.67(17)
C4-F9	1.334(2)	C7-C8-O2	120.04(17)
C5-F10	1.340(2)		
C5-F11	1.335(2)	O1-C8-O2	128.29(18)
C6-F12	1.342(2)		
C6-F13	1.336(2)	F1-C1-F2	107.97(19)
C7-F14	1.342(2)	F1-C1-F3	109.27(19)
C7-F15	1.347(2)	F2-C1-F3	108.3(2)
C8-O1	1.281(2)	F4-C2-F5	108.89(18)
C8-O2	1.209(2)	F6-C3-F7	108.28(16)
		F8-C4-F9	108.72(15)
		F10-C5-F11	108.82(15)
		F12-C6-F13	108.40(15)
		F14-C7-F15	107.63(16)

6.3 X-ray crystal structure of perfluorodecanoic acid monohydrate (PFDA·H_2O)

Attempts were made to grow the crystal of PFDA using CH_2Cl_2, D_2O, liquid SO_2, n-hexane, ethanol, isopropanol and n-butanol. Crystals of perfluorodecanoic acid (PFDA) were obtained only from its solution in n-butanol in its hydrated form as PFDA·H_2O. PFDA·H_2O crystallizes in the monoclinic $P2_1/c$ space group with four formula unit of PFDA·H_2O in the unit cell. The thermal ellipsoid plot of PFDA·H_2O is shown in Figure 6.3(a). The concise crystal data for PFDA·H_2O has been given in Table 6.1. The bond lengths and bond angles are given in Table 6.3.

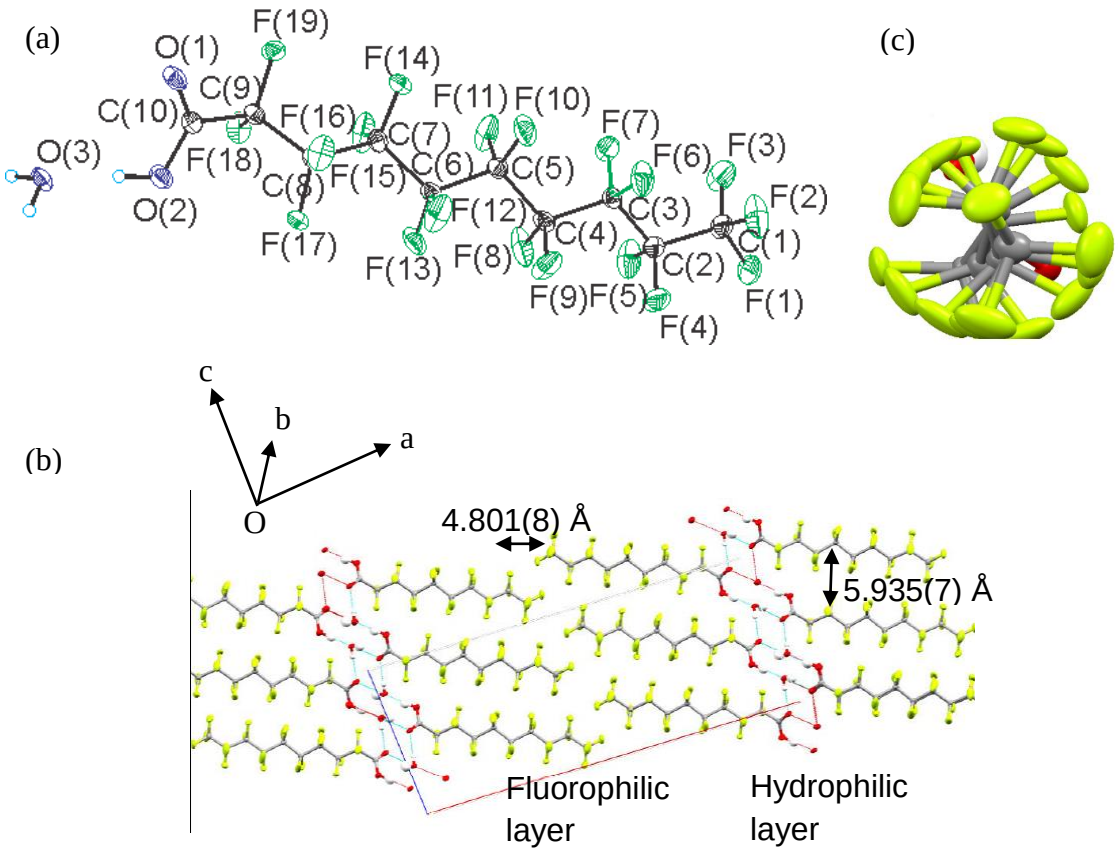

Figure 6.3 (a) Thermal ellipsoid plot of PFDA·H_2O at 50% probability level in the crystal structure of PFDA·H_2O (b) Arrangement of fluorophilc perfluoro chains having hydrophilic channel in PFDA·H_2O which includes water molecules between two perfluorooctanoic molecules and a distance of 4.801(8) Å between two opposite perfluoro chains and an interlayer distance of 5.935(7) Å (c) helical view of PFDA unit in PFDA·H_2O.

The $–CF_2$ groups, in perfluorodecanoic acid monohydrate, adopts a distorted anti conformation to form a helical structure just as they do in PFOA·H_2O. The C–F bond lengths in PFDA·H_2O range from 1.308(6) Å to 1.353(5) Å and the C–C–C bond angles range from 112.8(4) to 115.5(5)°. The C–F bond lengths and bond angles in PFDA·H_2O are similar to what have been found for PFOA·H_2O (1.309(3) to 1.342(2) Å). The water molecule is hydrogen bonded with two PFDA molecules resulted in a layered structure. Due to the hydrogen bonding between the water molecule and the perfluorodecanoic acid, the RO···O distance is 2.486(5) Å which is similar to what has been found in the case of

PFOA·H_2O (2.503(2) Å) but smaller than the RO···O distance of 2.794(3) Å found for 4-bromo-6-oxotetrahydro-3H,8H-pyrano [3,4-d] pyrrolo [1,2-c] [1,3] oxazole-8-carboxylic acid monohydrate[17] and 2.786(8) Å found in case of the hydrated 11-aminoundecanoic acid.[18]

In the packing diagram of PFDA·H_2O (Figure 6.3b) two layers, i.e. a fluorophilic and a hydrophilic layer, are observed. The distance between parallel perfluoro chains is 5.935(7) Å and the distance between the perfluoro chains (between the carbons of two consecutive –CF_3 groups) is 4.801(8) Å.

Table 6.3 Bond lengths (Å) and bond angles (°) for PFDA·H_2O

Bond lengths (Å)		Bond angles (°)	
C1-F1	1.312(6)	C1-C2-C3	115.5(4)
C1-F2	1.322(7)	C2-C3-C4	114.7(4)
C1-F3	1.308(6)	C3-C4-C5	114.2(4)
C2-F4	1.318(6)	C4-C5-C6	114.3(4)
C2-F5	1.341(7)	C5-C6-C7	114.0(4)
C3-F6	1.340(6)	C6-C7-C8	114.6(4)
C3-F7	1.340(5)	C7-C8-C9	115.1(4)
C4-F8	1.333(6)	C8-C9-C10	112.8(4)
C4-F9	1.328(6)	C9-C10-O1	120.6(4)
C5-F10	1.320(6)	C9-C10-O2	111.4(4)
C5-F11	1.339(6)	O1-C10-O2	128.0(4)
C6-F12	1.337(6)	F1-C1-F2	107.4(5)
C6-F13	1.318(6)	F1-C1-F3	109.7(5)
C7-F14	1.338(6)	F2-C1-F3	107.5(5)
C7-F15	1.331(6)	F4-C2-F5	108.6(5)
C8-F16	1.340(6)	F6-C3-F7	107.8(4)
C8-F17	1.334(5)	F8-C4-F9	109.3(5)
C9-F18	1.342(6)	F10-C5-F11	108.6(4)
C9-F19	1.353(5)	F12-C6-F13	108.7(4)
C10-O1	1.210(6)	F14-C7-F15	108.9(4)
C10-O2	1.284(6)	F16-C8-F17	108.3(4)
		F18-C9-F19	108.0(4)

6.4 X-ray crystal structure of sodium perfluorooctanoate (SPFO)

The crystal growth for SPFO was attempted from CH_2Cl_2, D_2O, 2,2,2-trifluoroethanol, methanol, and ethanol but the crystals suitable for X-ray diffraction of SPFO were obtained from its solution in ethanol. SPFO crystallizes in the monoclinic $P2_1/c$ space group with four formula unit of SPFO in the unit cell. The thermal ellipsoid plot of SPFO is shown in Figure 6.4(a). The concise crystal data for SPFO has been given in Table 6.1. The bond lengths and bond angles are given in Table 6.4. The perfluoro chain of SPFO adopts the distorted anti conformation to form the helical structure in the same manner as they do in PFOA·H_2O. The C–F bond lengths in SPFO range from 1.311(9) Å to 1.359(8) Å while the bond angles range from 116.0(8) to 117.6(7)° in SPFO.

The RO···O distance found between two SPFO units is 3.570(9) Å, reflecting strong interactions between two SPFO units. Furthermore, the DSC and TGA measurements do not show any transition or weight loss around 100 °C, presenting support for the absence of water as observed in the crystal structure of SPFO.[19]

The packing diagram of SPFO (Figure 6.4b) shows two different types of layers, one is the fluorophilic layer and the other is hydrophilic. The distance between the fluorocarbon chains (from one carbon of the first chain to the parallel carbon of the second chain) is 5.65(1) Å and the distance between the perfluoro chains (between the carbons of two consecutive $–CF_3$ groups) is 4.82(2) Å.

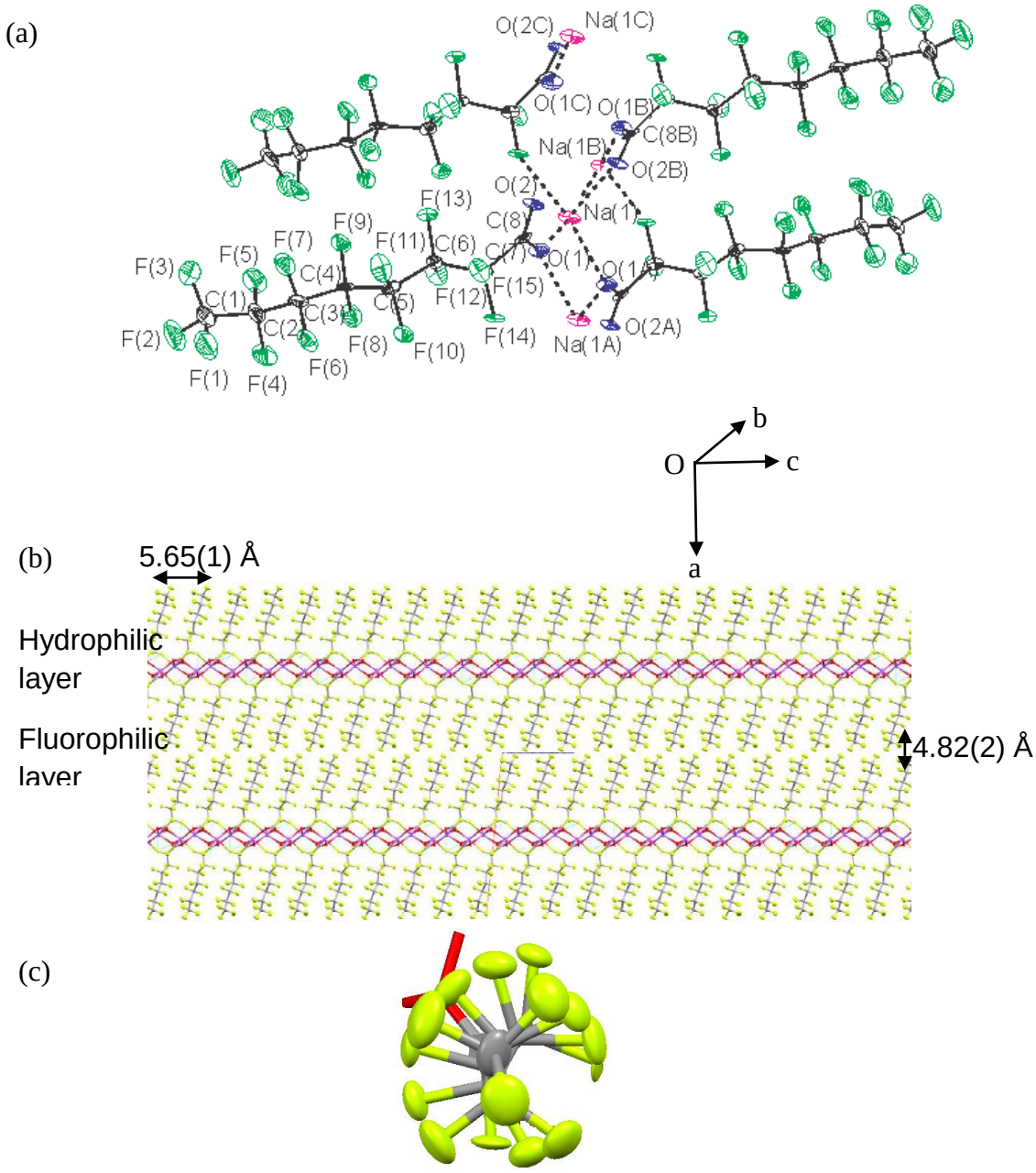

Figure 6.4 (a) Thermal ellipsoid plot of SPFO at 50% probability level in the crystal structure of SPFO (b) Arrangement of the hydrophilic and fluorophilic layers in SPFO. Packing arrangement of SPFO in unit cell with a distance of 4.82(2) Å between two opposite perfluoro chains and an interlayer distance of 5.65(1) Å (c) helical view of perfluoro chain in SPFO.

Table 6.4 Bond lengths (Å) and bond angles (°) for SPFO

Bond lengths (Å)		Bond angles (°)	
C1-F1	1.334(9)	C1-C2-C3	116.0(8)
C1-F2	1.311(9)	C2-C3-C4	117.7(8)
C1-F3	1.315(9)	C3-C4-C5	116.7(7)
C2-F4	1.345(8)	C4-C5-C6	117.6(7)
C2-F5	1.331(8)	C5-C6-C7	116.4(6)
C3-F6	1.346(8)	C6-C7-C8	114.9(6)
C3-F7	1.338(8)		
C4-F8	1.339(8)	C7-C8-O1	113.9(8)
C4-F9	1.349(8)	C7-C8-O2	116.6(8)
C5-F10	1.339(8)		
C5-F11	1.357(7)	O1-C8-O2	129.5(8)
C6-F12	1.320(8)		
C6-F13	1.354(8)	F1-C1-F2	107.8(8)
C7-F14	1.359(8)	F1-C1-F3	107.7(8)
C7-F15	1.350(7)	F2-C1-F3	107.9(8)
C8-O1	1.350(7)	F4-C2-F5	108.2(7)
C8-O2	1.228(9)	F6-C3-F7	106.3(6)
O1-Na1	2.337(6)	F8-C4-F9	106.7(6)
O2-Na1A	2.264(7)	F10-C5-F11	107.0(6)
		F12-C6-F13	108.3(6)
		F14-C7-F15	105.7(6)
		C8-O1-Na1	138.8(5)

6.5 X-ray crystal structure of sodium perfluorobutyrate (SPFB)

The crystals of SPFB were obtained from its solution in ethanol. SPFB crystallizes in the monoclinic *C2/c* space group with eight formula unit of SPFB in the unit cell. The thermal ellipsoid plot of SPFB is shown in Figure 6.5 at 50% probability level. The concise crystal data for SPFO has been given in Table 6.1. The bond lengths and bond angles are given in Table 6.5.

Sodium perfluorobutyrate chains arrange themselves along *a*-axis in the unit cell. The usual distorted anti conformation is adopted by the perfluoro chains in the same manner

as they do in SPFO. The C–F bond lengths in SPFB range from 1.312(6) Å to 1.370(5) Å and the C–C–C bond angles are 114.3(4) to 118.7(5)°. The C–F bond lengths in SPFB are similar to what have been found for SPFO (1.311(9) to 1.359(8) Å). Similarly, the bond angles are also similar to what were found for PFOA (116.0(8) to 117.6(7)°) in section 6.3.1. The RO···O distance between two SPFB molecule is 3.499(5) Å also similar to what has been found in the case of SPFO (3.570(9) Å).

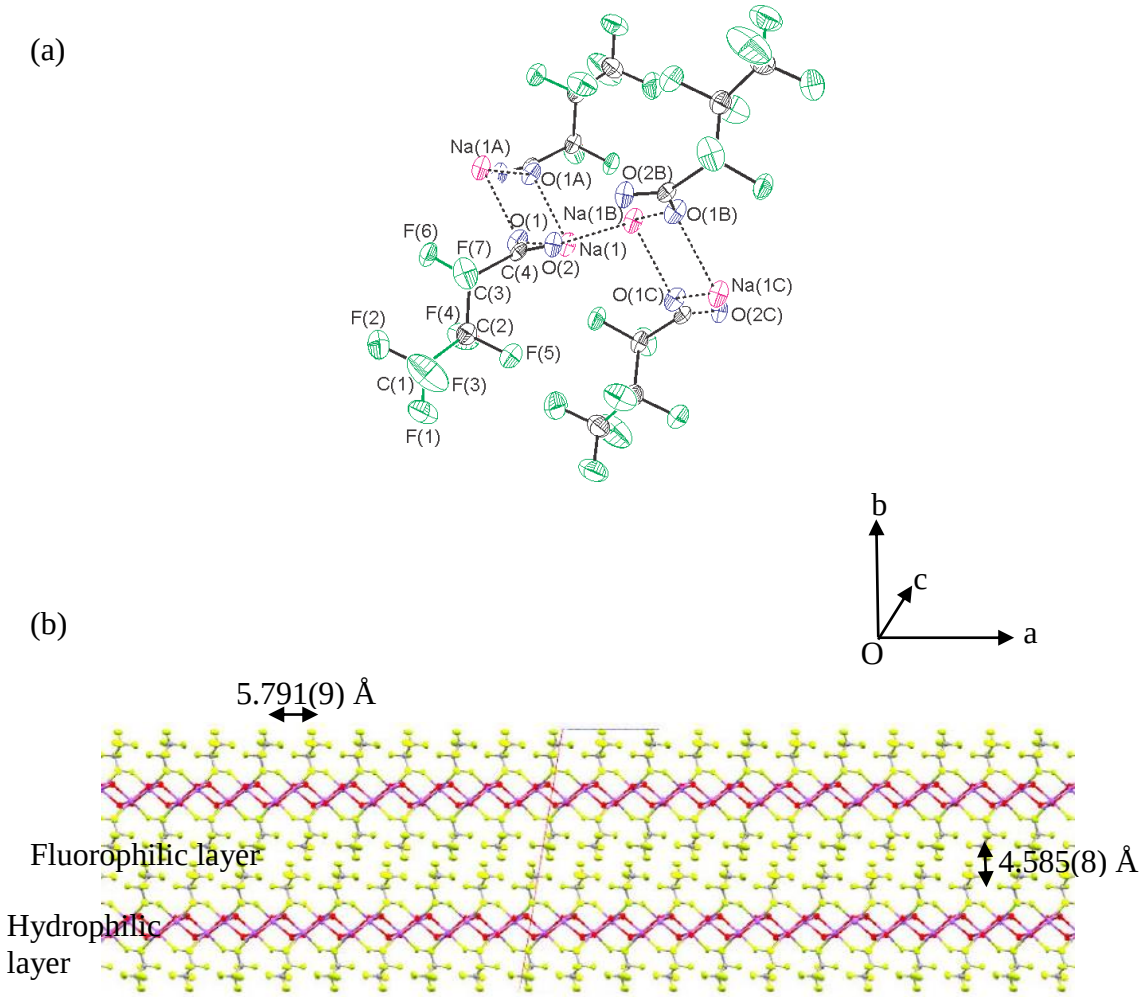

Figure 6.5 (a) Thermal ellipsoid plot of SPFB at 50% probability level in the crystal structure of SPFB (b) Arrangement of the hydrophilic and fluorophilic layers in SPFB with a distance of 4.585(8) Å between two opposite perfluoro chains and an interlayer distance of 5.791(9) Å.

Table 6.5 Bond lengths (Å) and bond angles (°) for SPFB

Bond lengths (Å)		Bond angles (°)	
C1-F1	1.312(7)	C1-C2-C3	118.7(5)
C1-F2	1.320(7)	C2-C3-C4	114.3(4)
C1-F3	1.312(6)		
C2-F4	1.345(5)	C3-C4-O1	114.8(4)
C2-F5	1.340(6)	C3-C4-O2	116.3(4)
C3-F6	1.353(5)		
C3-F7	1.370(5)	O1-C4-O2	128.9(4)
C4-O1	1.241(5)		
C4-O2	1.237(5)	F1-C1-F2	107.8(5)
O1-Na1A	2.370(4)	F1-C1-F3	106.9(5)
O2-Na1	2.293(4)	F2-C1-F3	107.9(5)
		F4-C2-F5	106.7(4)
		F6-C3-F7	105.1(3)
		C4-O2-Na1	123.6(3)

In the packing diagram of SPFO (Figure 6.5b), there are two different types of layers, fluorophilic and hydrophilic. The interlayer distance between the fluorocarbon chains is 5.791(9) Å and the distance between two consecutive perfluoro chains (between the carbons of two consecutive $–CF_3$ groups) is 4.585(8) Å.

6.6 Conclusion

The X-ray crystallography of perfluoro carboxylic acids and carboxylayes without any hydrogen atom in the chain (except for carboxylic acid group) is being reported for the first time. Future work may include efforts to the get the anhydrous crystal structures of carboxylic acids.

References:

1. Post, G. B.; Cohn, P. D.; Cooper, K. R. *Envi. Res.* **2012**, *116*, 93.

2. Screening Assessment Report, Perfluorooctanoic Acid, its Salts, and its Precursors, Environment Canada, August 2012.

3. Alexander, J.; Auðunsson, A. G.; Benford, D.; Cockburn, A.; Cravedi, J.- P.; Dogliotti, E.; Domenico, A. D.; Fernández-Cruz, M. L.; Fink-Gremmels, J.; Fürst, P.; Galli, C.; Grandjean, P.; Gzyl, J.; Heinemeyer, G.; Johansson, N.; Mutti, A.; Schlatter, J.; Leeuwen, R.; Peteghem, C.; Verger, P. *J. Eur. Food Safety Authority* **2008**, *653*, 1.

4. Perforce, FP6-NEST INSIGHT, Perfluorinated Organic compounds in the European Environment, Scientific Report, June 2006.

5. Buchanan, G. W.; Munteanu, E.; Dawson, B. A.; Hodgson, D. *Magn. Res. Chem.* **2005**, *43*, 528.

6. Tsuji, M.; Inoue, T.; Shibata, O. *Colloids and Surfaces B: Biointerfaces* **2008**, *61*, 61.

7. Karoyo, A. H.; Borisov, A. S.; Wilson, L. D.; Hazendonk, P. *J. Phys. Chem. B* **2011**, *115*, 9511.

8. Harris, M. W.; Birnbaum, L.S. *Fundam. Appl. Toxicol.* **1989**, *12*, 442.

9. Guo, W.; Fung, B. M.; Christian, S. D. *Langmuir* **1992**, *8*, 446.

10. Wilson, L. D.; Siddall, S. R.; Verrall, R. E. *Can. J. Chem.* **1997**, *75*, 927.

11. Zemb, T.; Drifford, M.; Hayoun, M.; Jehanno, A. *J. Phys. Chem.* **1983**, 87, 4524.

12. Zhang, H. H.; Hogen-Esch, T. E.; Boschet, F.; Margaillan, A. *Langmuir* **1998**, *14*, 4972.

13. D'Angelo, M.; Onori, G.; Santucci, A. Prog. *Colloid Polym. Sci.* **1994**, *97*, 154.

14. Gonzalez-Perez, A.; Ruso, J. M.; Prieto, G.; Sarmiento, F. *Colloid Polym. Sci.* **2004**, *282*, 1133.

15. Buchanan, G. W.; Munteanu, E.; Dawson, B. A.; Hodgson, D. *Magn. Res. Chem.* **2005**, *43*, 528.

16. Kirsch, P. *Modern Fluoroorganic Chemistry*, WILEY-VCH Verlag GmbH & Co. KGaA: Weinhein, 2004, pp. 9.

17. Concepcion, F-F; Echevarria, A; Jagerovic, N.; Alkorta, I.; Elguero, J.; Langer, U.; Klein, O.; Minguet, B. M.; Limbach, H. H. *J. Am. Chem. Soc.* **2001**, *123*, 7898.

18. Sim, A. G. *Acta. Cryst.* **1955**, *8*, 833.

Chapter-7

7. Properties of 1-ethyl-3-methyl imidazolium bifluoride ($EMIMHF_2$)

7.1 Introduction

Ionic liquids/room temperature molten salts have their primary importance as non-volatile, non-flammable and unreactive liquids. These liquids usually have very high thermal, chemical and electrochemical stability.[1,2] Among the available ionic liquids, imidazolium cation-based ionic liquids are very important because of the resistance of these cations towards reduction.[3,4,5] Imidazolium ionic liquids have melting points below 100 °C, low viscosity, and high conductivity which can be explained in terms of charge delocalization on the imidazolium ring.[3,4,5] Because of these valuable properties, the detailed study of structural and dynamical properties of ionic liquids are of high importance not only from the theoretical point of view to understand their fundamental properties but also for their applications. Ionic liquids such as imidazolium tetrafluoroborate have been studied in the polymer composite form for the application as electrolytes in fuel cells.[7] One study based on the Radial Density Function (RDF) analysis (simulation work) states that the imidazolium cations, e.g. 1-butyl 3-methylimidazolium cation, have faster self-diffusion coefficients than their counter anions, e.g. BF_4^-, inside the Nafion network.[7]

Electrolytic studies on salts such as KHF_2 revealed that the protons present in this solid are responsible for the conduction of current (H_2 is generated at the anode as a result of electrolysis and F_2 is generated at the cathode).[6] A series of imidazolium fluorohydrogenate $[F(HF)_n]^-$ (n = 1–2.6) salts ranging from liquid to solid at ambient temperature was synthesized by Rika Hagiwara et al. and were shown to be ionic liquids with very high conductivities.[8,9,10] These fluorohydrogenate ionic liquids were studied using the pulse field gradient solution NMR technique to explore the conductivity

mechanism and it was proposed that the dispersion of the anionic charge over a larger fluorohydrogenate anion results in faster migration of that anion.[11,12]

In the solid state, such ionic liquids usually exhibit restricted motion, especially translational motion. Some motion, however, can be observed due to rotation of the alkyl groups, inversion of the rings in the molecule, migration of labile hydrogens and internal rotation of small molecules within larger structures. The focus of the present study is to analyze 1-ethyl-3-methylimidazolium bifluoride with solid-state NMR techniques to characterize important structural and dynamical properties.

7.2 Results and discussion

7.2.1 X-ray crystallography

The HF_2^- anion is of significant interest because it contains the strongest hydrogen bond known and it may exist either in the symmetric or unsymmetric form depending on the symmetry of the surrounding crystal field. 1-ethyl-3-methylimidazolium bifluoride ($EMIMHF_2$) was found to exist in two different modifications, a low-temperature phase and a room-temperature phase.[9] The low-temperature structure is discussed in the present study by X-ray crystallography, whereas the room temperature modification has been reported previously.[9]

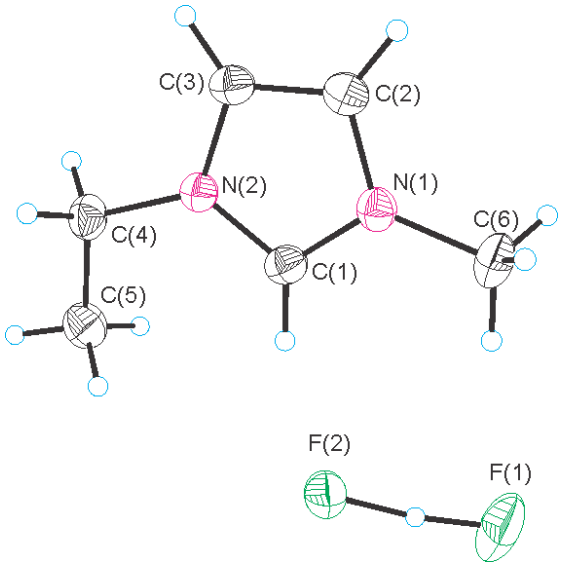

Figure 7.1 Thermal ellipsoid plot of 1-ethyl-3-methylimidazolium bifluoride at 50% probability level in the crystal structure of 1-ethyl-3-methylimidazolium bifluoride ($EMIMHF_2$)

The low temperature phase of 1-ethyl-3-methylimidazolium bifluoride ($EMIMHF_2$) crystallizes in triclinic space group *P–1* with two molecular units in the unit cell. The concise crystallographic data has been given in Table 7.1 while the bond lengths and bond angles are given in Table 7.2. The crystallographic data for two different phases of $[EMIM][HF_2]$ are compared in Table 7.1. The crystallography for room-temperature $[EMIM][HF_2]$ was performed at 25 °C[9] while the data set for the low-temperature phase was collected at –120 °C. Because of poorer crystal quality, the uncertainties associated with the unit cell dimensions of the low temperature phase of 1-ethyl-3-methylimidazolium bifluoride are higher compared to the uncertainties associated with the known unit cell dimensions of ambient temperature phase of 1-ethyl-3-methylimidazolium bifluoride. The volume for the low-temperature phase is, as expected, smaller than that of the room-temperature phase.[9]

Table 7.1 Selected crystallographic data for [EMIM][HF_2], for symmetric and unsymmetric HF_2^-.

	[EMIM][HF_2] (Unsymmetric HF_2^- unit)	[EMIM][HF_2][c] (Symmetric HF_2^- unit)
Chem formula	$C_6H_{12}N_2F_2$	$C_6H_{12}N_2F_2$
Crystal system	Triclinic	Monoclinic
Space group	P–*1*	$P2_1/m$
a (Å)	6.710(12)	7.281(1)
b (Å)	7.234(13)	6.762(1)
c (Å)	8.354(15)	8.403(1)
α (°)	72.359(18)	
β (°)	78.343(18)	107.26(1)
γ (°)	88.72(2)	
V (Å^3)	378.1(12)	395.09(18)
Z	2	2
mol wt (g mol^{-1})	150.17	150.17
ρ_{calcd} (g cm^{-3})	1.26	1.26
T (°C)	–120	25
R_1[a]	0.0540	0.062
wR_2[b]	0.1443	0.169

[a] R_1 is defined as $\Sigma||F_o| - |F_c||/\Sigma|F_o|$ for $I > 2\sigma(I)$. [b] wR_2 is defined as $[\Sigma[w(F_o^2 - F_c^2)^2]/\Sigma w(F_o^2)^2]^{½}$ for $I > 2\sigma(I)$. [c]$EMIMHF_2$ structure details has been taken from reference 9.

Table 7.2 Bond lengths (Å) and Bond angles (°) in 1-ethyl-3-methylimidazolium bifluoride ($EMIMHF_2$) crystal

Bond lengths (Å)		Bond angles (°)	
N1-C1	1.331(3)	N12-C1-N2	107.8(2)
N1-C3	1.379(4)	C1-N1-C3	109.30(19)
N1-C4	1.472(3)	C1-N2-C2	109.2(2)
N2-C1	1.329(3)	F1-H10-F2	168.3
N2-C2	1.377(3)		
N2-C6	1.459(4)		
F1-H10	1.27(4)		
F2-H10	1.00(4)		

In the low-temperature phase of [EMIM][HF_2], the hydrogen atom in HF_2^- could be found in the difference map and its location was freely refined showing an unsymmetric HF_2^- anion. The unsymmetric F–H···F unit (F1–H10: 1.27(4) Å; F2–H10: 1.00(4) Å) is not perfectly linear (168.3°). The F···F distance of 2.257(4) Å in $EMIMHF_2$ is fairly close to what has been observed in the case of other bifluoride salts ([$(CH_3)_4N$][HF_2]: 2.213(4) Å; [p-toludinium][HF_2]: 2.260(4) Å).[14,15,16,17] The geometrical parameters for the $EMIM^+$ cation are in agreement with the known $EMIMHF_2$ crystal structure at 25 °C.[9] $EMIMHF_2$ crystallizes in a layered structure made up of $EMIM^+$ cation and HF_2^- anion. The distance between the planes of two imidazolium rings is 3.331 Å (Figure 7.2).

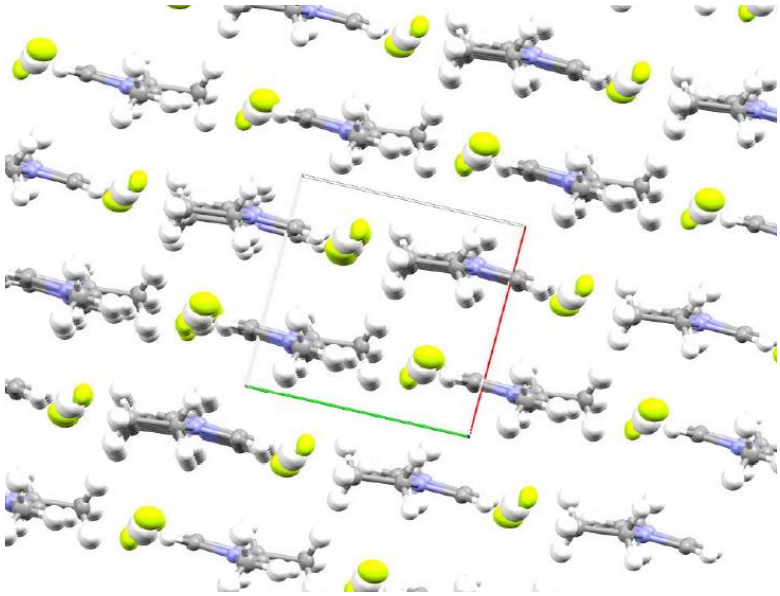

Figure 7.2 Thermal ellipsoid plot of 1-ethyl-3-methylimidazolium bifluoride at 50% probability level in the crystal structure of 1-ethyl-3-methylimidazolium bifluoride ($EMIMHF_2$)

The H···F contacts between HF_2^- and protons of the imidazolium ring in $EMIMHF_2$ are 2.001 Å (H1···F2), 2.116 Å (H2···F1) and 2.114 Å (H3···F1) which are less than the sum of the van der Waal's radii (2.67 Å) and compare well with the room temperature structure. The local environment of HF_2^- is very similar to that in the room temperature structure.

7.2.2 Solution and Solid State NMR spectroscopy of 1-ethyl-3-methylimidazolium bifluoride

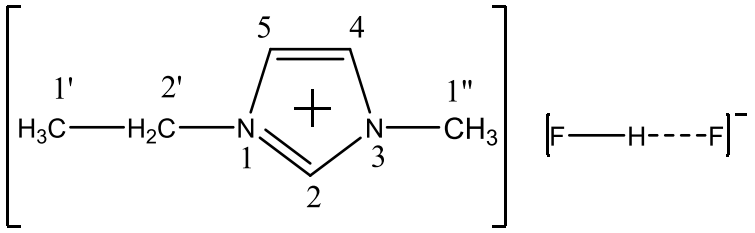

(Scheme-I)

7.2.2.1 ^{1}H and ^{13}C NMR spectroscopy

The comparison of solution- and solid-state ^{1}H NMR spectra of $EMIMHF_2$ is shown in Figure 7.3. Figure 7.3(a) shows the solution-state NMR spectrum in DMSO-d6 solvent while 7.3 (b) shows the solid-state MAS NMR spectrum. Due to the broad resonances in the ^{1}H MAS NMR spectrum, the solid-state spectrum was deconvolved with different contributions based on the available features in the spectrum and the areas of the contributions were compared. It was difficult to separate the 2': $–CH_2$ and 1": $–CH_3$ contributions and thus the sum of these contributions was deconvolved as a single peak. The areas for the imidazolium proton contributions of imidazolium rings agrees well with the number of protons present. The small sharp signals in the solid-state NMR spectrum signals point to different mobile contributions present in the imidazolium cation. The broad signal at 8.19 ppm might be due to the background signal from the Torlon cap of the rotor. The chemical shifts for the protons in the solid state are close to those obtained in the solution NMR experiment.

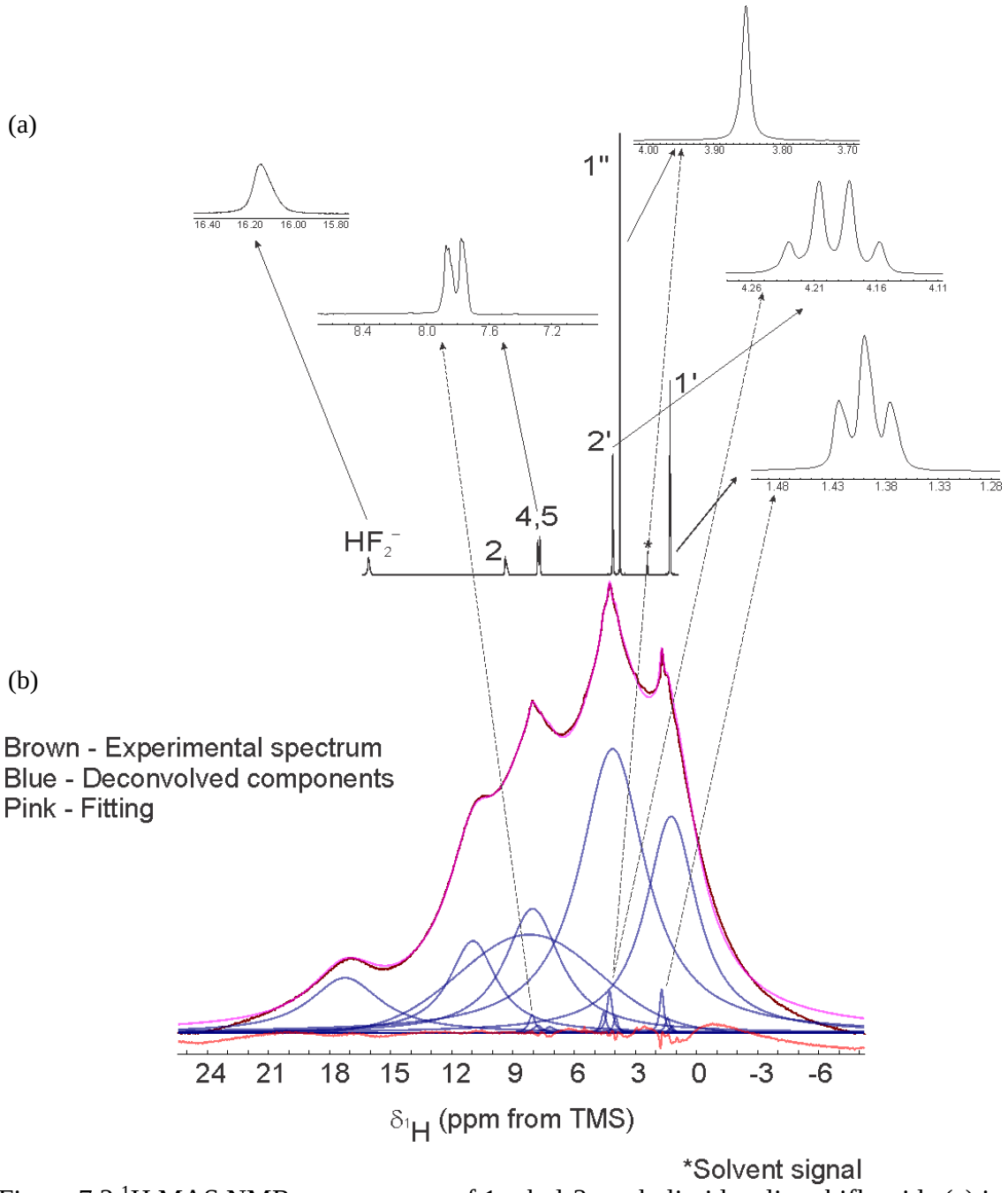

Figure 7.3 ^{1}H MAS NMR spectroscopy of 1-ethyl-3-methylimidazolium bifluoride (a) in solution state using DMSO-d6 as solvent at 20 °C (b) solid-state ^{1}H NMR spectrum with deconvolution at 14 kHz MAS spinning rate at –40 °C.

The chemical shifts for the methyl group on the imidazolium ring is shifted to higher frequency due to their attachment to the more electronegative nitrogen atom in the 1-ethyl 3-methyl imidazolium ring when compared to the methyl group on the alkyl chain. The 4,5

ring proton positions are in the range of aromatic protons (6.0 to 8.0 ppm) while the proton on the 2-position is shifted out of aromatic range because of its connectivity to two more electronegative nitrogen atoms. The HF_2^- signal appears at the highest frequency compared to the other proton signals in $EMIMHF_2$ due to the highest electronegativity of the fluorine atoms.

Table 7.3 Comparison of ^1H NMR chemical shifts of $EMIMHF_2$ in solution and solid state

Solution State (21 °C)		Solid State (–40 °C)	Assignments
Solvent: DMSO-d6			
δ (ppm)	$^3J(^1H\text{-}^1H)$, Hz	δ (ppm); Integration (Area)	
1.40 (triplet)	7.1	1.23; 2.84	$–CH_3$ (1')
3.85 (singlet)	-	4.11; 4.77	$–CH_3$ (1")
4.19 (quartet)	7.2		$–CH_2$ (2')
7.81 (doublet)	27.7	8.03; 1 .76	–CH (4,5)
9.46 (singlet)	-	10.97; 1.10	–CH (2)
16.10 (singlet)	-	17.24; 1.00	HF_2^-

The ^{13}C NMR chemical shifts for the 1-ethyl-3-methylimidazolium cation unit in the solution and solid state are given in Table 7.4 and the spectra are shown in Figure 7.4. In the solid-state NMR spectrum, there are some broad features underneath the imidazolium cation signals and the methylene signal of the ethyl chain is probably due to the contribution from the less mobile imidazolium part.

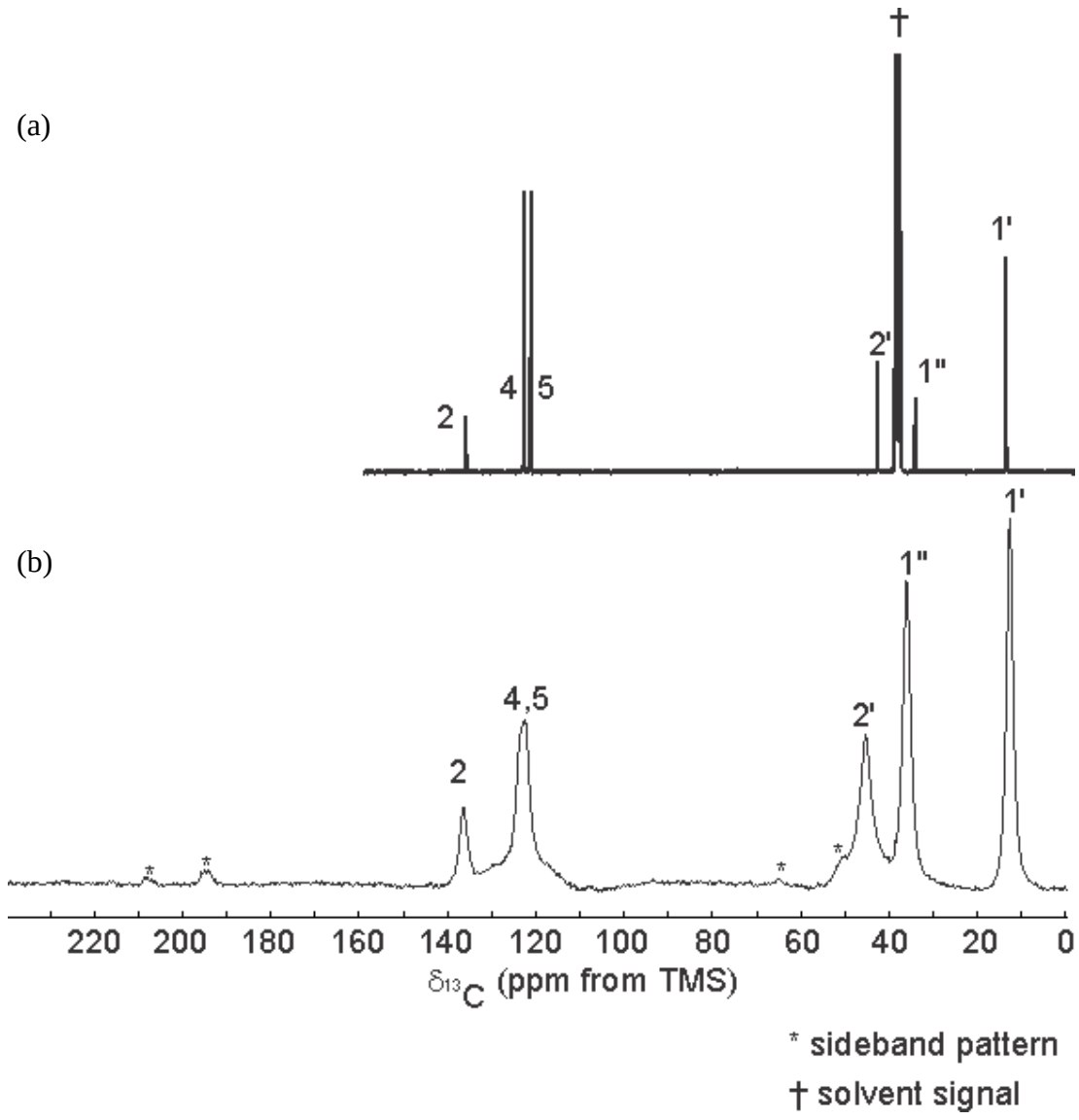

Figure 7.4 (a) $^{13}C\{^{1}H\}$ solution NMR spectroscopy of 1-ethyl-3-methylimidazolium bifluoride in DMSO-d6 solvent at 20 °C (b) ^{13}C $\{^{1}H–^{13}C$ CP$\}$ with 1 ms contact time NMR spectroscopy of 1-ethyl-3-methylimidazolium bifluoride in the solid state at 9 kHz spinning rate at –40 °C.

Table 7.4 Comparison of ^{13}C NMR chemical shifts of $EMIMHF_2$ in solution and solid state

Solution state (20 °C)	Solid state (–40 °C)	Assignments
Solvent – DMSO		
δ (ppm)	δ (ppm)	
15.13	12.6	$–CH_3$ (1')
35.57	36.0	$–CH_3$ (1")
44.03	45.3	$–CH_2$ (2')
122.0	122.4	–CH (5)
123.6	123.8	–CH (4)
136.6	136.4	–CH (2)

7.2.2.2 ^{19}F NMR spectroscopy

The ^{19}F NMR chemical shift for the bifluoride (HF_2^-) unit is found at –141.2 ppm of a solution of $EMIMHF_2$ in DMSO-d6 solvent at 21 °C (Figure 7.5(a)). The direct polarization experiment on ^{19}F in solid state at –15 °C provided no discernable or very weak fluorine signal for HF_2^- because of the large ^{19}F background signal coming from the FEP material used to make the insert (Figure 7.6). Thus, the ^{1}H–to–^{19}F cross polarization technique was applied to filter out the FEP signals. Two isotropic fluorine signals were observed at –141.2 and –144.8 ppm using a short contact time of 50 μs as shown in Figure 7.5 (c) while only one isotropic fluorine signal at –141.2 ppm was obtained using a longer contact time (160 μs) as shown in Figure 7.5 (b). The presence of two fluorine signals with short contact time indicates the presence of two different fluorine environments: one which is less mobile and the other which is more mobile.

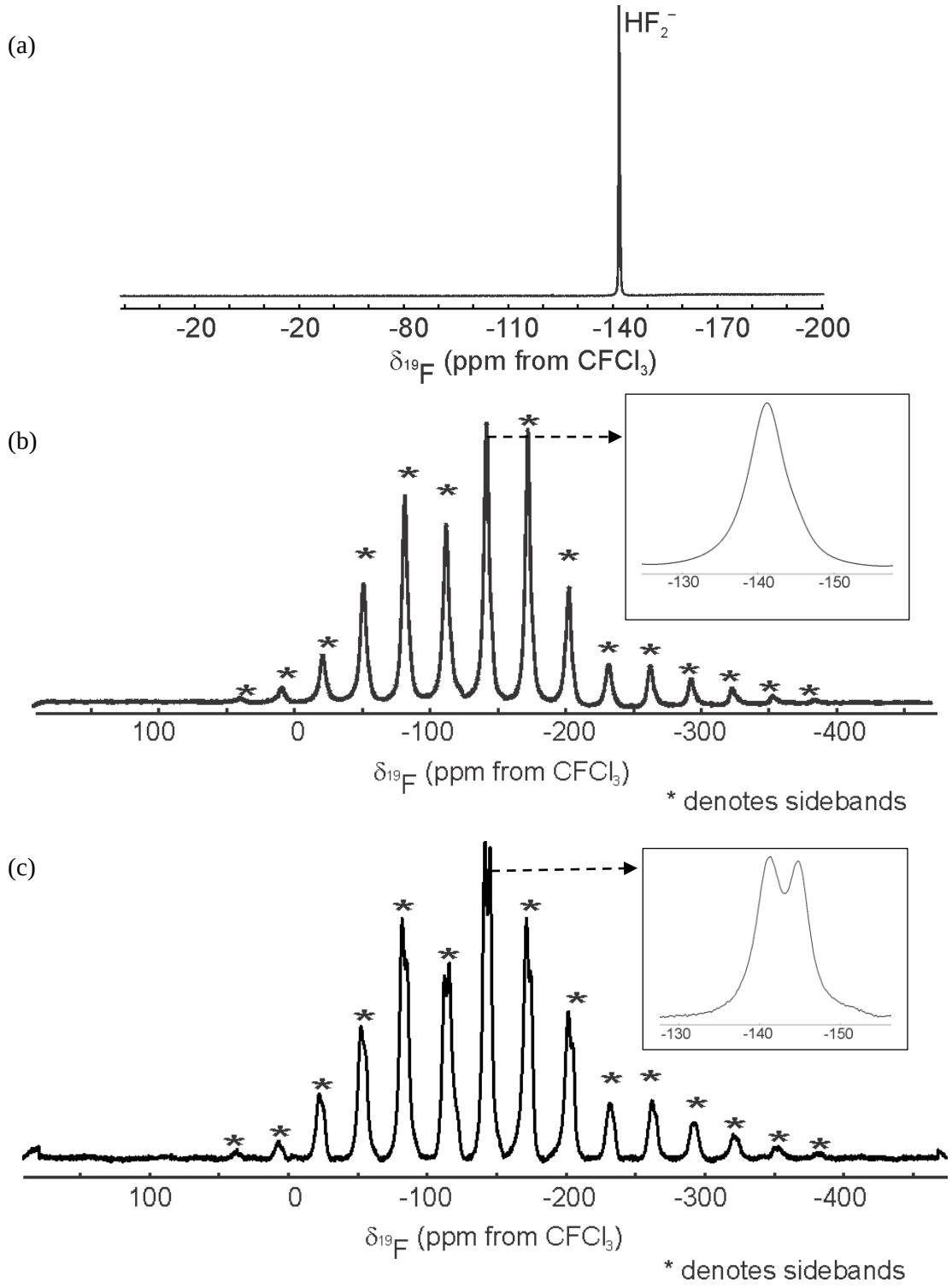

Figure 7.5 (a) ^{19}F signal in solution state using DMSO-d6 solvent and $^{19}F\{^{1}H$-to-^{19}F CP} MAS NMR spectra with (b) 160 μs and (c) 50 μs contact time NMR spectroscopy of 1-ethyl-3-methylimidazolium bifluoride in the solid state at 14 kHz spinning rate at –40 °C. The isotropic signal is at –141.2 ppm for 160 μs contact time while with 50 μs contact time, two signals were obtained at –141.2 and –144.8 ppm respectively.

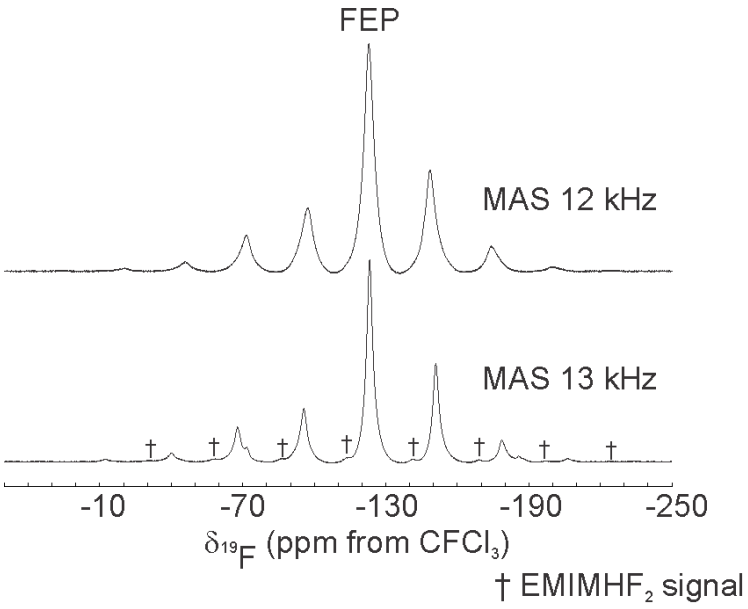

Figure 7.6 ^{19}F DP NMR spectrum in solid state using different spinning rate at –40 °C.

7.2.3 ^{1}H–to–^{19}F and ^{19}F–to–^{1}H CP build-up experiments with magic angle spinning

7.2.3.1 ^{1}H–to –^{19}F CP build-up experiment and simulation of the spectra

The ^{1}H–to–^{19}F CP build-up curve shows the presence of two different types of fluorine environments at contact time periods between 10 μs to 180 μs (Figure 7.7). The intensity of the ^{19}F signal at –144.8 ppm builds up until a contact time of 60 μs and then decreases until it vanishes at 160 μs. The signal at –141.2 ppm (more mobile phase) increases gradually up to 200 μs and then decreases (Figure 7.8). This signal is taking longer time to build up, and is considered to represent a more mobile environment. The signal at –144.8 ppm represents the less mobile environment.

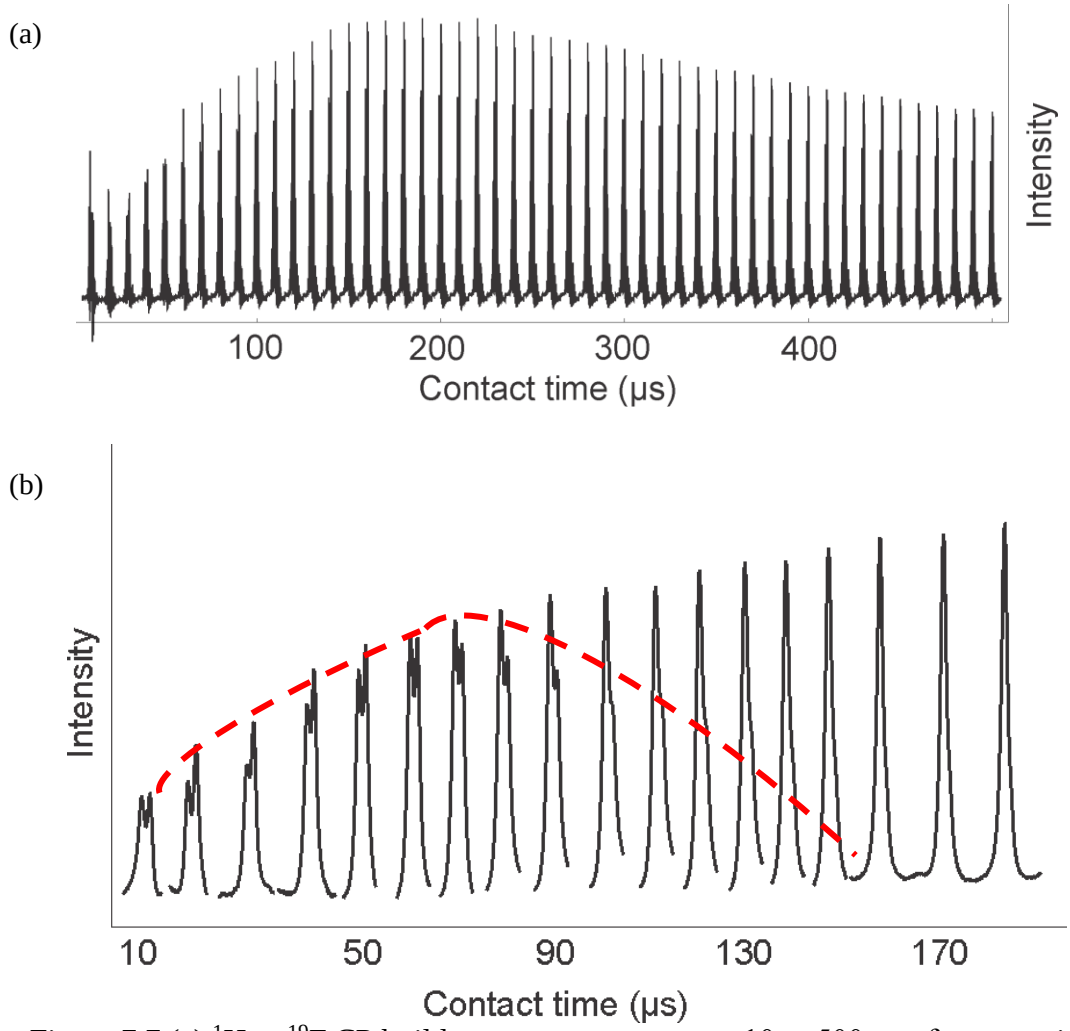

Figure 7.7 (a) ^{1}H to ^{19}F CP build-up curve over a range 10 to 500 μs of contact-time periods in the steps of 10 μs interval (b) Extension of ^{1}H to ^{19}F CP build up curve for the contact time over a range of 10 to 180 μs.

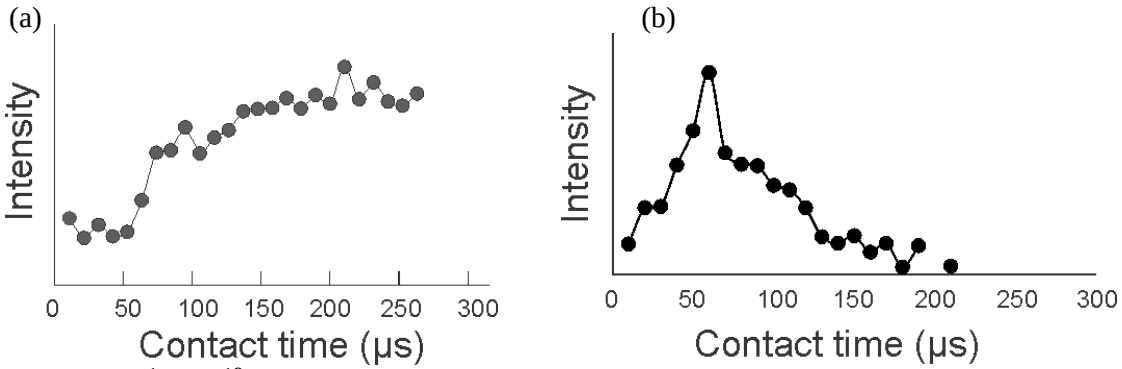

Figure 7.8 ^{1}H to ^{19}F CP build-up curve over a range of 0 to 300 μs contact-time periods for ^{19}F signal at (a) –141.2 ppm (more mobile component) and (b) at –144.8 ppm (less mobile component).

The ^{19}F NMR spectra obtained in the ^{1}H–to–^{19}F CP build up array were simulated using the SIMPSON software.[18] For simulating the resultant spectra, the maximum value for the chemical shielding anisotropy (CSA) for the ^{19}F and ^{1}H shielding tensors were taken from the solid-state NMR work on KHF_2 by Hecke et al.[19,20] Smaller CSA value can arise because of motional scaling. Unfortunately, $^{1}H\{^{19}F\}$ and $^{19}F\{^{1}H\}$ decoupling did not work in the present work. Hence, the dipolar coupling values between H–F and F–F were calculated based on the crystal structure parameters obtained by Hagiwara for $EMIMHF_2$ at 25 °C.[9] The Euler angle (β) (defining the displacement of the object from z-axis in the principal axis system) used in the simulation work was then varied to match the simulated spectra with the experimental one. Due to the presence of overlap of the signals, distortion in the base line and contribution from FEP signal, the experimental spectra were first deconvolved (Figure 7.9) and then matched with the simulation results. The results obtained from the simulation work are summarized in Table 7.5.

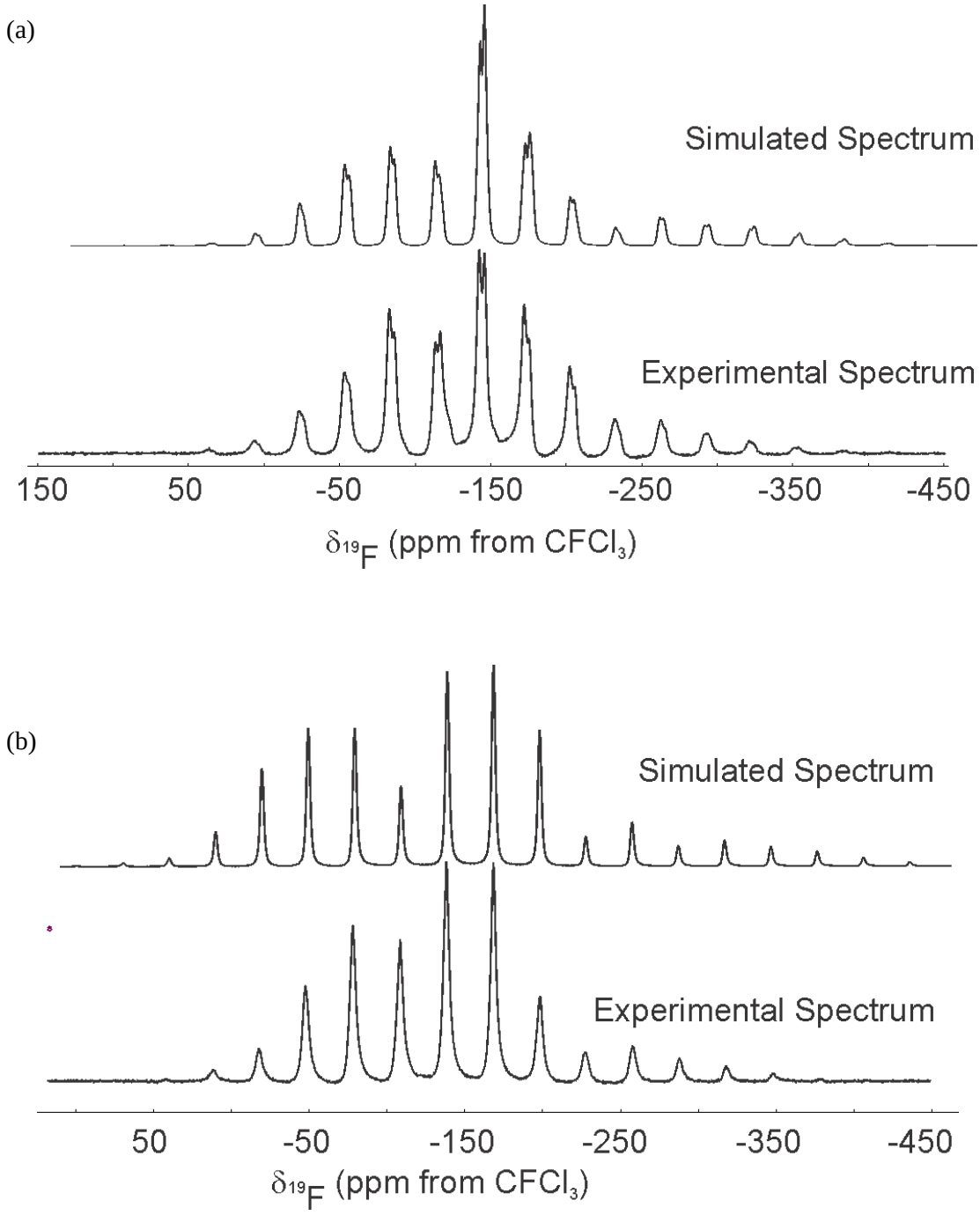

Figure 7.9 ^{1}H–to–^{19}F CP MAS NMR simulated and experimental spectra for (a) 60 μs and (b) 160 μs at 14 kHz MAS spinning rate.

Table 7.5 SIMPSON simulation results for the ^{19}F and ^{1}H tensors of HF_2^- anion in $EMIMHF_2$

Contact time (μs)	60		160	
Nucleus	^{1}H	^{19}F	^{1}H	^{19}F
CSA (ppm)[a]	44	74	44	84
H–F dipolar coupling (kHz)[b]	68.8	68.8	88.8	88.8
F–F dipolar coupling (kHz)[c]	10.7	10.7	9.8	9.8
Angle, β (°)[d]	140	140	180	180
Asymmetry (η)[e]	0.3	0.3	0	0

The uncertainties associated with the ^{19}F CSA,[a] ^{1}H–^{19}F dipolar couplings and ^{19}F–^{19}F dipolar couplings,[b,c] asymmetry[e] and β[d] angle are ±3 ppm, ±0.5 kHz, ±0.1 and ±5°, respectively.

The results obtained from simulating the ^{19}F and ^{1}H tensors of HF_2^- anion in $EMIMHF_2$ suggest the presence of $H_2F_3^-$ and $H_3F_4^-$ anions beside HF_2^- (scheme II). The dipolar coupling values, asymmetry and CSA values for ^{19}F tensor are different for the non-linear bifluoride contributions compared to the linear bifluoride contribution (CSA: 74.0 versus 84.0 ppm; ^{1}H–^{19}F dipolar coupling: 68.8 versus 88.8 kHz). It indicates the deviation of ^{19}F tensors from linearity for different fluorohydrogenate anions contributions in $EMIMHF_2$, which might be present as an impurity from the starting material $EMIM(HF)_{2.3}$. It should be noted that the fluorine in HF_2^- and μ (bridging) fluorine in $H_2F_3^-$ and $H_3F_4^-$ anions (Scheme II) have one, two and three neighboring protons, respectively. Thus, in the ^{1}H-to-^{19}F CP build-up experiment, the ^{19}F signal for $H_3F_4^-$ anion will experience more efficient cross polarization from ^{1}H and will appear at the short contact times followed by the $H_2F_3^-$ and HF_2^- at the longer contact time periods.

It was noticed in the simulations that a perfect match between the experimental and the simulated spectrum is difficult to obtain where the experimental spectrum represents a combination of different contributions.

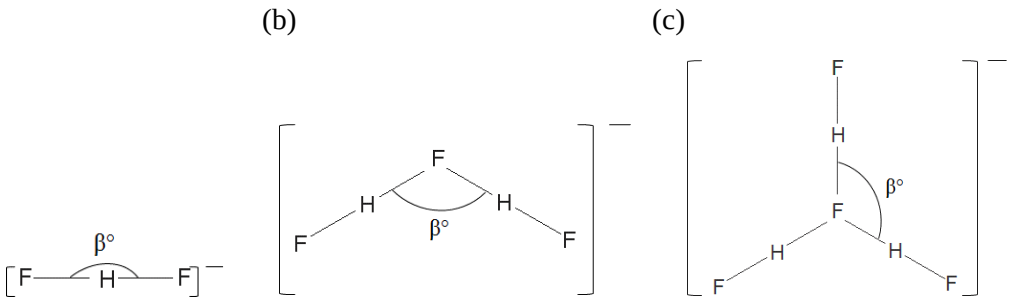

(Scheme-II) The geometries for HF_2^-, $H_2F_3^-$ and $H_3F_4^-$ anions.

7.2.3.2 ^{19}F–to–^{1}H CP build up experiment

The ^{19}F–to–^{1}H CP build up curve is shown in Figure 7.10 (a). The intensity of the bifluoride signal gradually deceases as the contact time increases while the intensities for the basal protons of the imidazolium cation increases gradually at the same time. The intensity for the imidazolium protons is shown in Figure 7.10 (b) which shows an increase with the increasing contact time while the intensity of the bifluoride proton signal is showing a decrease as shown in Figure 7.10 (c). The increase in intensity for the protons of the imidazolium ring indicates the more dynamic behavior of imidazolium cation as compared to the bifluoride anion because the more dynamic contribution takes more time in signal build-up whereas the less dynamic contribution builds up very fast. Initially, only the signals from HF_2^- will show up at short contact times because of the strong covalent bonding between proton and fluorine. As the contact period is increased, the imidazolium proton signals come up due to the short contacts between ^{1}H of imidazolium ring and the ^{19}F of HF_2^-.

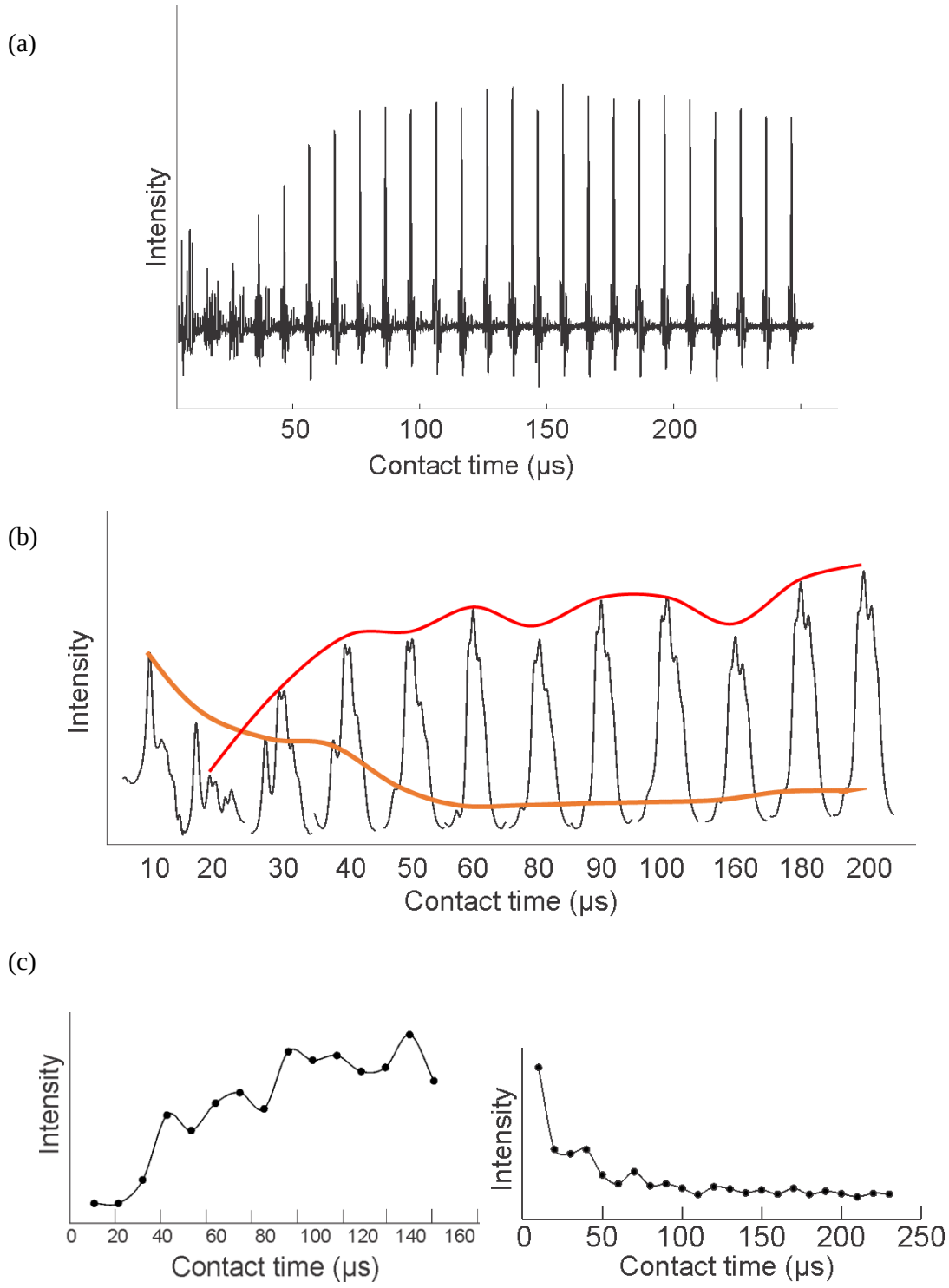

Figure 7.10 (a) The plot of intensity of the $EMIMHF_2$ proton signals over a range 10 – 250 μs of contact-time periods in the steps of 10 μs interval in ^{19}F –to-^{1}H CP build-up (b) expansion of the isotropic signal of array shown in 7.10a (c) ^{1}H imidazolium ring protons signal increasing intensity and ^{1}H signal decreasing intensity of the bifluoride protons as a function of contact time.

The ^{1}H NMR spectra obtained in the ^{19}F–to–^{1}H CP build up array were simulated using the SIMPSON software.[18] The values for CSA, ^{1}H–^{19}F dipolar coupling obtained in the ^{19}F simulation was used for simulating the ^{1}H experimental spectrum. The simulated spectrum at 160 μs is shown in the following figure 7.11.

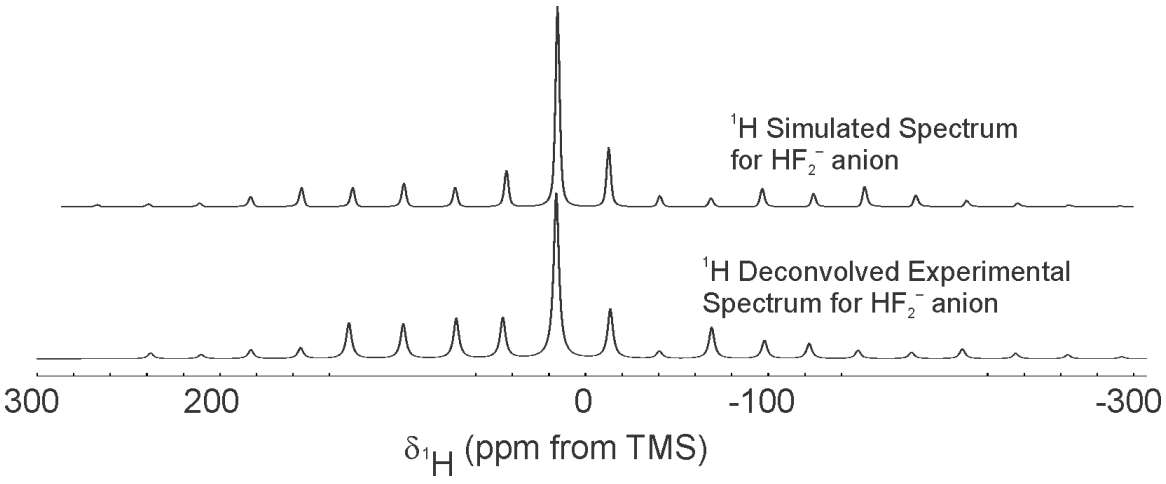

Figure 7.11 ^{19}F–to–^{1}H CP MAS NMR spectra simulation for 160 μs contact time and at 14 kHz MAS spinning rate

7.2.4 Dipolar-dephasing experiments with magic angle spinning

Dipolar-dephasing experiments were performed on the ^{13}C resonance by applying a variable delay on the ^{1}H resonance in the ^{1}H–to–^{13}C cross-polarization NMR experiment. It provides a direct measure of the dipolar coupling strength of C–H bond associated with the particular carbon nucleus. The magic angle spinning removes the chemical shielding anisotropy yielding narrow ^{13}C resonances. The ^{13}C–^{1}H dipolar coupling has an $1/r^3$ dependence, where r is the inter-nuclear distance between carbon and proton. This coupling strength is greater for the carbons directly bonded to protons as compared to the protons on the neighboring carbons. Thus, for a short dephasing delay only the directly bonded proton-carbon couple will be affected and the signal will disappear after the coupling strength of ^{13}C–^{1}H bond length is passed. If the signal is still present, it indicates the occurrence of

some dynamical process related to the mobility for that particular ^{13}C–^{1}H bond. The ^{13}C–^{1}H dipolar coupling is responsible for the rapid T_2 relaxation of the ^{13}C. If an array of spectra is collected with this experiment, the different types of ^{13}C environments can be distinguished based on their relaxation rates and the shape of the curves. The dipolar dephasing experiments were performed on the imidazolium ring of the $EMIMHF_2$ at –40 °C (Figure 7.12). The ^{13}C signals at 121.3 ppm and 123.4 ppm persisted even after the application of the required total dephasing delay, which was calculated based on the inter-nuclear C–H distance (1.09 Å for aromatic ring systems). Based on this distance the carbon signal should dephase in about 42 μs but the imidazolium carbon signals at 4 and 5 position survive even after this dephasing time period up to about 60 μs. The persistence of the signal after total dephasing delay indicated the presence of molecular dynamics in the imidazolium ring at –40 °C. The presence of dynamics in the imidazolium ring was confirmed on repeating this experiment by warming up the sample. As a consequence of higher temperature, the dephasing time of the imidazolium carbon signals increased a bit.

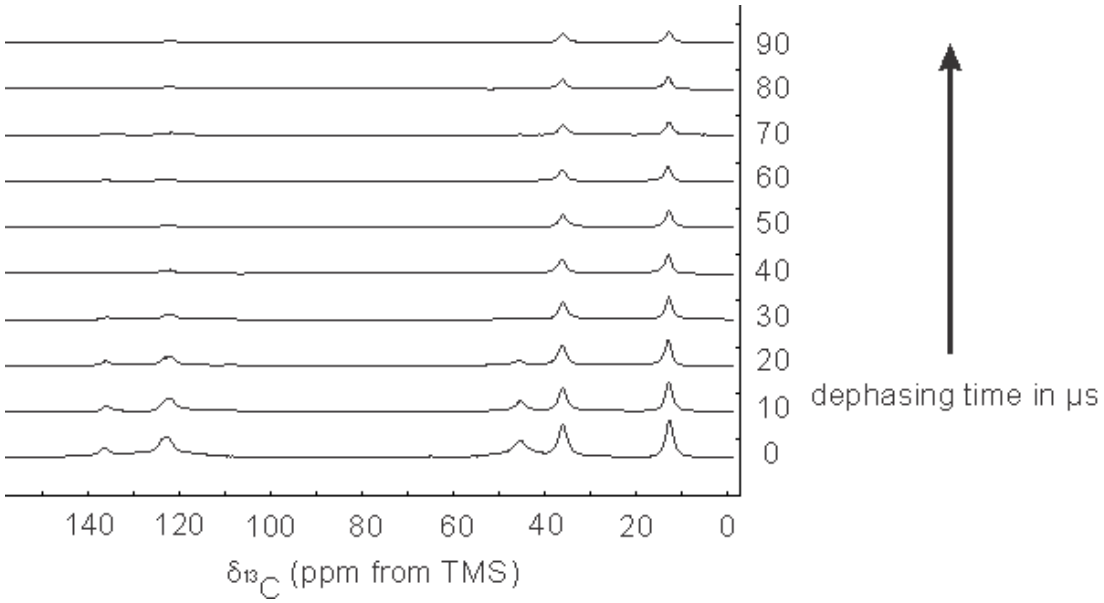

Figure 7.12 Dipolar dephasing experiments with magic angle spinning of 1-ethyl-3-methylimidazolium bifluoride at MAS 9 kHz and –40 °C.

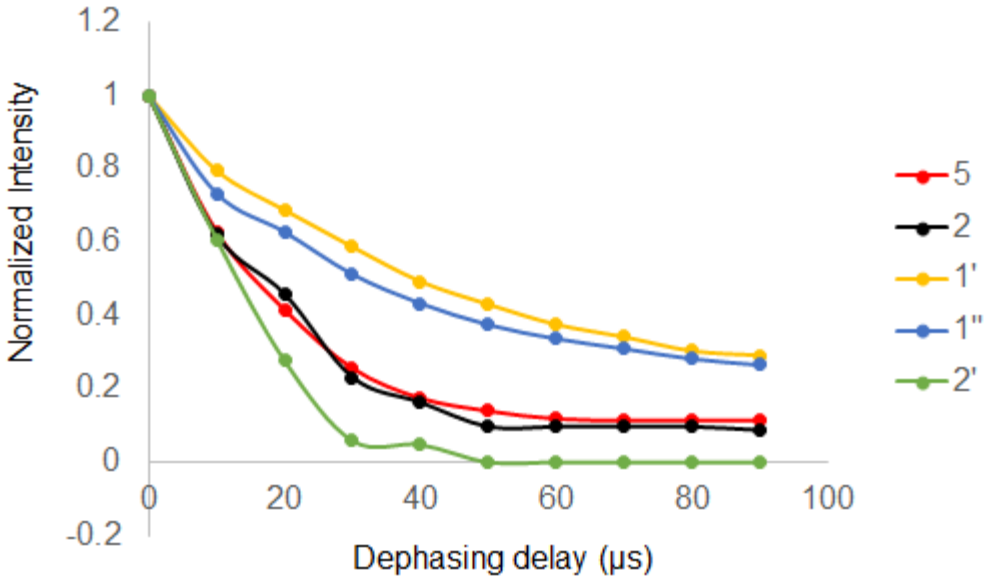

Figure 7.13 Intensity (I/I_0) versus dephasing delay graph of the dipolar dephasing experiments with the magic angle spinning for 1-ethyl-3-methylimidazolium bifluoride at MAS 9 kHz and –40 °C.

Table 7.6 ^{13}C NMR chemical shifts of $EMIMHF_2$ in solid state dipolar-dephasing spectra

δ (ppm)	Identification	Assignments
12.6	1’	$–CH_3$
36.0	1”	$–CH_3$
45.3	2’	$–CH_2$
122.4	5	–CH
123.8	4	–CH
136.4	2	–CH

It is evident from the results of dipolar dephasing experiments (Figure 7.13) that the highly mobile $–CH_3$ groups on the imidazolium cation as well as on the alkyl chain dephase very slowly because of rapid motion of the methyl group. The imidazolium ring protons dephase relatively faster compared to the $–CH_3$ groups because of the less dynamics of the ring system whereas the $–CH_2$ group dephase very rapidly due to its comparatively more rigid nature as compared to the $–CH_3$ group and because of its direct attachment to the nitrogen of the imidazolium ring.

7.3 Conclusion

Based on the results from simulations of 1D ^{1}H and ^{19}F spectra and dipolar-dephasing experiments, it can be concluded that the presence of dynamics is evident for the 1-ethyl-3-methylimidazolium cation in $EMIMHF_2$ at 14.0 kHz at –40 °C. The simulation results suggests the presence of some kind of agglomerated domain structure for the fluorohydrogenate anions in the form of $H_2F_3^-$ and $H_3F_4^-$ anions besides HF_2^- and thus signifies the importance of CP dynamics in detecting impurities in the material.

References

1. Domanska, U. *Pure Appl. Chem.* **2005**, *77*, 3, 543.

2. Eike, D. M.; Brennecke, J. F.; Maginn, E. J. *Green Chem.* **2003**, *5*, 323.

3. Wilkes, J. S.; Zaworotko, M. J. *J. Chem. Soc. Chem. Comm.* **1992**, 965.

4. Wilkes, J. S. *ACS Symp. Ser., Am. Chem. Soc.* **2002**, *818*, 214.

5. Wilkes, J. S. *Green Chem.* **2002**, *4*, 73.

6. Pollock, J. M.; Sharan, M. *J. Chem. Phys.* **1967**, *47*, 4064.

7. Sun, D., Zhou, J. *Am. Inst. Chem. Eng.* **2013**, *59*, 2630.

8. Hagiwara, R.; Nakamori, Y.; Matsumoto, K., Ito, Y. *J. Phys. Chem. B* **2005**, *109*, 5445.

9. Matsumoto, K; Tsuda, T.; Hagiwara, R.; Ito, Y., Tamada, O. *Solid State Sci.* **2002**, 4, 23.

10. Hagiwara, R.; Hirashige, T.; Tsuda, T., Ito, Y. *J. Fluorine Chem.* **1999**, *99*, 1.

11. Saito, Y. Hirai, K.; Matsumoto, K.; Hagiwara, R.; Minamizaki, Y. *J. Phys. Chem. B* **2005**, *109*, 2942. (b) Matsumoto, K; Tsuda, T.; Hagiwara, R.; Ito, Y.; Tamada, O. *Solid State Sci.* **2002**, *4*, 23.

12. Enomoto, T.; Nakamori, Y.; Matsumoto, K.; Hagiwara, R. *J. Phys. Chem. C* **2011**, *115*, 4324.

13. Williams, J. M.; Schneemeyer, L. F. *J. Am. Chem. Soc.* **1973**, *95*, 5780.

14. Wilson, W. W.; Christe, K. O. *Can. J. Chem.* **1989**, *67*, 1898.

15. Troyanov, S. I. *Crystallography Reports* **2005**, *50*, 5, 773.

16. Rush, J. J.; Schroeder, L. W.; Melveger, A. J. *J. Chem. Phys.* **1972**, *56*, 6, 2793.

17. Ostlund, N. S.; Ballenger, L. W. *J. Am. Chem. Soc.* **1975**, *97*, 1237.

18. Bak, M.; Rasmussen, J. T.; Nielsen, N. C. *J. Magn. Res.* **2000**, *147*, 296.

19. Hecke, P. V.; Spiess, H. W.; Haeberlen, U. *J. Magn. Res.* **1976**, *22*, 103.

20. Hecke, P. V.; Spiess, H. W.; Haeberlen, U. *J. Magn. Res.* **1976**, *22*, 93.

Chapter-8

8. Conclusion and future directions

The crystal structures of two modifications of $[SF_3][SbF_6]$ (γ- and α-phases) and of $[SF_3][AsF_6]$ were characterized. The structure for the β-phase of $[SF_3][SbF_6]$ still needs to be conclusively characterized. Deoxofluorination reactions for two ketones, two carboxylic acids and an alcohol were done from $[SF_3][SbF_6]$ and $[SF_3][AsF_6]$ using SO_2, CH_3CN, and CH_2Cl_2 solvents. More substrates need to be used for a complete establishment of the use of $[SF_3][SbF_6]$ and $[SF_3][AsF_6]$ as deoxofluorinating reagents in organic chemistry. A series of adducts between $[SF_3][MF_6]$ (M = Sb, As) and nitrogen bases were studied and conclusively characterized. The 1:2 ratio between the SF_3^+ cation of $[SF_3][MF_6]$ (M = Sb, As) salts and nitrogen ligands was conclusively shown at low temperature. The synthesis and conclusive characterization of a 1:1 adduct of $[SF_3][MF_6]$ (M = Sb, As) salts and nitrogen bases is still pending. The reactions of $[SF_3(N\text{-base})_x]^+$ cation with highly Lewis acidic compounds, such as AsF_5 and SbF_5, can be studied to explore the synthesis of $[SF_2(N\text{-base})_x]^{2+}$ compounds. The nitrogen bases can be replaced with oxygen bases to study $[SF_3(O\text{-base})][MF_6]$ and $[SF_3(O\text{-base})_2][MF_6]$ (M = Sb, As) compounds to better understand the reactive intermediate species in the deoxofluorination reactions of carbonyl compounds.

The $WOF_4{\cdot}SO_2$ adduct was identified in the solid state and conclusively characterized by X-ray crystallography and Raman spectroscopy. The first X-ray structure of WOF_5^- in the form of $[(CH_3)_4N][WOF_5]$ was characterized without any disorder and more accurate metric parameters. The mono substituted product of WOF_4 with CF_3CH_2OH, i.e. $WOF_3(OCH_2CF_3)$ was conclusively characterized as its CH_3CN adduct, i.e. $CH_3CN{\cdot}WOF_3(OCH_2CF_3)$. Attempts should be made to synthesize the products in which

more fluorine atoms can be substituted from WOF_4. Also the chemistry of WOF_4 involving the driving force of H–F bond formation can be extended to different aliphatic and aromatic alcohols.

The first X-ray crystallographic results for perfluoro carboxylic acids and carboxylates have been reported. Future work may include efforts to the get the anhydrous crystal structures of these perfluoro carboxylic acids to explore their dimeric form.

The solid state NMR spectroscopy for the $EMIMHF_2$ imidazolium ionic liquid provided the indications of dynamics and sources of impurity present in this salt.

APPENDIX

Appendix – Chapter3

Table 3A1. Crystal data and structure refinement for $[SF_3][AsF_6]$

Empirical formula	F_9SAs
Formula weight, g mol^{-1}	163.98
Temperature, K	143(2)
Wavelength, pm	71.073
Crystal System	Orthorhombic
Space group	$Cmc2_1$
Unit cell dimensions, Å	a = 20.308(14)
	b = 8.369(6)
	c = 11.091(7)
Volume, 10^2 $Å^3$	18.85(2)
Z	8
Density(calculated), mg mm^{-3}	2.938
Absorption coefficient, mm^{-1}	5.866
F(000)	1560
Crystal size, mm^3	0.40 × 0.24 × 0.09
Theta range for data collection	2.01° – 29.23°
Index ranges	$-27 \leq l \leq 27$
	$-10 \leq l \leq 10$
	$-14 \leq l \leq 14$
Reflections collected	14074
Independent reflections	2490 [R(int) = 0.0322]
Completeness to theta[27.55°]	96.8%
Refinement method	Full matrix Least-squares on F^2
Data/restraints/parameters	2490 / 1 / 158
Goodness-of-fit on F^2	1.298
Refine diff density_max	0.413
Refine diff density_ min	–0.516

Table 3A2. Crystal data and structure refinement for γ-$[SF_3][SbF_6]$

Empirical formula	F_9SSb
Formula weight, g mol^{-1}	324.81
Temperature, K	143(2)
Wavelength, pm	71.073
Crystal System	Monoclinic
Space group	$P2_1/n$
Angle-β,º	96.0138(12)°
Unit cell dimensions, Å	a = 7.6921(10)
	b = 10.5450(13)
	c = 8.0879(10)
Volume, 10^2 $Å^3$	6.5243(14)
Z	4
Density (calculated), mg mm^{-3}	3.307
Absorption coefficient, mm^{-1}	4.669
F(000)	592
Crystal size, mm^3	0.43 × 0.28 × 0.19
Theta range for data collection	2.56° - 27.55°
Index ranges	$-7 \leq h \leq 7$,
	$-13 \leq k \leq 13$,
	$-16 \leq l \leq 16$
Reflections collected	8134
Independent reflections	1664 [R_{int} = 0.017]
Completeness to theta [27.55°]	99.2%
Refinement method	Full matrix Least-squares on F^2
Data/restraints/parameters	1664/1/114
Goodness-of-fit on F^2	1.092
Refine diff density_max	0.515
Refine diff density_min	–0.400

Table 3A3. Crystal data and structure refinement for α-$[SF_3][SbF_6]$

Empirical formula	F_9SSb
Formula weight, g mol^{-1}	324.81
Temperature, K	143(2)
Wavelength, pm	71.073
Crystal System	Monoclinic
Space group	$P2_1/c$
Angle-β,º	98.06(3)°
Unit cell dimensions, Å	a = 5.621(12)
	b = 11.85(2)
	c = 11.19(2)
Volume, 10^2 $Å^3$	7.38(3)
Z	4
(calculated), mg mm^{-3}	2.923
Absorption coefficient, mm^{-1}	4.128
F(000)	592
Crystal size, mm^3	0.33 × 0.30 × 0.09
Theta range for data collection	2.52° - 26.46°
Index ranges	$-2 \leq h \leq 7$,
	$-14 \leq k \leq 14$,
	$-13 \leq l \leq 10$
Reflections collected	1735
Independent reflections	1365 [R(int) = 0.0321]
Completeness to theta[27.55°]	90.0%
Refinement method	Full matrix Least-squares on F^2
Data/restraints/parameters	1365 / 0 / 101
Goodness-of-fit on F^2	2.698
Refine diff density_max	1.897
Refine diff density_ min	–2.298

Appendix – Chapter4

Table 4A1. Crystal data and structure refinement for $[SF_3(C_5H_5N)_2][SbF_6]\cdot CH_2Cl_2$

Empirical formula	$C_{11}H_{12}Cl_2F_9N_2SSb$
Formula weight, g mol^{-1}	567.951
Temperature, K	153(2)
Wavelength, pm	71.073
Crystal System	Monoclinic
Space group	*C*2/*c*
Angle-β,º	108.0420(10)°
Unit cell dimensions, Å	a = 10.9147(14)
	b = 12.6434(16)
	c = 14.3462(18)
Volume, 10^2 $Å^3$	18.824(4)
Z	4
Density (calculated), mg mm^{-3}	1.5826
Absorption coefficient, mm^{-1}	3.569
F(000)	1768
Crystal size, mm^3	0.37 × 0.44 × 1.15
Theta range for data collection	2.54° – 27.62°
Index ranges	$-14 \leq h \leq 14$,
	$-16 \leq k \leq 16$,
	$-18 \leq l \leq 18$
Reflections collected	10885
Independent reflections	2181 [R_{int} = 0.0162]
Completeness to theta[27.55°]	99.5%
Refinement method	Full matrix Least-squares on F^2
Data/restraints/parameters	2181 / 0 / 145
Goodness-of-fit on F^2	4.242
Refine diff density_max	0.546
Refine dff density_min	–0.661

Table 4A2. Crystal data and structure refinement for $[SF_3(C_5H_5N)_2][AsF_6]\cdot CH_2Cl_2$

Empirical formula	$C_{11}H_{12}AsCl_2F_9N_2S$
Formula weight, g mol^{-1}	521.121
Temperature, K	153(2)
Wavelength, pm	71.073
Crystal System	Monoclinic
Space group	C_2/c
Angle-β,º	107.463(3)°
Unit cell dimensions, Å	a = 10.836(3)
	b = 12.472(3)
	c = 14.118(3)
Volume, 10^2 $Å^3$	18.201(8)
Z	4
Density (calculated), mg mm^{-3}	1.8328
Absorption coefficient, mm^{-1}	4.384
F(000)	1512
Crystal size, mm^3	0.32 × 0.36 × 0.69
Theta range for data collection	2.56° – 27.47°
Index ranges	$-14 \leq h \leq 14$,
	$-16 \leq k \leq 16$,
.	$-18 \leq l \leq 18$
Reflections collected	10418
Independent reflections	2083 [R_{int} = 0.0204]
Completeness to theta[27.55°]	99.7%
Refinement method	Full matrix Least-squares on F^2
Data/restraints/parameters	2083 / 0 / 143
Goodness-of-fit on F^2	0.866
Refine diff density_max	0.539
Refine diff density_min	–1.001

Table 4A3. Crystal data and structure refinement for $[SF_3(C_5H_5N)_2][SbF_6]\cdot C_5H_5N$

Empirical formula	$C_{15}H_{15}F_9N_3SSb$
Formula weight, g mol^{-1}	562.12
Temperature, K	153(2)
Wavelength, pm	71.073
Crystal System	Monoclinic
Space group	*C*2/*c*
Angle-β,º	125.1550(10)°
Unit cell dimensions, Å	a = 26.913(3)
	b = 8.5689(10)
	c = 18.447(2)
Volume, 10^2 $Å^3$	34.782(7)
Z	8
Density (calculated), mg mm^{-3}	2.0690
Absorption coefficient, mm^{-1}	3.540
F(000)	3040
Crystal size, mm^3	0.25 × 0.30 × 0.38
Theta range for data collection	1.85° – 27.53°
Index ranges	$-34 \leq h \leq 34$,
	$-11 \leq k \leq 11$,
	$-23 \leq l \leq 23$
Reflections collected	19324
Independent reflections	4007 [R_{int} = 0.0257]
Completeness to theta[27.55°]	99.9%
Refinement method	Full matrix Least-squares on F^2
Data/restraints/parameters	4007 / 0 / 250
Goodness-of-fit on F^2	0.986
Refine diff density_max	0.464
Refine diff density_min	–0.444

Table 4A4. Crystal data and structure refinement for $[SF_3(C_5H_5N)_2][AsF_6]\cdot C_5H_5N$

Empirical formula	$C_{15}H_{15}AsF_9N_3S$
Formula weight, g mol^{-1}	515.29
Temperature, K	153(2)
Wavelength, pm	71.073
Crystal System	Monoclinic
Space group	*C*2/*c*
Angle-β,º	124.417(4)°
Unit cell dimensions, Å	a = 26.704(10)
	b = 8.521(3)
	c = 17.984(7)
Volume, 10^2 $Å^3$	33.76(2)
Z	8
Density (calculated), mg mm^{-3}	1.9541
Absorption coefficient, mm^{-1}	4.406
F(000)	2752
Crystal size, mm^3	0.21 × 0.25 × 0.46
Theta range for data collection	1.85° – 20.16°
Index ranges	$-25 \leq h \leq 25$,
	$-8 \leq k \leq 8$,
	$-17 \leq l \leq 17$
Reflections collected	9936
Independent reflections	1620 [R_{int} = 0.0836]
Completeness to theta[27.55°]	100.0%
Refinement method	Full matrix Least-squares on F^2
Data/restraints/parameters	1620 / 0 / 250
Goodness-of-fit on F^2	1.044
Refine diff density_max	0.311
Refine diff density_min	–0.429

Table 4A5. Crystal data and structure refinement for $[SF_3(C_5H_5N)_2][SbF_6]\cdot CH_3CN$

Empirical formula	$C_{12}H_{13}F_9N_3SSb$
Formula weight, g mol^{-1}	524.071
Temperature, K	153(2)
Wavelength, pm	71.073
Crystal System	Triclinic
Space group	P*–1*
Angle-α,º	71.363(2)°
Angle-β,º	78.440(2)°
Angle-γ,º	79.556(2)°
Unit cell dimensions, Å	a = 7.6743(15)
	b = 9.0613(18)
	c = 14.160(3)
Volume, 10^2 $Å^3$	9.068(3)
Z	2
Density (calculated), mg mm^{-3}	1.8497
Absorption coefficient, mm^{-1}	3.569
F(000)	848
Crystal size, mm^3	0.77 × 0.15 × 0.24
Theta range for data collection	1.54° – 27.79°
Index ranges	$-10 \leq h \leq 10$,
	$-11 \leq k \leq 11$,
	$-18 \leq l \leq 18$
Reflections collected	10923
Independent reflections	4223 [R_{int} = 0.0354]
Completeness to theta[27.55°]	98.4%
Refinement method	Full matrix Least-squares on F^2
Data/restraints/parameters	4223 / 0 / 240
Goodness-of-fit on F^2	1.029
Refine diff density_max	2.196
Refine diff density_min	–0.638

Table 4A6. Crystal data and structure refinement for $[SF_3(CH_3CN)_2][SbF_6]$

Empirical formula	$C_4H_6F_9N_2SSb$
Formula weight, g mol^{-1}	406.92
Temperature, K	153(2)
Wavelength, pm	71.073
Crystal System	Orthorhombic
Space group	*Pnma*
Unit cell dimensions, Å	a = 13.546(13)
	b = 12.717(12)
	c = 6.992(7)
Volume, 10^2 $Å^3$	12.04(2)
Z	4
Density (calculated), mg mm^{-3}	2.1634
Absorption coefficient, mm^{-1}	3.816
F(000)	1020
Crystal size, mm^3	0.09 × 0.15 × 0.18
Theta range for data collection	3.01° – 27.81°
Index ranges	$-17 \leq h \leq 17$,
	$-16 \leq k \leq 16$,
	$-9 \leq l \leq 9$
Reflections collected	13609
Independent reflections	1486 [R_{int} = 0.0261]
Completeness to theta[27.55°]	99.9%
Refinement method	Full matrix Least-squares on F^2
Data/restraints/parameters	1486 / 0 / 87
Goodness-of-fit on F^2	2.329
Refine diff density_max	0.549
Refine diff density_ min	–0.382

Table 4A7. Crystal data and structure refinement for $[SF_3(Phen)][SbF_6]\cdot CH_2Cl_2$

Empirical formula	$C_{14}H_{16}Cl_4F_9N_2SSb$
Formula weight, g mol^{-1}	684.922
Temperature, K	153(2)
Wavelength, pm	71.073
Crystal System	Monoclinic
Space group	$P2_1/c$
Angle-β,º	94.5460(10)°
Unit cell dimensions, Å	a = 13.2776(11)
	b = 9.0216(8)
	c = 18.6778(16)
Volume, 10^2 $Å^3$	22.303(3)
Z	4
Density (calculated), mg mm^{-3}	1.9658
Absorption coefficient, mm^{-1}	1.891
F(000)	1308
Crystal size, mm^3	0.33 × 0.13 × 0.07
Theta range for data collection	1.54° – 27.61°
Index ranges	$-17 \leq h \leq 17$,
	$-11 \leq k \leq 11$,
	$-24 \leq l \leq 24$
Reflections collected	25476
Independent reflections	5153 [R_{int} = 0.0536]
Completeness to theta[27.55°]	99.4%
Refinement method	Full matrix Least-squares on F^2
Data/restraints/parameters	5153 / 0 / 281
Goodness-of-fit on F^2	1.016
Refine diff density_max	1.360
Refine diff density_min	–0.529

Table 4A8. Crystal data and structure refinement for $[SF_2(DMAP)_2][SbF_6]_2 \cdot CH_3CN$

Empirical formula	$C_{15}H_{23}F_{14}N_5SSb_2$
Formula weight, g mol^{-1}	814.948
Temperature, K	153(2)
Wavelength, pm	71.073
Crystal System	Monoclinic
Space group	*C2/c*
Angle-β,º	107.0°
Unit cell dimensions, Å	a = 12.806(8)
	b = 10.699(7)
	c = 22.056(15)
Volume, 10^2 $Å^3$	28.92(3)
Z	4
Density (calculated), mg mm^{-3}	1.8038
Absorption coefficient, mm^{-1}	3.193
F(000)	2268
Crystal size, mm^3	0.21 × 0.22 × 0.36
Theta range for data collection	1.93° – 27.64°
Index ranges	$-16 \leq h \leq 16$,
	$-13 \leq k \leq 13$,
	$-28 \leq l \leq 28$
Reflections collected	9249
Independent reflections	2369 [R_{int} = 0.0742]
Completeness to theta [27.55°]	70.6%
Refinement method	Full matrix Least-squares on F^2
Data/restraints/parameters	2369 / 0 / 190
Goodness-of-fit on	F^2 1.013
Refine diff density_max	0.760
Refine diff density_min	–0.755

Table 4A9. Crystal data and structure refinement for $[SF(DMAP)_4]_2[SbF_6]_3 \cdot 2CH_3CN$

Empirical formula	$C_{60}H_{86}F_{20}N_{18}S_2Sb_3$
Formula weight, g mol^{-1}	1868.852
Temperature, K	153(2)
Wavelength, pm	71.073
Crystal System	Monoclinic
Space group	*C2/c*
Angle-β,º	107.4588(14)°
Unit cell dimensions, Å	a = 16.0316(18)
	b = 17.4013(19)
	c = 19.832(2)
Volume, 10^2 $Å^3$	52.777(10)
Z	4
Density (calculated), mg mm^{-3}	2.2667
Absorption coefficient, mm^{-1}	2.333
F(000)	3040
Crystal size, mm^3	0.15 × 0.19 × 0.33
Theta range for data collection	1.77° – 27.57°
Index ranges	$-20 \leq h \leq 20$,
	$-22 \leq k \leq 22$,
	$-25 \leq l \leq 25$
Reflections collected	29235
Independent reflections	5913 [R_{int} = 0.0718]
Completeness to theta [27.55°]	96.8%
Refinement method	Full matrix Least-squares on F^2
Data/restraints/parameters	5913 / 0 / 370
Goodness-of-fit on F^2	1.113
Refine diff density_max	1.461
Refine diff density_min	–1.149

Appendix – Chapter5

Table 5A1. Crystal data and structure refinement for $WOF_4 \cdot SO_2$

Empirical formula	$W_1O_3S_1F_4$
Formula weight, g mol^{-1}	339.91
Temperature, K	153(2)
Wavelength, pm	71.073
Crystal System	Monoclinic
Space group	$P2_1/c$
Angle-α,º	90°
Angle-β,º	90.530(2)°
Angle-γ,º	90°
Unit cell dimensions, Å	a = 7.7097(15)
	b = 7.2274(14)
	c = 10.244(2)
Volume, 10^2 $Å^3$	570.78(19)
Z	4
Density (calculated), mg mm^{-3}	3.956
Absorption coefficient, mm^{-1}	20.629
F(000)	600
Crystal size, mm^3	0.12 × 0.07 × 0.02
Theta range for data collection	2.64° – 29.09°
Index ranges	$-10 \leq h \leq 10$,
	$-9 \leq k \leq 9$,
	$-13 \leq l \leq 13$
Reflections collected	8547
Independent reflections	1474 [R_{int} = 0.0794]
Completeness to theta[27.55°]	95.9%
Refinement method	Full matrix Least-squares on F^2
Data/restraints/parameters	1474 / 0 / 83
Goodness-of-fit on F^2	1.023
Refine diff density_max	1.697
Refine diff density_min	–1.576

Table 5A2. Crystal data and structure refinement for $[(CH_3)_4N][WOF_5]$

Empirical formula	$C_4H_{12}N_1W_1OF_5$
Formula weight, g mol^{-1}	369.00
Temperature, K	153(2)
Wavelength, pm	71.073
Crystal System	Tetragonal
Space group	*P4/n*
Angle-α,º	90°
Angle-β,º	90°
Angle-γ,º	90°
Unit cell dimensions, Å	a = 8.205(3)
	b = 8.205(3)
	c = 6.989(2)
Volume, 10^2 $Å^3$	470.5(3)
Z	2
Density (calculated), mg mm^{-3}	2.604
Absorption coefficient, mm^{-1}	12.311
F(000)	340
Crystal size, mm^3	0.05 × 0.08 × 0.11
Theta range for data collection	2.92° – 27.47°
Index ranges	$-10 \leq h \leq 10$,
	$-10 \leq k \leq 10$,
	$-9 \leq l \leq 9$
Reflections collected	5020
Independent reflections	537 [R_{int} = 0.0514]
Completeness to theta [27.55°]	98.7%
Refinement method	Full matrix Least-squares on F^2
Data/restraints/parameters	537 / 0 / 32
Goodness-of-fit on F^2	1.105
Refine diff density_max	1.745
Refine diff density_min	–0.436

Table 5A3. Crystal data and structure refinement for $CH_3CN{\cdot}WOF_3(OCH_2CF_3)$

Empirical formula	$C_4H_5N_1W_1O_2F_6$
Formula weight, g mol^{-1}	396.94
Temperature, K	153(2)
Wavelength, pm	71.073
Crystal System	Monoclinic
Space group	*$P2_1/c$*
Angle-α,º	90°
Angle-β,º	97.386(2)°
Angle-γ,º	90°
Unit cell dimensions, Å	a = 8.1236(12)
	b = 12.7219(19)
	c = 8.9834(13)
Volume, 10^2 $Å^3$	920.7(2)
Z	4
Density (calculated), mg mm^{-3}	2.864
Absorption coefficient, mm^{-1}	12.618
F(000)	720
Crystal size, mm^3	0.10 × 0.04 × 0.21
Theta range for data collection	2.53° – 27.49°
Index ranges	$-10 \leq h \leq 10$,
	$-16 \leq k \leq 16$,
	$-11 \leq l \leq 11$
Reflections collected	10600
Independent reflections	2117 [R_{int} = 0.0664]
Completeness to theta[27.55°]	99.8%
Refinement method	Full matrix Least-squares on F^2
Data/restraints/parameters	2117 / 0 / 129
Goodness-of-fit on F^2	1.109
Refine diff density_max	1.674
Refine diff density_min	–1.680

Appendix – Chapter6

Table 6A1. Crystal data and structure refinement for $PFOA{\cdot}H_2O$

Empirical formula	$C_8H_3O_3F_{15}$
Formula weight, g mol^{-1}	432.10
Temperature, K	153(2)
Wavelength, pm	71.073
Crystal System	Monoclinic
Space group	$P2_1/c$
Angle-α,º	90°
Angle-β,º	91.215(8)°
Angle-γ,º	90°
Unit cell dimensions, Å	a = 22.752(14)
	b = 5.309(3)
	c = 11.026(7)
Volume, 10^2 $Å^3$	1331.5(15)
Z	4
Density (calculated), mg mm^{-3}	2.155
Absorption coefficient, mm^{-1}	0.290
F(000)	840
Crystal size, mm^3	0.132 × 0.266 × 0.560
Theta range for data collection	2.92° – 27.47°
Index ranges	$-10 \leq h \leq 10$,
	$-10 \leq k \leq 10$
	$-9 \leq l \leq 9$
Reflections collected	5020
Independent reflections	537 [R_{int} = 0.0514]
Completeness to theta [27.55°]	98.7%
Refinement method	Full matrix Least-squares on F^2
Data/restraints/parameters	537 / 0 / 32
Goodness-of-fit on F^2	1.105
Refine diff density_max	1.745
Refine diff density_min	–0.436

Table 6A2. Crystal data and structure refinement for SPFO

Empirical formula	$C_8O_3F_{15}Na$
Formula weight, g mol^{-1}	452.05
Temperature, K	153(2)
Wavelength, pm	71.073
Crystal System	Monoclinic
Space group	$P2_1/c$
Angle-α,º	90°
Angle-β,º	95.472(18)°
Angle-γ,º	90°
Unit cell dimensions, Å	a = 22.43(4)
	b = 5.878(11)
	c = 9.626(17)
Volume, 10^2 $Å^3$	1263.0(4)
Z	4
Density (calculated), mg mm^{-3}	2.291
Absorption coefficient, mm^{-1}	0.318
F(000)	828
Crystal size, mm^3	0.126 × 0.147 × 0.409
Theta range for data collection	1.82° – 18.30°
Index ranges	$-19 \leq h \leq 19$,
	$-105 \leq k \leq 5$,
	$-8 \leq l \leq 8$
Reflections collected	4967
Independent reflections	913 [R(int) = 0.0946]
Completeness to theta [27.55°]	99.7%
Refinement method	Full matrix Least-squares on F^2
Data/restraints/parameters	913 / 0 / 236
Goodness-of-fit on F^2	1.421
Refine diff density_max	0.253
Refine diff density_min	–0.222

Table 6A3. Crystal data and structure refinement for PFDA·H_2O

Empirical formula	$C_{10}H_3O_3F_{19}$
Formula weight, g mol^{-1}	532.12
Temperature, K	153(2)
Wavelength, pm	71.073
Crystal System	Monoclinic
Space group	$P2_1/c$
Angle-α,º	90°
Angle-β,º	95.350(4)°
Angle-γ,º	90°
Unit cell dimensions, Å	a = 27.035(10)
	b = 5.396(2)
	c = 10.944(4)
Volume, 10^2 $Å^3$	1589.6(11)
Z	4
Density (calculated), mg mm^{-3}	2.223
Absorption coefficient, mm^{-1}	0.300
F(000)	1032
Crystal size, mm^3	0.106 × 0.218 × 0.778
Theta range for data collection	2.27° – 27.47°
Index ranges	$-34 \leq h \leq 34$,
	$-6 \leq k \leq 6$,
	$-14 \leq l \leq 14$
Reflections collected	16265
Independent reflections	3589 [R(int) = 0.0407]
Completeness to theta [27.55°]	99.0%
Refinement method	Full matrix Least-squares on F^2
Data/restraints/parameters	3589 / 0 / 302
Goodness-of-fit on F^2	1.108
Refine diff density_max	0.660
Refine diff density_min	–0.565

Table 6A4. Crystal data and structure refinement for SPFB

Empirical formula	$C_4F_7O_2Na$
Formula weight, g mol^{-1}	236.02
Temperature, K	153(2)
Wavelength, pm	71.073
Crystal System	Monoclinic
Space group	$P2_1/c$
Angle-α,º	90°
Angle-β,º	99.069(8)°
Angle-γ,º	90°
Unit cell dimensions, Å	a = 25.99(2)
	b = 6.113(5)
	c = 9.181(7)
Volume, 10^2 $Å^3$	1440.4(19)
Z	4
Density (calculated), mg mm^{-3}	1.048
Absorption coefficient, mm^{-1}	0.326
F(000)	912
Crystal size, mm^3	0.106 × 0.109 × 0.263
Theta range for data collection	1.59° – 21.30°
Index ranges	$-26 \leq h \leq 21$,
	$-6 \leq k \leq 6$,
	$-9 \leq l \leq 9$
Reflections collected	2333
Independent reflections	806 [R(int) = 0.0279]
Completeness to theta [27.55°]	99.1%
Refinement method	Full matrix Least-squares on F^2
Data/restraints/parameters	806 / 0 / 128
Goodness-of-fit on F^2	3.078
Refine diff density_max	0.384
Refine diff density_min	–0.254